Constraining gravity models with clusters of galaxies

by

Harry Wilcox

The thesis is submitted in partial fulfillment of the requirements for the award of the degree of
Doctor of Philosophy
of the
University of Portsmouth

November 2016

Declaration

Whilst registered as a candidate for the above degree, I have not been registered for any other research award. The results and conclusions embodied in this thesis are the work of the named candidate and have not been submitted for any other academic award.

The following chapters are based on the published work:

- Chapter 4 and 5 - Harry Wilcox, David Bacon, Robert C. Nichol, Philip J. Rooney, Ayumu Terukina, A. Kathy Romer, Kazuya Koyama, Gong-Bo Zhao, Ross Hood, Robert G. Mann, Matt Hilton, Maria Manolopoulou, Martin Sahlén, Chris A. Collins, Andrew R. Liddle, Julian A. Mayers, Nicola Mehrtens, Christopher J. Miller, John P. Stott, and Pedro T. P. Viana, *The XMM Cluster Survey: testing chameleon gravity using the profiles of clusters* MNRAS (September 11, 2015) Vol. 452 1171-1183

- Chapter 3 - Harry Wilcox, Robert C. Nichol, Gong-Bo Zhao, David Bacon, Kazuya Koyama and A. Kathy Romer, *Simulation tests of galaxy cluster constraints on chameleon gravity* MNRAS submitted

- Chapter 6 - Jeremy Sakstein, Harry Wilcox, David Bacon, Kazuya Koyama and Robert C. Nichol, *Constraining Beyond Horndeski Theories Using Galaxy Clusters* JCAP submitted

Abstract

An accepted explanation for the accelerated expansion of the late-time Universe is to modify the Einstein equation, either by adding a component to the energy-momentum tensor via dark energy, or to the Einstein tensor via a modification to gravity. The second of these options often involves the introduction of a scalar field, which couples to the matter components of the Universe and gives rise to a fifth force, of the same order of magnitude as gravity. Through a variety of experiments and astronomical observations, this fifth force has been demonstrated to be negligible on Terrestrial and Solar System scales. Therefore if it does act on large scales, it must be suppressed, or 'screened', on small scales.

In this thesis, I place constraints upon one of these screening methods, chameleon gravity. Chameleon gravity postulates the existence of a scalar field that couples with matter to mediate a fifth force. If it exists, this fifth force would influence the hot X-ray emitting gas filling the potential wells of galaxy clusters. However, it would not influence the cluster's weak lensing signal. Therefore, by comparing X-ray and weak lensing profiles, upper limits can be placed on the strength of a fifth force.

To do so I first present two hydrodynamical simulations, one evolved under ΛCDM+GR and the other under $f(R)$. From these two simulations I generate X-ray surface brightness and weak lensing profiles for a number of simulated clusters. Using these profiles I test many of the assumptions of the technique used to constraint $|f_{\rm R0}|$. I then use these profiles to test the analytic pipelines developed to constrain $f(R)$ gravity by applying a full MCMC analysis. From doing so I find constraints on the modified gravity parameters of $|f_{\rm R0}| < 8.3 \times 10^{-5}$.

Next I outline the creation of a sample of 58 clusters, including 12 new to the literature, with high quality weak lensing data from CFHTLenS and X-ray data from XCS. By stacking these clusters I use a multi-parameter MCMC analysis to constrain the two chameleon gravity parameters (β and ϕ_∞). The fits are consistent with general relativity, not requiring a fifth force. In the special case of $f(R)$ gravity (where $\beta = \sqrt{1/6}$), I set an upper limit on the background field amplitude today of $|f_{\rm R0}| < 6 \times 10^{-5}$ (95% CL). This

is one of the strongest constraints to date on $|f_{\rm R0}|$ on cosmological scales. These fits are also found to be consistent with those recovered from the $f(R)$ simulations.

Finally I look at the future of this method, beginning with forecasting the constraints that this technique will be able to place on $f(R)$ gravity using the Dark Energy Survey, finding $|f_{R0}|> 2 \times 10^{-5}$. Next I discuss how the X-ray surface brightness profiles might be improved by removing contaminating point sources from the X-ray images and find that doing so leads to a reduction in the error bars of $\sim 5\%$. I end this thesis by detailing how the techniques discussed within can be applied to constrain other modified gravity theories, namely the Vainshtein mechanism. Doing so I am able to place competitive constraints upon Vainshtein gravity, including the first ever constraint on a particular parametrisation.

Acknowledgements

I would first like to thank my supervisors, Bob Nichol and David Bacon, for all their guidance and assistance throughout this project, leading me to become a far better researcher for it. My thanks also go out to Kathy Romer for her much valued input and guidance throughout my entire university career.

Being at the ICG has allowed me to tap into a wealth of experience and expertise that have greatly aided this endeavour, so to that end I also extend my particular thanks to Kazuya Koyama, Gong-bo Zhao and Jeremy Sakstein.

Additionally, to all those associates who have enriched my time throughout this PhD, both inside and outside the ICG, I offer my thanks, in no particular order, to Cullan, Tom, Claire, Nick, David, Weeman, Phil, James, Alan and Julian.

Lastly, I would like thank Mum, Dad, Gran, Grandpa, Tom and Jack for all their support, enjoyment and encouragement over the years. And most of all to Sarah who, aside from undertaking the arduous task of proofreading this thesis (for which I apologise for my seeming hatred of apostrophes!), was always there and a constant source of support.

Contents

List of Figures

List of Tables

Chapter 1

Introduction: Cosmology and Gravitation

One of the biggest surprises in modern cosmology was that measurements of supernovae by two teams in the late '90s (Riess et al. 1998, Perlmutter et al. 1999) suggested the Universe everywhere was currently undergoing a period of accelerated expansion. An accepted explanation for this accelerated expansion of the late-time Universe is to modify the Einstein field equations, either by adding a component to the energy-momentum tensor via dark energy, or to the Einstein tensor via a modification to gravity (Milgrom 1983, Clifton et al. 2012). The latter often involves the introduction of a scalar field coupled to the matter components of the Universe, giving rise to a fifth force of the same order of magnitude as gravity (Jain et al., 2013).

Through a variety of experiments and astronomical observations, this fifth force has been demonstrated to be negligible at terrestrial and solar system densities (Wagner et al., 2012). Therefore, if a fifth force does exist it must be suppressed, or 'screened', in high density regions and only take effect in low density regions.

In this chapter I begin with a discussion of general relativity and look at two of its important consequences, the Einstein field equations and the hydrostatic equation. I will then review a possible method to provide a screening for the fifth force – the chameleon mechanism. I then discuss a widely used set of models which include a chameleon, $f(R)$ gravity. Continuing on I look into some of the predicted effects in the presence of such a screening.

1.1 General Relativity

Any discussion of gravity must begin with Einstein's famous theory - General Relativity (GR, Einstein 1916). The underlying idea behind this theory is the equivalence principle. This states that a body's inertial mass is equal to its gravitational mass. As a consequence, a body freely falling under gravity cannot distinguish its situation from one where it is stationary but without a gravitational field present.

GR provides a description of gravity as a geometric property of space-time, governed by the energy and momentum of matter and radiation within it. To quote John Archibald Wheeler "Space-time tells matter how to move; matter tells space-time how to curve" (Wheeler, 2010). To define a space-time metric that describes this curvature, an expression for a line element showing the separation of two points is first needed

$$ds^2 = g_{\mu\nu} dx^\mu dx^\nu, \tag{1.1}$$

where $g_{\mu\nu}$ is the the metric tensor, which in a flat space-time $g_{\mu\nu} = (-1, 1, 1, 1)$. The Riemann curvature tensor, which describes how the curvature of space-time departs from the Euclidean result, can then be defined from this metric,

$$R^\rho{}_{\sigma\mu\nu} = \partial_\mu \Gamma^\rho{}_{\sigma\nu} - \partial_\nu \Gamma^\rho{}_{\sigma\mu} + \Gamma^\rho{}_{\lambda\mu}\Gamma^\lambda{}_{\sigma\nu} - \Gamma^\rho{}_{\lambda\nu}\Gamma^\lambda{}_{\sigma\mu}, \tag{1.2}$$

where $\Gamma^\rho{}_{\sigma\nu}$ are the Christoffel symbols. These describe an affine connection, allowing the parallel transport of vectors around a curved space-time, and are derived from the metric and its derivatives

$$\Gamma^\rho{}_{\sigma\nu} = \frac{1}{2} g^{\rho\gamma} \left(\frac{\partial g_{\gamma\nu}}{\partial x^\sigma} + \frac{\partial g_{\gamma\sigma}}{\partial x^\nu} - \frac{\partial g_{\sigma\nu}}{\partial x^\gamma} \right). \tag{1.3}$$

Where there is curvature, a vector parallel transported around a closed path will not return with its original orientation and the Riemann tensor is used to measure this difference. In a flat space-time, transporting vectors around a closed loop does not alter their orientation so $\Gamma^\rho{}_{\sigma\nu} = 0$ and therefore $R^\rho{}_{\sigma\mu\nu} = 0$.

The Riemann tensor can then be contracted over to find the Ricci tensor. The Ricci tensor can then be contracted over to find the Ricci scalar

$$R_{\mu\nu} = R^{\rho}_{\mu\rho\nu} \qquad\qquad R = g^{\mu\nu}R_{\mu\nu}. \tag{1.4}$$

Combining these two along with the metric tensor leads to the Einstein curvature tensor, $G_{\mu\nu}$, used throughout GR

$$G_{\mu\nu} = R_{\mu\nu} + \frac{1}{2}g_{\mu\nu}R. \tag{1.5}$$

The energy momentum tensor

As GR is a description of the relation between matter and curvature, the tensor defined above must relate to a tensor describing the energy density of the Universe. For this the energy momentum tensor for a perfect fluid is used. This tensor fulfils the cosmological principle and describes the energy and momentum of space-time as a function of its pressure, P, and density, ρ,

$$T^{\mu\nu} = (\rho c^2 + p)U^{\mu}U^{\nu} + pg^{\mu\nu}, \tag{1.6}$$

where U is the four velocity of the fluid. From this energy momentum conservation can be neatly defined as

$$T^{\mu}_{\nu;\mu} = 0, \tag{1.7}$$

where the semicolon above indicates a covariant derivative.

The Einstein field equations

It is possible to derive the EFE from the space-time action, the integral of a system over its Lagrangian. By first deriving a Lagrangian to describe space-time and another

Lagrangian to describe the energy and matter in the Universe, $\mathcal{L}_{\mathcal{M}}$, the Einstein-Hilbert action is

$$S = \int \left(\frac{c^4}{16\pi G} R + \mathcal{L}_{\mathcal{M}} \right) \sqrt{-g} d^4x, \tag{1.8}$$

where G is Newton's gravitational constant. By applying the principle of least action, $\delta S = 0$, to Equation 1.8 it is possible to more rigorously derive the Einstein equation, discussed in greater detail in Appendix B, with the result stated here

$$G_{\mu\nu} = \frac{8\pi G}{T}_{\mu\nu}. \tag{1.9}$$

Hydrostatic equilibrium in GR

It is possible to derive from GR, an equation which describes the relation of a fluids pressure, to it's density, known as the hydrostatic equilibrium equation. Taking the equation for a perfect fluid, Equation 1.6, and plugging it into the EFE (Equation 1.9) allows the derivation (Oppenheimer and Volkoff, 1939)

$$\frac{dP}{dr} = -\frac{GM(r)\rho(r)}{r^2} \left(1 + \frac{P(r)}{\rho(r)c^2} \right) \left(1 + \frac{4\pi r^3 P(r)}{M(r)c^2} \right) \left(1 - \frac{2GM(r)}{rc^2} \right)^{-1}. \tag{1.10}$$

Taking the non-relativistic limit,

$$\left(1 + \frac{P(r)}{\rho(r)c^2} \right) \left(1 + \frac{4\pi r^3 P(r)}{M(r)c^2} \right) \left(1 - \frac{2GM(r)}{rc^2} \right)^{-1} \xrightarrow{c \gg P(r), M(r)} 1, \tag{1.11}$$

equation 1.10 can be simplified into its common form

$$\frac{dP}{dr} = -\frac{GM(r)\rho(r)}{r^2}. \tag{1.12}$$

This is the hydrostatic equilibrium equation. This relation is later used in Section 1.5 when it is used as an assumption describing the dynamical state of clusters (described in Section 2.1) and investigated in Section 5.5.

1.2 Theoretical cosmology

The Friedmann-Lemaître-Robertson-Walker Metric

The cosmological principle states that on the largest scales the Universe is both isotropic and homogeneous, that is there is no preferred direction and the Universe is the same everywhere. The most general metric that fulfils these requirements is the Friedman-Lemaître-Robertson-Walker metric (FLRW, Friedmann 1922, Lemaître 1931, Robertson 1935, Walker 1937), which in spherical coordinates is given by

$$\mathrm{d}s^2 = \mathrm{d}t^2 - a(t)^2 \left(\frac{\mathrm{d}r^2}{1 - kr^2} + r^2 \mathrm{d}\theta^2 + r^2 \sin^2 \mathrm{d}\phi^2 \right), \tag{1.13}$$

where t is the proper time – the time measured on a world line by a clock moving with that world line and a is the scale factor, which measures the relative expansion of the Universe as a function of time, and is commonly normalised $a = 1$ at present when the curvature is flat. Then r is the comoving coordinate distance, a distance that remains constant if two objects are only moving with the Hubble flow. Finally k represents the spatial curvature, which takes one of three values, -1, 0 or $+1$. A negative curvature, $k = -1$, corresponds to an open Universe, a zero curvature, $k = 0$, corresponds to flat Universe and a positive curvature, $k = 1$, corresponds to a closed Universe.

The value of the Ricci scalar (described in Equation 1.4) in an FLRW Universe (Carroll, 1997) can be calculated, which will be useful when calculating the Universe's properties in a modified gravity framework.

By calculating the Christoffel symbols, described in Equation 1.3, and plugging them into the Ricci tensor (described in 1.4), it can be seen that the only relevant non-zero factors are the trace, and these components have the values

$$R_{00} = -3 \left(\frac{\ddot{a}}{a} \right) \qquad R_{ij} = \delta_{ij}(2\dot{a}^2 + \ddot{a}a). \tag{1.14}$$

assuming where that $k = 0$. Contracting over the Ricci tensor then gives the Ricci scalar for an FLRW Universe,

$$R = -6\left[\frac{\ddot{a}}{a} + \left(\frac{\dot{a}}{a}\right)^2\right]. \tag{1.15}$$

The Friedmann equation

The Friedmann equation (Friedmann, 1922) relates the evolution of the scale factor with time to the density, ρ, and pressure, P, of a Universe that is described by an FLRW metric (Equation 1.13)

$$\left(\frac{\dot{a}}{a}\right)^2 = \frac{8\pi G}{3}\rho - \frac{kc^2}{a^2}. \tag{1.16}$$

Taking the derivative of Equation 1.16 gives the acceleration equation

$$\frac{\ddot{a}}{a} = -\frac{4\pi G}{3}\left(\rho + 3P\right), \tag{1.17}$$

where the pressure, P, arises from the conservation of energy. The Friedmann equation can rewritten in terms of the Hubble parameter, $H(t)$, which is used to describe the rate of change of the scale factor

$$\frac{\dot{a}}{a} = H(t). \tag{1.18}$$

The value of the Hubble parameter at the present redshift (i.e. 0: redshift is discussed in more detail later in this section) is commonly referred to as the Hubble constant, $H(t_0) = H_0$. If a galaxy's motion is purely due to the expansion of the Universe (i.e. it has no peculiar velocity), this motion is known as Hubble flow. The Hubble constant can then be used to relate a galaxy's velocity, v, to its proper distance, d,

$$v = H_0 d. \tag{1.19}$$

H_0 has SI units of s^{-1}, but is commonly quoted in units of $\mathrm{kms}^{-1}\mathrm{Mpc}^{-1}$. It is however far more common to quote measurements of H_0 in terms of the dimensionless parameter h_0, defined as

$$H_0 = 100h_0 \mathrm{kms}^{-1}\mathrm{Mpc}^{-1}. \tag{1.20}$$

Since its definition, the Hubble constant has become one of the most popular parameters of the Universe to measure, with the best current measurements suggesting $h_0 = 0.678 \pm 0.009$ (Planck Collaboration, 2014). The sources of this measurement is discussed in Section 1.3.

The Friedmann equation relates the evolution of the scale factor with the total energy density in the Universe. By rewriting Equation 1.16 in terms of the Hubble parameter it is possible to define a critical density, ρ_c, which will ensure a flat Universe (i.e. $k = 0$)

$$\rho_c = \frac{3H^2}{8\pi G}. \tag{1.21}$$

From this the density parameter can be defined to be the ratio of some density component of the Universe (be it matter, ρ_m, radiation, ρ_γ or a cosmological constant ρ_Λ) to ρ_c, i.e.

$$\Omega_i \equiv \frac{\rho_i}{\rho_c}. \tag{1.22}$$

The total energy density of the Universe can then be defined as the sum of its different density components, which in a flat Universe is exactly equal to 1

$$\Omega \equiv \Omega_m + \Omega_\gamma + \Omega_\Lambda = 1. \tag{1.23}$$

In a Universe that exhibits spatial curvature, $\Omega \neq 1$ and the total density will contain a contribution from the curvature, Ω_k. It is thought that in the Universe, $\Omega \approx 1$ as $\Omega_k \approx 0$ (Planck Collaboration, 2015b).

Redshift

In the early 20th century, by measuring the recession velocity and distance of 22 galaxies Edwin Hubble discovered that the Universe was expanding (Hubble, 1929). One consequence of this fact is that photons emitted from sources that are cosmological distances

away will have had their wavelengths stretched by the time they reach us.

This can be seen by considering the FLRW metric for a null geodesic, $ds^2 = 0$, the path upon which photons travel for a light ray emitted at time t_e and observed later at time t_o,

$$\int_{t_e}^{t_o} \frac{\mathrm{d}t}{a(t)} = \int_0^D \frac{\mathrm{d}r}{1 - kr^2}. \tag{1.24}$$

This is known as the comoving distance, which grows as the Universe expands. Objects that have no motion apart from the expansion of the Universe will have a constant comoving distance separation and are said to move with the Hubble flow. As the comoving coordinate, r, is constant, photons will undergo time dilation dependent upon the expansion of the Universe between time t_e and t_o. This leads to the relation

$$\frac{\mathrm{d}t_e}{a(t_e)} = \frac{\mathrm{d}t_o}{a(t_o)}, \tag{1.25}$$

which can be written in terms of the redshift, z, given by

$$1 + z = \frac{\nu_e}{\nu_o} = \frac{a(t_o)}{a(t_e)}, \tag{1.26}$$

where the ν factors are the photon's frequency. It is more common to think of redshift as a change in a photon's wavelength due to a difference in scale factor, or

$$1 + z = \frac{\lambda_o}{\lambda_e} = \frac{1}{a(t_e)}. \tag{1.27}$$

Laboratory experiments have very accurately measured the rest wavelengths of the photons seen from astronomical bodies, by measuring the wavelengths of photons emitted by their celestial counterparts. Using this information, the object's redshift can be measured.

Cosmological distance measurements

Due to the expansion of space-time and its curved nature the concept of distance in cosmology can become ambiguous. Consequently several differing definitions of distance are used in astronomy and the most common described below.

I have already defined one of these, the **comoving distance**, r in Equation 1.24.

Another measure of distance is the **luminosity distance**, which is the the distance measured to an object under the assumption that the inverse square law for luminosity was always true

$$D_L = \left(\frac{L}{4\pi F}\right)^2, \tag{1.28}$$

where L is the sources intrinsic luminosity and F its measured flux. The luminosity distance can also be defined by the relationship between and objects absolute magnitude, M, and its apparent magnitude, m,

$$D_L = 10^{\frac{m-M}{5}+1}. \tag{1.29}$$

The **angular diameter distance** relates an objects true size, A, with its apparent angular size, Ω,

$$D_A = \frac{A}{\Omega}. \tag{1.30}$$

In a flat Universe this can be related to the objects comoving distance and luminosity

$$D_A = \frac{r}{1+z} = \frac{D_L}{(1+z)^2}. \tag{1.31}$$

In weak lensing this is the distance measure most commonly used.

1.3 Cosmological probes

There is much observational evidence that the Universe is currently undergoing a period of accelerated expansion, where the second derivative of the scale factor, a, is positive. This section will describe three of the main observables that support this paradigm: Type 1a supernovae, the Large Scale Structure (LSS) of the Universe and the Cosmic Microwave Background (CMB).

1.3.1 Supernovae Type 1a

A white dwarf star that is a part of a binary system will occasionally gain mass from its companion, either through accretion or by merging. If the total mass of the white dwarf increases to reach the Chandrasekhar limit ($\sim 1.38 M_{\odot}$), electron degeneracy pressure is no longer sufficient to prevent further gravitational collapse. This causes the white dwarf to explode in a supernova (Mazzali et al., 2007). This type of supernova is known as a Supernova Type 1a (SN1a) and is thought to always occur from the same mass progenitor. The temporal evolution of the luminosity follows a characteristic light curve as shown in Figure 1.1.

These light curves are standardisable by correcting for the colour and stretch (Phillips, 1993). To correct for the colour the peak of each of the lightcurves in Figure 1.1 are placed at the same magnitude. The decline rate of the brightness after maximum light is proportional to the width of the maximum and the peak brightness, allowing the lightcurves to be 'stretched' to fit atop each other. From the measured flux it then becomes possible to infer the supernova's distance via the inverse square law. This distance measurement is known as the luminosity distance and is given by

$$D_L = \sqrt{\frac{L}{4\pi F}}, \tag{1.32}$$

where L is the luminosity and F the flux. The luminosity distance of the supernova can be plotted against redshift to make a Hubble diagram, as shown in Figure 1.2. By comparing the measured luminosity distances at different redshifts to the expected luminosity distances under the assumption of different cosmological models, it becomes possible to place constraints upon cosmological parameters. It was from this that two teams discovered the acceleration of the Universe.

1.3.2 LSS

Initial perturbations in the very early Universe caused spherical shells of baryonic matter coupled with photons, to be driven outwards at the speed of sound. These pressure waves then ceased once the Universe had cooled sufficiently for the photons to decouple from the matter, causing the matter to freeze in shells of overdensity at the sound horizon.

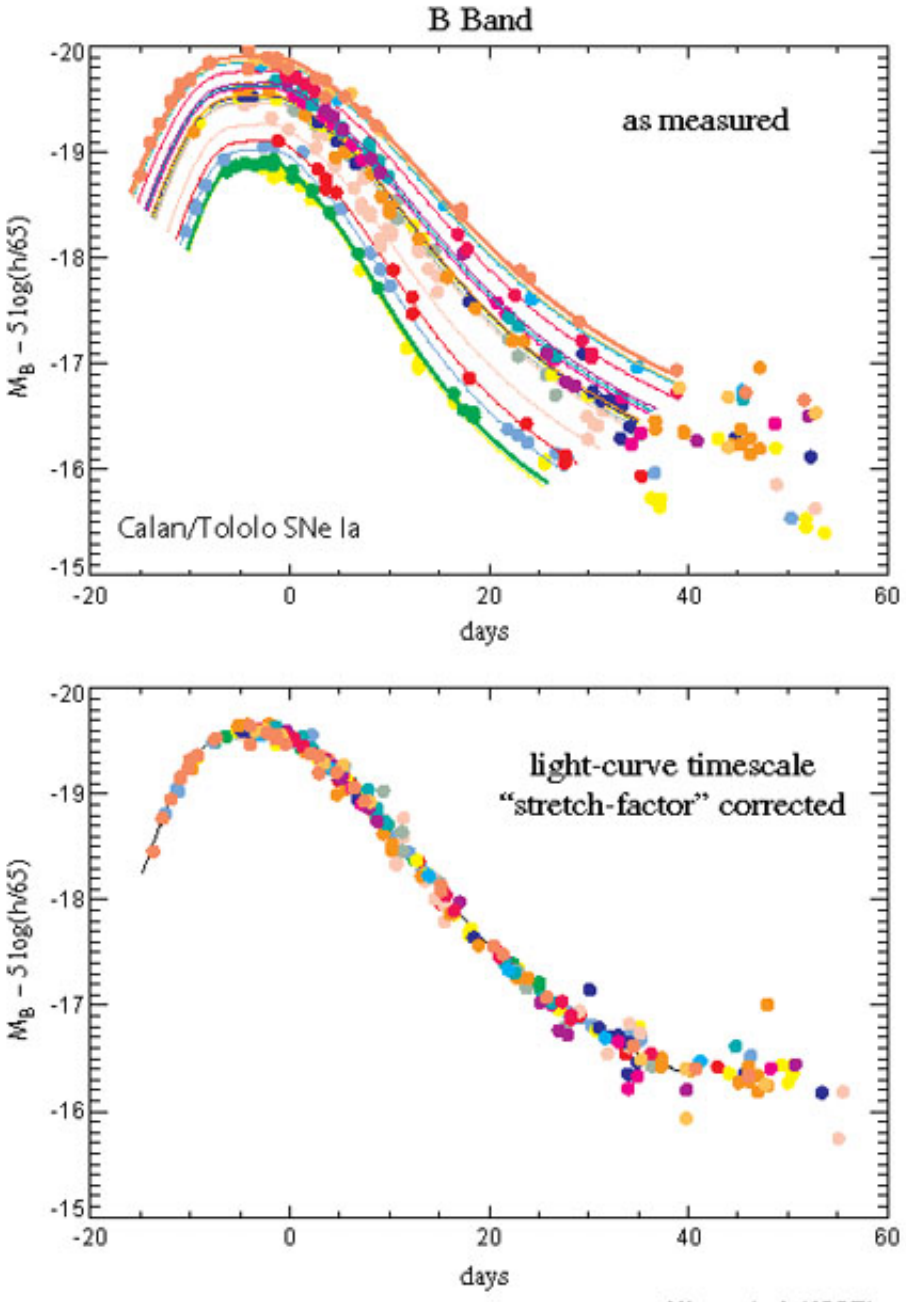

FIGURE 1.1: B-band lightcurves for low-redshift SNIa from the Calan-Tololo survey on top. Each different coloured line represents a different supernova. The bottom plot shows the same lightcurves after corrections showing how the lightcurves of type 1a supernovae are standardisable and can therefore be used as cosmological candles. Figure from Frieman et al. (2008).

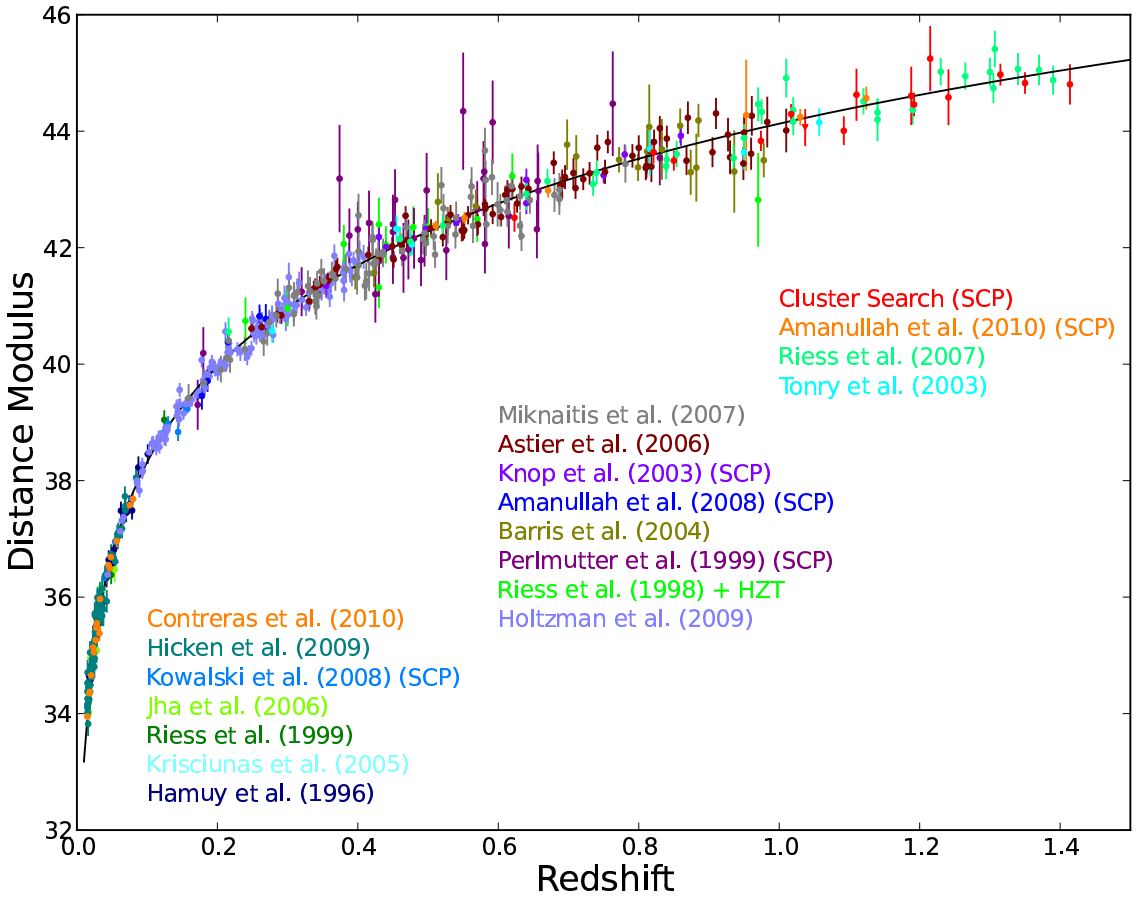

FIGURE 1.2: Distance modulus (the difference between apparent mangitude, the measured brightness from the Earth, and absolute magnitude, the objects intrinsic brightness) against redshift of SNN1a collated from many surveys. This figure shows there is a relationship between a supernova's intrinsic brightness and its redshift. Figure from Suzuki et al. (2012).

This means that today there is a preferred length scale in the Universe at which galaxies are separated (Eisenstein, 2005). This effect is known as Baryon Acoustic Oscillations (BAO), and provides a standard ruler in the Universe.

The BAO signal is weak and only present at large scales, therefore requiring large volume surveys in order to detect its existence. The Baryon Oscillation Spectroscopic Survey (BOSS, Anderson et al. 2014) has measured this overdensity using the matter correlation function in a volume of 14.5Gpc^3, shown in Figure 1.3. Here the BAO feature is seen as a bump in the correlation function at ~ 110Mpc, which can be used to constrain a number of cosmological parameters including dark energy parameters.

Another probe of the underlying cosmology measured by the large scale structure is Redshift Space Distortions (RSD, Kaiser 1987). These distortions arise when the distance to an object is inferred using the Hubble relation by measuring its redshift (as discussed in

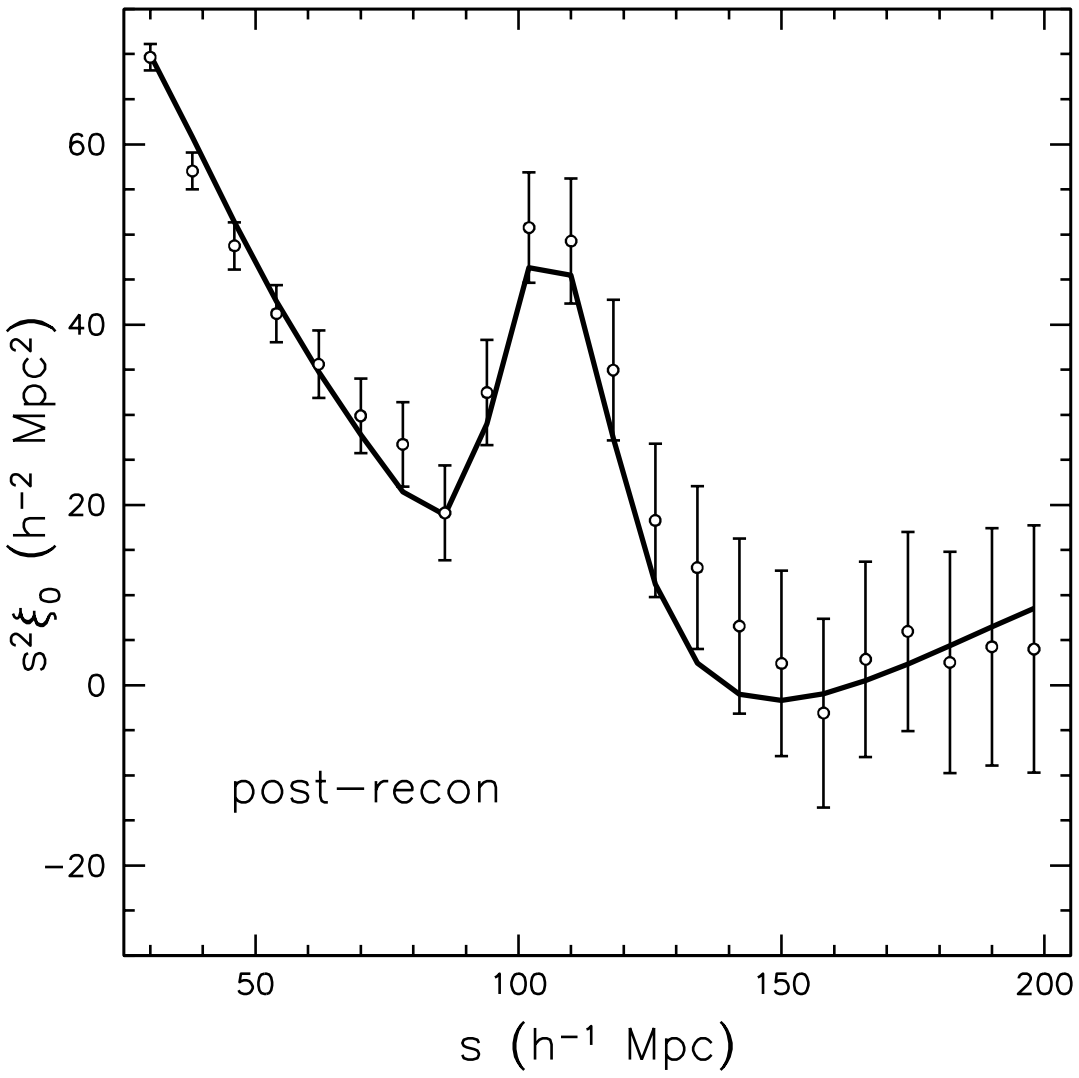

FIGURE 1.3: Figure showing the correlation of BOSS galaxies as a function of separation (circles) along with a best fit model. This figure clearly shows an abundance of correlated galaxies at $\approx 120 h^{-1}$Mpc - this is the BAO feature. Figure from Anderson et al. (2014).

Section 1.2). Galaxies, however, have peculiar velocities as they fall into nearby potential wells meaning that a galaxy's measured redshift is a mixture of both its Hubble flow and this additional motion. This results in a elongation of the distribution of galaxies at small scales (where peculiar velocities are comparable to the Hubble flow) and a squashing of the distribution at large scales. These distortions can then be used to probe cosmology (Percival and White, 2009).

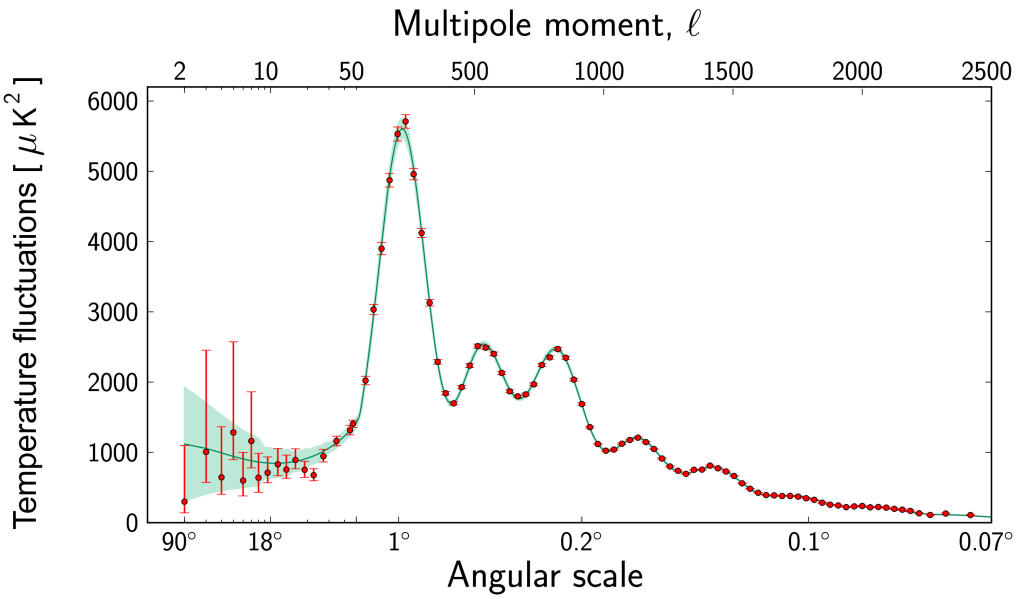

FIGURE 1.4: Planck2015 CMB power spectrum showing temperature fluctuations in the CMB as a function of angular scale. The red points here are the measured data and associated errors while the green line is the theoretical prediction. From the peaks in this data, contraints can be placed upon many cosmological factors. Figure from Planck Collaboration (2015a).

1.3.3 CMB

When the Universe began it was very hot and filled with a dense plasma of photons, protons and electrons. This plasma was so dense the photons were coupled to the matter because the mean free path of each electron was very short due to Thomson scattering (Thomson and Thomson, 1933) by the electrons. However, as the Universe began to expand it also began to cool down to the temperature at which these photons could decouple from the baryonic matter and free stream away. This decoupling occurred at $z \sim 1100$, when the photons had a temperature $T \sim 3000$K (Hinshaw et al., 2009). As the Universe has evolved and expanded these photons have redshifted and cooled down to $T \sim 3$K today. This radiation is known as the Cosmic Microwave Background (CMB). The WMAP satellite first accurately measured the anisotropies in the CMB to 1 part in 10^5, suggesting that at some point in time these photons must have all been in casual contact (Bennett et al., 2013) to have reached a thermal equilibrium. More recently the Planck satellite has made the most accurate measurements of the CMB power spectrum, shown in Figure 1.4.

The size and position of the peaks in the power spectrum carry information about a range of cosmological parameters (Tojeiro, 2006). The position of the first peak is highly dependent upon the curvature of the Universe and the total energy density, and indicates that the Universe is close to being flat and at the critical density. The position of this peak is also slightly dependent upon the presence of dark energy, where more dark energy would increase the size of the Universe and therefore move this peak to larger scales.

The amplitude of the odd peaks is also governed by the gravitational compression of the plasma in the early Universe, so is enhanced in the presence of baryons while the even peaks' amplitude are associated by how much the plasma rarefies. The third peak is sensitive to the ratio of dark matter to radiation and is used as to measure the energy density of dark matter. The damped tail of the CMB power spectrum can be used as a consistency check on the other measurements (Sànchez and Parijskij, 2012).

Using the CMB power spectrum from the Planck satellite, Planck Collaboration (2015b) have placed some of the tightest constraints on a range of cosmological parameters that are all consistent with a ΛCDM Universe.

1.4 Modified gravity

Currently the most successful and popular paradigm used to explain the observed accelerated expansion of the Universe is ΛCDM. In this model the EFE (Equation 1.9) become modified with the addition of a cosmological constant, Λ, also known as dark energy, which permeates all of space and causes this acceleration,

$$R_{\mu\nu} - \frac{1}{2}g_{\mu\nu}R = 8\pi G T_{\mu\nu} + \Lambda g_{\mu\nu}. \tag{1.33}$$

This model also posits the existence of Cold Dark Matter (CDM), a type of matter that does not interact electromagnetically and is therefore invisible. Currently there are many candidate particles for dark matter, such as the WIMP (Jungman et al., 1996) or axions (Turner, 1990), with teams around the globe engaged in searches for these hypothetical particles.

However there are no such viable candidates for dark energy, with its best theoretically motivated source, the vacuum energy of empty space, disagreeing with observations by a

factor of 10^{120} (Weinberg 1989, Martin 2012). Dark energy also suffers from the coincidence problem (Carroll, 2002). Throughout the vast majority of the Universe's history, the Universe was dominated by matter and radiation, while in the future the Universe will become completely dominated by dark energy. It therefore seems coincidental that humanity is currently living through the short period of the Universe's history in which the contribution to the energy density from both matter and dark energy are comparable.

These issues have led cosmologists to investigate other explanations for the accelerated expansion of the Universe (as described in Section 1.3). One potential alternative to dark energy is to modify the theories of gravity to account for this accelerated expansion. Discussed below is a popular modification to gravity that will later be tested using observational data.

1.4.1 Chameleon Mechanism

One model that includes a screening capable of passing solar system tests (discussed in Section 2.3), while still producing a non-negligible modification to gravity is the chameleon mechanism (Khoury and Weltman, 2004). In this approach, the scalar field coupling strength is sensitive to the depth of the local gravitational potential. In regions with a large potential well, this screening suppresses the fifth force and gravity behaves as predicted by GR. However when the potential becomes small, the fifth force is unsuppressed and gravity becomes 'modified' compared to GR (Lombriser, 2014).

The simplest models exhibiting this behaviour are the so called chameleon fields, which have properties dependent upon their surroundings. The simplest models of this type have potentials that are a monotonic function of the scalar field. Commonly used is the inverse power law potential

$$V(\phi) = \frac{\Lambda^{4+n}}{\phi^n}, \tag{1.34}$$

where Λ and n are model constants (Terukina and Yamamoto, 2012). The choice of potential is not important for the analysis as within the cluster the scalar field, ϕ, is not dependent upon Λ and n, as detailed below.

By definition, the action of the chameleon field satisfies

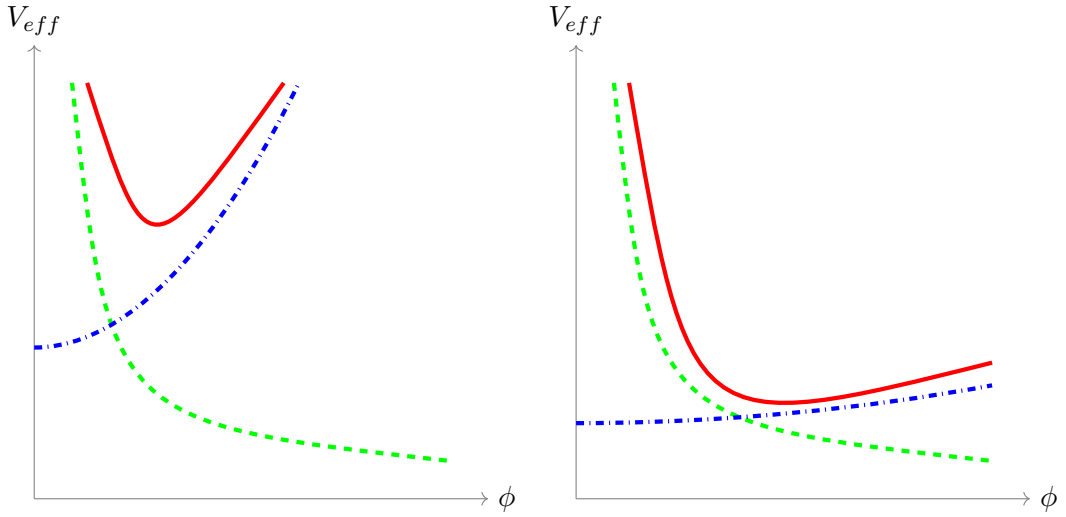

(A) Large ρ (B) Small ρ

FIGURE 1.5: The chameleon effective potential, V_{eff} in solid red is the summation of its two components. In dashed green the actual potential, $V(\phi)$ and in dot dashed blue the coupling of the chameleon field to the local matter density, ρ. Figure 1.5a shows the case for a large density and Figure 1.5b for a small density showing that in high density regions the chameleon field is suppressed.

$$S = \int \left(\frac{M_{\rm Pl}^2}{2} R - \frac{1}{2} \partial\phi^2 - V(\phi) \right) \sqrt{-g} d^4x - \int \mathcal{L}(\psi_i, g_{\mu\nu}) d^4x, \tag{1.35}$$

where $M_{\rm Pl}$ is Planck mass. The equation of motion that can be derived from this is then

$$\nabla^2 \phi = V_{,\phi} + \frac{\beta}{M_{\rm Pl}} \rho \exp(\beta\phi / M_{\rm Pl}), \tag{1.36}$$

(Khoury and Weltman, 2004), where β[1] is the coupling between matter and the scalar field; ϕ gives the position dependent screening efficiency; $M_{\rm Pl}$ is the Planck mass and ρ is the matter density. It can be seen from this equation that the dynamics of the scalar field are not solely governed by $V(\phi)$, but by an effective potential

$$V_{eff}(\phi) = V(\phi) + \rho \exp(\beta\phi / M_{\rm Pl}), \tag{1.37}$$

where the potential is dependent upon the density of matter, ρ. Although $V(\phi)$ is monotonic, provided that $\beta > 0$, V_{eff} will exhibit a minimum at a finite field value, $\phi = \phi_{\rm min}$. Therefore

[1]Here this β is different to the β used to describe X-ray surface brightness profiles in Section 2.2.2.

$$V_{,\phi}(\phi_{\rm min}) + \frac{\beta}{M_{\rm Pl}}\rho\exp(\beta\phi_{\rm min}/M_{\rm Pl}) = 0. \tag{1.38}$$

The mass associated with this field at the minimum is then given by

$$m^2_{\rm min} = V_{,\phi\phi}(\phi_{\rm min}) + \frac{\beta^2}{M^2_{\rm Pl}}\rho\exp(\beta\phi_{\rm min}/M_{\rm Pl}) \tag{1.39}$$

Equations 1.38 and 1.39 show that the local value of the field and its mass are dependent upon the local matter density Figure 1.5a shows this in a high density situation and Figure 1.5b in a low density situation. At high densities the field has a smaller value, with a steeper potential and large effective mass. In Planck units mass is inversely proportional to length, so this large mass gives the field a very short range. As tests of gravity on Earth and within the solar system (discussed in more detail in 2.3) are made on macroscopic scales the microscopic range of the screened field allows it to evade local tests of gravity.

A consequence of the chameleon field is the arising of an additional force known as the chameleon fifth force, defined as

$$F_\phi = -\frac{\beta}{M_{\rm Pl}}\nabla\phi. \tag{1.40}$$

1.4.2 $f(R)$ gravity

There is a set of gravity models known as $f(R)$ models, that were first developed in Buchdahl (1970). These models are generalised forms of GR and are therefore some of the simplest modified gravity theories. They are popular due to this simplicity; the fact that they do not require the introduction of any new type of matter; and can match the observed accelerated expansion (as described in Section 1.3). These models however are generally ruled out by solar system tests of gravity (Brax et al. 2008, discussed further in Section 2.3).

These models can however bypass these restrictions by employing a chameleon mechanism, (as discussed in Section 1.4.1) to suppress them in high density environments. These models can be formulated as a scalar-tensor theory where the fifth force arises from modifying the Einstein-Hilbert action (shown for GR in Equation 1.8) by adding a scalar function,

$f(R)$, to the Ricci scalar (Capozziello 2002; Nojiri and Odintsov 2003). To do so a fixed coupling strength of the extra scalar degree of freedom to matter must be employed to properly normalise the field and therefore $\beta = \sqrt{1/6}$ (Starobinsky, 2007). The modified form of the Einstein-Hilbert action is then

$$S = \int \left(\frac{1}{16\pi G}[R + f(R)] + \mathcal{L}_{\mathcal{M}} \right) \sqrt{-g} d^4x. \tag{1.41}$$

It is of interest to note that a constant f is a cosmological constant.

If this action is varied with respect to the metric tensor the modified Einstein equation can be derived (Buchdahl, 1970)

$$G_{\mu\nu} + f_{\mathrm{R}} R_{\mu\nu} - \left(\frac{f}{2} - \Box f_{\mathrm{R}} \right) g_{\mu\nu} - \nabla_\mu \nabla_\nu f_{\mathrm{R}} = 8\pi G T_{\mu\nu}, \tag{1.42}$$

where $G_{\mu\nu} = R_{\mu\nu} - R g_{\mu\nu}/2$ is the Einstein tensor, $f_{\mathrm{R}} = \mathrm{d}f/\mathrm{d}R$ is an extra scalar degree of freedom called a scalaron and $\Box = \nabla_\nu \nabla^\nu$ is the d'Alembertian operator. On scales much smaller than the horizon, the quasi-static approximation holds true (Oyaizu 2008a, Noller et al. 2014). This allows Equation 1.42 to be simplified to the field equation for f_R

$$\nabla^2 f_{\mathrm{R}} = -\frac{1}{3}[\delta R(f_R) + 8\pi G \delta \rho_{\mathrm{M}}], \tag{1.43}$$

where δR represents the perturbations in the scalar curvature and $\delta\rho$ the perturbations in the matter density.

By considering Equation 1.42 in the Newtonian limit, the Poisson equation for the modified gravitational potential (Hu and Sawicki, 2007) can be obtained

$$\nabla^2 \Phi = \frac{16\pi G}{3}\delta\rho - \frac{1}{6}\delta R. \tag{1.44}$$

It is desirable that these models are able to reproduce late time acceleration of the Universe whilst still suppressing the fifth force in high-density environments, such as the solar system (Chiba et al., 2007), due to prior observational constraints within these two regions. It is also desirable that such a model is able to match the observed structure growth at

high redshift (Linder and Jenkins, 2003). These requirements can be achieved in a model exhibiting a chameleon mechanism, such as the model proposed by Hu and Sawicki (2007),

$$f(R) = -m^2 \frac{c_1 (R/m^2)^n}{c_2 (R/m^2)^n + 1}, \tag{1.45}$$

where $m^2 = H_0^2 \Omega_m$, n is the scaling index that modulates the scalar field amplitude, and c_1 and c_2 are integration constants that are later fixed. One assumption of this model is that both dark and baryonic matter are coupled to the chameleon field. It is possible to construct models in which the baryonic component is not coupled (i.e. see Li and Barrow 2011a, Li and Barrow 2011b), but the method, described below, is insensitive to such a parametrisation.

In Equation 1.45, $R \to 0$ will in turn cause $f(R) \to 0$. In this case, from Equation 1.41, the unmodified action is recovered and no cosmological constant is present. However, in the high curvature regime where $R \gg m^2$, Equation 1.45 can be expanded as

$$\lim_{m^2/R \to 0} f(R) \approx -\frac{c_1}{c_2} m^2 + \frac{c_1}{c_2^2} m^2 \left(\frac{m^2}{R} \right)^n. \tag{1.46}$$

In the limiting case where the integration constants $c_1/c_2^2 \to 0$, c_1/c_2 becomes a cosmological constant, and for a finite c_1/c_2^2 the curvature becomes frozen in and decouples from the matter density. This creates a class of models that are able to accelerate much like ΛCDM. As the model is required to accurately mimic the expansion history of ΛCDM,

$$\frac{c_1}{c_2} \approx 6 \frac{\Omega_\Lambda}{\Omega_m}. \tag{1.47}$$

This leaves just two parameters, n and c_1/c_2^2 to control the evolution of the model. A small c_1/c_2^2 leads to a closer mimicry of ΛCDM, while a large n causes mimicry to last until later in the Universe's evolution.

Having defined these parameters the derivative of $f(R)$ can be written as

$$f_{\mathrm{R}} = -n \frac{c_1}{c_2} \left(\frac{m^2}{R} \right)^{n+1}, \tag{1.48}$$

which holds in the limit $c\left(\frac{R}{m^2}\right)^2 \ll 1$. This requirement is also needed for such a model to be compatible with observations.

It is often more convenient to replace the parameters c_1 and c_2 with the value of f_R at today's redshift, $f_{\mathrm{R}0}$ (Sotiriou and Faraoni, 2010). This can be done by first considering the Ricci scalar in a FLRW Universe (Equation 1.15), with the modification due to $f(R)$ gravity

$$R = -6\left[\frac{\ddot{a}}{a} + \left(\frac{\dot{a}}{a}\right)^2\right] - 2f. \tag{1.49}$$

By combining this with the Friedmann equation (Equation 1.16) and the acceleration equation (Equation 1.17) the Ricci scalar can be rewritten in terms of the energy densities (Equation 1.22)

$$R = 3m^2\left(a^{-3} + 4\frac{\Omega_\Lambda}{\Omega_m}\right). \tag{1.50}$$

Plugging this into Equation 1.48 constrains both c_1 and c_2 when given n, $f_{\mathrm{R}0}$, Ω_Λ, Ω_m and H_0. It is therefore possible to characterise these models using just two parameters, n and $f_{\mathrm{R}0}$. It is possible to relate $f(R)$ gravity to ϕ_∞, the parameter that controls the effectiveness of the screening mechanism, (ϕ in Equation 1.40 at infinity) via the relation (Joyce et al., 2014)

$$f_\mathrm{R}(z) = -\sqrt{\frac{2}{3}}\frac{\phi_\infty}{M_\mathrm{Pl}}, \tag{1.51}$$

So a constraint upon chameleon gravity can directly translate to a constraint upon $f(R)$ gravity. By fixing $n = 1$ and the value of β, any constraints upon these theories can be stated as a single variable.

1.5 Effects of modified gravity on clusters

One of the most significant observational consequences of a chameleon fifth force is that in shallow potential wells, gravity becomes modified. It is hypothesised that a fifth force

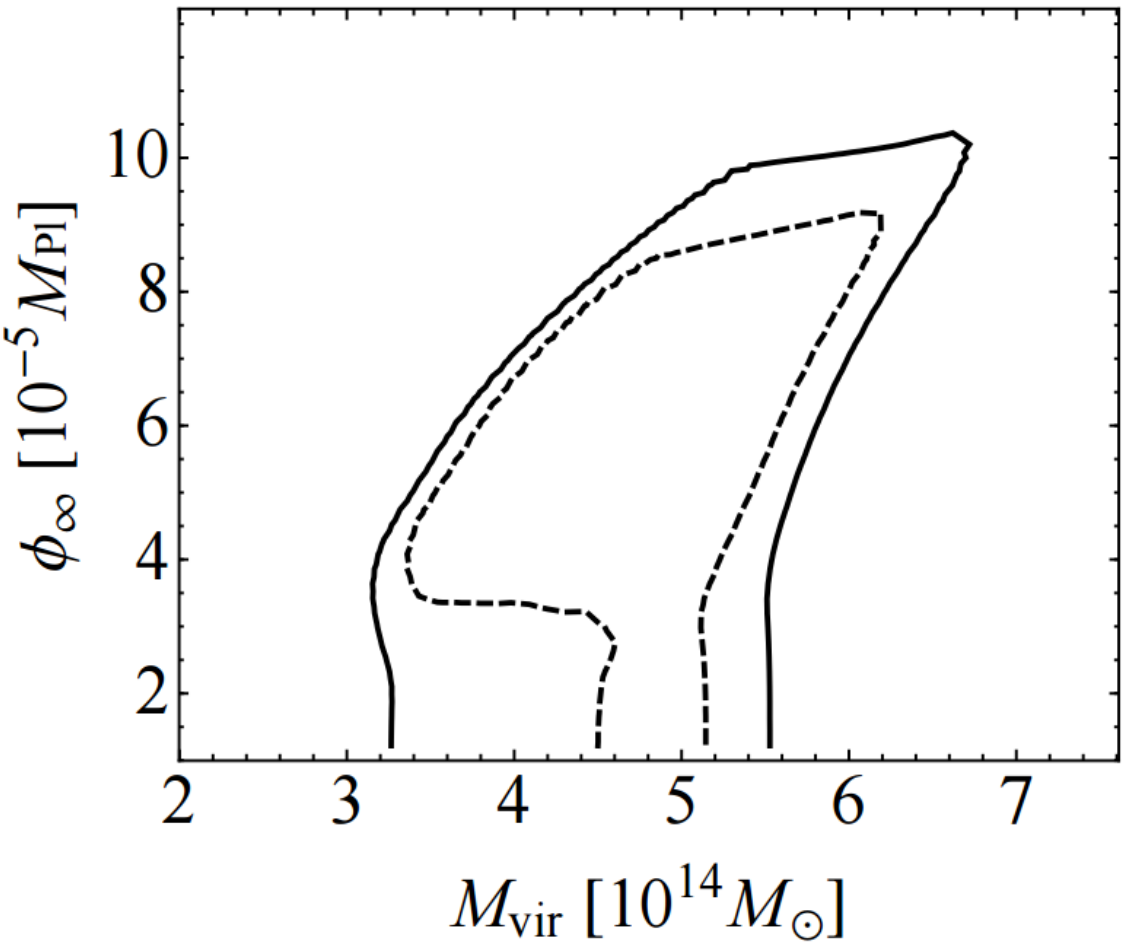

FIGURE 1.6: The likelihood surface of the $\phi_\infty - M_{\rm vir}$ plane, fitting to the temperature profile of the cluster Hydra A when $\beta = 1$. The contour levels of the inner dashed curve and the outer solid curve are at the 90% and 99% confidence levels respectively. This figure demonstrates that it is possible to place constraints upon the chameleon parameters using a galaxy cluster. Figure from Terukina and Yamamoto (2012).

would therefore be screened in the dense cores of galaxy clusters (discussed in Section 2.1), but not in the rarefied cluster outskirts (Burikham and Panpanich 2012, Lombriser et al. 2012a). In a chameleon gravity model, the intracluster gas (described in Section 2.1) would feel the fifth force in addition to gravity in the cluster outskirts, i.e. the gas will be slightly more compact and the temperature boosted (Arnold et al., 2014), compared to the influence of GR alone. This in turn would lead to an increase to the cluster's hydrostatic mass (shown in Equation 1.12 for GR).

Looking for a deviation from GR in the hydrostatic profile was first attempted in Terukina and Yamamoto (2012). In this work, the authors used the X-ray temperature profile of the Hydra A cluster, a medium sized cluster at a distance of $220 h^{-1}$Mpc (Sato et al., 2012). The X-ray observations upon which this temperature profile was derived came

from the X-ray satellite Suzaku (Mitsuda et al., 2007). By fitting over the hydrostatic profile in the chameleon regime (as discussed later in this section), with a fixed coupling strength, $\beta = 1$ (as described in Equation 1.36), they were able to to constrain $\phi_\infty < 10^{-4}$. Figure 1.6 shows the 2D likelihood surface from Terukina and Yamamoto (2012) for the chameleon screening efficiency, ϕ_∞ (described later in this section) and the virial mass (the mass enclosed within the virial radius – the radius at which the cluster's potential energy is twice its kinetic energy). A fixed β was selected, as opposed to fitting over β as this thesis does in Chapter 5, due to the limited data quality available, which prevented useful constraints at a range of β values being obtained. The authors also could not obtain constraints in the special case $\beta = \sqrt{1/6}$, which corresponds to an $f(R)$ gravity, as described in Section 1.4.2, due to the small data sample.

Under the assumption that the dark matter comprising the cluster can be modelled by an NFW profile (discussed in more depth in Section 2.1), an analytic solution to Equation 1.40 (Pourhasan et al. 2011, Burikham and Panpanich 2012, Terukina and Yamamoto 2012) can be derived. This will allow the hydrostatic equilibrium equation (shown in Equation 1.12) to be redefined in the presence of chameleon gravity. This model can then be fit real data to constrain chameleon gravity (discussed in Chapter 5).

The solution to the chameleon fifth force, Equation 1.40, in the cluster's interior is first considered. In the interior, the scalar field is in the minimum of the effective potential (i.e. $\nabla^2\phi = 0$). This is the regime where the chameleon mechanism suppresses the scalar field so no fifth force is present,

$$\frac{\beta\rho(r)}{M_{\rm Pl}} + V_{,\phi} = 0. \tag{1.52}$$

Inputting the density profile from an NFW (Equation 2.1), this becomes

$$\frac{\beta}{M_{\rm Pl}} \frac{\rho_s}{\frac{r}{r_s}\left(1+\frac{r}{r_s}\right)^2} + V_{,\phi} = 0 \tag{1.53}$$

Recalling that the potential is defined in Equation 1.34 as $V = \Lambda^{4+n}/\phi^n$, Equation 1.53 becomes

$$\phi_{\rm int}(r) = \left[n \frac{r}{r_s} \left(1 + \frac{r}{r_s} \right)^2 \Lambda^{4+n} \frac{M_{\rm Pl}}{\beta \rho_s} \right]^{\frac{1}{n+1}}, \tag{1.54}$$

$$\phi_{\rm int}(r) = \phi_s \left[\frac{r}{r_s} \left(1 + \frac{r}{r_s} \right)^2 \right]^{\frac{1}{n+1}}, \tag{1.55}$$

where $\phi_s^{n+1} = n\Lambda^{4+n} \frac{M_{\rm Pl}}{\beta \rho_s}$ represents the value of the chameleon field within the cluster. This is the definition of the strength of the chameleon field within the cluster, where the density is high and this field is suppressed. It should be noted that as $r \to 0$ the fifth force tends to infinity. This is however an artefact of the NFW profile (which tends to an infinite density as $r \to 0$), while the fifth force is zero elsewhere in the cluster interior.

Next the solution to Equation 1.36, the chameleon fifth force, in the cluster's exterior is considered. In this regime the density of the cluster is low so the chameleon field is no longer suppressed and provides an additional force in the cluster outskirts. For this solution the contribution of the scalar field potential is much less than that of the matter density and the chameleon field, such that $V_{,\phi} \ll \nabla^2 \phi$. In this case

$$\nabla^2 \phi_{\rm ext}(r) = \frac{\beta \rho(r)}{M_{\rm Pl}}, \tag{1.56}$$

which can be evaluated

$$\phi_{\rm ext}(r) = -\frac{\beta \rho_s r_s^2}{M_{\rm Pl}} \frac{\ln(1 + r/r_s)}{r/r_s} - \frac{C}{r/r_s} + \phi_\infty, \tag{1.57}$$

where C and ϕ_∞ are integration constants. Here, ϕ_∞ can be interpreted as the minimum of the chameleon field and therefore its cosmological background value. Due to the deep potential well inside the cluster, the chameleon field will become highly suppressed, meaning $\phi_s \ll \phi_\infty$. Equation 1.55 can then be approximated as $\phi_{\rm int}(r) \approx 0$.

By connecting the two solutions to the chameleon field, first in the cluster's interior (Equation 1.55) and second in the cluster's exterior (Equation 1.57) it is possible to define the hydrostatic equation in the presence of a chameleon field. The integration constant, C, and the transition scale can be determined by realising that at some critical transition radius, r_c, the interior and exterior solutions to the chameleon field must match (i.e.

$\phi_{\rm int}(r_c) = \phi_{\rm ext}(r_c)$). In this model this is the radius at which the chameleon screening is 'switched on' and becomes a fifth force, causing deviations from the expected GR measurement. It is also required that their derivatives match (i.e. $\phi'_{\rm int}(r_c) = \phi'_{\rm ext}(r_c)$). This yields

$$C \approx -\frac{\beta \rho_s r_s^2}{M_{\rm Pl}} \ln\left(1 + \frac{r_c}{r_s}\right) + \phi_\infty \frac{r_c}{r_s} \tag{1.58}$$

$$\phi_\infty - \frac{\beta \rho_s r_s^2}{M_{\rm Pl}} \left(1 + \frac{r_c}{r_s}\right)^{-1} \approx 0. \tag{1.59}$$

The solution to the chameleon field within the cluster has now been derived and the interior solution conntected to the exterior solution. It becomes possible to rewrite the hydrostatic equilibrium equation and use the above solutions to produce an analytic model that can be used to fit the X-ray surface brightness profiles of clusters, detailed in Chapter 5. The validity of this analytic solution is considered in Pourhasan et al. (2011) and Lombriser et al. (2012a), as well as discussed in further detail in Chapter 3.

Both the chameleon field interior and exterior solutions (Equations 1.55 and 1.57 respectively), and the critical radius (Equations 1.58 and 1.59) at which the chameleon fifth force begins to take effect, are independent of the parameters describing the scalar field potential, Λ and n (defined in Equation 1.34). This is because ϕ_∞ is a degree of freedom, and has the potential to differ from the cosmological background value of the scalar field depending upon the local environment of the cluster. The effect of a cluster's local environment upon the scalar field is investigated in Chapter 5.

By measuring the properties of X-ray gas (described in Section 2.2.2), it is possible to infer, under the assumption of hydrostatic equilibrium, the cluster's mass and density from its X-ray surface brightness or SZ effect profiles (Reiprich and Böhringer 2002, Kettula et al. 2015). In the presence of a chameleon field, the hydrostatic equation (Equation 1.12) is modified,

$$\frac{1}{\rho(r)} \frac{P(r)}{dr} = -\frac{GM(r)}{r^2} - \frac{\beta}{M_{Pl}} \frac{{\rm d}\phi(r)}{{\rm d}r}, \tag{1.60}$$

in turn modifying the inferred mass. The cluster's mass then becomes

$$M_{\rm tot}(< r) = M_{\rm hydro}(r) + M_{\phi}(r), \tag{1.61}$$

where $M_{\rm tot}$ is the cluster's total mass, $M_{\rm hydro}$ is the cluster's mass inferred from hydrostatic equilibrium (assuming GR) and

$$M_{\phi}(r) = -\frac{r^2}{G}\frac{\beta}{M_{\rm Pl}}\frac{d\phi(r)}{dr} \tag{1.62}$$

is the mass enhancement due to the chameleon field.

By contrast, weak gravitational lensing is dependent only upon the gravitational deflection of light by matter along the line of sight, therefore providing a technique to measure the underlying mass distribution without assuming hydrostatic equilibrium. Crucially for this study, the fifth force would not modify the deflection of light through the cluster (compared to GR) because the scalar chameleon field is coupled to the trace of the energy-momentum tensor (Hui et al., 2009), which does not couple to photons. This can also be shown by considering the parallel to the modified Poisson equation (Equation 1.44, Arnold et al. 2014) for Ψ,

$$\nabla^2\Psi = \frac{8\pi G}{3}\delta\rho + \frac{1}{6}\delta R. \tag{1.63}$$

This is the Newtonian potential, which comes from the FLRW metric. The lensing potential, which defines the deflection of light, is the sum of the potentials in Equations 1.44 and 1.63, $\Phi_L = (\Psi + \Phi)/2$, giving

$$\nabla^2\Phi_L = \frac{1}{2}\left(\frac{16\pi G}{3}\delta\rho - \frac{1}{6}\delta R + \frac{8\pi G}{3}\delta\rho + \frac{1}{6}\delta R.\right) = 4\pi G\delta\rho = \nabla^2\Phi_N. \tag{1.64}$$

Here Φ_N is the Newtonian gravitational potential and is unchanged from GR, therefore the deflection angle described in Equation 2.23 is unchanged, as are weak lensing mass estimates.

This leads to the relation

$$M_{\rm hydro}(r) + M_{\phi}(r) = M_{\rm WL}, \tag{1.65}$$

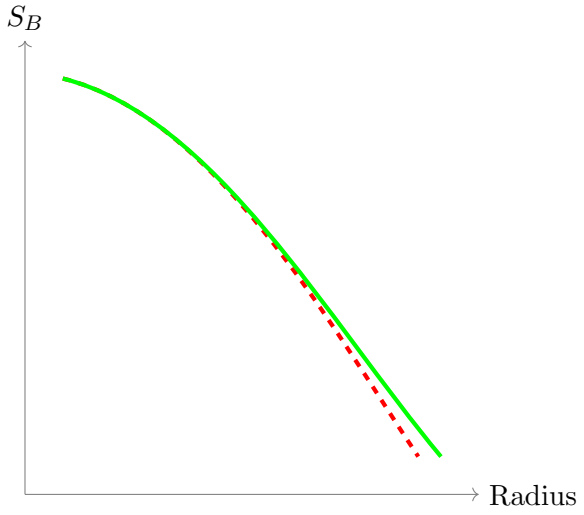

FIGURE 1.7: A cartoon demonstrating the effect of the fifth force on a cluster's X-ray surface brightness profile. Shown in solid green is the profile under GR, while in dashed red the profile under the influence of the fifth force is shown.

where $M_{\rm WL}$ is the mass recovered from weak lensing measurements.

The equations presented above (principally Equation 1.65) describe how the cluster's mass is affected in the presence of a chameleon field. However they also describe how the X-ray surface brightness (described in Section 2.2.2) and weak lensing (described in Section 2.2.5) profiles are affected. The effect of the chameleon screening is demonstrated in Figure 1.7 where the fifth force can be seen to compress the X-ray surface brightness profile when compared with GR.

Therefore, it is possible to search for evidence of a fifth force by comparing the X-ray surface brightness and/or SZ effect profiles of clusters, which probe the modified hydrostatic masses, with their gravitational lensing shear profiles, which probe the unmodified masses (Ostriker and Vishniac 1986, Terukina and Yamamoto 2012). One advantage of comparing profiles over masses is that there are potential mass biases between hydrostatic and lensing mass measurements (e.g. Nelson et al. 2012, Nelson et al. 2014) that have the potential to wipe out any detectable differences due to the fifth force (as seen in Arnold et al. (2014) and discussed further in Section 5.5). When using the cluster profiles, their shape is of much more interest than their amplitude, and the profile's shape is not degenerate with much of the astrophysics which potentially causes bias in mass measurements. Another advantage is for each cluster many more points of data are available to be measured (several points along a profile as opposed to a single mass measurement), which,

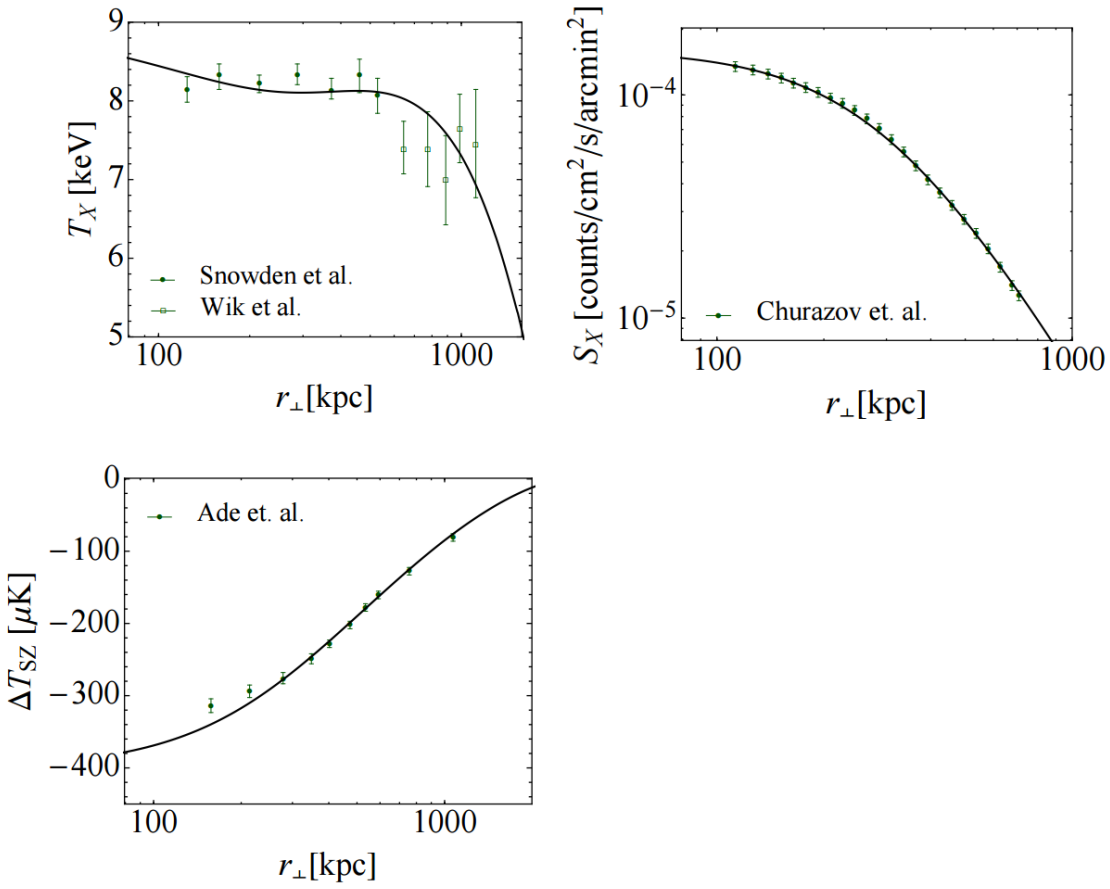

FIGURE 1.8: X-ray temperature (top-left), surface brightness (top-right), and SZ effect (bottom) profiles for the Coma cluster as a function of radius, shown as black points with associated errors. The best fit chameleon gravity models can be seen in solid black, which allow constriants to be placed upon $f(R)$. Figure from Terukina et al. (2014).

providing sufficient signal, will grant the models greater constraining power. It is for these reasons this thesis continues by considering cluster profiles.

The techniques required to measure X-ray surface brightness profiles are discussed in greater detail in Section 2.2.2 and weak lensing profiles in Section 2.2.5.

1.5.1 Previous uses of this technique

The technique of comparing the hydrostatic profiles of galaxy clusters, derived from X-rays (described in Section 2.2.2) or the SZ effect to the lensing profile (described in Section 2.2.5) was first used in Terukina et al. 2014 (T14). In T14 work the authors were able to constrain $f(R)$ gravity models using a combination of lensing shear, X-ray surface brightness, X-ray temperature and Sunyaev-Zel'dovich (SZ) profiles for the Coma cluster (a massive cluster at $z = 0.02$).

The profiles used to constrain $f(R)$ gravity in this work are shown in Figure 1.8. Here the X-ray temperature is shown in the top left, with the inner region data from the XMM X-ray satellite (detailed further in Section 4.2.2, Snowden et al. 2008) and the outer region from the Suzaku X-ray satellite (Wik et al., 2009). In the top right the X-ray surface brightness profile from XMM (Churazov et al., 2012) is shown and the bottom plot shows the SZ profile from the Planck satellite (Planck Collaboration, 2013). In this work, due to the lack of available weak lensing data, a single data point encapsulating the virial mass was available to contrast against the modified hydrostatic profile. The impact of this is discussed in Section 1.6.

Combining these measurements, T14 performed an MCMC analysis (MCMC is described in detail in Section 5.2) of the parameter space describing the cluster profiles in the modified gravity regime by fitting over the observational data sets described above. The results of this MCMC are shown in the best fit models as black lines in Figure 1.8. Under the assumption of hydrostatic equilibrium, they obtained constraints of $|f_{\rm R0}|< 6 \times 10^{-5}$. They also examined the assumption of hydrostatic equilibrium, and concluded that any contribution of non-thermal pressure was small compared to the reconstructed mass.

Alongside the profile comparison method for constraining $f(R)$ gravity described here there have been many other measurements of $|f_{\rm R0}|$ at a range of scales. These constraints are discussed in detail in Section 2.3.

1.6 Summary and thesis outline

In this chapter I have given a overview of the current state of cosmology. The observed accelerated expansion of the Universe is commonly explained with either the addition of dark energy or by modifying GR. I have described the current observational evidence in support of an accelerating Universe, namely SN1a, LSS and the CMB and how these probes are used to measure cosmological parameters. I have discussed how the most popular paradigm to explain this expansion is ΛCDM. I have furthered this discussion by noting some of this theory's shortcomings, namely the vast disagreement between theoretical and observational measurements of dark energy and the coincidence problem. These motivate the investigation of another mechanism that could explain this observed

expansion, namely modified gravity. I have described how one of these modifications to gravity might present itself, in a difference of X-ray and lensing profiles.

Also in this chapter, I have reviewed Terukina et al. (2014), who investigated these profiles for the Coma cluster, discussed in Section 1.5.1. The Coma cluster is at a low redshift, meaning its weak lensing shear signal is low (the weak lensing signal around clusters is described in detail in Section 2.2.5). The strength of this technique comes from the observed tension between the lensing measurement, which in chameleon gravity follows GR, and the hydrostatic profiles, which become modified in the presence of a chameleon field. As Terukina et al. (2014) only had a single data point of lensing data, it is difficult to observe a tension between this and the hydrostatic profiles, potentially reducing the constraints on the chameleon parameters. Moreover the Coma cluster is known to have non-spherical geometry (Fitchett and Webster 1987, Briel et al. 1992, Colless and Dunn 1996), which is one assumption made in the analytical model described in Section 1.5, potentially biasing the results.

These factors motivate me to take the Terukina et al. (2014) method further. I do this using many more clusters at a much higher redshift. I aim to measure much higher signal to noise weak lensing shear profiles as well as averaging out non-spherical cluster shapes. I carefully control the cluster sample to ensure confidence in my results and perform many tests to the data to check its quality and to carefully control for systematics as well as verifying all these techniques against simulations. I also take the concept put forward in Terukina et al. (2014) and apply it to another modified gravity, namely the Vainshtein mechanism (described in Section 6.3). These factors allow highly competitive constraints on gravity with a thorough understanding of the systematics involved to be obtained.

In Chapter 2 I discuss in further detail the nature of X-ray cluster measurements and weak lensing signal and elaborate on the nature of galaxy clusters themselves. I also discuss different probes of modified gravity to compare their constraining power to the technique outlined in this thesis.

In Chapter 3 I use two hydrodynamical simulations, one evolved under ΛCDM+GR, the other under the influence of $f(R)$ gravity, to perform multiple tests of the analytic models. I also use these simulations to test the cluster sphericity and the suitability of the NFW profile. I then test the MCMC profiles by constraining the gravity models within the simulations.

In Chapter 4 I discuss the surveys used throughout this thesis. I then describe the creation of the dataset used to measure gravity, comprised of 58 X-ray selected clusters. I detail how the X-ray and lensing profiles were created and the tests to the data to ensure its suitability.

In Chapter 5 I investigate the environment of the cluster sample and test the sample is in hydrostatic equilibrium. I then describe the MCMC fitting technique used to constrain gravity as well as present the results.

Finally in Chapter 6 I discuss the future of this work by forecasting the constraints that would be obtained using a far larger dataset. I also detail a few refinements upon the techniques in earlier chapters. I continue by using the techniques to constrain the Vainshtein mechanism, a different screening mechanism, and present the results including the first measurement of a particular parametrisation of Vainshtein. I finish by presenting the conclusions.

Chapter 2

Introduction: Probes and Gravity Observables

In this chapter I introduce the observational tools that I shall later use to constrain gravity models.

I begin by describing the focus of this thesis, galaxy clusters, and discuss the properties they have that make them such useful cosmological tools. I will then discuss the observables through which I will probe these clusters. The first of these observables are X-rays, high energy photons emitted from the cluster due to its high temperature. I will describe their history and emission mechanisms and then lay out the equations required to test modified gravity using X-rays.

I then move on to the other major probe used throughout this endeavour - gravitational lensing. Here I begin by describing the fundamental physics behind lensing. I will describe the fundamental physics behind lensing, and an observational consequence, weak lensing, as well as how weak lensing can be used to reconstruct the density field in the Universe.

I finish this chapter by discussing other probes that have been employed in the search for modified gravity throughout the last decade on a variety of astronomical scales.

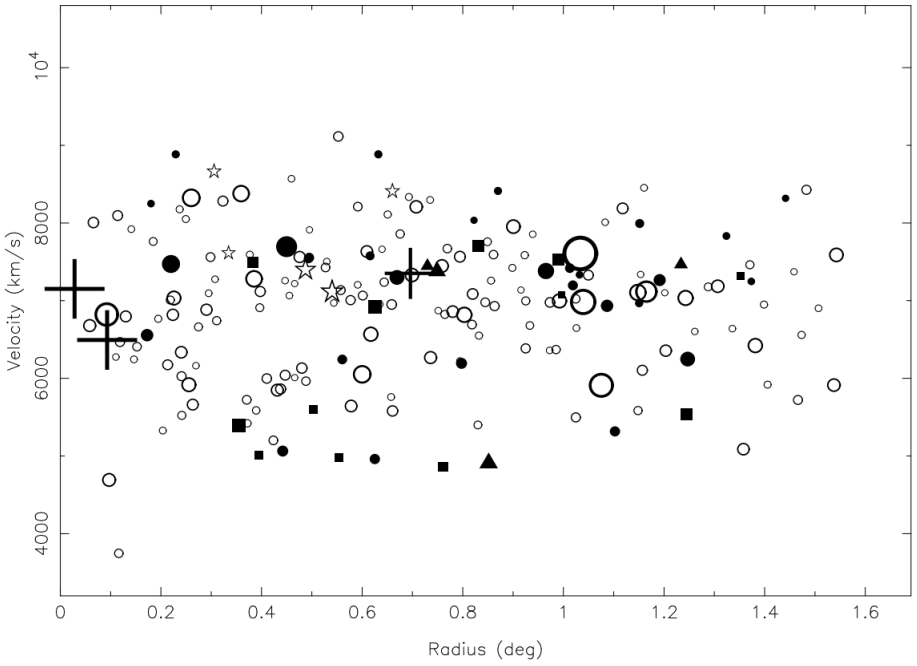

FIGURE 2.1: Distribution of radial velocities as a function of radius from the cluster centre for galaxies in the Coma cluster. The different symbols indicate different galaxy morphology. This figure shows that a galaxy's orbital velocity is independent of its radial distance from the cluster centre. Figure from Castander et al. (2001).

2.1 Clusters

Galaxy clusters are the largest virialised objects in the Universe, with masses of $10^{13-15} M_{\odot}$ and sizes up to several megaparsecs. They typically contain hundreds of galaxies, the majority of which are early type ellipticals. Clusters are commonly said to be comprised of old galaxies with low star formation rates – making typical cluster galaxies redder than field galaxies.

Fritz Zwicky was the first to apply the virial theorem to galaxy clusters in 1933 and correctly concluded that the observed masses of clusters were much to small too be consistent with the galaxy velocity dispersions (Zwicky 1933, Zwicky 1937). Zwicky inferred that the majority of the matter was unseen and coined the name dark matter to describe this missing matter.

More recently Castander et al. (2001) have measured the velocities of 196 galaxies within the Coma cluster. In Figure 2.1 these velocities are shown, where it is clear to see that the galaxy's velocity is independent of its radial distance. This contrasts with other gravitational systems with large central mass concentrations, such as the solar system, in

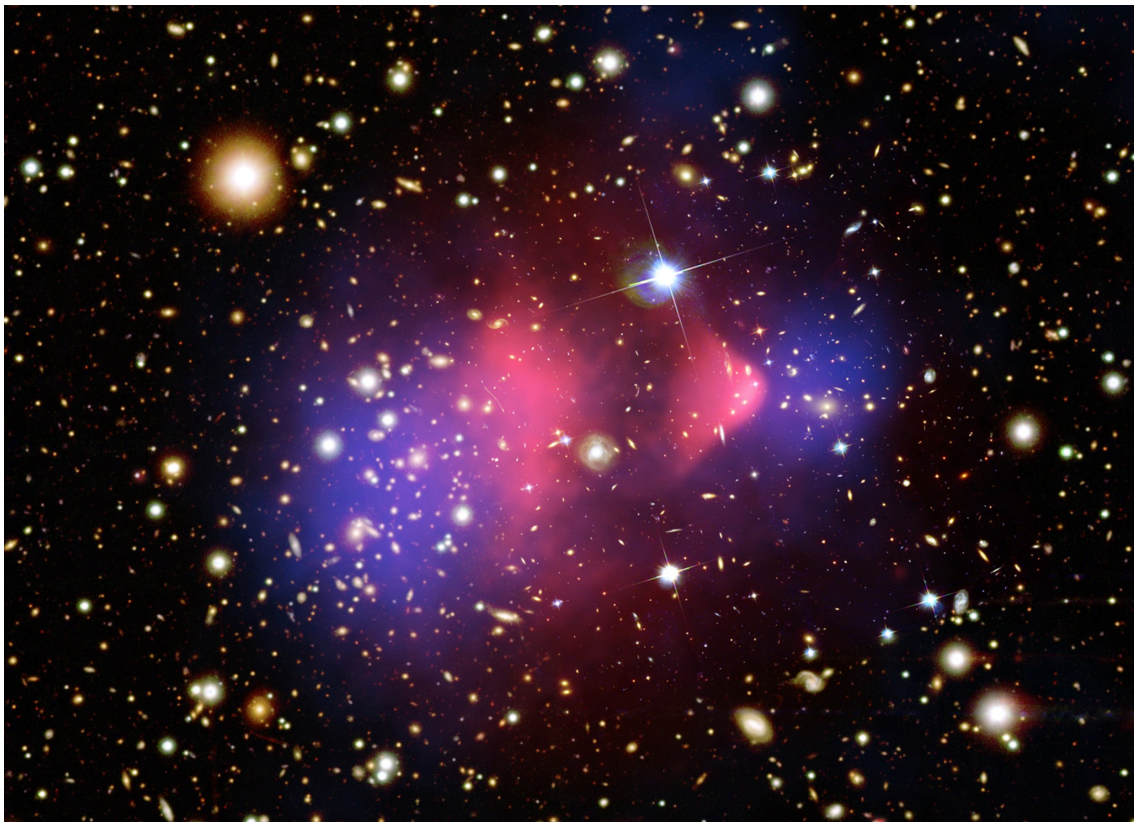

FIGURE 2.2: Image of the Bullet cluster. Shown in pink is the intra-cluster gas distribution, in blue the dark matter distribution and in yellow the optical galaxies. This figure shows that the bulk of a clusters mass is not in the intracluster gas, but dark matter. Image courtesy of NASA.

which the rotational velocity falls of as a function of radius. This agrees with Zwicky's inference that there is a large amount of unseen mass at all radii of the cluster.

When the first X-ray observations of clusters were made it was discovered that clusters are filled with hot, low density intra-cluster gas (these X-ray observations are discussed in Section 2.2.1). From these X-ray measurements, and later on SZ measurements (Grego et al., 2001), it was deduced that this gas accounts for $\sim 15\%$ of the total cluster mass (Lea et al., 1973). Combining this with measurements of the mass contained within the galaxies comprising the cluster, around $\sim 3\%$ (Ettori et al., 2009), means that it is possible to infer that the majority (around $\sim 80\%$) of a cluster's mass is dark matter.

More recently galaxy clusters have again provided some of the strongest evidence of the existence of dark matter (Markevitch et al., 2004). Figure 2.2 shows the Bullet cluster. In pink the distribution of the hot X-ray emitting gas is shown, while in blue and yellow the dark matter and optical galaxies are shown respectively. This system comprises of two colliding galaxy clusters. The size of a single galaxy is very small compared to the

whole cluster so the galaxies pass by each other without interacting. The intracluster mediums, however, interact as they pass through each other, causing them to slow down and lag behind the galaxies. However, gravitational lensing (discussed in Section 2.2.3) has revealed that the bulk of the cluster's mass (shown in blue) surrounds the galaxies. As the galaxies only make up a fraction of the total mass, the majority of the system's mass must be collisionless and not in the intra-cluster gas.

These haloes are believed to have formed from small initial density perturbations, caused by quantum fluctuations, and, via hierarchical structure growth (Press and Schechter, 1974), gravitated together to form the massive cluster haloes seen today. This means that clusters trace the large scale structure of the Universe and their abundance is highly reliant upon the underlying cosmology (Tinker et al., 2012). Combined with clusters being the smallest objects that contain a representative sample of the matter make up of the Universe, this makes clusters a competitive probe of cosmology and excellent laboratories for searching for modified gravity (i.e. Narikawa and Yamamoto 2012, Lam et al. 2012, Li et al. 2016).

One property of galaxy clusters that make them especially useful as a cosmological probe is their self similarity (Press and Schechter, 1974). Clusters, at the same redshift, of all masses are identical when they are scaled by their mass: this is known as strong self-similarity (Bower, 1997). The matter density within the Universe is proportional to $\frac{1}{a(t)^3}$ meaning the density at high redshifts was higher than it is today (Bryan and Norman, 1998). Therefore, clusters at high redshift are expected to have higher densities than those at low redshifts. However if this evolution is accounted for (Maughan et al., 2012) then a cluster at high redshift is identical to one at low redshift. This relation is known as weak self-similarity.

Because of these self-similarities galaxy clusters are thought to possess a universal profile describing their dark matter distribution (Dubinski and Carlberg, 1991). There have been many studies investigating this idea, and many different profiles suggested (Bertschinger, 1998).

In this study, the Navarro-Frenk-White (NFW; Navarro et al. 1996) model is adopted for the dark matter halo mass distribution, which is found to fit the dark matter distributions of clusters well (i.e. Coe et al. 2010, Limousin et al. 2013, Niikura et al. 2015) and described

by:

$$\rho(r) = \frac{\rho_{\rm c}\delta_{\rm c}}{\frac{r}{r_{\rm s}}(1+\frac{r}{r_{\rm s}})^2}, \tag{2.1}$$

where r here and throughout is the radial distance from the halo centre, $\rho_{\rm c} = 3H^2(z)/8\pi G$ is the critical density at a given redshift, $H(z)$ is the Hubble parameter at a given redshift (described in Equation 1.18), G is Newton's Gravitational Constant, $\delta_{\rm c}$ is the characteristic overdensity, given by

$$\delta_{\rm c} = \frac{200}{3}\frac{c^3}{\ln(1+c) - c/(1+c)}, \tag{2.2}$$

where c is a dimensionless concentration parameter and $r_{\rm s}$ is the scale radius given by

$$r_{\rm s} = \frac{1}{c}\left(\frac{3M_{200}}{4\pi\rho_{\rm c}\delta_{\rm c}}\right)^{1/3}, \tag{2.3}$$

where M_{200} is the mass enclosed by r_{200}, the radius at which the dark matter halo's average density is two hundred times the critical density (given by Equation 1.21),

$$M(<r_{200}) = 4\pi\delta_{\rm c}\rho_{\rm c}r_{\rm s}^3\left(\ln(1+c) - \frac{c}{1+c}\right). \tag{2.4}$$

The NFW profile described in Equation 2.1 is an direct, empirical fit to ΛCDM N-body simulations (i.e. Cole and Lacey 1996, Tissera and Dominguez-Tenreiro 1998, Bahé et al. 2012), but it is not immediately obvious that this profile would pertain to cluster profiles in the $f(R)$ regime (as described in Section 1.4.2). However it has been shown (Lombriser et al. 2012a, Moran et al. 2015) that the NFW profile is able to provide fits to both modified gravity and concordance cosmology that are equally good, sharing the same χ^2. It should be noted that the simulations in Lombriser et al. (2012a) were generated using a fixed $\beta = \sqrt{1/6}$, as opposed to the general chameleon gravity model investigated here. However, as the β range being probed here is around this value, any modifications to the profiles are expected to be similar, suggesting the suitability of the NFW profile. In Chapter 3 further checks using hydrodynamical simulations of modified gravity models are performed, allowing this assumption to be verified.

The gas within clusters follows a different profile from the underlying dark matter distribution, because of the different physics felt by the gas due to each particle interacting with others through electrostatic forces. This leads the gas profile to differ from the dark

matter profile (Makino et al., 1998) and follow a *beta-model*[1], b_1, electron density profile (e.g. Cavaliere and Fusco-Femiano 1978);

$$n_e(r) = n_0 \left(1 + \left[\frac{r}{r_1}\right]^2\right)^{b_1}. \tag{2.5}$$

Adopting the Terukina et al. (2014) approach allows the chameleon mechanism to be described using three parameters. The first of these, β, is the coupling between matter and the scalar field (see Equation 1.36). The second, ϕ_∞, describes the position dependent screening efficiency. The third, r_c, is a critical radius, i.e. the distance from the dark matter halo centre at which the screening mechanism takes effect (Terukina and Yamamoto, 2012),

$$r_c = \frac{\beta \rho_s r_s^3}{M_{Pl}\phi_\infty} - r_s, \tag{2.6}$$

where ρ_s is the density at this radius. These parameters are discussed further in Section 1.5.

Another property of galaxy clusters that makes them excellent cosmic laboratories is that they are often (in the ideal isolated case) in hydrostatic equilibrium – the pressure forces within the cluster are balanced by gravity, described in Equation 1.12. This allows the direct relation of a cluster's density, and therefore X-ray luminosity (as described in Equation 2.14), with its mass. This assumption about a cluster's dynamic state has, however, been up for much debate (i.e. Allen 1998, Ota and Yoshida 2016).

The constraints on the CMB from the Planck satellite (discussed in Section 1.3) were found to be in tension with the cosmological constraints obtained from cluster counts (Planck Collaboration, 2014). The Planck team suggest that this is due to a hydrostatic bias in the cluster mass measurements from XMM (we discuss XMM in Section 4.2.2) of $\sim 20\%$. von der Linden et al. (2014) suggest this tension could be alleviated using high quality lensing mass measurements to reduce this tension. Israel et al. (2015) suggest that this tension could even be due to instrumental uncertainties in the X-ray satellites.

Recently, however, Maughan et al. (2015) compare the X-ray and caustic mass profiles of 16 massive clusters concluding *"There is no indication of any dependence of the mass ratio on the X-ray morphology of the clusters, indicating that the hydrostatic masses are*

[1]The *beta* in this model is not the same as the β in Equation 1.36.

not strongly systematically affected by the dynamical state of the clusters." While Thölken et al. (2016) performed a detailed X-ray analysis of the galaxy group UGC03957 beyond r_{200}, and offer mixed conclusions about the dynamical state of the measured group depending on the observable used. This effect is discussed further in Chapter 3.

2.2 Cluster probes

2.2.1 X-rays

X-rays are an energetic part of electromagnetic spectrum, with wavelengths between 0.01 and 10 nanometres, and energies between 0.1 keV and 100 keV. X-ray radiation is commonly divided into two categories: soft X-rays, where a photon's energy is below 10 keV; and hard X-rays where the energy is above 10 keV (Attwood, D T, 2000).

The high energy of X-rays necessitates that their thermal emission can only occur in astrophysical sources in excess of 10^7K, such as galaxy clusters, black holes and supernova remnants. Non-thermal emission of X-rays typically arises from synchrotron radiation, when charged particles are accelerated in a curved path. Both these emission types are discussed in Section 2.2.2.

Due to the ionising nature of X-rays they are readily absorbed by the atmosphere. This means that any X-ray observatories should be located very high, preferably above the atmosphere. Historically this was achieved using balloons and rockets, however now dedicated satellites such as XMM (Jansen et al., 2001), Chandra (Weisskopf et al., 2000) and Suzaku (Mitsuda et al., 2007) are placed in orbit to make observations.

The major difficulty in the creation of an X-ray telescope, is that as X-rays are so energetic, they pass through most matter, including mirrors. This means that the traditional orientation of using mirrors or lenses to focus light as applied in visible light astronomy must be adapted to observe X-rays. In X-ray telescopes the mirrors, typically coated in gold or iridium, are turned almost perpendicular to the detector so the X-ray photon can 'graze-off' the mirror (Arnaud et al., 2011). The angle at which this is achieved is energy dependent but usually very small (the grazing angle for a 2KeV photon on a gold mirror is $< 2°$: Als-Nielsen and McMorrow 2011). In order to focus the X-rays down to a point,

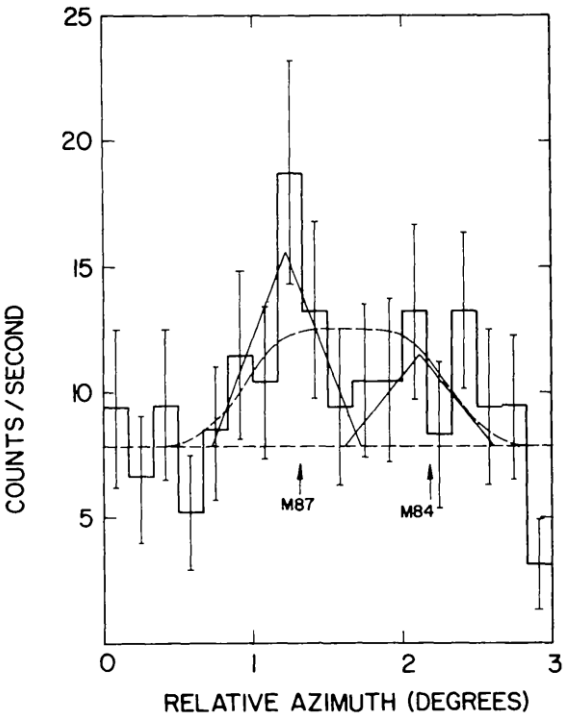

FIGURE 2.3: The azimuthal distribution of X-ray counts from the Virgo cluster. The two peaks indicate the positions two X-ray bright galaxies within the cluster. This figure is the first detection of the Virgo cluster. Figure from Kellogg et al. (1971).

X-ray telescopes use large arrays of nested mirrors, each one slightly offset from the last, to focus the X-rays on to the detector (Spiga et al., 2009).

Due to the ready absorption of X-rays by the atmosphere, the first discovery of astrophysical X-rays was not until 1948, when an X-ray detector on the nose cone of a V2 rocket observed the sun (Friedman et al., 1951). The first extrasolar source of X-rays was not then discovered until 1962, when a detector aboard another rocket detected the X-ray binary system Scorpius X-1 (Giacconi, 2003).

The first dedicated X-ray telescope to be launched was Uhuru in 1970. Uhuru performed a uniform all sky survey, cataloguing 339 X-ray sources (Forman et al., 1978) including supernova remnants, Seyfert galaxies and binary systems.

Since those initial observations many more sources of astrophysical sources of X-rays have been discovered. One of the most important discoveries has been the diffuse X-ray emission from the intracluster medium (Kellogg et al. 1971, Forman et al. 1972). Figure 2.3 shows the first X-ray detection of the Virgo cluster in Kellogg et al. (1971). This telescope operated by sweeping across an area in bands and measuring the X-ray count

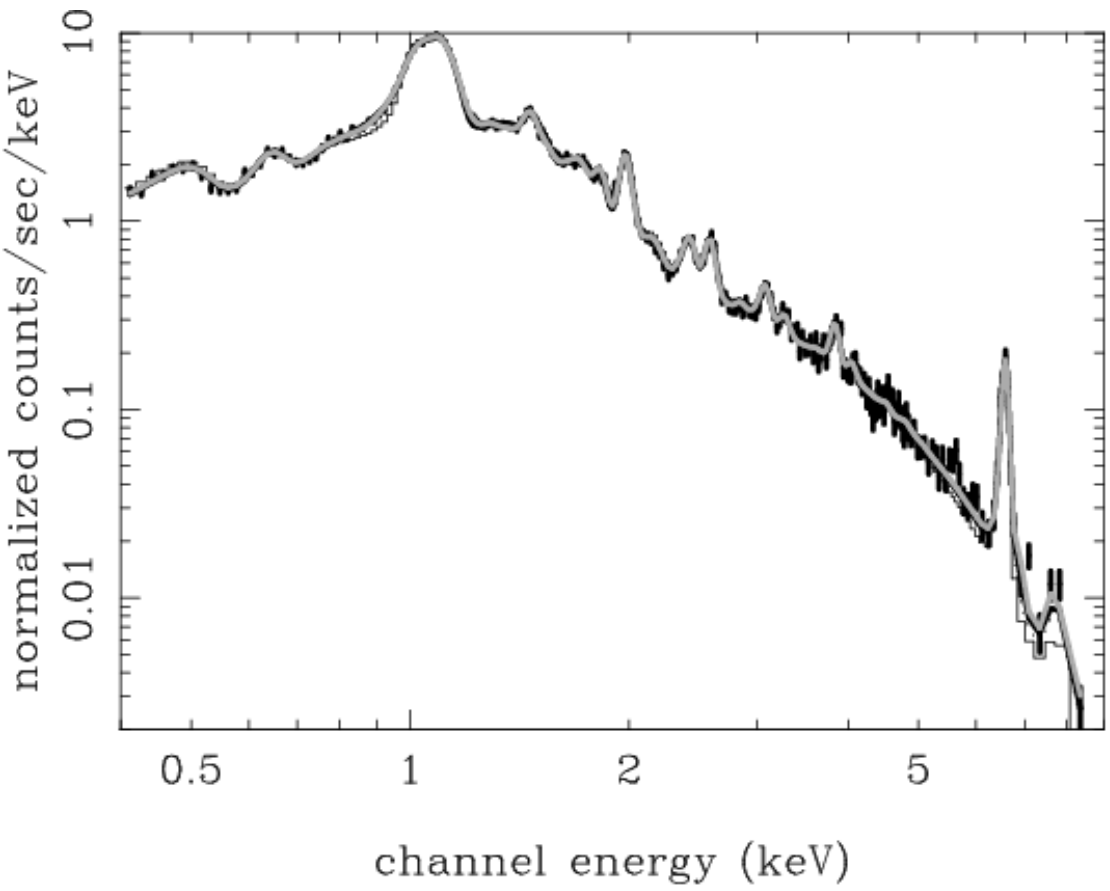

FIGURE 2.4: X-ray spectrum of the Centaurus cluster showing both continuum and line emission in black. In grey the best fit model is shown. Figure from of Matsushita et al. (2007).

rate. Here the X-ray emission around the cluster galaxies can be seen clearly. This initial observation by the Uhuru X-ray satellite took place over three days with a total exposure time of 381 seconds. The authors measured the X-ray temperature to be $T_X > 2.5 \times 10^7$K and the extent of the X-ray emission to be 1° - 2° in diameter.

These initial observations provided the first indications that the majority of baryonic matter in clusters is in hot intracluster gas, and these X-ray observations have provided new insight into the structure and formation of the Universe (Sarazin, 1986).

2.2.2 X-rays in clusters

The hot diffuse gas that makes up the intra-cluster medium is one of the most luminous sources of X-rays in the Universe, second only to active galactic nuclei. The X-rays themselves are primarily due to thermal emission from this gas, which leads to a spectrum

comprised of continuum and line emission. An example of such a spectrum is shown in Figure 2.4.

The majority of the X-ray continuum arises from three distinct processes. The largest contribution to this spectrum arises from thermal bremsstrahlung (free-free) emission, with lesser contributions from recombination (free-bound) emission and two-photon (bound-bound) decay.

Bremsstrahlung radiation is produced when a charged particle, such as an electron, is accelerated by another charged particle, typically an atomic nucleus. This radiative process begins and ends with the electron being free. Recombination occurs when the electron is captured by the nucleus, causing a photon to be emitted.

The two photon emission occurs when an electron collides with a bound electron in the 1S shell, exciting the bound electron into the 2S shell. The decay from 2S to 1S, however, is forbidden by quantum mechanics (Spitzer and Greenstein, 1951). Normally a second electron would excite the bound electron further. However, as the density of the intracluster gas is very low (typically 10^{-3} atoms/cm^3, Sarazin 1986), this additional collision is unlikely. The electron then decays back to the 1S orbit while emitting two photons, whose combined energy equals the energy difference between the 2S and 1S states (Kaastra et al., 2008).

Other than this continuum emission, line emissions are also present in X-ray spectra. Line emission begins when an atom is excited. There are several processes that can cause this to happen, however in clusters the most important is bound-bound emission. An electron is excited to a higher energy state after a collision and decays back down by radiating a photon of a characteristic wavelength.

It can be useful to fit a model to a cluster spectrum. The bulk of this spectrum is caused by the thermal bremsstrahlung emission (Gronenschild and Mewe, 1978) given by summing over the ions involved in the collisions. Here the derivation presented in Longair (2011) is followed.

The acceleration of an electron as it becomes deflected by an ion of charge Z (Larmor, 1897) is

$$a(t) = \frac{Ze^2}{m_e(b^2 + v^2t^2)}, \tag{2.7}$$

where m_e is the electron's mass, b is the impact parameter – the closest separation between the electron and ion, and v is the electron's velocity. The electric dipole field at a distance r from the electron is (Laud, 2011)

$$E(t) = \frac{ea(t)}{c^2 r}\sin\theta = \frac{Ze^3\sin\theta}{m_e c^2 r(b^2 + v^2t^2)}. \tag{2.8}$$

Taking the Fourier transform of this then leads to

$$E(\nu) = \int_{-\infty}^{\infty} E(t)\exp(2\pi i\nu t)dt = \frac{Ze^3\sin\theta}{m_e c^2 r}\int_{-\infty}^{\infty}\frac{\exp(2\pi i\nu t)}{b^2 + v^2t^2}dt = \frac{Ze^3\sin\theta}{m_e c^2 r}\frac{\pi}{bv}\exp(-2\pi\nu b/v). \tag{2.9}$$

From this, the spectrum radiated from a single electron is

$$\frac{dW}{d\omega} = \frac{c}{2\pi}\int r^2 E(\nu)^2 d\Omega = \frac{4\pi^2}{3}\frac{Z^2e^6}{m_e^2c^3b^3v^2}\exp(-4\pi\nu b/v). \tag{2.10}$$

This then produces a spectrum that is flat for $\omega \ll v/b$ and falls off exponentially when $\omega \gg v/b$. The approximation that all electrons have the same velocity, v, is made and that both electrons and ions have equal number densities $n_e = n_i$. Then the collision rate per unit volume between the impact parameters b and db is given by $n_e n_i 2\pi b db v$. From this the power per unit volume is

$$\frac{dW}{d\omega dt dV} = n_e n_i v\int_{b_{min}}^{\infty}\frac{dW}{\nu}2\pi b db = \frac{8\pi^3}{3}\frac{Z^2e^6}{m_e^2c^3v}\int_{b_{min}}^{b_{max}}\frac{db}{b}. \tag{2.11}$$

As the spectrum for a single electron falls off exponentially when $\omega > v/b$, the exponential can be approximated as a step function when $\omega \sim v/b$, equivalent to setting $b_{max} \sim v/b$ and ignoring the exponential. These approximations and simplifications can be dealt with by including them in the Gaunt factor, g_{ff}, – a correction for quantum mechanical effects (Gaunt, 1930). The lower integration limit can be set by considering the high energy regime, as is present in clusters. The high energy of the each electron means that each

has a large velocity: the uncertainty principle stops the electron from getting any closer than $b_{min} \sim \hbar/m_e v$ (Heisenberg, 1927). As the electrons within the intracluster medium have a distribution of energies, instead of all electrons possessing the same velocity (as was earlier assumed), they will have a Maxwell-Boltzmann distribution of velocities (Maxwell, 1860),

$$dP = \exp(mv^2/2kT)4\pi v^2 dv, \tag{2.12}$$

where T is the electron temperature. The velocity distribution can be averaged over, leading to

$$\epsilon^{ff}(\nu) = \int_{v_{min}}^{\infty} \frac{dW}{d\omega dt dV} dP(v). \tag{2.13}$$

Taking Equations 2.11 and 2.12, plugging them into Equation 2.13 and evaluating leads to the thermal bremsstrahlung emission equation

$$\epsilon^{ff}(\nu) = \frac{32\pi e^6}{3m_e c^2}\left(\frac{2\pi}{3m_e k_B T_X}\right)^{0.5} n_e \exp\left(\frac{-h\nu}{k_B T_X}\right)\sum_i n_i Z_i^2 g_{ff}(Z, T_X, \nu), \tag{2.14}$$

where k_B is the Boltzmann constant; T_X is the cluster temperature; h is the Planck constant and Z and n_i are the charges and densities of the ions involved in the collision respectively.

The emissivity for line emission is given by (Osterbrock, 1974):

$$\int \epsilon^{line}(\nu)d\nu = n(X_i)n_e \frac{h^3\nu\Omega(T_X)B}{4\omega_{gs}(X_i)}\left(\frac{2}{\pi^3 m_e^3 k_B T_X}\right)^{0.5} \exp -\Delta E/k_B T_X, \tag{2.15}$$

where X_i represents the energy levels of the ion; Ω is the collision strength; B is the branching ratio; ω is the statistical weight of the levels and ΔE is the excitation energy above the ground state.

These two emission processes are typically combined into a single emissivity, which increases with the electron density (described in Equation 2.5), and whose other properties are only dependent on the electron temperature. This can be written as

$$\epsilon_\nu = \sum_{X_i} n(X_i) n_e \lambda_c(X_i T_e), \tag{2.16}$$

where $\lambda_c(X_i T_e)$ is the cooling function, which is a function of the ion and the temperature.

Equations 2.14 and 2.15 are dependent upon the properties of the cluster, such as the gas temperature and elemental abundances, so by fitting to the cluster's spectrum it is possible to be informed about the cluster's nature.

As discussed in Section 2.1, galaxy clusters are approximately in hydrostatic equilibrium. In the presence of a fifth force, such as the one described in Equation 1.40, the hydrostatic equilibrium equation is modified with an additional pressure force. Terukina and Yamamoto (2012) showed that the hydrostatic equilibrium equation in the presence of a fifth force (Equation 1.40) is:

$$\frac{1}{\rho_{\rm gas}(r)} \frac{dP_{\rm gas}(r)}{dr} = -\frac{GM(<r)}{r^2} - \frac{\beta}{M_{\rm Pl}} \nabla\phi, \tag{2.17}$$

where $\rho_{\rm gas}$ is the gas density, M the total mass within a radius r, and $P_{\rm gas}$ is the electron pressure.

In an ideal cluster, i.e. one that is isolated, isothermal, and spherical, this total pressure is felt by the electrons and ions in the ionised intracluster plasma, so that $P_{\rm gas} = n_{\rm e} kT$, where $n_{\rm e}$ is the electron number density, and T is the electron temperature. Then the standard *beta-model* (equation 2.5) is adopted to describe the gas distribution within the cluster.

Integrating Equation 2.17 gives

$$P_{\rm e}(r) = P_{\rm e,0} + \mu m_{\rm p} \int_0^r n_e(r) \left(-\frac{GM(<r)}{r^2} - \frac{\beta}{M_{\rm Pl}} \frac{d\phi(r)}{dr} \right) dr, \tag{2.18}$$

where $P_{\rm e,0}$ is the electron gas pressure at $r = 0$, given by $P_{\rm e,0} = n_{\rm e,0} kT$ and $n_{\rm e,0} = 5n_0/(2+\mu)$ and $M(<r)$, the halo mass. Equation 2.18 can be re-expressed by taking the integral of Equation 2.16 so

$$S_{\rm B}(r_\perp) = \int \epsilon_\nu = \int n(X_i) n_e \gamma_c(X_i T_e). \tag{2.19}$$

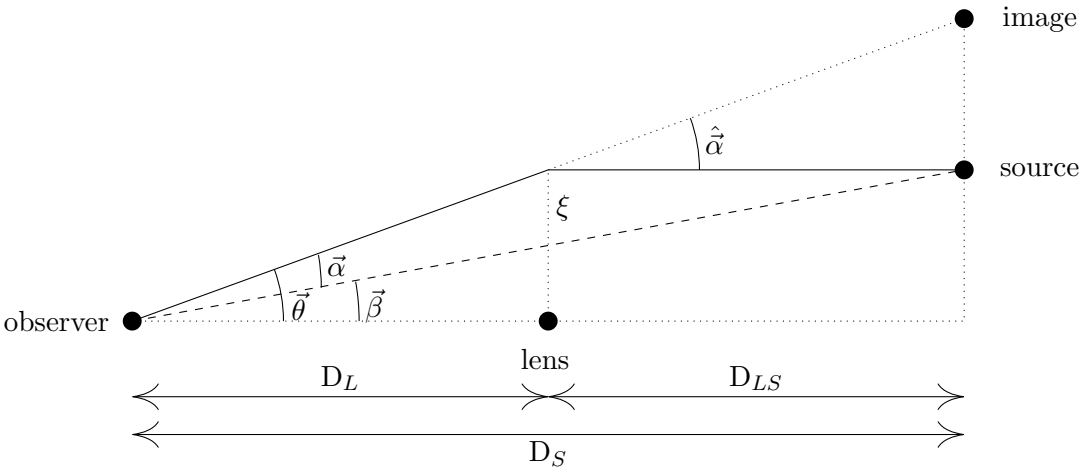

FIGURE 2.5: Diagram of a gravitationally lensed system showing the geometry involved in the lensing of a light beam by a lens on its path to a source. An explanation of the symbols is shown in Section 2.2.3. Figure author's own.

To simplify Equation 2.16, the assumption is made that the gas within the intracluster medium is dominated by hydrogen such that $n(X_i) = n_e$. This leads to

$$S_{\rm B}(r_\perp) = \frac{1}{4\pi(1+z)^4} \int n_{\rm e}^2 \left(\sqrt{r_\perp^2 + z^2}\right) \lambda_c(T_{\rm gas}) dz, \tag{2.20}$$

where $r_\perp$ is the projected distance from the cluster centre and z the cluster redshift. This gives the surface brightness, $S_{\rm B}(r_\perp)$, using the temperature and electron density dependent cooling function (see Section 4.3.2) and is later used in Section 5.2 to compare stacked X-ray cluster profiles to the chameleon model.

2.2.3 Gravitational lensing

Gravitational lensing is the deflection of light as it passes near massive objects in the Universe. It proves to be a fitting name as this matter behaves much like a conventional lens distorting and magnifying light rays. This effect was first described by Einstein's theory of general relativity in 1916 (Einstein, 1916). Soon after its publication in 1919, Eddington led his famous expedition in Africa to measure the bending of light around the sun during a solar eclipse. The measured offset was consistent with Einstein's prediction (Dyson et al., 1920), twice the deflection as predicted from Newtonian gravity, lending credibility to the theory.

The strength of the lensing signal is dependent upon both the mass of the lensing object and the geometry of the source-lens-observer system, as shown in Figure 2.5.

In this figure, the three distances (D_L, D_S and D_{LS}) are angular diameter distances, where this is a ratio of an objects real size, r, to its angular size as viewed from Earth, Θ,

$$D_A \propto \frac{r}{\Theta}. \tag{2.21}$$

A light ray from the source is deflected by an angle $\hat{\vec{\alpha}}$ due to the lensing mass at a distance D_L from the observer. This causes an image to be seen at an angle $\vec{\theta}$. Without the lensing mass the source would be observed at the angle $\vec{\beta}$. Here it is clear that a more prominent signal will be seen if the source and lens are well separated and well aligned along the line of sight of the observer. Outlined below is the underlying physics of gravitational lensing, following the derivations in Schneider et al. (1992) and Bartelmann and Schneider (2001).

In the thin lens approximation, where the depth of the lens along the line of sight is much smaller than D_L and D_{LS}, the deflection angle, $\hat{\vec{\alpha}}$, at the position of the impact parameter, ξ (Schutz, 1985), is defined by

$$\hat{\vec{a}} = \frac{4GM(<\xi)}{c^2\xi}, \tag{2.22}$$

for a circularly symmetric lens. This deflection is twice the angle predicted by Newtonian mechanics, and famously measured by Eddington. The correct deflection is related to the Newtonian prediction via the relation

$$\hat{\vec{a}} = \frac{2}{c^2}\int \nabla\Phi_\perp dl, \tag{2.23}$$

by integrating along the null geodesic and taking the gradient of the Newtonian potential, $\nabla\Phi_\perp$.

Here it is of note that space is acting just like an optical lens with a refractive index $n = 1 - \frac{2\Phi}{c^2}$. It is therefore highly appropriate that this are of study is referred to as lensing as results used in conventional optical lensing directly translate across to gravitational lensing. A further note is, as the deflection angle is dependent only upon the intervening potential, the measured deflection is invariant on the source of the matter acting as the lens, be it baryonic or dark in nature.

This in turn means that gravitational lensing is a purely geometric effect. Figure 2.5 shows that, in the small angle approximation,

$$\vec{\theta} D_S = \vec{\beta} D_S + \hat{\vec{\alpha}} D_{LS}. \tag{2.24}$$

The reduced deflection angle is defined by

$$\vec{a} = \frac{D_{LS}}{D_S} \hat{\vec{a}}. \tag{2.25}$$

From this, and Figure 2.5, it is possible to simply read off the relation

$$\vec{\beta} = \vec{\theta} - \vec{\alpha}. \tag{2.26}$$

This is known as the lens equation, one of the fundamental equations of gravitational lensing. It allows mapping from the source plane to the image plane and raytracing to reconstruct unlensed images from lensed ones.

Unfortunately the real Universe is more complex than the simple diagram of an isolated point mass shown in Figure 2.5, with any line of sight likely to contain many separate clumps of matter. Thankfully the lens equation holds true for any superposition of lenses, provided the thin lens approximation (that is the extent of the lensing matter is $\ll D_L, D_{LS}$) holds true.

If the 3D distribution of matter, $\rho(\vec{\theta}, z)$, is projected down into a single plane, the dimensionless convergence as can be defined as

$$\kappa(\vec{\theta}) = \frac{4\pi G}{c^2} \int \frac{D_{LS} D_L}{D_S} \rho dD_S, \tag{2.27}$$

where the integral is along the line of sight to the source. It is useful to combine all the constant factors together into the critical surface mass density, Σ_c (Kneib and Natarajan, 2011)

$$\Sigma_c = \frac{c^2}{4\pi G} \frac{D_S}{D_{LS} D_L}, \tag{2.28}$$

which contains all of the relevant geometric distances. The convergence, as introduced in Equation 2.27, can then be simplified into the compact form

$$\kappa(\vec{\theta}) = \frac{\Sigma(\vec{\theta})}{\Sigma_c}. \tag{2.29}$$

Continuing, the gravitational potential can be projected into the 2D lensing potential, ψ. This is achieved by first rewriting the deflection angle, $\vec{\alpha}$, in terms of the convergence, κ,

$$\vec{a}(\vec{\theta}) = \frac{1}{\pi}\int \kappa(\vec{\theta'})\frac{\vec{\theta}-\vec{\theta'}}{|\vec{\theta}-\vec{\theta'}|^2}d^2\vec{\theta'}, \tag{2.30}$$

and knowing the deflection angle can be written as the gradient of the lensing potential, $\vec{\alpha} = \nabla\psi$, allows the lensing potential as a function of the convergence to be obtained

$$\psi(\vec{\theta}) = \frac{1}{\pi}\int \kappa(\vec{\theta'})\ln|\vec{\theta}-\vec{\theta'}|d^2\vec{\theta'}. \tag{2.31}$$

This satisfies the Poisson equation, and can be rewritten as

$$\kappa = \frac{1}{2}\nabla^2_\theta\psi. \tag{2.32}$$

By measuring the position of a single, weakly lensed object, such as from a point source, it would be impossible to infer its true position or learn anything about the lensing mass. This is because galaxies have a range of intrinsic sizes and ellipticities, so measuring the ellipticity distortion due to lensing on an object with an unknown ellipticity is impossible. Thankfully source objects in the real Universe (typically galaxies) are extended, and therefore light emitted from differing locations on the source pass by lenses at subtly different impact parameters. This in turn causes different parts of the source to be lensed differently, distorting its shape.

2.2.4 Weak lensing

Weak gravitational lensing is the small-scale coherent distortion of background sources by an intervening lens. This lens can be any sufficiently concentrated mass, such as an

individual galaxy or galaxy group. The strongest weak lensing signals are present around galaxy clusters due to their large masses, as described in Section 2.1.

These distortions are completely described by the lensing equation (Equation 2.26 and discussed in Section 2.2.4), allowing the mapping between source and image planes. In the regime of weak lensing (where $\kappa \ll 1$), these distortions can be expressed as a Jacobian matrix (Wambsganss, 1998)

$$\mathcal{A}_{ij}(\vec{\theta}) = \frac{\partial \beta_i}{\partial \theta_j} = \delta_{ij} - \frac{\partial^2 \psi}{\partial \theta_i \partial \theta_j}, \tag{2.33}$$

which after some rearranging leads to

$$\mathcal{A}(\vec{\theta}) = \begin{pmatrix} 1 - \kappa(\vec{\theta}) - \gamma_1(\vec{\theta}) & -\gamma_2(\vec{\theta}) \\ -\gamma_2(\vec{\theta}) & 1 - \kappa(\vec{\theta}) + \gamma_1(\vec{\theta}) \end{pmatrix}. \tag{2.34}$$

Here the convergence is introduced as

$$\kappa = \frac{1}{2}(\partial_1^2 + \partial_2^2)\psi, \tag{2.35}$$

and two components of shear

$$\gamma_1 = \frac{1}{2}(\partial_1^2 - \partial_2^2)\psi, \tag{2.36}$$

$$\gamma_2 = \partial_1 \partial_2 \psi. \tag{2.37}$$

Figure 2.6 shows the effect of gravitational lensing upon a circular galaxy. To better understand what effect this is having, Equation 2.34 can be rewritten

$$\mathcal{A}(\vec{\theta}) = (1 - \kappa) \begin{pmatrix} 1 & 0 \\ 0 & 1 \end{pmatrix} - \sqrt{\gamma_1^2 + \gamma_2^2} \begin{pmatrix} \cos(2\phi) & \sin(2\phi) \\ \sin(2\phi) & -\cos(2\phi). \end{pmatrix} \tag{2.38}$$

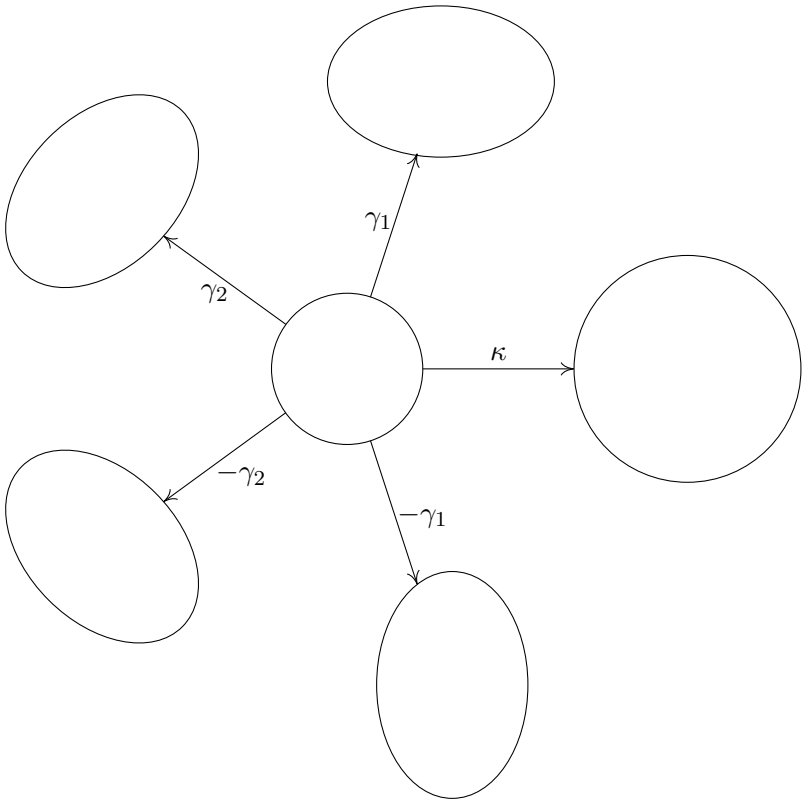

FIGURE 2.6: Diagram showing the effect of convergence and shear upon a cartoon galaxy. Converge modulates the galaxies apparent size and the shear modulates any observed stretching of the galaxies image. Figure author's own.

This shows that the two components of shear stretch out the galaxy. Firstly the γ_1 component stretches the galaxy along the x and y axes, while the γ_2 component stretches the galaxy along the axes 45° to this.

It is possible to combine both shear components into a single complex value,

$$\gamma = \gamma_1 + i\gamma_2 = |\gamma| e^{2i\phi} \tag{2.39}$$

where ϕ is the direction of the shear and $|\gamma|$ its magnitude. Finally it can be seen that the convergence produces an enlargement of the source. As gravitational lensing conserves surface brightness, the magnification, the ratio of lensed and unlensed solid angles, can be defined as

$$\mu = \frac{1}{\det \mathcal{A}} = \frac{1}{(1-\kappa)^2 - \gamma^2}. \tag{2.40}$$

In an idealised situation, perfectly round background sources would be lensed and therefore allow the matter distribution along all lines of sight to be reconstructed. Unfortunately the most abundant sources in the Universe are galaxies, which exhibit a typical ellipticity of 30%, while the distortions due to lensing are typically $< 1\%$.

In order to be able to detect a signal, the shapes of many galaxies are measured to obtain a statistically significant result that is representative of the populations average. One common use is to measure the distortions of galaxies due to the large scale structure of the Universe to measure a quantity known as cosmic shear. Cosmic shear was first measured by Kaiser et al. (2000), Bacon et al. (2000), Wittman et al. (2000) and Van Waerbeke et al. (2001) and later used to constrain the cosmological parameters Ω_0 and σ_8 in Maoli et al. (2001).

If a galaxy cluster is massive enough however, it becomes possible to use weak lensing to probe the dark matter distribution within. The first detection of this type came from Tyson et al. (1990) who measured the coherent distortion of background galaxies around two clusters. In Figure 2.7, histograms of galaxy alignment behind one of these clusters are shown. It is clear to see the preferential tangential alignment of blue background galaxies compared to the red cluster galaxies and blue galaxies from comparison fields.

The final common use of weak lensing is to measure the lensing of background galaxies by foreground galaxies in a technique known as galaxy-galaxy lensing. This type of detection can be used to investigate the dark matter distribution of an ensemble of galaxies. Brainerd et al. (1996) reported the first detection of galaxy-galaxy lensing.

In Section 2.2.3 the definitions for the shear that occurs in galaxies caused by massive lenses have been defined. However, as these quantities cannot be directly measured, instead the shapes of galaxies are measured and the shear inferred from these shapes. Here I will briefly describe one method for measuring this shear, known as `LENSFIT` (Miller et al., 2013).

THis techniques takes a model fitting approach to each galaxy. This involves the creation of two galaxy models to describe the two dominant populations of source galaxies. The first one is modelled purely by a bulge and fit using a de Vaucouleurs profile (de Vaucouleurs, 1948) (a Sérsic profile with $n = 4$, see below). The second contains two components, a bulge and a disk, both modelled by a pure exponential - the disk having

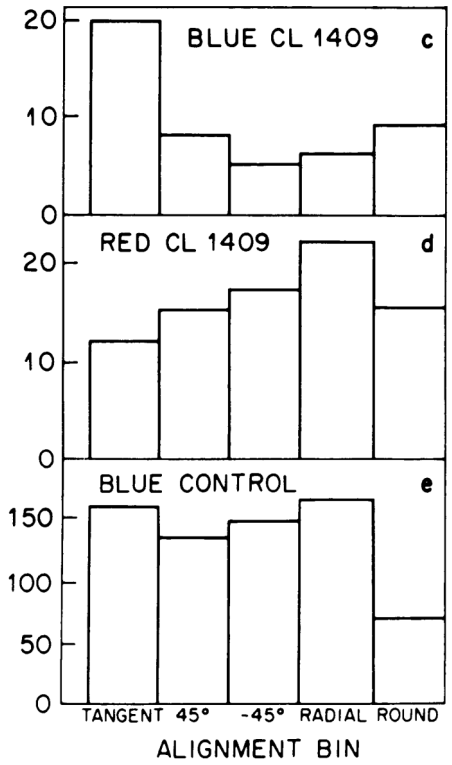

FIGURE 2.7: Histograms of the major axis alignments relative to the center of the cluster CL 1409 for c) Blue background galaxies, d) Red cluster galaxies, e) Blue galaxies in comparison fields. These plots show that clusters behind the cluster are tangentially aligned with it. Figure from Tyson et al. (1990).

a Sérsic index of 1, and the bulge a Sérsic index of 4 (Sérsic, 1963). The Sérsic profile equation is shown below

$$I(r) = I_0 \exp\left(-\left[\frac{r}{\alpha}\right]^{\frac{1}{n}}\right), \tag{2.41}$$

where I_0 is the galaxy's central brightness, α is a scale length and n is known as the Sérsic index which controls the surface brightness fall-off. `LENSFIT` then uses a seven parameter fit to each galaxy: bulge fraction; central surface brightness; size; ellipticity, e_1, e_2 and galaxy position, x, y.

The central surface brightness and the two galaxy positions x and y, describing the galaxy's position within the image, can then be marginalised over. The other parameters are then simultaneously fit, minimising the χ^2, while sampling the ellipticity likelihood surface. This can be achieved by first generating a course ellipticity grid (separated by intervals of 0.16 in ellipticity), at which each point a full marginalisation of the other parameters is carried out. A finer ellipticity grid is then constructed around the position

in ellipticity space with the highest likelihood and a further full marginalisation of the other parameters carried out. The position here with the highest likelihood is then taken as the best fit for the two ellipticity components, e_1 and e_2.

Since the first weak lensing detection 25 years ago, the field of weak lensing has drastically improved in both scale and accuracy, with the latest weak lensing surveys measuring the shapes of millions of objects to high accuracy (i.e. Abbott et al. 2016). This in turn has allowed lensing to emerge as a cosmological probe. Kilbinger et al. (2013) have used 154 square degrees from CFHTLenS (a lensing survey discussed in greater detail in Section 4.2.1) to measure the 2D cosmic shear correlation function. By combining this data set with those from the CMB and BAO measurements (as described in Section 1.3) Kilbinger et al. (2013) were able to obtain some of the most accurate cosmological parameters.

More recently Jee et al. (2015) investigated cosmic shear from the Deep Lens Survey, a 20 square degree survey, a precursor survey to LSST (LSST Dark Energy Science Collaboration, 2012) with a limiting magnitude of $r = 27$. Using the auto and cross correlations of the lensing signal in five redshift bins combined with CMB data, the authors constrained $H_0 = 68.6^{+1.4}_{-1.2}$, consistent with and of similar constraining power to the world leading Planck satellite measurements, alongside other cosmological parameters to a similar level of accuracy.

2.2.5 Weak lensing in clusters

As weak lensing provides mass estimates that require no assumption of the dynamical state of the matter being probed, weak lensing is becoming increasingly popular to study the lensing signal around galaxy clusters.

If the clusters are massive enough this is can be performed on a cluster-by-cluster basis. Recently projects such as the Canadian Cluster Comparison Project (CCCP Hoekstra et al. 2012), Weighing the Giants (WtG, von der Linden et al. 2014) and the Local Cluster Substructure Survey (LoCuSS, Okabe and Smith 2015) have begun to measure the individual masses of tens of clusters. These studies have been used to greatly improve a variety of mass-observable relations (such as X-ray temperature, optical richness – a measure of the number of galaxies that the cluster contains – and the SZ effect, e.g. Okabe

et al. 2010). In turn this leads to the tighter constraining of cosmological parameters (e.g. Mantz et al. 2015).

It is rare that an individual cluster is massive enough to produce a detectable weak lensing signal. However, as cosmological predictions of the formation of structure are of a statistical nature, it is possible to use the ensemble averages of a range of cluster properties to constrain cosmology. Large-scale lensing surveys such as the Canada France Hawaii Telescope Lensing Survey (CFHTLenS, Heymans et al. 2012), the Kilo Degree Survey (KiDS, de Jong et al. 2013a) and the Dark Energy Survey (DES, The Dark Energy Survey Collaboration 2005) have taken accurate lensing measurements over hundreds of square degrees.

Johnston et al. (2007) measured the lensing signal around 130,000 stacked galaxy clusters (cluster stacking is discussed in more detail in Section 4.3.3) in 12 richness bins. The results of these stacks can be seen in Figure 2.8: an increase in cluster richness (associated with a larger mass) can be seen to lead to a stronger lensing signal. Here Johnston et al. (2007) have measured the mean excess projected mass density, $\Delta\Sigma$, a measure of the projected mass density within an aperture minus the mass density at that aperture. From these fits Johnston et al. (2007) were able to accurately calibrate the mass richness relation. The authors go on to discuss how such a work could be used to measure the cluster mass function, which in turn measures cosmological parameters.

The expression used in Johnston et al. (2007) and throughout this thesis to fit the weak lensing shear profiles (under the assumption of an underlying NFW profile) as a function of radius is given in Wright and Brainerd (2000) and is reproduced below:

$$\gamma_{NFW}(x) = \begin{cases} \frac{r_s \delta_c \rho_c}{\Sigma_c} g_<(x) & : x < 1, \\ \frac{r_s \delta_c \rho_c}{\Sigma_c} [\frac{10}{3} + 4ln(\frac{1}{2})] & : x = 1, \\ \frac{r_s \delta_c \rho_c}{\Sigma_c} g_>(x) & : x > 1, \end{cases} \tag{2.42}$$

where $g_<(x)$ and $g_>(x)$ are functions depending only on the dimensionless factor $x = r/r_s$.

$$g_<(x) = \frac{8 \operatorname{arctanh} \sqrt{(1-x)/(1+x)}}{x^2 \sqrt{1-x^2}} + \frac{4}{x^2} \ln\left(\frac{x}{2}\right) - \frac{2}{x^2-1} + \frac{4 \operatorname{arctanh} \sqrt{(1-x)/(1+x)}}{(x^2-1)\sqrt{1-x^2}}, \tag{2.43}$$

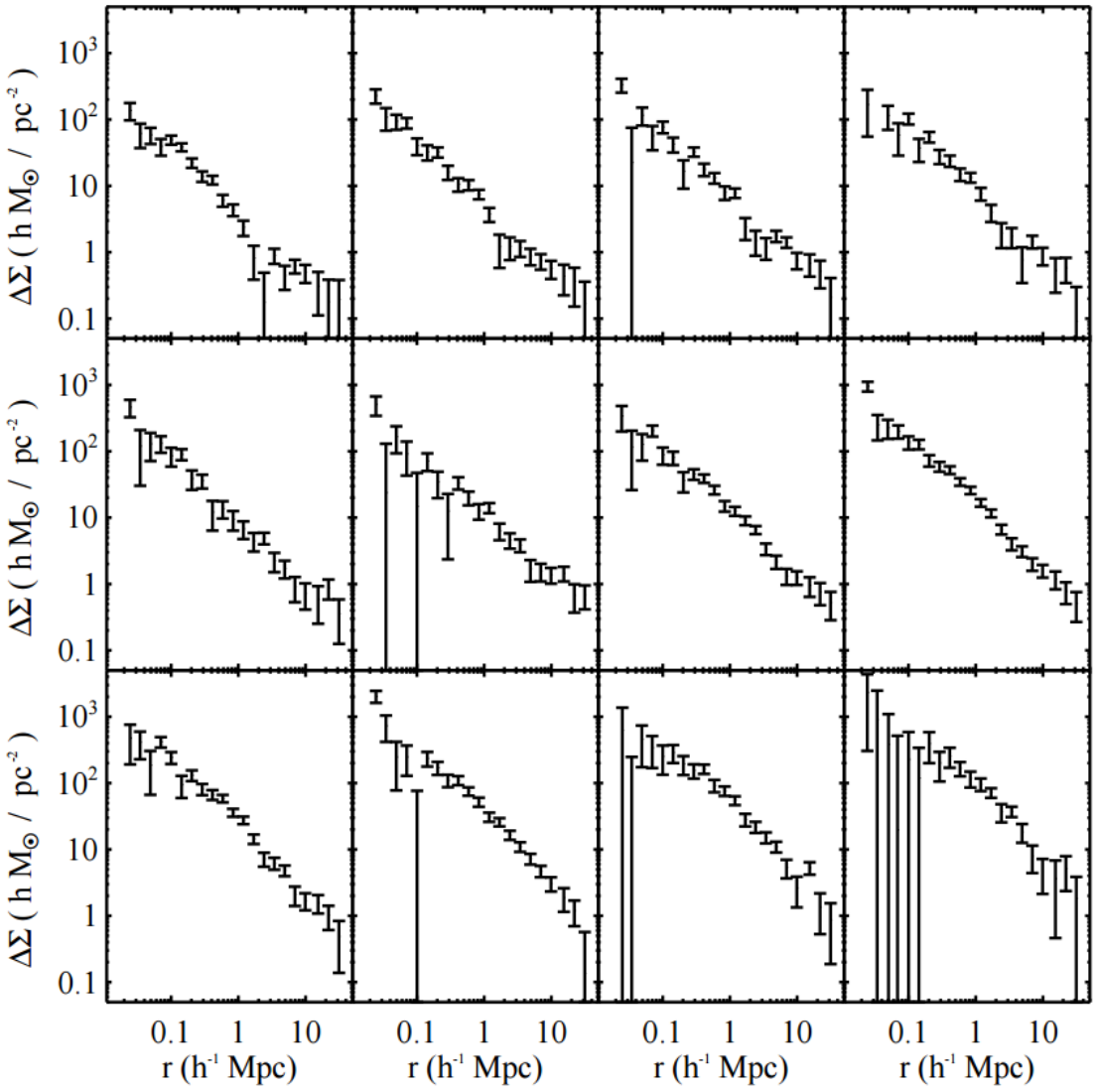

FIGURE 2.8: Weak lensing profiles for 12 stacked richness bins increasing in richness from top left to bottom right as a function of radius with associted errors. Here the lowest richness bin contains 58788 galaxies and the richest bin 47. This figure shows that larger clusters generate a larger lensing signal. Figure from Johnston et al. (2007).

$$g_>(x) = \frac{8\arctan\sqrt{(x-1)/(1+x)}}{x^2\sqrt{1-x^2}} + \frac{4}{x^2}\ln\left(\frac{x}{2}\right) - \frac{2}{x^2-1} + \frac{4\arctan\sqrt{(x-1)/(1+x)}}{(x^2-1)^{3/2}}. \tag{2.44}$$

Using Equation 2.42 it is possible to describe the shape of the main dark matter halo and the baryons associated with it. This profile is commonly known as the 1-halo term, as it arises from the presence of a single halo. However clusters are not isolated from the Universe, forming at the meeting points of filaments. This correlated matter can lead to a modification of the cluster profile known as the 2-halo term. The tangential shear profile

due to the 2-halo term is given by (Oguri and Takada 2011, Oguri and Hamana 2011):

$$\gamma_{t,2h}(\theta; M, z) = \int \frac{l}{2\pi} J_2(l\theta) \frac{\bar{\rho}_m(z) b_h(M; z)}{(1+z)^3 \Sigma_{cr} D_A^2(z)} P_m(k_l; z) dl, \tag{2.45}$$

where J_2 is the second order Bessel function, $\bar{\rho}_m$ is the mass density, b_h is halo bias, D_A is the angular diameter distance, P_m the linear power spectrum and $k_l = l/((1+z)D_A(z))$.

The total shear profile of the cluster is then given by the sum of equations 2.42 and 2.45 as

$$\gamma_t = \gamma_{NFW} + \gamma_{t,2h}. \tag{2.46}$$

Theses results are used in Section 4.2.1 to test the lensing data used to constrain gravity in Chapter 5.

2.2.6 Mass maps

Most studies constraining cosmology using shear measurements elect to utilise various N-point statistics (e.g. 2-pt in Jarvis et al. 2006, Bacon et al. 2003 and 3-pt in Vafaei et al. 2010). However, using gravitational lensing it is also possible to reconstruct the projected mass density to make mass maps showing the distribution of dark matter over a survey area (i.e. Van Waerbeke et al. 2013, Vikram et al. 2015). These maps can then potentially capture information not readily available from two point statistics.

These maps can be useful in several ways. They allow a probing of the dark matter distribution in the Universe. The density of matter peaks can be used to measure the number of dark matter halos as a function of mass and redshift, and also to constrain cosmological parameters (Jain and Van Waerbeke 2000, Dietrich and Hartlap 2010).

Correlating the projected density with similar maps from different wavelength surveys, such as gas and light maps, can place constraints upon other observables such as the mass to light ratio and galaxy bias (Amara et al. 2012, Shan et al. 2014). Maps of this type can also be used to identify super clusters and voids, the detection of which is often difficult. This difficulty firstly arises in the array of definitions of what constitutes a void and consequently there is disagreement over the edges of these regions Shandarin et al. (2006). Also, even if a universal definition were agreed upon the diffuse nature of these

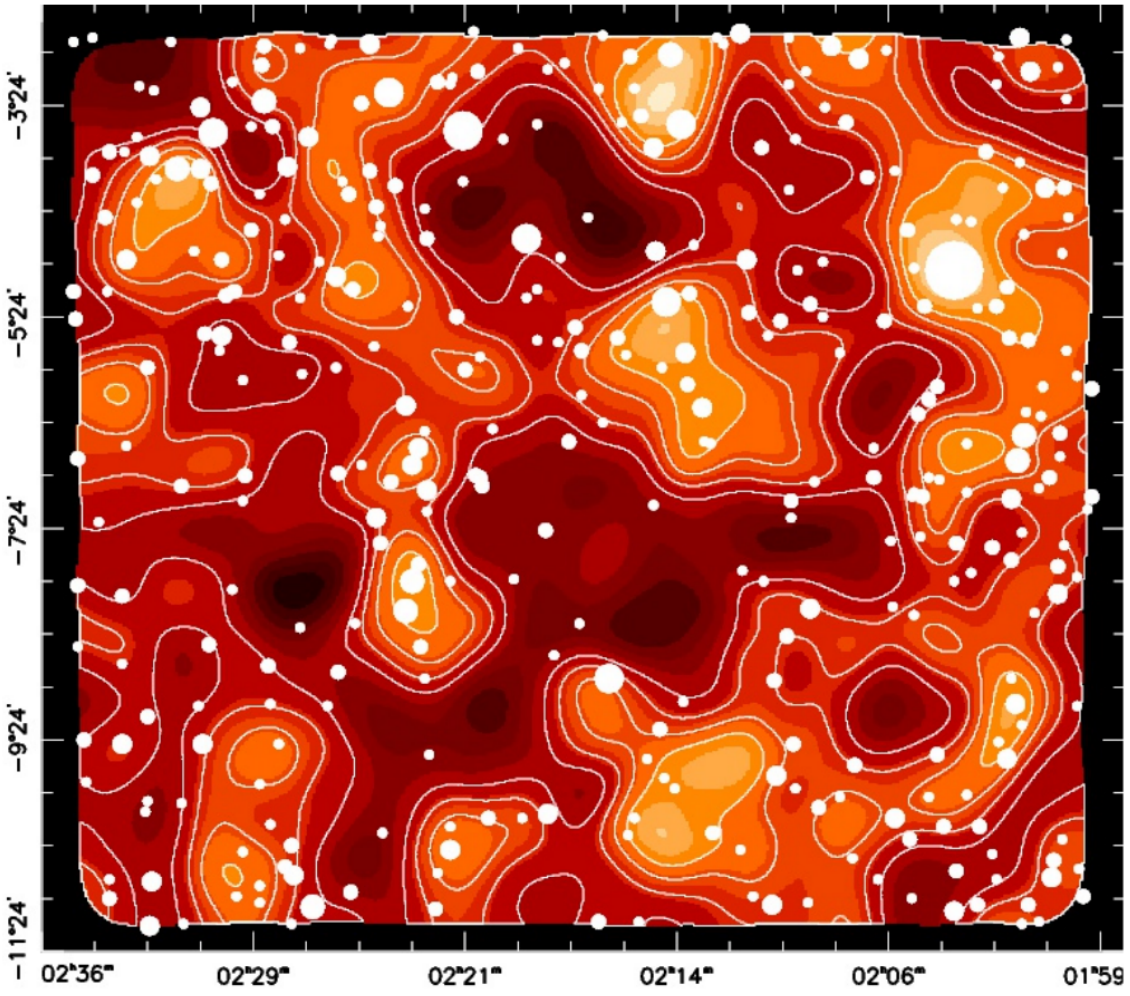

FIGURE 2.9: Projected mass density of 64 square degrees from CFHTLenS, lighter areas denote regions of higher density. The white circles denote the predicted mass peaks from the projected galaxy density distribution. Figure from Van Waerbeke et al. (2013).

giant structures makes detecting the interface between void or super cluster with the background density very tricky.

One popular technique for performing this density reconstruction is the Kaiser-Squires inversion (Kaiser and Squires, 1993). In this method, relationships between shear, convergence and the lensing potential described in Equations 2.29, 2.36 and 2.37 are defined. These are made by taking the Fourier transformation of these quantities

$$\widetilde{\gamma}_1 = \frac{1}{2}(k_1^2 - k_2^2)\widetilde{\psi}, \tag{2.47}$$

$$\widetilde{\gamma}_2 = k_1 k_2 \widetilde{\psi}, \tag{2.48}$$

$$\widetilde{\kappa} = \frac{1}{2}(k_1^2 + k_2^2)\widetilde{\psi}. \tag{2.49}$$

With some gentle rearranging it is possible to relate $\widetilde{\kappa}$ to the two components $\widetilde{\gamma_1}$ and $\widetilde{\gamma_2}$

$$\widetilde{\kappa} = \frac{k_1^2 + k_2^2}{k_1^2 - k_2^2}\widetilde{\gamma_1} \qquad \widetilde{\kappa} = \frac{k_1^2 + k_2^2}{2k_1k_2}\widetilde{\gamma_2}. \tag{2.50}$$

A linear combination of these two equations is considered to find

$$\widetilde{\kappa} = a\frac{k_1^2 + k_2^2}{k_1^2 - k_2^2}\widetilde{\gamma_1} + (1-a)\frac{k_1^2 + k_2^2}{2k_1k_2}\widetilde{\gamma_2}. \tag{2.51}$$

Then minimising $\langle\widetilde{\kappa}^2\rangle$ with respect to a, finds $a = (k_1^2 - k_2^2)/k^4$ (Kaiser and Squires, 1993), leading to an estimator of

$$\widetilde{\kappa} = \frac{1}{k_1^2 + k_2^2}[(k_1^2 - k_2^2)\widetilde{\gamma_1} + 2k_1k_2\widetilde{\gamma_2}]. \tag{2.52}$$

A limitation of the Kaiser-Squires is that, as the ellipticities of galaxies are statistically uncorrelated, they form a white noise power spectrum that integrates to infinity for large spatial frequencies. A way to mitigate this effect is to remove the high frequency components, for example by implementing a Gaussian filter such as

$$W_\theta = \frac{1}{\pi\sigma^2}\exp\left(-\frac{|\theta|^2|}{2\sigma^2}\right). \tag{2.53}$$

By first smoothing the shear data using Equation 2.53, then implementing Equation 2.52, it becomes possible to measure the projected surface density of an area simply given the shear measurements of the galaxies within that area.

Figure 2.9 shows a projected density map from Van Waerbeke et al. (2013), one of the largest areas to be reconstructed using this method. The data for this map came from CFHTLenS and this plot is used during tests to shear data (discussed further in 4.2.1).

2.3 Probes of modified gravity

Section 1.5 described the effect that $f(R)$ gravity would have on both X-ray surface brightness and weak lensing cluster profiles. The techniques used to measure X-ray surface brightness profiles are discussed in Section 2.2.2 and how to measure weak lensing profiles in Section 2.2.5. By jointly fitting these two profiles it becomes possible to constrain $f(R)$ gravity, which is shown and further discuss in Chapter 5.

Figure 2.10 shows several profiles of the same galaxy cluster using several different observables. The top left plot here shows the cluster's X-ray surface brightness against its radius. The solid blue line here is the cluster under the influence of GR, while the dashed blue line is the cluster under the influence of $f(R)$ gravity as described in Equation 2.20. Here it can be seen that in the presence of a chameleon field the surface brightness is compressed at the cluster's outskirts. The dashed black vertical line also shown is r_c as described in Equation 2.6.

The top right plot of Figure 2.10 shows the same cluster's hydrostatic mass (as described in Equations 5.9 and 5.11) against radius. Once more the solid blue line is the cluster under the influence of GR, the dashed blue line includes the additional $f(R)$ term and the dashed black line is r_c. This plot shows that in the presence of a chameleon field the mass inferred from hydrostatic equilibrium is reduced.

Finally the bottom plot of Figure 2.10 shows the same cluster's weak lensing profile, as described by Equation 2.42. The solid blue line here is the profile under the influence of GR, which lies completely on top off the clusters profile with an additional $f(R)$ gravity term, as this profile is not altered (as described in Section 1.5). Once more the dashed line here is r_c.

This figure shows how the cluster profile is expected to differ from the GR prediction under the influence of $f(R)$ gravity. Of importance to note is that the strongest deviations away from the GR prediction (beyond r_c, where $f(R)$ gravity is no longer screened) occur at or outside the cluster's r_{200}. Therefore this technique of constraining f_R gravity relies strongly upon the NFW prediction of the cluster's profile (as described in Section 2.1).

Alongside comparing cluster profiles as described above, there are many other techniques that are used to place constraints upon $f(R)$ gravity at a range of scales; these are discussed below.

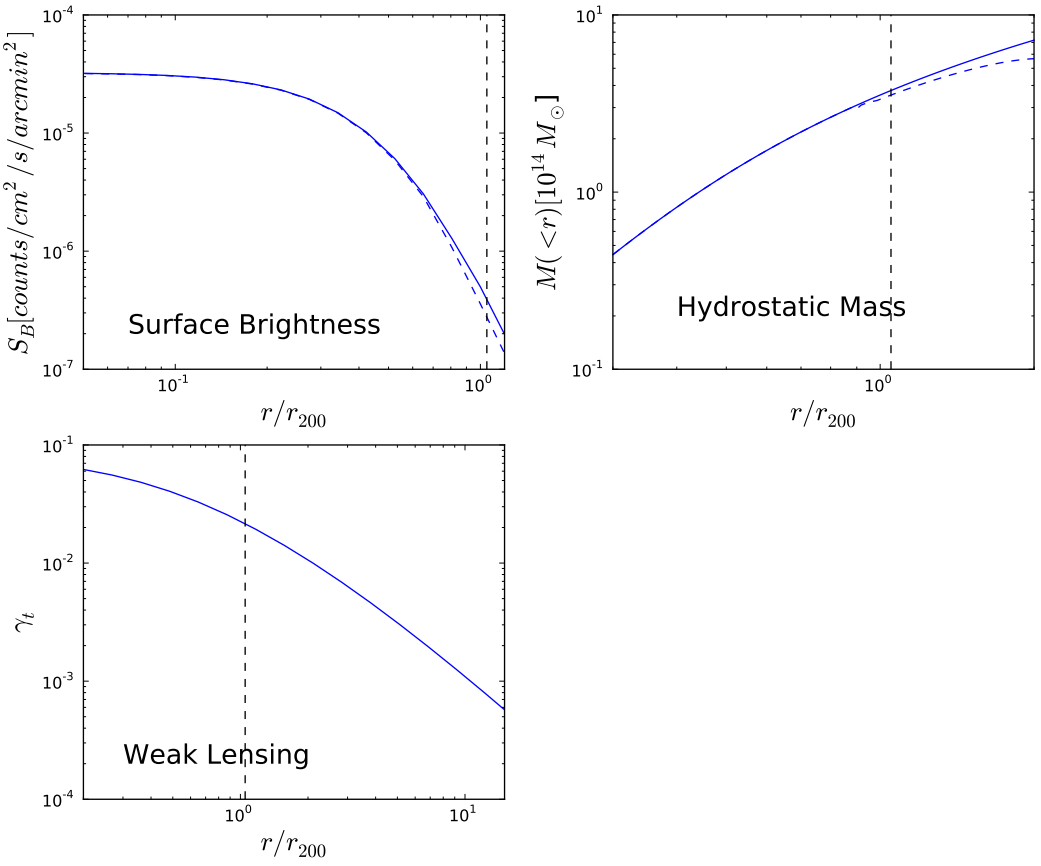

FIGURE 2.10: Three plots to show how a clusters profile measured using various metrics varies in the presence of $f(R)$ gravity. In each three plots the solid blue line is the cluster under GR, while the dotted line is the same cluster in the presence of $f(R)$ gravity. The top left figure here shows the X-ray surface brightness against radius, top right the hydrostatic mass against radius and bottom shows the lensing profile against radius. In each case the dotted line here is r_c.

The current tightest constraints on deviations from GR come from the Eöt-Wash experiment (Stubbs et al., 1987). This experiment tests the weak equivalence principle, which states that an object's inertial mass and its gravitational mass are equal. This is measured by the Eötvös parameter, also known as the gravitational slip,

$$\eta = 1 - \frac{\Phi}{\Psi}, \tag{2.54}$$

where Φ and Ψ are the two space-time potentials. Using a finely tuned torsion balance comprised of beryllium-aluminium and beryllium-titanium test pairs, Wagner et al. (2012) constrained $\eta < 10^{-13}$. Torsion balances are sensitive to the angle between the forces on their test mass, such that if the forces are parallel there will be no torque. The Eöt-Wash

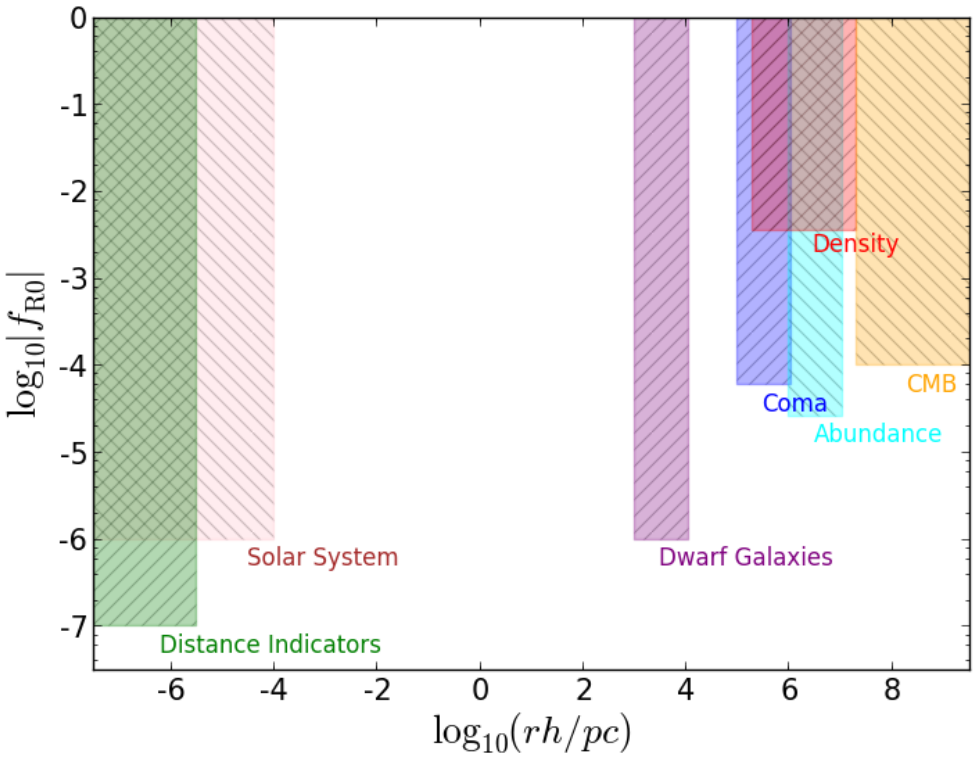

FIGURE 2.11: Comparison of current constraints on $f(R)$ gravity discussed in this section as a funciton of scale. The shaded areas denote regions of parameter space that are ruled out by the associated test. Adapted from Terukina et al. (2014).

experiment tests the equivalence principle by comparing the ratio of inertial forces from the Earth's rotation with the gravitational force on the test masses. If these forces are unequal a torque in the torsion fiber would then be observed.

However, as chameleon screening is dependent upon the depth of the local potential, it is expected in dense environments, such as inside the milky way, to preserve equivalence. As discussed earlier, in the presence of a fifth force, it might be possible to detect a non-zero η. There have been earlier attempts to constrain f_{R0} using a variety of different astrophysical probes over a huge range of scales. The latest constraints are summarised in Figure 2.11.

These constraints are discussed in more detail below, starting with those measurements made at the smallest scale, within the solar system, before moving up in scale through dwarf galaxies and distance indicators, to galaxy clusters and the Cosmic Microwave Background (CMB).

An aside to note is that while all the tests and constraints below are for $f(R)$ gravity, as described in Section 1.4.2, there are a whole host of other modified gravity models describing a much larger parameter space. One such parametrisation is Vainshtein gravity (Vainshtein, 1972), which is discussed in Section 6.3.

2.3.1 Solar system tests

Within the solar system, tests of gravity have been performed that provide similar constraints on gravity to those from the Eöt-Wash experiment. The most accurate of these are the lunar laser ranging tests that have been regularly performed since the moon landings (Bender et al., 1973). In these experiments, a powerful laser pulse, containing $\sim 10^{18}$ photons, is aimed at one of five retroreflectors located on the moon's surface. A handful of photons are then detected back on Earth, allowing a very accurate distance measurement to the moon to be made. From this, a measurement of the Earth's and moon's acceleration due to the Sun can be made. The equivalence principle asserts that despite the two bodies different masses and compositions, this acceleration is equal. Williams et al. (2012) use this acceleration to measure the difference in the Earth's and moon's gravitational and inertial mass, finding the difference to be $< 10^{-13}$, in strong agreement with GR.

Hu and Sawicki (2007) also present theoretical arguments using the dynamical state of the solar system to place constraints directly upon $|f_{R0}| < 10^{-6}$.

2.3.2 Dwarf Galaxies

Massive galaxies, such as the Milky Way, are expected to be massive enough that the critical radius (described in Equations 1.58 and 1.59) at which the gravitational potential falls enough to 'turn off' the chameleon screening and therefore modify gravity, is larger than the radius of the galaxy. In this case the galaxy is said to be self screened as GR is preserved throughout the galaxy and it is not influenced by the fifth force. However dwarf galaxies, with virial masses $M < 10^{11} M_{\odot}$ can have densities low enough to cause the critical radius to sit inside the galaxy radius, thereby leading to a chameleon fifth force being felt in the galaxy.

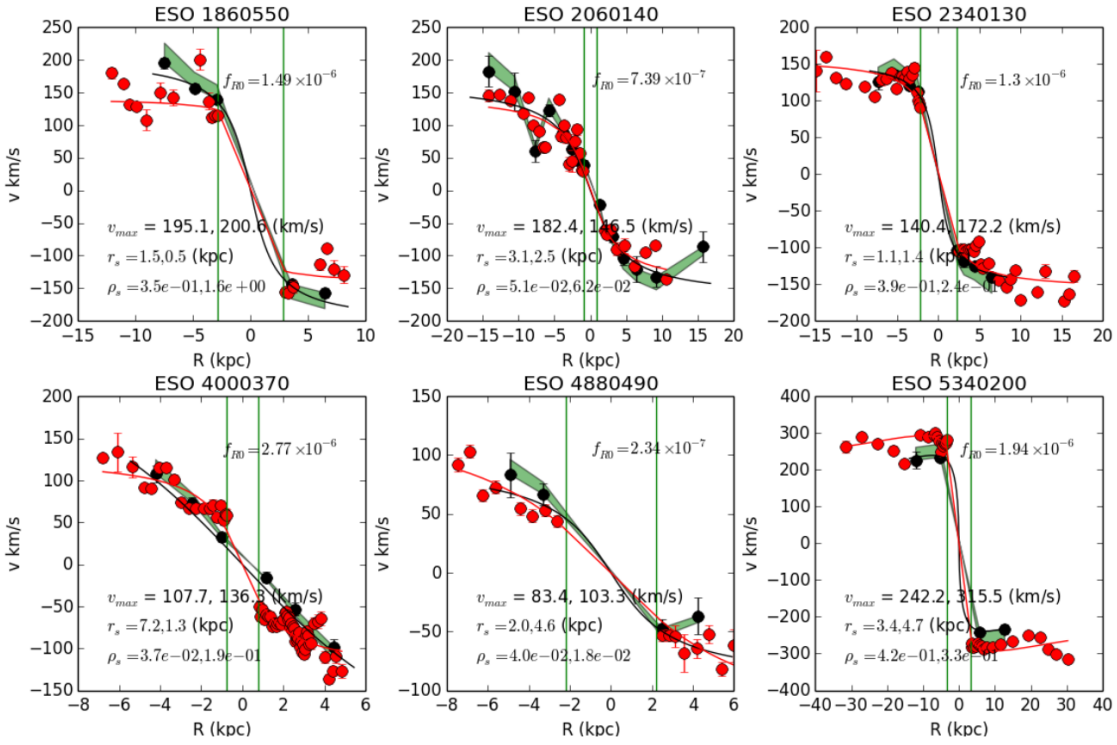

FIGURE 2.12: The rotation curves of the six galaxies investigated in Vikram et al. (2014). The black and red points show the stellar and gaseous rotation data respectively, while the black and red curves show the fits to these data. The green shaded region shows the $f(R)$ prediction for the gas rotation curve assuming the galaxy is completely unscreened. This figure shows that there is no measurable difference between the two, placing constraints upon the chameleon parameters.

One caveat to these searches for modified gravity in dwarf galaxies is that they must be in low density regions. Otherwise these dwarf galaxies may sit in the potential well of a more massive companion and be within the critical radius of this companion, which suppresses the fifth force. In this situation the dwarf is said to be environmentally screened (this is discussed in further detail in Section 5.4).

Hui et al. (2009) discuss the observational consequences such an effect would have, concluding that stars and diffuse gas within a dwarf galaxy would have different velocities due to the stellar component being self-screening. Jain (2011) suggests that an asymmetry in rotation curve of the stellar disc may be present. Finally Jain and VanderPlas (2011) discuss the warping of the stellar disc of a such as dwarf galaxy as it falls towards a more massive companion. Within the dwarf galaxy the dark matter feels the enhanced fifth force towards the companion, while the stars just feel GR. This causes the dark matter to move more quickly towards the companion, making the stars 'lag' behind.

In Vikram et al. (2013) and Vikram et al. (2014) (V14) the authors describe the situation

in which stars, being unscreened due to their high density, rotate around the galactic core as predicted by GR. However, diffuse clouds of gas within the galaxy will be unscreened and feel the fifth force caused by modified gravity. This means that at a given radius the gas within unscreened galaxies will have a higher velocity than the stars within that galaxy. Jain and VanderPlas (2011) predict this can result in a $10-15\%$ variation in observed orbital velocities.

V14 used the stellar and gaseous rotation curves of six low surface brightness galaxies measured in Pizzella et al. (2008), which can be seen in Figure 2.12, as the black and red points respectively. Models were fitted to these curves, from which the rotation velocities for both stars and gas were obtained, as shown by the black and red curves on Figure 2.12. The average difference in velocity was found to be $\langle \delta_v/v \rangle = 0.07 \pm 0.13$ implying that the difference in velocity between these two observables was minimal and consistent with GR. From these fits the authors were able to to rule out values of $|f_{R0}| < 10^{-6}$ on kiloparsec scales.

2.3.3 Distance Indicators

Nearby distance indicators can be found in gravitational fields with a range of strengths, enabling them to be used for tests of gravity. Chang and Hui (2011) and Davis et al. (2012) conclude that while main sequence stars are likely to be self screened, those in the red giant branch might feel the effects of the fifth force, due to their low densities, when present in unscreened galaxies. Feeling this enhanced force would lead to these stars having smaller radii, hotter surface temperatures and higher luminosities than predicted by GR.

Different observational signatures are expected from red giants at different stages of evolution. Stars at the tip of the red giant branch with $M \lesssim 2M_{\odot}$ are known to have near universal luminosities (Ferrarese et al., 2000). It then becomes possible to constrain the fifth force by comparing the distance inferred from the measured luminosity to the distance inferred from water masers, (a distance measure that is purely geometric and therefore immune to the fifth force) in the same galaxies.

Jain et al. (2013) used the measured distance to water masers in the galaxy NGC4258 (Herrnstein et al., 2005), a Milky Way mass galaxy 7Mpc away. They then compared these

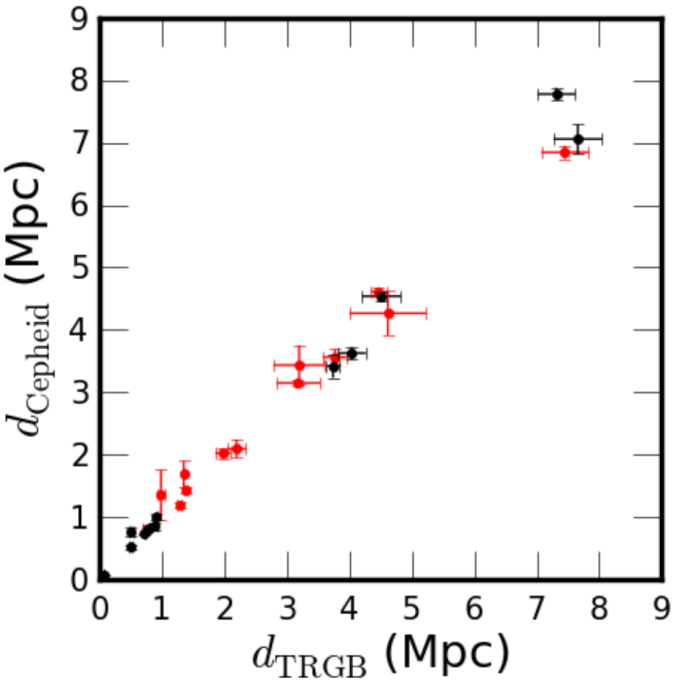

FIGURE 2.13: The distances to galaxies inferred using the Cepheid P - L relation against the distances inferred from the tip of the red giant branch stars. The black points are for screened galaxies and the red unscreened. This figure shows that the inferred distance to both screened and unscreened galaxies is the same, placing further constraints upo nchamelon gravity. Figure from Jain et al. (2013)

distances to those inferred from those at the tip of the giant red branch (Freedman and Madore, 2010). Using this method Jain et al. (2013) found the distances to be consistent with GR and placed constraints of $|f_{R0}| < 2 \times 10^{-6}$ on stellar scales.

Another subset of red giants is a group known as Cepheid variables, giant stars with $\sim$ 3–10$M_{\odot}$. There is a strong relationship between a Cepheid variable's luminosity and pulsation length (Udalski et al., 1999). By comparing this relationship in both screened and unscreened galaxies an offset should be observed in the presence of a fifth force. Jain et al. (2013) discuss this as a possible test for modified gravity, but do not do so due to the need for higher quality data from future surveys.

Jain et al. (2013) however combined these two methods using a sample of 25 galaxies with both Cepheid and red giant distances from the literature. The distances to each galaxy using both distance estimates were then compared and split into two samples, those galaxies that are screened and those that are unscreened, classified by their mass and environment (Zhao et al., 2011b). Figure 2.13 shows the relation between these two distance estimates in both the screened and unscreened cases. The authors then performed a likelihood analysis to determine the best fit for the fractional difference between these

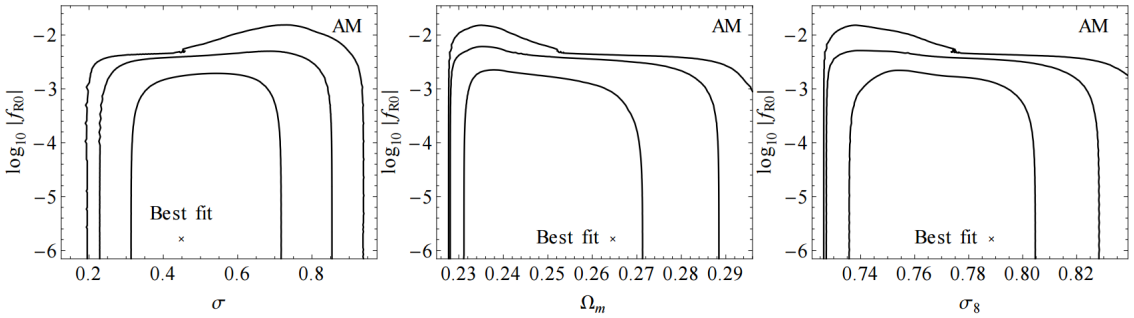

FIGURE 2.14: Results of the $f(R)$ gravity model fits to 5891 stacked clusters for three cosmological parameters. On each plot the best fit is shown. The three contours on each plot are the 1σ, 2σ and 3σ levels. Figure from Lombriser et al. (2012b).

two distance estimates. This difference was found to be consistent with GR in both the screened and unscreened sample. Jain et al. (2013) were able to place constraints of $|f_{R0}| < 5 \times 10^{-7}$ on stellar scales, the tightest constraints on this parameter using astrophysical techniques.

2.3.4 Cluster density profiles

N-body simulations of modified gravity suggest that in the presence of $f(R)$ gravity, the halo density profiles of clusters exhibit an enhancement at a few virial radii when compared to GR simulations of the same expansion history (Schmidt, 2009). As the Universe evolves, the modifications to gravity tend to increase at later times. This causes a pileup of matter around the infall regions of clusters, which would present itself as a bump in the matter density around the cluster's virial radius. In contrast the central region of the cluster would have formed at earlier times when these force modifications were weak, so would have evolved as predicted in GR.

Lombriser et al. (2012b) measured the density profiles via weak lensing of 5891 clusters from the Sloan Digital Sky Survey (Aihara et al., 2011). These clusters were then stacked (the process of cluster stacking is discussed in greater detail in Chapter 4) to boost the signal to noise. Using an MCMC likelihood analysis of the parameter space, constraints were placed upon $|f_{R0}|$ against three cosmological parameters, shown in Figure 2.14. The best fit for each parameter pair is also plotted, showing that the model prefers a small $|f_{R0}|$. The authors found the profiles to be consistent with GR and were able to place a constraint of $|f_{R0}| < 3.5 \times 10^{-3}$.

2.3.5 Cluster abundance

Using simulations and theoretical arguments, Schmidt et al. (2009) and Lombriser et al. (2014) consider a fifth force with strength $|f_{R0}| < |\Phi| \sim 10^{-6}$–$10^{-5}$, where Φ is the typical Newtonian potential of a galaxy. From doing so they calculate that the abundance of massive haloes in the Universe should be enhanced. These models predict enhanced gravitational forces below the local Compton scale of the scalaron which leads to a boost to the clumping of dark matter.

By mapping the modifications expected from $f(R)$ onto a Sheth-Tormen halo mass function (Sheth and Tormen, 1999) and comparing it to the halo mass function of Tinker et al. (2008), Schmidt et al. (2009) were able to place constraints of $|f_{R0}| < 10^{-4}$ using this method.

More recently Cataneo et al. (2015) sampled 94 X-ray clusters with X-ray luminosities and gas masses from Mantz et al. (2015). This sample was combined with data from the CMB, type 1a supernova and BAO (discussed in Section 1.3). The authors used an MCMC to fit a cluster mass function (that is the number of clusters as a function of mass, Tinker et al. 2008) to this combined sample and were able to place constraints of $|f_{R0}| < 2.6 \times 10^{-5}$ at megaparsec scales.

2.3.6 Cosmic Microwave Background

The temperature anisotropies within the CMB are known to be affected by modifications to gravity (Acquaviva et al. 2004, Daniel et al. 2010). As CMB photons free stream from the surface of last scattering they may encounter time evolving potential wells. As photons fall into these potentials they lose or gain a non-zero net energy due to the shallowing or deepening of these wells. This is known as the Integrated Sachs-Wolfe (ISW) effect (Sachs and Wolfe, 1967), and imprints on the CMB at large scales. Under ΛCDM this effect is expected to occur at late times, however in $f(R)$ theories an ISW effect can occur at earlier redshifts and with different magnitudes (Song et al., 2007).

The amplitude of small scale fluctuations in the CMB is connected to the growth of the matter density fluctuations as they evolve in redshift. The evolution of the matter density is strongly dependent upon the gravity acting upon it. These potential deviations could

then be imprinted upon the CMB via lensing, so the measured lensing amplitude might differ from that expected under GR (Calabrese et al., 2009).

Using a combination of these techniques, Giannantonio et al. (2010) and Hu et al. (2013) have constrained these modifications to gravity with Dossett et al. (2014) tightening the constraint to $|f_{R0}| < 10^{-4}$ at gigaparsec scales.

2.4 Summary

In this chapter I introduced the observational probe that I will later use to constrain gravity on cosmological scales, galaxy clusters. Clusters have been highly successful cosmological probes describing the Universe. During the past century they have been the subject of many varied tests, both astrophysical and cosmological.

I then discussed the two observables of clusters that I will later use to constrain modified gravity, beginning with X-rays. Here I discussed the emission mechanisms present in clusters and the form a modified profile would take. I then discussed gravitational lensing, deriving many of the fundamental equations and their impact on structures in the Universe. Next I discussed the different types of lensing that are used to measure the Universe.

Finally I ended this chapter by over-viewing some of the recent measurements of both GR and $f(R)$ gravity at a range of cosmological scales to put this later work into context.

Chapter 3

Simulating $f(R)$ gravity

3.1 Overview

This chapter discusses the simulations published in Wilcox et al. (2016).

To place constraints upon chameleon gravity, using the technique described in Chapter 1 I have made make several simplifying assumptions, including: *i)* All clusters were in hydrostatic equilibrium, with no significant additional non-thermal pressure affecting their profiles (discussed in Section 5.5); *ii)* Stacking clusters produces a fair representation of spherically-symmetrical profiles by minimising line-of-sight projection effects; (discussed throughout Chapter 4); *iii)* Dark matter haloes in chameleon gravity are well described by an NFW profile (Navarro et al., 1996); (discussed in Section 2.1).

The first of these assumptions is partially tested in Section 5.5, where I found that the cluster profiles were consistent with no additional (non-thermal) pressure at, and beyond, the virial radius of the stacked cluster profiles. The other assumptions are tested in this chapter, which also provides a confirmation of the analytical modelling presented in Chapter 5 for simultaneously describing changes to the X-ray and lensing profiles of clusters due to modifications of gravity.

I have performed these tests using two new hydrodynamical cosmological simulations: one evolved using the concordance ΛCDM+GR model, and the other evolved using $f(R)$ gravity with a background field amplitude of $|f_{\rm R0}|= 10^{-5}$ (as discussed in Section 1.4.2). This value of $|f_{\rm R0}|$ was chosen to be consistent with present observational limits on this

parameter; smaller values would have resulted in a modification to gravity that could not be measured within these present simulations (due to an insufficient number of haloes), nor with the cluster sample i present in Chapter 4.

This chapter starts with a description of the cosmological simulations used throughout this chapter and the techniques used to generate suitable simulated data products. I then discuss the creation of the stacked X-ray and weak lensing cluster profiles, and test the assumptions discussed above. Next, I present results from the MCMC fitting of the simulated stacked cluster profiles. I end this chapter by discussing these results.

3.2 Simulating Clusters

3.2.1 Cosmological Simulations

In this chapter I used two new hydrodynamical simulations created using the `MGENZO` software; a variant of the `ENZO`[1] software, that works with with modified gravity theories. This software is a variant of the well-established `ENZO` code and is fully described in Zhao et al. (in prep), who performed and created the simulations used here. However, the analysis performed throughout this chapter all was my own (that is from Section 3.2.2 onwards). `MGENZO` has been extensively studied using several independent N-body codes including `MGMLAPM` (Zhao et al., 2011a) and `ECOSMOG` (Li et al., 2012). The `MGENZO` code uses the same algorithm to solve for the non-linear scalar field equations as the `MGMLAPM` and `ECOSMOG` code. Previous results from `MGENZO` have been validated against other N-body and hydro-dynamical simulations of the Hu-Sawicki model, including the code comparison work of Winther et al. (2015) and Hammami et al. (2015). These papers show that all these independent codes give consistent solutions for the scalar field, as well as the power spectrum and the mass function of dark matter. Here I provide an overview of the theoretical details of these two new simulations.

Rewriting Equation 1.49, the Ricci scalar in an FLRW Universe, in terms of the density parameters Ω_M and Ω_Λ (discussed in Section 1.2) gives

$$\bar{R} \simeq 3H_0^2 \left[\Omega_M (1+z)^3 + 4\Omega_\Lambda\right], \tag{3.1}$$

[1] Available at http://enzo-project.org/

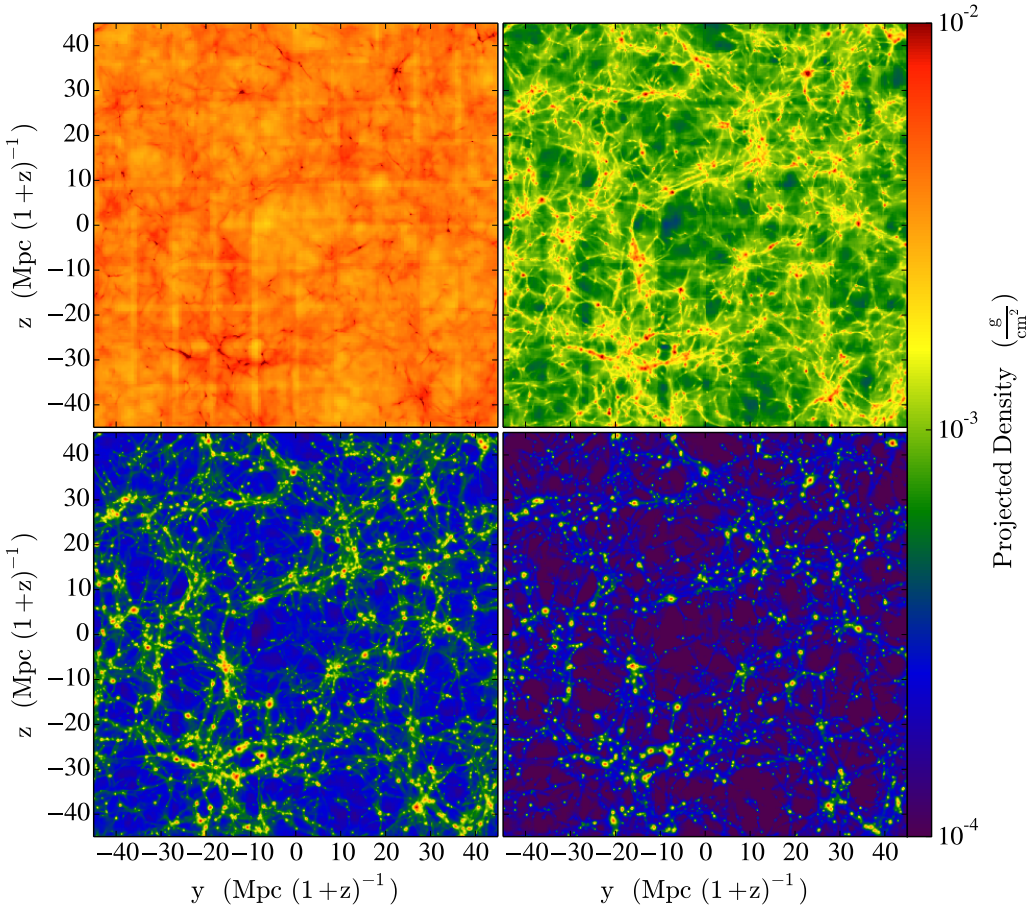

FIGURE 3.1: Snapshot of density from full ΛCDM+GR simulation at four different redshifts, from top left clockwise: $z = 5, z = 2, z = 0.4, z = 1$ across the whole simulation size looking down the simulation's x-axis. A colour bar is provided along the right hand y-axis showing the density range. This figure shows the evolution of the simulation as time progresses.

which at today's redshift (and assuming a flat cosmology) becomes

$$\bar{R}_0 \equiv \bar{R}(z=0) \simeq 3H_0^2\,(1+3\Omega_\Lambda)\,. \tag{3.2}$$

Combining Equation 3.2 with the derivative of f_R, given by Equation 1.48, allows f_R to be written in terms of f_{R0}, the value at $z = 0$ (discussed in Section 1.4.2)

$$f_R \simeq f_{\rm R0}\left[\frac{3H_0^2(1+\Omega_\Lambda)}{-R}\right]^{n+1}. \tag{3.3}$$

From this the perturbations in the scalar field, δR, can be defined as

$$\delta R(f_{\rm R}) = 3H_0^2 \left\{ (1+3\Omega_\Lambda) \left(\frac{f_{\rm R0}}{f_{\rm R}} \right)^{\frac{1}{n+1}} - \left[\Omega_M (1+z)^3 + 4\Omega_\Lambda \right] \right\}. \tag{3.4}$$

The scalar field $f_{\rm R}$ can then be solved numerically by combining Equation 1.43 with Equation 3.4, given the model parameters $f_{\rm R0}$ and n with background cosmological parameters.

The modified Poisson equation for the gravitational potential Φ can be obtained by summing the 00 and ii component of the modified Einstein equation in the Hu-Sawicki f(R) model (discussed in Section 1.4.2), namely

$$\nabla^2 \Phi = \frac{16\pi G}{3} a^2 \delta\rho_{\rm M} + \frac{a^2}{6} \delta R(f_{\rm R}). \tag{3.5}$$

Which differs from normal GR simulations with the inclusion of the f_R term, as in the limit of ordinary GR this equation reduces to

$$\nabla^2 \Phi = 4\pi G \delta\rho_{\rm M}. \tag{3.6}$$

The dynamics of the system were determined by Equations 1.43 and 3.6. Equation 1.43 is a non-linear Poisson equation, and it had to be solved numerically on a regular, or self-adaptive, grid using iteration methods (Li et al., 2012, Oyaizu, 2008b, Puchwein et al., 2013, Zhao et al., 2011a).

For the $f(R)$ model, using block adaptive mesh refinement (block AMR), `MGENZO` solved the non-linear Poisson equation of the scalar field (Equation 1.43). The modified Newton potential Φ could then be solved. Given Φ, the hydrodynamical system for baryons and dark matter particles is numerically solved (Equations 1-4 in Bryan et al. 2014). In particular, I used one available $f(R)$ simulation with $|f_{\rm R0}| = 10^{-5}$ and $n = 1$ and, for comparison, a ΛCDM+GR simulation. Both simulations had 2×128^3 particles of mass $4 \times 10^{11} {\rm M}_\odot$ in a cubic box of 128 Mpc/h on a side. Both simulations also had identical initial conditions and background cosmological parameters, namely $\Omega_b = 0.044$, $\Omega_c = 0.226$, $\Omega_\Lambda = 0.73$ and $H_0 = 71 {\rm kms}^{-1}{\rm Mpc}^{-1}$. Each simulation was evolved to $z = 0.4$, which is close to the mean redshift of the cluster sample described in Chapter 4 ($\bar{z}_{cluster} = 0.33$).

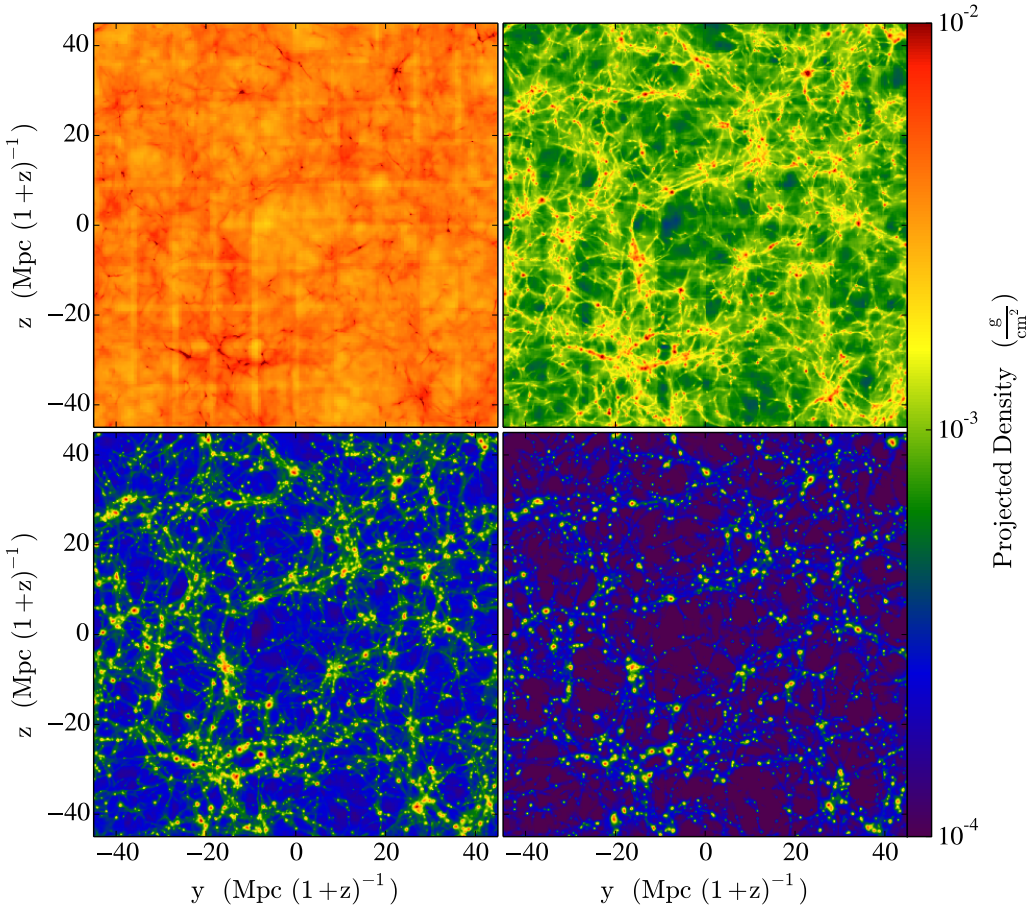

FIGURE 3.2: Same as Figure 3.1, but in the chameleon gravity case. Once more this plot shows the entire 2D extent of the simulation, projected along the x-axis. Also shown is a colour bar to indicate the matter densities.

Each simulation provided the location and temperature of all particles (assuming the equipartition of kinetic energy), which was then used to determine the density and pressure of the gas (assuming the ideal gas law). Neither simulation included any additional feedback processes (e.g. from active galactic nuclei or supernovae) and therefore will not include an additional non-thermal pressure component that could affect the temperature and density of galaxy clusters (Rasia et al. 2004, Ota and Yoshida 2015).

Shown in Figures 3.1 and 3.2 is the projected density (baryons and dark matter) for the two simulations in four redshift slices ($z = 5, 2, 1, 0.4$). These plots clearly show the evolution of the simulations from near uniform matter distributions to the clusters, filaments and voids that now populate the Universe.

3.2.2 Finding Dark Matter Haloes

To accurately test the assumptions of this cluster stacking technique, I found all the clusters within the simulations and stacked their profiles. To do this the 'Rockstar' Friends-of-Friends (FOF) algorithm (Behroozi et al., 2013) was used to locate the main dark matter haloes in both the simulations (Section 3.2.1). The FOF algorithm grouped together all particles linked in pairs according to some specified separation (known as the linking length). All particles grouped together were then classified as a halo. Here, the default linking length of 0.28 times the mean particle separation was used. For each simulation, I obtained a catalogue of halo locations (centre-of-mass) and masses. All haloes are at $z = 0.4$, which was close to the mean redshift of the sample presented in Chapter 4 ($z = 0.33$).

I imposed a threshold mass of $\mathrm{M} > 10^{13}\mathrm{M}_{\odot}$ to select a similar mass range as the sample in Chapter 4; this gave a typical mass $\simeq 4 \times 10^{13}\mathrm{M}_{\odot}$. The choice of this threshold was a compromise to ensure that there are sufficient haloes for the tests, while still containing the most massive systems studied in Chapter 5 (which had a typical mass of $\simeq 8 \times 10^{13}\mathrm{M}_{\odot}$). Lowering the threshold would have significantly increased the number of haloes available to us, but would have resulted in adding much lower mass systems (i.e., galaxy groups) than used in the previous analysis. This could have biased the study as such lower mass systems are more likely to be unscreened in the simulations.

Above this threshold mass, I found 103 clusters (or haloes) in the ΛCDM+GR simulation and 113 clusters in the $f(R)$ simulation. Interestingly, it has been shown that the abundance of massive clusters is enhanced in the presence of a fifth force (with $|f_{\mathrm{R0}}| \sim 10^{-5}$), which is reflected in the numbers in the samples (Schmidt et al. 2009, Lombriser et al. 2014). The locations of these haloes in each simulation are shown in Figures 3.3 and 3.4.

I found $\simeq 4\%$ of the volume in our $f(R)$ simulation was contaminated by unrealistic particle velocities, leading to an extremely low density ($< 10^{7}\mathrm{M}_{\odot}/\mathrm{Mpc}^{-3}$), but exceptionally hot ($> 5 \times 10^{8}\mathrm{K}$), extended bubble surrounding the most massive dark matter halo in the simulation. This bubble was potentially caused by the lack of realistic feedback mechanisms (as described in Section 3.2.1). This bubble was found to be centred upon the most massive cluster in the simulation, in a high concentration of clusters. The large potential surrounding these clusters may have accelerated nearby particles to unrealistic velocities, as these particles had no feedback to slow them down.

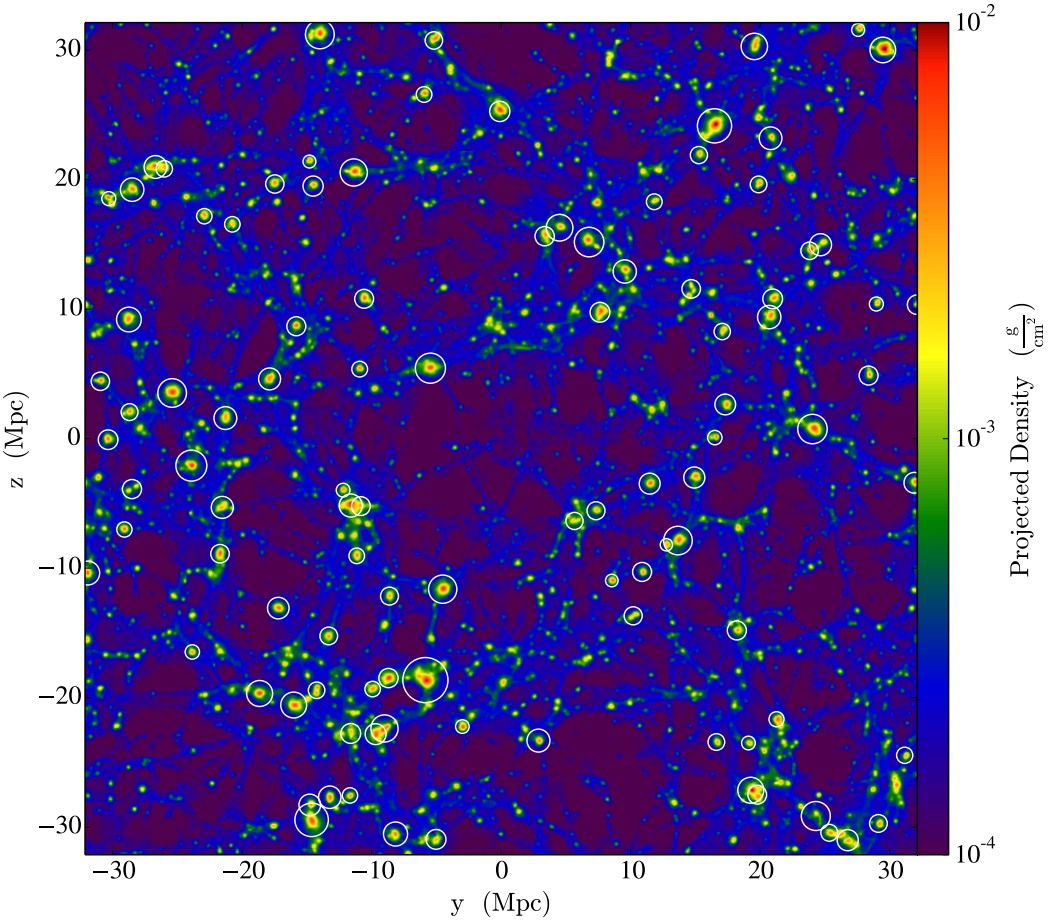

FIGURE 3.3: Snapshot of the total mass density for the ΛCDM+GR simulation at $z = 0.4$. I highlight all halos above $M > 10^{13} M_{\odot}$. The simulation has been projected along one side of the simulation box. Here the distance scale is a comoving distance and the mass density scale is shown along the plot's right hand y-axis. This figure shows the cosmic web and how clusters form at the crossing points of filaments.

The bubble affected 14 nearby clusters, which were enclosed by it, on average doubling their temperature profiles at the virial radius. Therefore I removed these 14 haloes, leaving 99 clusters in total for the $f(R)$ simulation. This bubble is not visible in the density map in Figure 3.4.

In Figure 3.5a I show four randomly chosen clusters taken from the ΛCDM+GR simulation for illustrative purposes. Figure 3.5b shows the same four clusters from the $f(R)$ simulation. I will refer back to these four clusters throughout the chapter to better illustrate the process of making the weak lensing and surface brightness profiles. In Table 3.1 I list the characteristics of these four clusters (see Section 3.3.2 for details on how the ellipticity, ϵ, was measured).

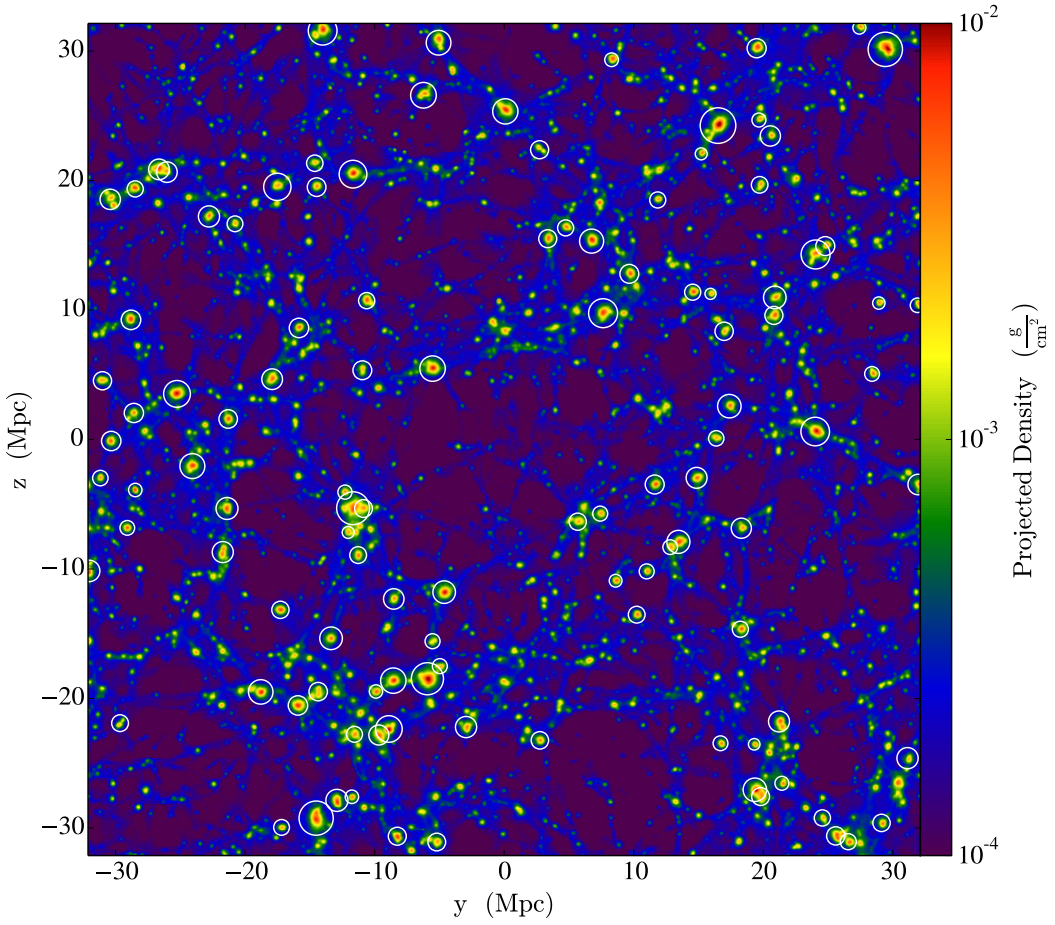

FIGURE 3.4: The same as Figure 3.3 but for the $f(R)$ simulations case.

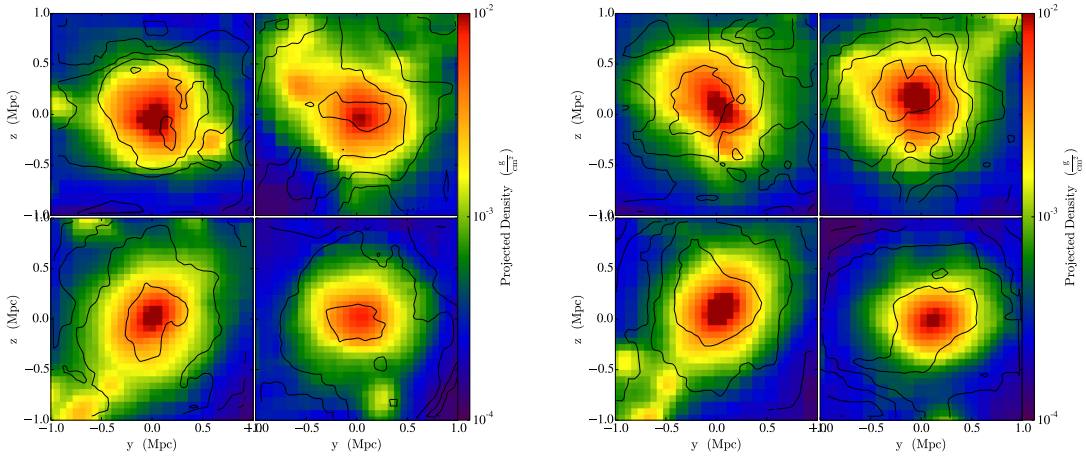

(A) ΛCDM+GR (B) $f(R)$

FIGURE 3.5: In Figure 3.5a a mosaic of four (projected) cluster profiles taken from the ΛCDM+GR simulation at $z = 0.4$. The coloured contours are the density, while the black contour lines are the gas temperature. Figure 3.5b shows the same four clusters but from the $f(R)$ simulations. The density scale in each plot is the same, as indicated by the density colour bar to the right of each plot.

	ΛCDM+GR			$f(R)$		
Cluster	Mass ($10^{13}M_{\odot}$)	ϵ	Temp (keV)	Mass ($10^{13}M_{\odot}$)	ϵ	Temp (keV)
1	8.4	0.20	2.5	9.6	0.23	2.8
2	3.1	0.39	1.5	3.5	0.36	1.7
3	6.6	0.40	2.0	7.4	0.40	2.2
4	1.4	0.10	1.4	1.8	0.11	1.5

TABLE 3.1: Sample properties of four representative clusters from the two hydrodynamic simulations.

3.2.3 Creating X-ray images

To mimic the sample described in Chapter 4, and test the methodology of this technique, I needed to produce X-ray profiles for the simulated haloes or clusters. This was achieved using the `PHOX` software (Biffi et al., 2012), as implemented in `Python` (ZuHone et al., 2014). The software took, as primary input, the output particle parameters from the hydrodynamical simulations, namely position, density, temperature and velocity. For each cluster, I inputed the particle information for a cube of size 2Mpc centred on each halo. As metallicity is also required for `PHOX`, but unavailable from the simulations, I assumed a constant value of $0.3Z_{\odot}$ for all clusters, which was suitable for the outskirts of clusters (Simionescu et al., 2011).

The `PHOX` software has three main steps. First, it generated a large Monte-Carlo sample of available photons (typically ten times the amount expected from an observation) in a three-dimensional volume surrounding the cluster. This was achieved by converting the given density, temperature and metallicity of each particle (or 'gas element' as described in Biffi et al. 2011) into a spectrum of photons using a model for the emissivity of the intracluster medium from `XSPEC` (Arnaud, 1996) assuming a thermal `APEC` model (Smith et al., 2001), which is suitable for such hot, low-density, fully-ionised plasmas. The spectral model was created with a resolution of 2000 energy bins, between 0.5keV and 2.0keV. For each cluster, I also created an array of different photon samples spanning a range of possible collecting areas and exposure times to facilitate the generation of realistic XMM observations in stage three of `PHOX` (below).

The second stage of `PHOX` involved projecting the three-dimensional distribution of photons to obtain two-dimensional maps for each cluster. I selected a line-of-sight for each cluster that was aligned with the z-axis in the main cosmological simulations and projected the data into the plane perpendicular to this line-of-sight. This stage also corrected for

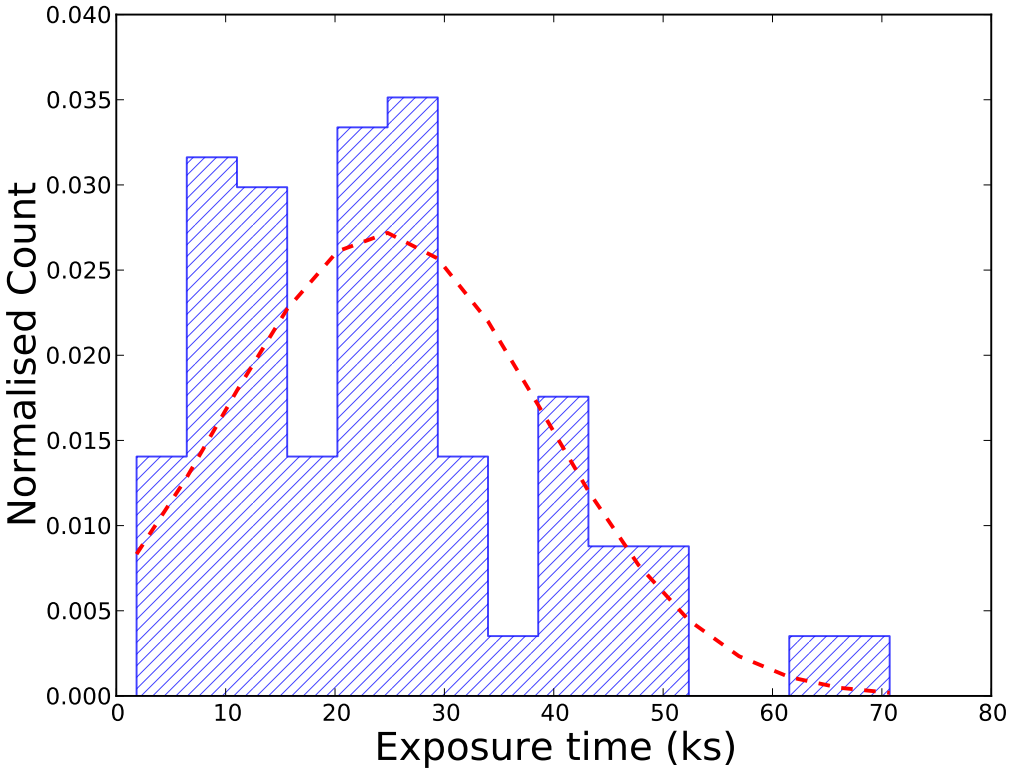

FIGURE 3.6: The distribution of exposure times (kilo-seconds) for the real XMM cluster observations described in Chapter 4. Shown in red is the fitted Gaussian distribution to these data. This plot shows that the clusters have a wide range of exposure times.

doppler shifts along the line-of-sight due to the motion of the gas, and corrected for the cosmological redshift.

Next, `PHOX` simulated the observing time, which is estimated using the distribution of exposure times for the real clusters in the sample described in Chapter 4 (see Figure 3.6). For simplicity, I fitted this distribution of exposure times with a Gaussian, giving a mean exposure time of $24,591$ seconds and a dispersion of $12,745$ seconds. Then, for each simulated cluster, a random exposure time was drawn from the fitted Gaussian distribution and used in `PHOX` (I did not allow negative exposure times, but simply drew from the Gaussian again). The redshift for the simulated clusters was assumed to be $z = 0.4$ to be consistent with the simulations, and is close to the mean of the cluster sample described in Chapter 4.

Finally, stage two of `PHOX` corrected for the effects of absorption by gas in the Milky Way. The software used the `wabs` absorption model (Morrison and McCammon, 1983), which is implemented through `XSPEC`, and takes the galactic column density, N_H, as an input.

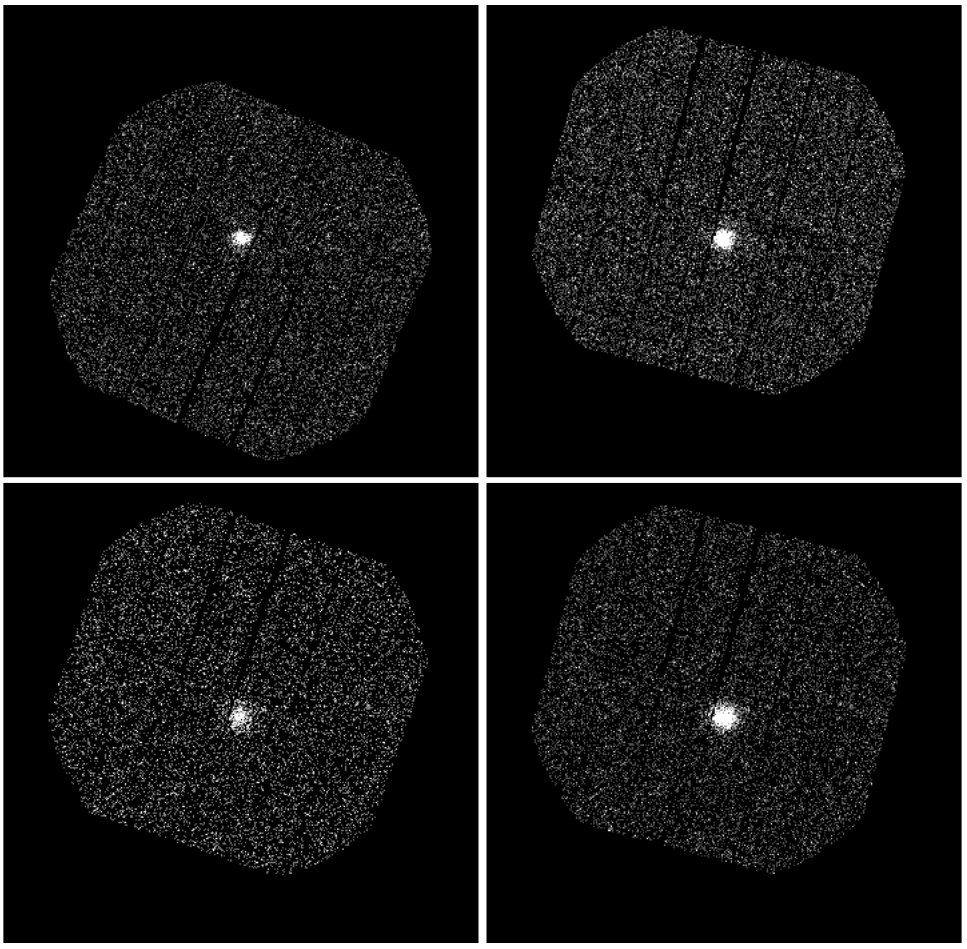

FIGURE 3.7: A mosaic of the same four simulated clusters shown in Figure 3.5 (ΛCDM+GR) created using PHOX as discussed in Section 3.2.3. Each cluster is shown on the same scale and this figure aims to show the noise level associated with X-ray observations of clusters.

I assumed a constant value of $10^{21}\mathrm{cm}^{-2}$ for all clusters, which is a reasonable given the observed galactic column density for the sample described in Chapter 4. The column density was found using the HEASARC[2] N_H tool (Kalberla et al., 2005).

The third stage of PHOX involved adding realistic telescope effects to the simulated images. This was achieved using simx, a convolution tool that contains the point-spread function (PSF) and detector response function for a number of well-known X-ray telescopes. For this thesis, I selected the PN camera of XMM-Newton telescope (as described in Section 4.2.2). The simx tool also adds a realistic background.

In Figure 3.7, I show images of the X-ray surface brightness profiles for the same four simulated clusters shown in Figure 3.5. These images show the characteristics of the XMM instrument and cosmetically look similar to real XMM observations of clusters. The

[2]http://heasarc.gsfc.nasa.gov/cgi-bin/Tools/w3nh/w3nh.pl

only major difference was the lack of additional X-ray sources serendipitously detected in the outskirts of each XMM image. For comparison, a typical XCS image contains approximately ten bright serendipitously-detected point-sources per observation, with more fainter sources. I ignored this difference in the simulations as the probability of having overlapping point sources was still relatively small, and would have been corrected in the real data by excluding flux from that overlapping source when constructing cluster profiles. I also assume all the simulated clusters were observed on-axis, which is not true for the real XCS cluster sample. I investigated the effect of moving the simulated clusters off-axis using `simx` and found no significant effect on the results.

3.2.4 Estimating the weak lensing signal around clusters

I estimated the shear lensing signal around each of the simulated clusters as the numerical simulations did not include individual galaxies, nor simulate the effects of gravitational lensing. I therefore calculated the expected lensing convergence, κ, as detailed in Bartelmann and Schneider (2001), which can be approximated by

$$\kappa(\vec{\theta}) = \frac{3H_0^2\Omega_m}{2c^2} \sum_i \Delta_{\chi i}\chi_i \frac{(\chi_{clust} - \chi_i)}{\chi_{clust}} \frac{\delta_i(\vec{\theta})}{a_i}, \tag{3.7}$$

along the line-of-sight, assuming a flat universe. The summation was over the co-moving distance χ_i, using bins of width $\Delta_{\chi i}$, while H_0 is the Hubble constant, Ω_m is the matter density, a_i is the scale factor (in bin i), and δ_i is the over-density in that bin.

The lensing convergence was measured in the simulations by first determining r_{200} for each simulated cluster (i.e., the radius at which the average density of the halo reaches two hundred times the critical density). Then, I extracted a cylinder of radius $10 \times r_{200}$, centred on each cluster, that extended the length of the whole cosmological simulation (128 Mpc/h). This cylinder was then divided into ten redshift slices (thickness $\Delta z = 0.02$), and then each slice was pixelated into a 100×100 grid. The density in each pixel, $\rho(z_i)$ was determined, and the over-density in each pixel calculated as

$$\delta_i = \frac{\rho(z_i) - \bar{\rho}(z_i)}{\bar{\rho}(z_i)}. \tag{3.8}$$

where $\bar{\rho}(z_i)$ is the mean pixel density in each redshift slice. The κ for each pixel was then calculated using Equation 3.7, with the error on κ (σ_κ) given by

$$\sigma_\kappa^2 = \frac{3H_0^2\Omega_m}{2c^2}\sum_i \Delta_{\chi i}\chi_i \frac{(\chi_{clust}-\chi_i)}{\chi_{clust}}\frac{\delta_i}{a_i}\frac{1}{\bar{n}_i}. \tag{3.9}$$

This pixelated map of convergence was converted into a shear field, from which tangential shear (γ_t) was then inferred, using the Kaiser & Squires inversion technique given in Kaiser and Squires (1993) and discussed in detail in Sections 2.2.6 and 4.2.1. To make the shear measurements more realistic, I added a random shear noise component to the pixelated values behind each cluster using a distribution of shear noise values constructed directly from the galaxy source catalogue of CFHTLenS (Heymans et al., 2012), which I used to construct the weak lensing profiles in Chapter 4. In Figure 3.8 I show the pixelated convergence around the same four clusters from Figure 3.5.

3.3 Testing the assumptions

3.3.1 Making stacked cluster profiles

I followed the exact same prescription as used in Section 4.3.2 to create the stacked X-ray profile and the method of Section 4.3.3 to create lensing profiles for the simulated clusters. To generate the stacked X-ray surface brightness profile, I first extracted a square region of size r_{200} around each individual simulated cluster and re-sampled the data, via linear interpolation, to a common grid of 500 by 500 pixels. I then stacked the images, first re-scaling the overall amplitude of the images by the mean to reduce covariances (as discussed in Section 4.3.3). The mean value of each pixel was then measured and binned into 19 logarithmic annuli out to r_{200}. As in Sections 4.3.2 and 4.3.3, I used bootstrap re-sampling, with replacement, to estimate the errors on the stacked profiles. I created 100 noise realisations of a cluster drawn randomly from the sample of 103 (99) clusters available in the ΛCDM+GR ($f(R)$) simulations to replicate the error methodology described in Chapter 4.

For the stacked lensing profile, I first estimated the tangential shear, γ_t (as discussed in Section 4.3.3), for each cluster and its noise component. The tangential shear in each pixel, around each cluster, calculated about the X-ray centroid, was binned into 19 equally

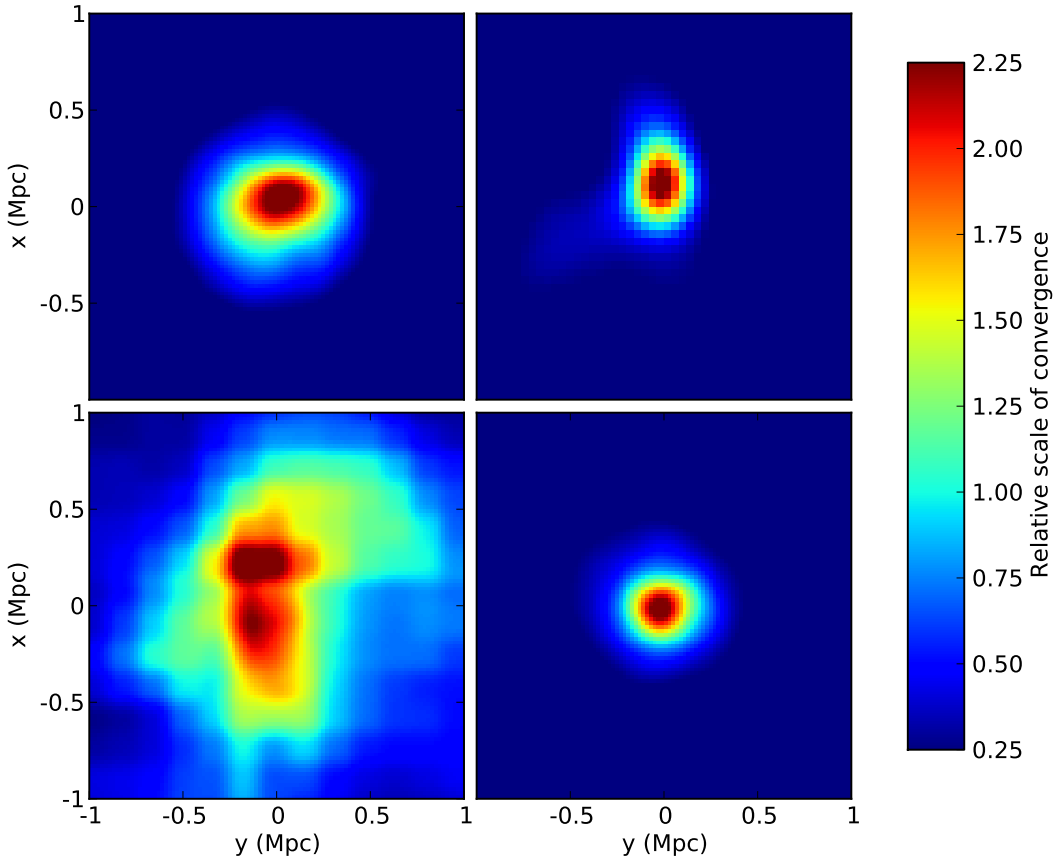

FIGURE 3.8: The pixelated convergence around the same four clusters in Figure 3.5, where redder areas indicated a larger convergence. Here all these clusters have been normalised to the same dynamic range.

spaced logarithmic bins out to a distance of $10 \times r_{vir}$. This was done by taking the virial radius measurement from `YT`, which works by interpolating from the clusters radial profile. For consistency with Section 4.3.3, I excluded the central $0.1 \times r_{vir}$. The shear in each bin was summed for all clusters and the mean shear measured (McKay et al., 2001). This provided the stacked weak lensing profile. I measured errors on the shear profile using the same bootstrap re-sampling method described above for the X-ray profiles.

3.3.2 Testing the stacked profiles

A key assumption of this technique was that stacking clusters would produce a spherically symmetric profile. I used these simulations to determine whether stacking clusters reduced possible line-of-sight projection effects that could hamper any analysis when applied to

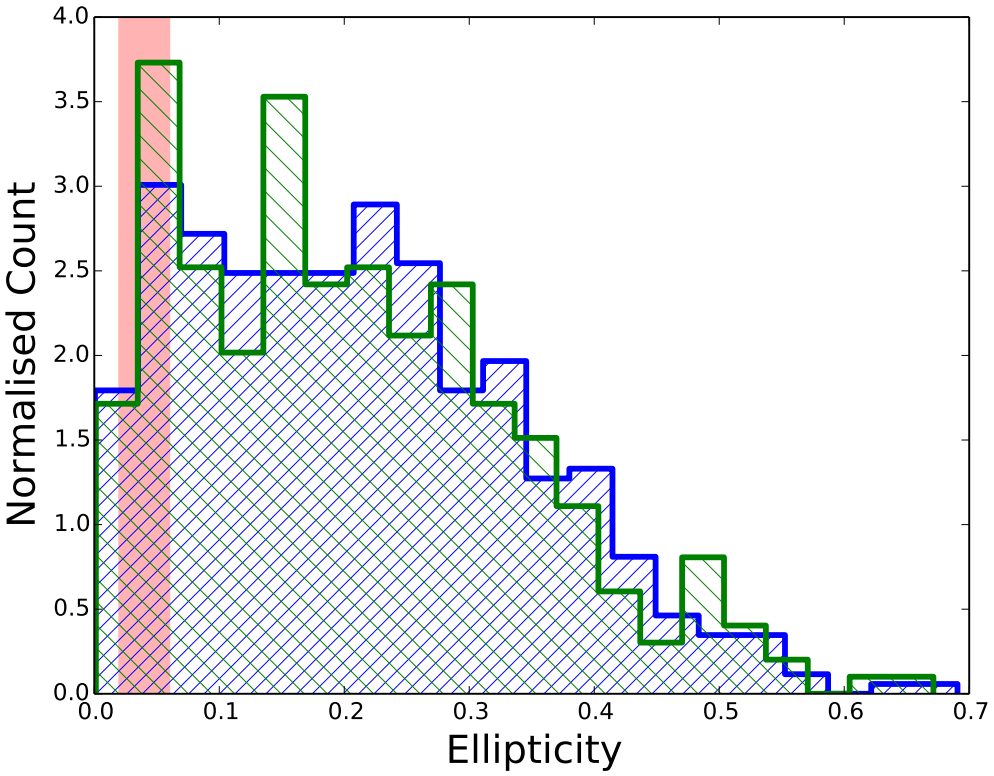

FIGURE 3.9: The normalised distribution of ellipticities for all cluster realisations (see text) for both simulations (ΛCDM is blue and $f(R)$ is green). The (pink) shaded region shows the range of measured ellipicities after stacking the clusters. This plot shows that stacking cluster produced a rounder cluster than any individual cluster.

a single cluster (as discussed in Section 1.5.1). To test this, I generated ten additional realisations per cluster, following the same methodology as given in Section 3.2.3, but now varying at random the line-of-sight direction for the projection of the three-dimensional photon distribution. I then determined the ellipticity, ϵ, for each individual cluster realisation by fitting a two-dimensional ellipsoid to the projected surface brightness distribution. This was done by first identifying the central point of the photon distribution, which was taken to be the pixel with the largest brightness. Next a value which was 80% of this value was calculated, then each pixel with this surface brightness was located. This generated an isophotal ring around the brightest pixel. To this ring a ellipse was then fitted which minimised the distance between the ellipse and the isophote, from which an ellipticity could be measured.

In Figure 3.9, I show the distribution of ellipticities determined across all realisations of all the clusters in both simulations. I found a mean ϵ of 0.21 ± 0.13, which demonstrated that

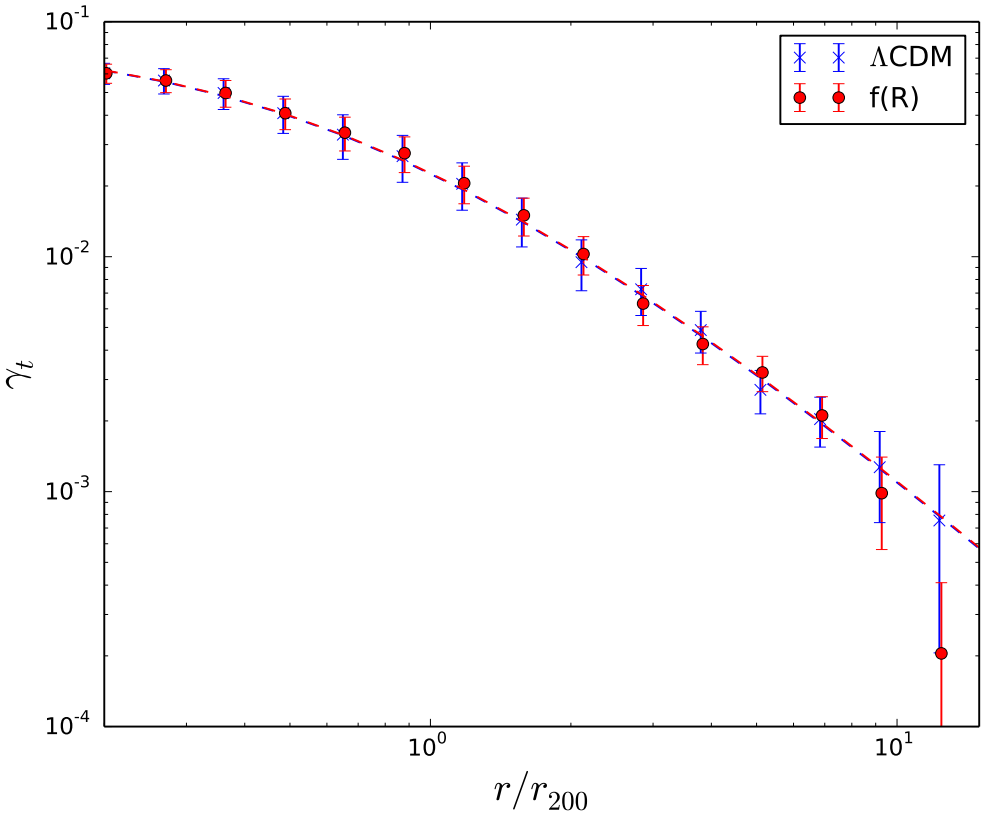

FIGURE 3.10: The stacked lensing profile for the ΛCDM+GR simulation (blue crosses) and the stacked lensing profile for the $f(R)$ simulation (red points). The dashed (blue) line is the best fit NFW profile to the ΛCDM+GR data, while the dashed (red) line is the same for the $f(R)$ profile. This figure shows that the lensing signal in $f(R)$ gravity and GR is the same.

many of the simulated clusters are non-spherical: This could have a significant effect when studying individual clusters (e.g. Coma cluster in Terukina et al. 2014). Interestingly, I saw no difference in the distribution of ellipticities between the two simulations (the mean ellipticity also the same).

I then created ten stacked two-dimensional profiles from the ten individual realisations of each cluster. I fitted an ellipse to each stack and computed the best-fit value of ϵ. Across the ten stacks, I found $\bar{\epsilon} = 0.04 \pm 0.02$, which indicates that these stacked profiles are close to spherical (within a few percent) averaging out the ellipticities seen in the individual clusters (Figure 3.9) .

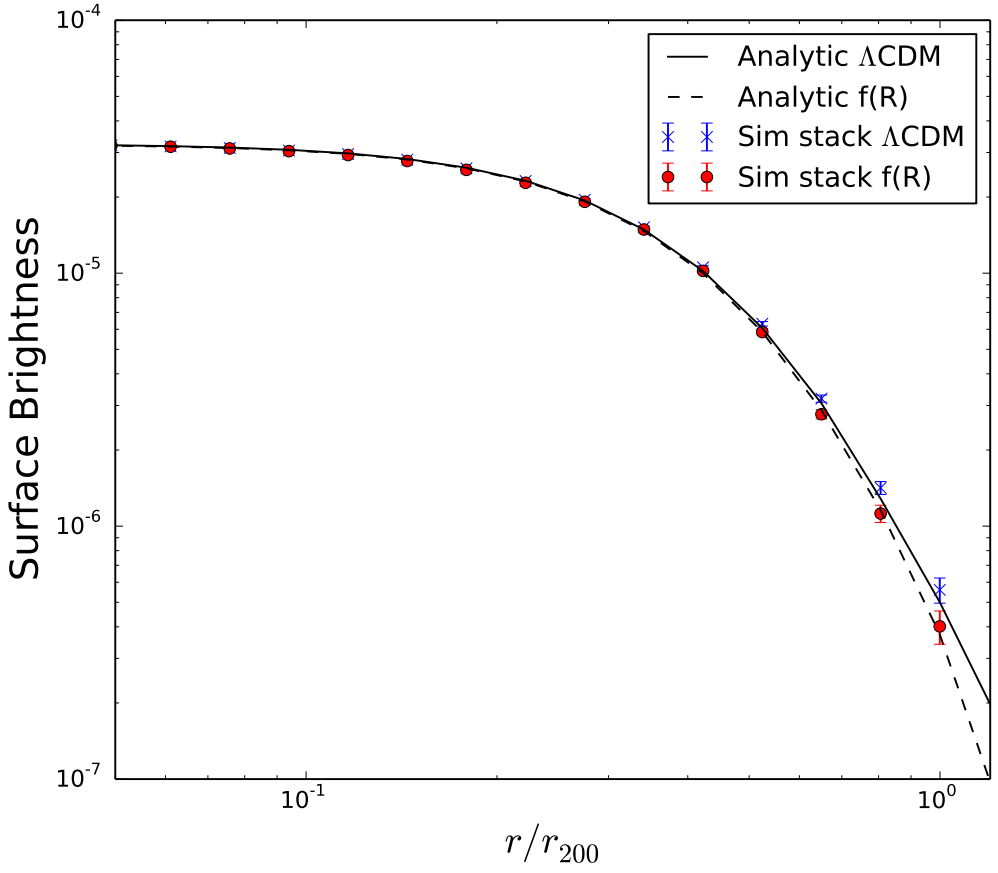

FIGURE 3.11: The stacked X-ray profile for the ΛCDM simulation (blue crosses) and the $f(R)$ simulation in (red points). Also shown is the best-fit ΛCDM model (black line) and the best-fit $f_{\rm R} = 10^{-5}$ line (dashed black line). This figure shows that the recovered X-ray signal differs between $f_{\rm R}$ and GR.

3.3.3 NFW profiles

Another key assumption made by this technique was that the NFW profile (as discussed in Section 2.1) was an appropriate model for the stacked weak lensing cluster profile. This should be the case as such relativistic measurements are not affected by $f(R)$ modifications to GR (as discussed in Section 1.5). However, due to the modified dynamics during the formation of structures, deviations from NFW may arise. In Figure 3.10, I show the simulated stacked weak lensing profile out to $10 \times r_{vir}$ for both the ΛCDM+GR and $f(R)$ simulation, along with the best-fit analytical NFW profiles. I used MCMC (as described in Section 5.2) to fit the NFW parameters c and M (as described in Section 2.1), running the chains for 1000 time steps and removing the first 200 steps as the 'burn in' phase. I

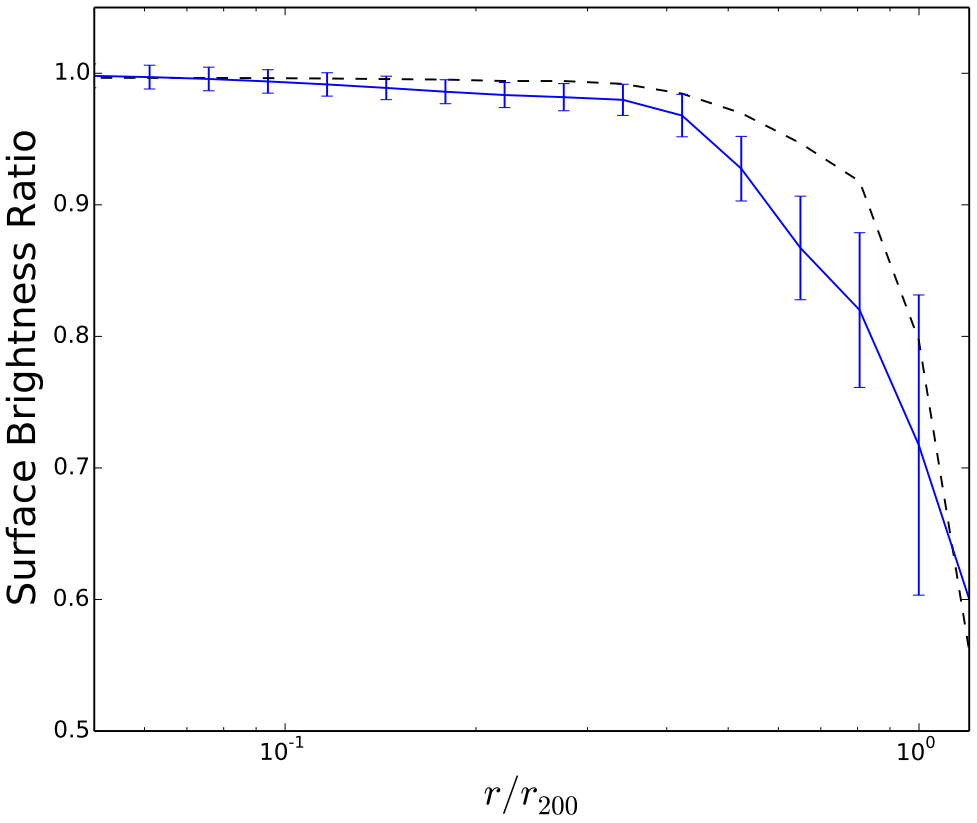

FIGURE 3.12: The observed ratio between the two simulated stacked X-ray surface brightness profile shown in Figure 3.11 (blue line). The dashed (black) line is the same ratio but now predicted using the analytical models from Figure 3.11. This figure shows that analytic model largely agrees with the simulations.

obtained a $\chi^2 \simeq 10$ (for 15 degrees of freedom) confirming the visual impression that the NFW model is a good representation of these lensing profiles in both simulations.

I found the same best-fit values for $c = 7.4^{+0.64}_{-0.65}$ and $M = 1.2^{+0.13}_{-0.13} \times 10^{13} M_{\odot}$ in both simulations. These values were reasonable for such dark matter haloes and consistent with other fits in the literature (Pourhasan et al. 2011, Arnold et al. 2014). Together, these results confirmed that an NFW profile is a good representation of the lensing profile of clusters in $f(R)$ models (as in the case of ΛCDM). I note that this test is the first time this assumption has been checked using simulated lensing profiles for $f(R)$ gravity.

3.3.4 Comparison with the analytic model

The simulated cluster profiles provided an ideal test for the analytical model described in Chapter 5 to explain the effect of chameleon gravity on the X-ray surface brightness profiles of clusters. In Figure 3.11, I show the X-ray surface brightness profile for both the ΛCDM+GR and $f(R)$ simulations. For comparison, I also show the expected theoretical profile using the model in Section 1.5 assuming GR (black line) and $f(R)$ gravity (dashed line). Here the latter would present itself as an additional pressure term in the hydrostatic equilibrium equation. This resulted in a steeper profile in the outskirts of the cluster and is the signal I am testing for.

In Figure 3.12, I show the ratio of the two simulated profiles (as the solid line) and, as discussed above, the two ratios deviate from unity in the outskirts of the cluster as the gas becomes unscreened. I also show in Figure 3.12 the analytical prediction for this effect based on the model used in Chapter 5 (where $f_{\rm R} = 10^{-5}$). I see the two curves agree well at small radii, while at large radii, the two are still in broad agreement (always within two sigma of each other). This demonstrates that the analytical model can reproduce the general effect of $f(R)$ gravity on the X-ray surface brightness profiles of clusters and possibly under-estimates the amplitude of the effect at intermediate radii (with the caveat that I have not included feedback in the simulations as discussed in Section 3.2.1).

3.4 Full MCMC analysis

A comprehensive test of the methodology was to fit the simulated stacked profiles using the full MCMC approach described in Chapter 5, and ensure I recovered the underlying cosmological parameters for the two hydrodynamical simulations (as discussed in Section 3.2.1). I used the *emcee* code (Foreman-Mackey et al., 2013) for the MCMC fitting, which implements a Metropolis-Hastings algorithm (MacKay, 2003) (as discussed in Section 5.2). Here I provide below a brief recap of the fitting technique used in Chapter 5.

I simultaneously fitted the analytical model to both the stacked X-ray and lensing cluster profiles. This model is given in Equations 2.1 and 2.20, and describes both the NFW fit to the lensing profile, and the modified hydrodynamic equilibrium equation for the X-ray surface brightness profile. The combined model has 8 parameters, namely c, M_{200}, n_0,

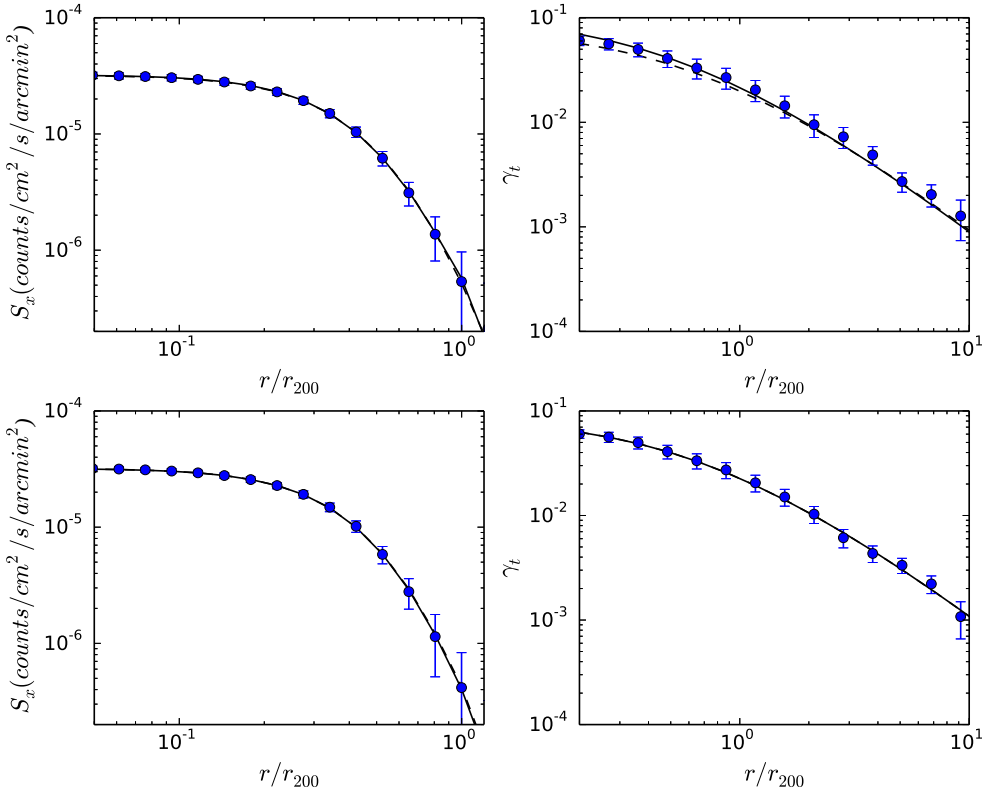

FIGURE 3.13: The X-ray surface brightness (left) and weak lensing (right) profiles for the two simulations: ΛCDM+GR (top) and $f(R)$ (bottom). For each profile, I present the best-fit analytical model (black line) with (dashed line), and without (solid line), the additional non-thermal pressure component. In most cases, these two models overlap significantly. The best-fit parameter values for the ΛCDM+GR simulations (top row), assuming no additional non-thermal pressure, are $T_0 = 26.5$ keV, $n_0 = 0.11 \times 10^{-2}\mathrm{cm}^{-3}$, $b_1 = -2.0, r_1 = 0.63$ Mpc, $M_{200} = 10.0 \times 10^{13}\mathrm{M}_{\odot}$, $c = 9.0, \beta = 3, \phi_{\infty} = 0.7 \times 10^{-4} M_{\mathrm{Pl}}$.

b_1, r_1, T_0 and the two re-scaled chameleon gravity parameters of $\beta_2 = \beta/(1+\beta)$ and $\phi_{\infty,2} = 1 - \exp(-\phi_{\infty}/10^{-4}M_{\mathrm{Pl}})$.

I also performed an extra fit to the profiles but included an additional unknown non-thermal pressure component (e.g., Nagai et al. 2007, Lau et al. 2009) to mimic possible systematic uncertainties. As described in Section 5.5, this additional pressure component was included in the model using a parametric function for the total pressure, such that $P_{total} = g^{-1}P_{sys} = (1-g)^{-1}P_{thermal}$, where P is the different pressure components, and g is a function of the cluster mass and radius.

I found the best-fit model parameters using a χ^2 statistic as described in Section 5.2.1. The MCMC chains were run in parallel using 128 walkers with 10000 time steps (the first 2000 iterations were removed as the 'burn in' phase). In the case of the weak lensing

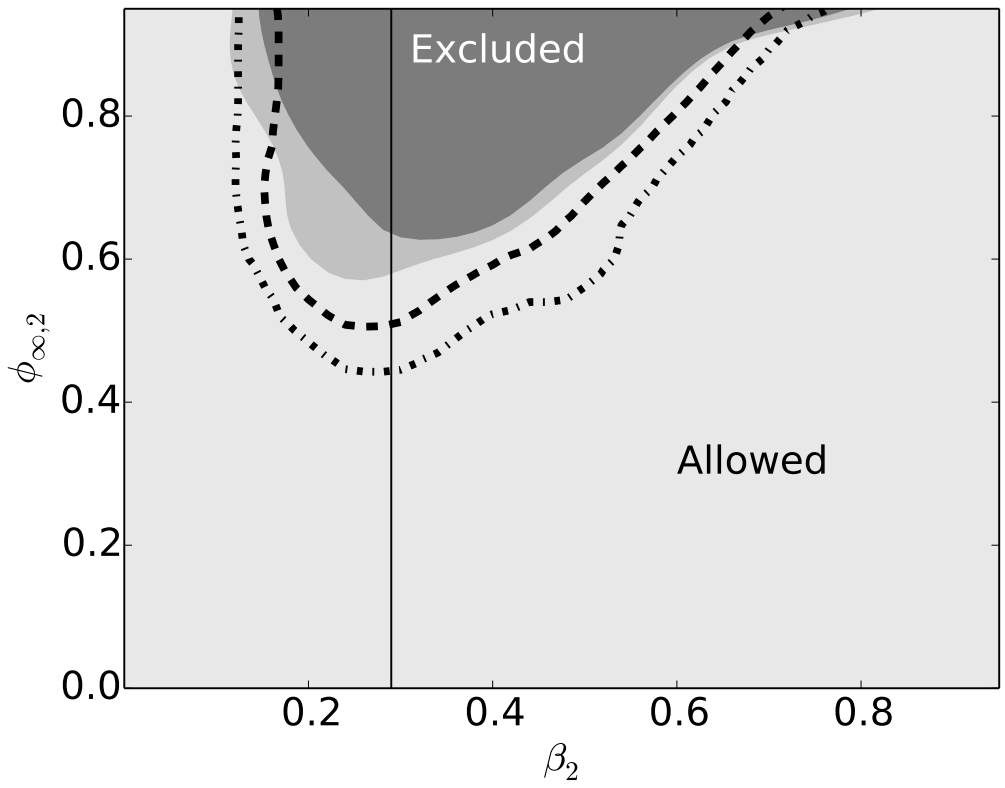

FIGURE 3.14: I show the 95% (light grey) and 99% (dark grey) confidence limits for the excluded region of the combined parameter space of the two re-normalised modified gravity parameters. This uses the X-ray surface brightness and lensing profiles from the ΛCDM+GR simulation where $\beta = 0$ and $\phi_\infty = 0$. Also shown are similar confidence limits from Chapter 5 using the real data (dashed line is the 95 per cent, dot-dashed 99 per cent contours) The vertical line is for $\beta = \sqrt{1/6}$, showing the constraints for $f(R)$ gravity models.

profile, I assumed the covariance matrix was diagonal and computed it from the profile data. For the X-ray surface brightness profiles, I measured the covariance matrix from the X-ray stack directly following the method described in Section 4.3.2.

3.4.1 Results

In Figure 3.13, I show the stacked X-ray surface brightness and weak lensing profiles from both the simulations. I also show the best-fit model to these data with, and without, the inclusion of an additional non-thermal pressure component (as discussed above). I present the X-ray surface brightness profiles out to the cluster virial radius (r_{vir}), while I extend the lensing profile to $10 \times r_{vir}$ (to be consistent with Chapter 5).

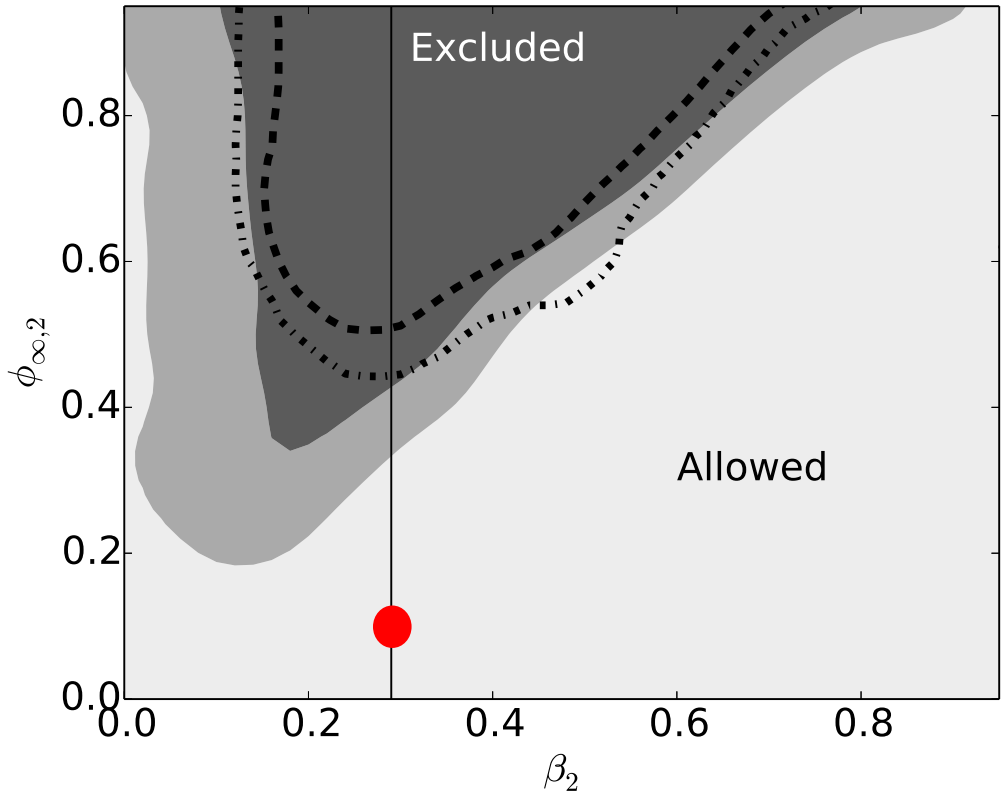

FIGURE 3.15: Same as Figure 3.14 but for the chameleon gravity simulation. The red circle indicates the position of the fiducial model.

These four plots show the inclusion of non-thermal pressure only affects the ΛCDM+GR models. This implies that there must be some degeneracy with the $f(R)$ gravity which compensate for this affect and mask its affect. An additional non-thermal pressure factor would 'blow out' the profile at large radii, while chameleon gravity would compress the profile. Therefore this non-thermal pressure could not be mistaken for chameleon gravity, but it would seek to dampen its affect.

For simplicity, I focus on the two chameleon gravity parameters in the model (β_2 and $\phi_{\infty,2}$) and show in Figure 3.14 the marginalised joint constraint on these two parameters using the simulated cluster profiles from the ΛCDM+GR simulation. I also show the joint constraints obtained in Chapter 5 for these two parameters, but using real data.

In Figure 3.15, I show a similar marginalised joint constraint on β_2 and $\phi_{\infty,2}$, but now using data from the $f(R)$ gravity simulation. I again show the constraints from Chapter 5, but from real data. I also mark the fiducial values of these modified gravity parameters for

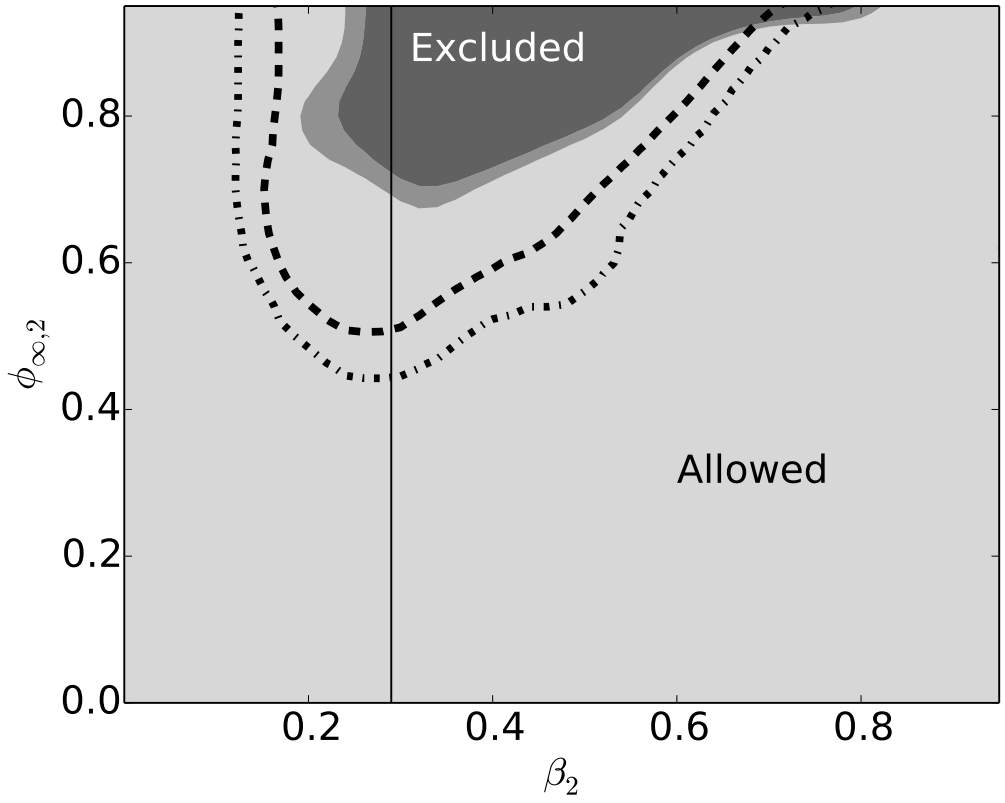

FIGURE 3.16: Same as Figure 3.14 (ΛCDM+GR) but with a non-thermal pressure component added.

the $f(R)$ gravity simulation. Figures 3.16 and 3.17 replicate these constraints, but with the additional non-thermal pressure component (Section 3.4). I note here that I found the non-thermal pressure component to be consistent with zero, which itself is consistent with the zero non-thermal pressure present within the simulations (e.g. feedback mechanism as discussed in Section 3.2.1).

One thing to note regarding the constraints presented in this section is that tighter constraints are obtained from the $f(R)$ simulation compared to the ΛCDM+GR simulation. In the presence of an initial modification to gravity, there is a genuine tension between the hydrostatic and lensing profiles in the f(R) simulation. In turn this leads to less parameter space which the model can investigate before it becomes inconsistent with one or other of the profiles. This therefore rules out more area in the β_2 versus $\phi_{\rm inf,2}$ plane, leading to more powerful constraints compared to ΛCDM+GR.

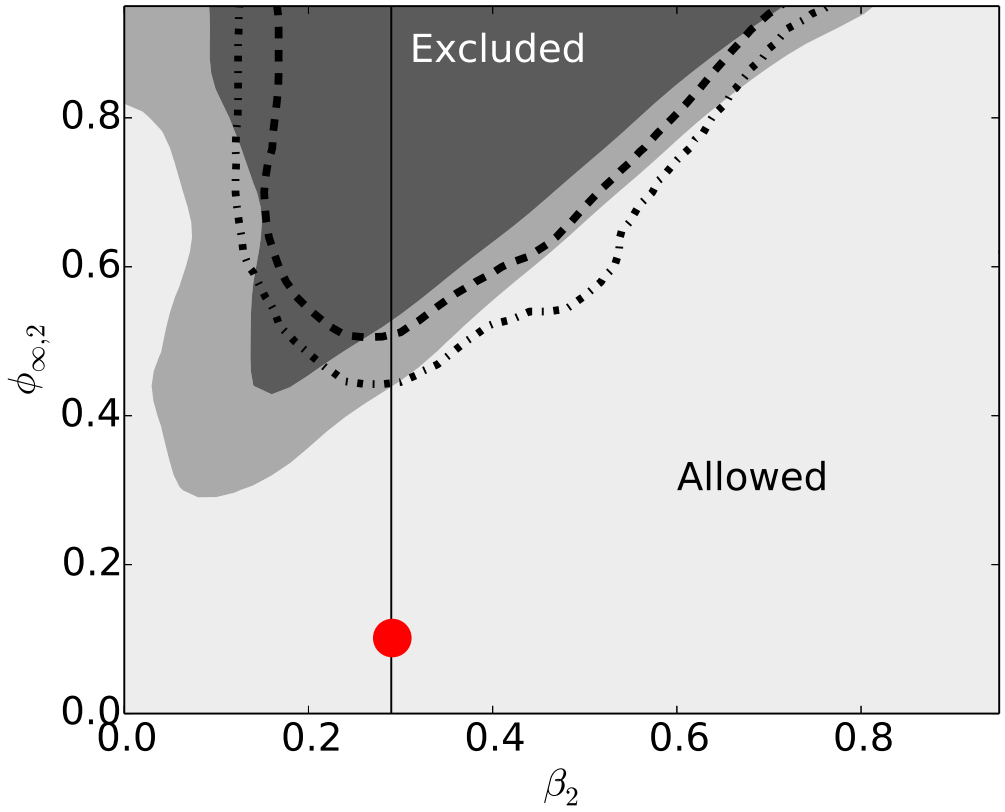

FIGURE 3.17: Same as Figure 3.15 (chameleon gravity) but with a non-thermal pressure component added. The red circle indicates the position of the fiducial model.

These figures show that I obtained meaningful constraints on these modified gravity parameters at a level consistent with Chapter 5. The size of the allowed regions for these joint constraints depends on the underlying simulation, and whether I included an additional pressure component or not. The most realistic constraint is given in Figure 3.14, which is for ΛCDM+GR with no additional non-thermal pressure. Here the constraints are close to those found in Chapter 5, which is reassuring (assuming the true cosmological model is ΛCDM+GR).

It is of particular note however that the constraints obtained here and shown in Figure 3.14 are slightly weaker than those obtained from the real data in Chapter 5. This is perhaps surprising as the constraints above were made using a stack of 103 clusters as opposed to the 58 real clusters that comprise the sample described in Chapter 4. One would expect a sample with more clusters of comparable properties to provide stronger constraints upon the chameleon parameters. The most likely reason for this disparity

is an over-estimate of the amplitude and errors associated with the simulated profiles. This would allow the analytic models being fit to both the X-ray and lensing profile to diverge by a greater amount before they became inconsistent and would therefore rule out a greater amount of parameter space.

The source of this over-estimation most likely arises for two reasons, both associated with the weak lensing profile. The first of these reasons would result in an amplitude modulation and is that the source galaxies used to generate the lensing profile in Section 3.2.4 where placed at the back of the simulation box as opposed to the median redshift of CFHTLenS (discussed in greater detail in Section 4.2.1). This median redshift was used when generating weak lensing profiles for the real clusters (as described in Section 4.3.3). As Equation 2.28 shows, the lensing signal is directly proportional to the separation between the lens and source. Therefore, placing the sources galaxies to close to the clusters will result in a amplitude modulation, which in turn will reduce the accuracy of the constraints obtained.

The source of the error over-estimation most likely arises from the way the errors were obtained in Section 3.2.4. In this section I have not divided the random shear components (which were drawn from the CFHTLenS distribution) by $\sqrt{N}$ (were N is the number of source clusters). This factor is required to account for the number of source galaxies in each pixel. This in turn would have reduced the errorbars upon the weak lensing profile and lead to tighter constraints upon the modified gravity parameters.

These joint constraints can be used to place an upper limit on $|f_{\rm R0}|$, which can then be compared to the constraints presented in Chapter 5 and, in the case of the $f(R)$ simulation, the input value of the simulation. Likewise, I placed an upper limit on $f(R)$ gravity by placing a constraint on ϕ_∞ as such models are a subset of the chameleon model for which $\beta = \sqrt{1/6}$ (shown as the vertical black line in Figures 3.14, 3.15, 3.16 and 3.17). These constraints are shown in Table 3.2, for both simulations with, and without, the extra systematic uncertainty. First shown in Table 3.2 is the value of ϕ_∞ when in $f(R)$ gravity, found as the value of ϕ_∞ where the $\beta = \sqrt{1/6}$ intersects the 95% excluded region. This value can then be related to f_R at the cluster's redshift ($z = 0.33$) using Equation 1.51.

	Without systematic error	With systematic error
ΛCDM - ϕ_∞	$< 8.7 \times 10^{-5} M_{\rm Pl}$	$< 1.1 \times 10^{-4} M_{\rm Pl}$
$f(R)$ - ϕ_∞	$< 4.0 \times 10^{-5} M_{\rm Pl}$	$< 5.7 \times 10^{-5} M_{\rm Pl}$
ΛCDM - $f_{\rm R}$	$< 7.1 \times 10^{-5}$	$< 9.6 \times 10^{-5}$
$f(R)$ - $f_{\rm R}$	$< 3.3 \times 10^{-5}$	$< 4.7 \times 10^{-5}$
ΛCDM - $f_{\rm R0}$	$< 8.3 \times 10^{-5}$	$< 1.1 \times 10^{-4}$
$f(R)$ - $f_{\rm R0}$	$< 3.8 \times 10^{-5}$	$< 5.5 \times 10^{-5}$

TABLE 3.2: Summary of constraints on modified gravity parameters from both simulations, with and without a non-thermal pressure component (95% CL).

The time-evolution of $f_{\rm R}(z)$ for a Hu-Sawicki model with $n = 1$ (where n is an additional degree of freedom of the model) follows (Li et al., 2013),

$$f_{\rm R}(z) = |f_{\rm R0}|[(1 + 3\Omega_\Lambda)/(\Omega_{\rm M}(1 + z)^3 + 4\Omega_\Lambda)]^2. \tag{3.10}$$

This evolution leads to a reduction in the magnitude of $f_{\rm R}$ by 27% at today's redshift when compared with the redshift at which the simulation was placed, $z = 0.4$, due to a higher background energy density at higher redshifts. When I have include fitting for a systematic error, the constraints are less stringent as the additional pressure can be degenerate with a fifth force, reducing the signal. The results of doing so are shown in Table 3.2.

For the ΛCDM+GR simulation, I found $|f_{\rm R0}| < 8.3 \times 10^{-5}$, which is in excellent agreement with the limit in Chapter 5 of $|f_{\rm R0}| < 6 \times 10^{-5}$. This validates the methodology in Chapter 5 and shows the technique can deliver competitive constraints upon the chameleon gravity model, i.e. the measurement presented in Chapter 5 still provides one of the best constraints on $|f_{\rm R0}|$ on cluster scales (Mpcs).

These simulations demonstrate that the methodology in Chapter 5 is capable of constraining chameleon gravity. However, I noticed that the constraints recovered in this Chapter are slightly less powerful than those presented in Chapter 5. In Chapter 5, I split the cluster sample into two separate bins based on their X-ray temperature ($T_x < 2.5$keV and $T_x > 2.5$keV). I found this split in temperature (mass) provided a stronger constraint on $|f_{\rm R0}|$ compared to a single mass bin. However, I was unable to replicate such binning here as the distribution of cluster temperatures and masses in the simulations was much narrower, missing the more massive ($T_x > 2.5$keV) halos due to the finite volume of the simulation box, as discussed in Section 3.2.1. I will need larger simulations to address

this issue and allow me to test modified gravity effects as a function of both mass and environment (as discussed in detail in W15). Future simulations should also include more realistic feedback mechanisms.

In Section 3.6, I present Figures 3.18, 3.19, 3.20 and 3.21, which show the full likelihood contours for joint constraints between all eight parameters in the analytical model. I provide constraints both with, and without, the additional pressure component. These joint constraints can be compared to the similar plot given in Section 3.4 for the real clusters.

3.5 Summary

In this Chapter, I investigated the methodology presented in Chapter 5 and tested some of the key assumptions made in that analysis. This was achieved using two nearly identical hydrodynamical simulations; one evolved using ΛCDM+GR and the other evolved using a modified gravity component of $|f_{\rm R0}|= 10^{-5}$. Using these simulations, I generated realistic stacked weak lensing and X-ray surface brightness profiles.

I used these stacked profiles to test the assumptions outlined in Section 3.1. First, I found that the stacking process for generating high signal-to-noise cluster profiles was fair and created representative lensing and X-ray surface brightness profiles compared to the underlying ensemble of clusters. Furthermore, I demonstrated that the stacking process created spherically symmetrical profiles, thus reducing the possible bias caused by any ellipticity in an individual cluster.

I also investigated the assumption that dark matter haloes in chameleon gravity are well described by the same NFW profile as used in ΛCDM. I found no difference between the fitted NFW parameters for both the $f(R)$ and ΛCDM simulated stacked lensing profiles confirming previous studies in the literature.

As a final test of the methodology, I have compared the simulations with predictions from the analytic model described in Section 2.2.2. The results of this test are summarised in Figure 3.11, which shows broad agreement between the analytical and numerical (simulation) results, with the latter showing a large deviation from ΛCDM for the same value of $|f_{\rm R0}|= 10^{-5}$.

In Section 3.4, I replicated the full MCMC analysis from Chapter 5, but now using the simulated stacked cluster profiles instead of real data. I also include the possibility of an additional (unknown) non-thermal pressure component in the intracluster medium, which would produce a significant systematic uncertainty in the modelling.

In the $f(R)$ case, I was able to recover a value of $|f_{\rm R0}| < 3.8 \times 10^{-5}$, which is fully consistent with the fiducial value of $|f_{\rm R0}| = 10^{-5}$ for the simulations. In the presence of an initial modification to gravity, there is a genuine tension between the hydrostatic and lensing profiles in the $f(R)$ simulation. In turn this led to less parameter space that the model can investigate before it becomes inconsistent with one or the other profiles. This therefore rules out more area in the β_2, $\phi_{\infty,2}$ plane, leading to more powerful constraints than compared to ΛCDM.

I have also constrained the profiles from both simulations, including a non-thermal pressure component; to account for unknown systematic errors (in astrophysics or the analysis). This obviously lessens the constraints as such uncertainties are degeneracy with any fifth force: that is, both affect the shape of the profile at large scales. The constraints with this extra pressure term are still consistent with the fiducial model.

3.6 Full MCMC contour plots

I present plots of the joint constraints on all 8 parameters used in Section 3.4

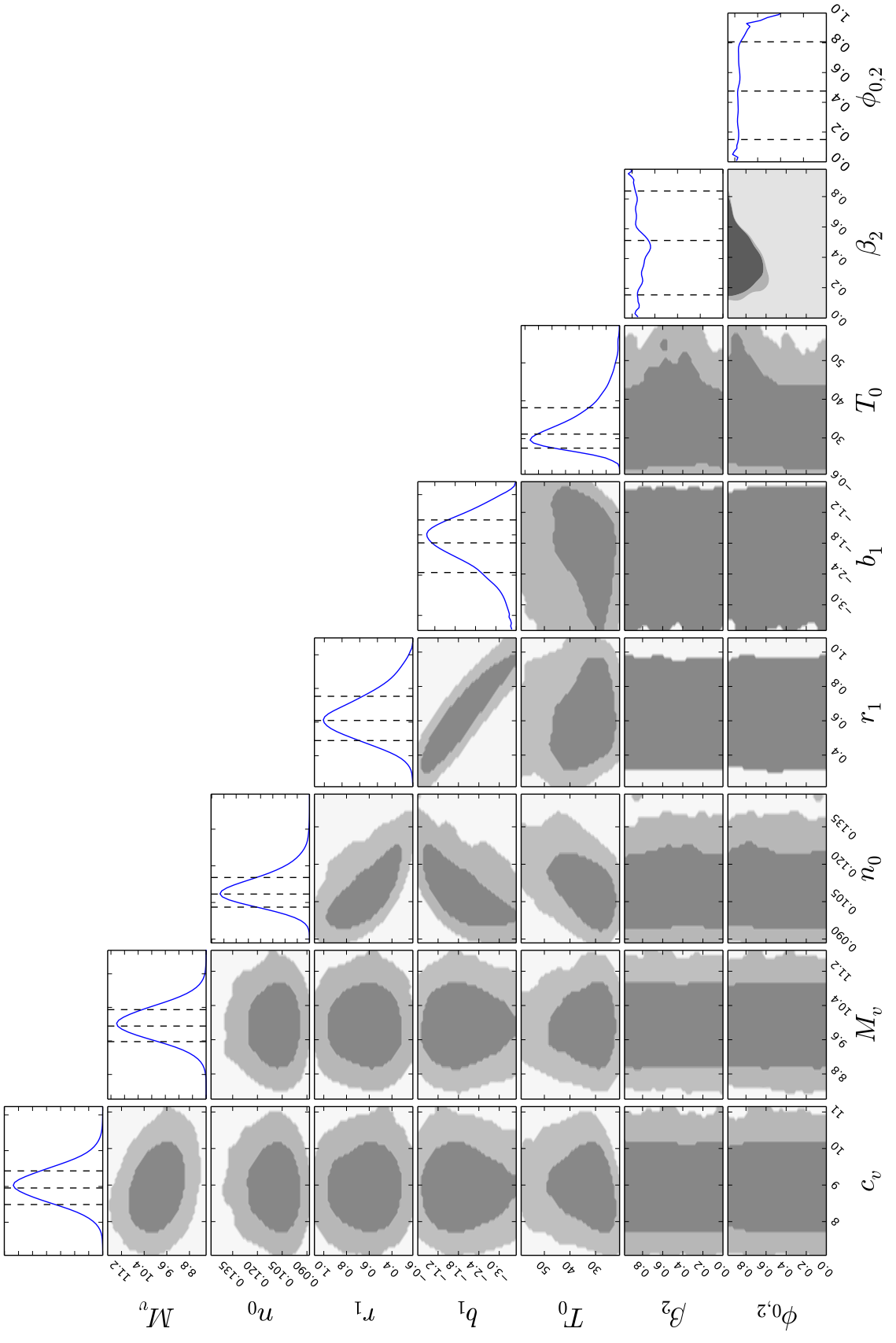

FIGURE 3.18: The 95% (dark grey region) and the 99% CL (light grey region) 2D marginalised contours for the 8 model parameters fitting the ΛCDM simulation: T_0 [keV], n_0 [10^{-2}cm^{-3}], b_1, r_1 [Mpc], M_{200} [10^{13}M$_\odot$], c, β_2, $\phi_{\infty,2}$ used in the MCMC analysis. The rightmost plots show the 1D likelihood distributions.

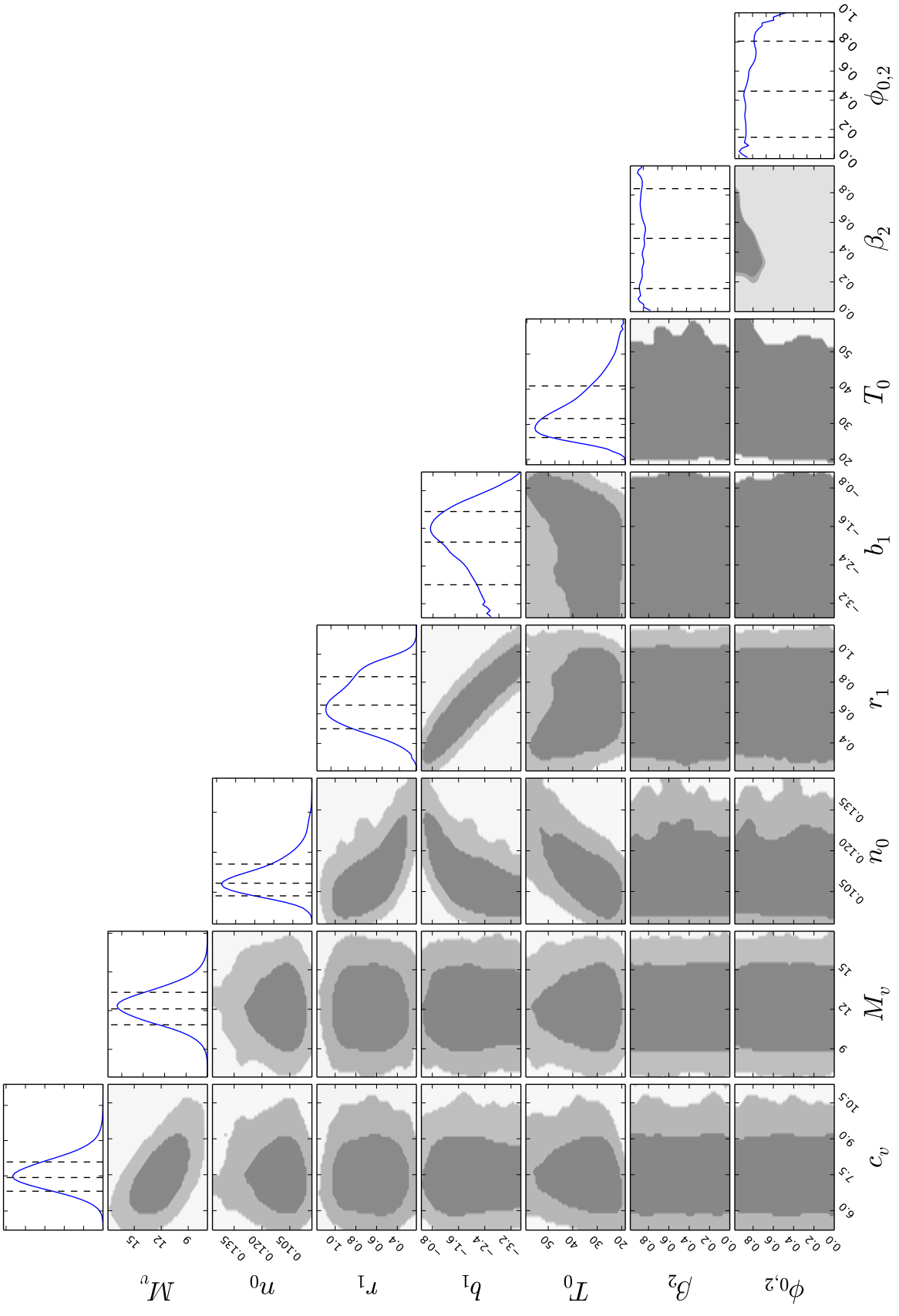

FIGURE 3.19: The 95% (dark grey region) and the 99% CL (light grey region) 2D marginalised contours for the 8 model parameters fitting the ΛCDM simulation with the inclusion of a systematic error: T_0 [keV], n_0 [$10^{-2}\mathrm{cm}^{-3}$], b_1, r_1 [Mpc], M_{200} [$10^{13}\mathrm{M}_\odot$], c, β_2, $\phi_{\infty,2}$ used in the MCMC analysis. The rightmost plots show the 1D likelihood distributions.

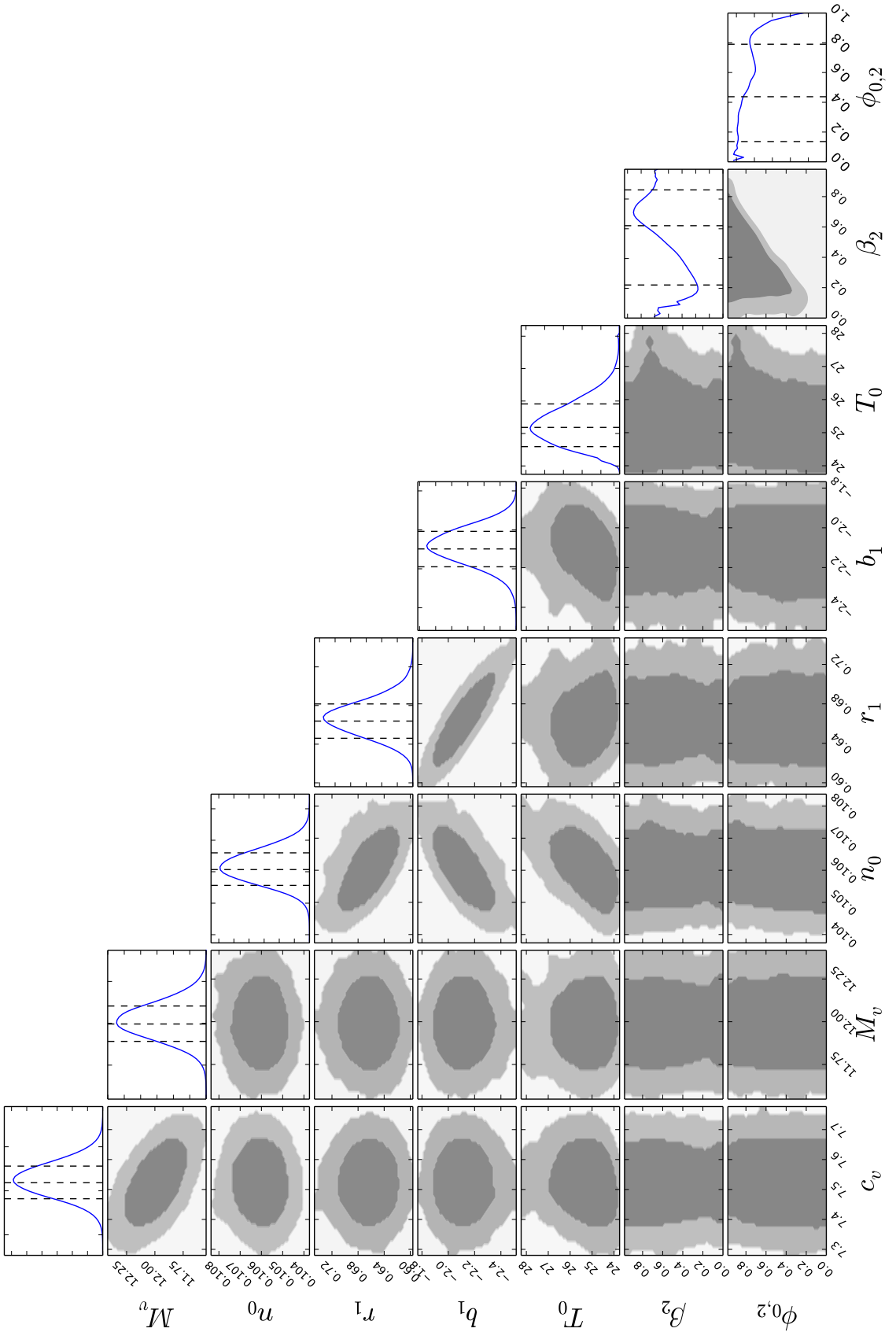

FIGURE 3.20: The 95% (dark grey region) and the 99% CL (light grey region) 2D marginalised contours for the 8 model parameters fitting the chameleon gravity simulation: T_0 [keV], n_0 [$10^{-2}\mathrm{cm}^{-3}$], M_{200} [$10^{13}\mathrm{M}_\odot$], c, β_2, $\phi_{\infty,2}$ used in the MCMC analysis. The rightmost plots show the 1D likelihood distributions.

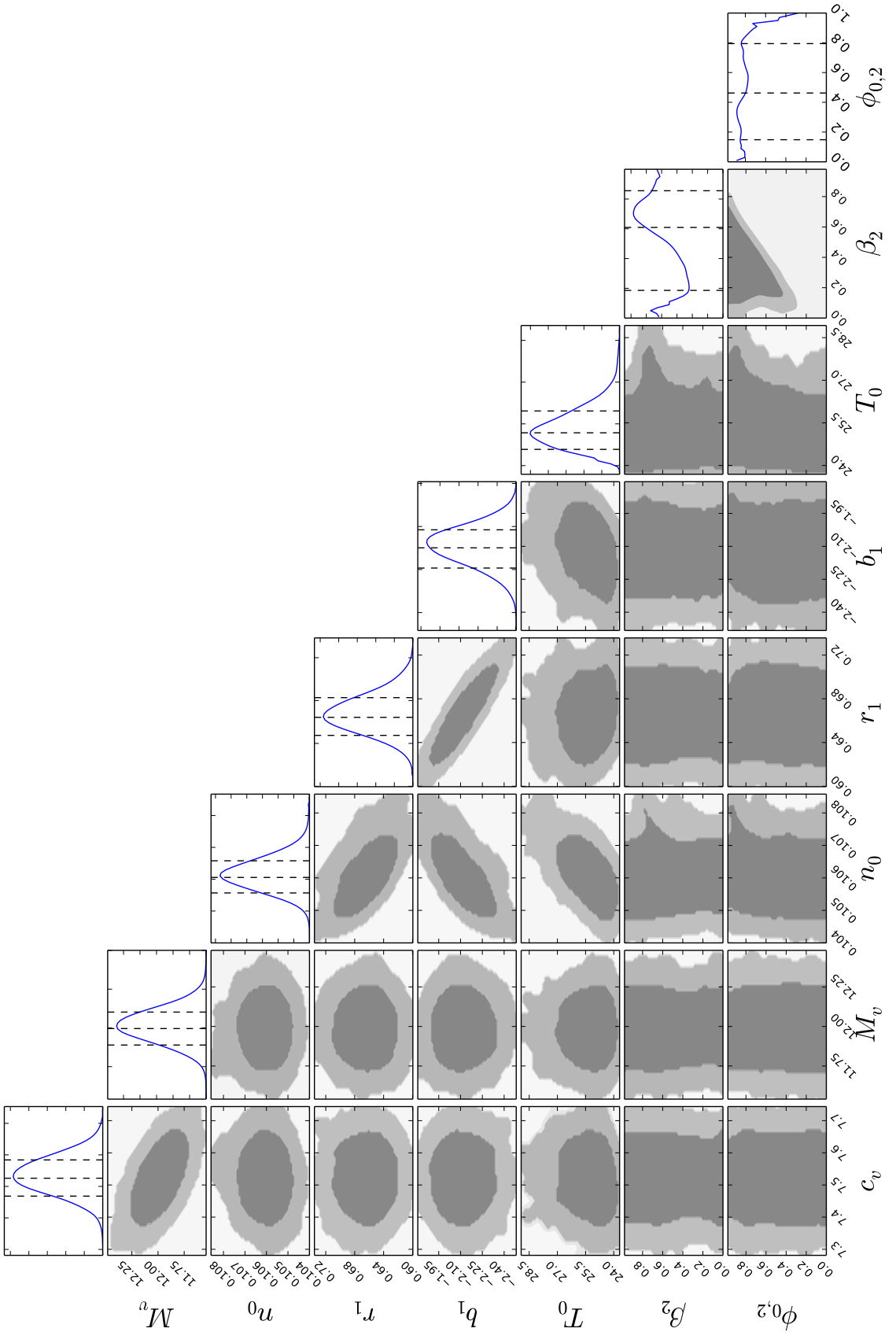

FIGURE 3.21: The 95% (dark grey region) and the 99% CL (light grey region) 2D marginalised contours for the 8 model parameters fitting the chameleon gravity simulation with the inclusion of a systematic error: T_0 [keV], n_0 $[10^{-2}\mathrm{cm}^{-3}]$, b_1, r_1 [Mpc], M_{200} $[10^{13}\mathrm{M}_\odot]$, c, β_2, $\phi_{\infty,2}$ used in the MCMC analysis. The rightmost plots show the 1D likelihood distributions.

Chapter 4

Generating the cluster sample

4.1 Overview

This chapter discusses the cluster sample published in Wilcox et al. (2015).

As discussed in Section 1.4.1, the chameleon gravity model postulates the existence of a scalar field that couples with matter to mediate a fifth force. If it exists, this fifth force would influence the hot X-ray emitting gas filling the potential wells of galaxy clusters. However, it would not influence the cluster's weak lensing signal. Therefore, by comparing X-ray and weak lensing profiles, one can place upper limits on the strength of a fifth force.

In order to perform this measurement I must first obtain a suitable sample of clusters with both good quality X-ray and weak lensing data. I begin here by discussing the two main sources of the data.

I first discuss the creation of the X-ray cluster sample going from the raw XMM exposures to the finalised catalogue (I describe XMM in Section 4.2.2). I then describe the techniques used to create both the X-ray stacked profile and weak lensing stacked profile.

I end this chapter by performing tests upon the dataset and derived profiles to ensure their suitability for gravity tests.

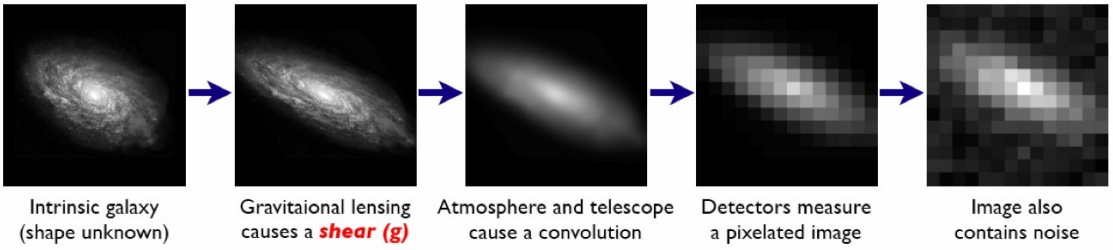

FIGURE 4.1: The stages of going from a galaxy's true shape to its measured shape. Figure from (Bridle et al., 2009). This figure illustrates the difficulty in measuring the shear of a galaxy.

4.2 Data

To be able to implement the tests of gravity described in Section 1.5 I first need to construct accurate X-ray and lensing profiles (as described in Section 1.5). To do so I use data from two high quality datasets, described below.

4.2.1 CHFTLenS

The Canada France Hawaii Telescope (CFHT) is a 3.6 metre optical and infrared telescope, operational since 1979, located atop the 4200 metre dormant volcano Mauna Kea in Hawaii. CFHT has 4 instruments that can be used with the telescope: Megacam, a 340 megapixel optical and near infrared camera with a field of view of 1 degree; Wide-field InfraRed Camera (WIRCam), a 16 megapixel infrared detector with a field of view of 20 arcminutes; an Echelle SpectroPolarimetric Device for the Observation of Stars at CFHT (ESPaDOnS), a high-resolution echelle spectrograph and spectropolarimeter; and the Spectromètre Imageur à Transformée de Fourier pour l'Etude en Long et en Large de raies d'Emission (SITELLE), a wide field optical integral field unit.

In this work I have made use of public weak lensing data (galaxy ellipticities and photometric redshifts) provided by the Canada France Hawaii Telescope Lensing Survey (CFHTLenS, Heymans et al. 2012), obtained using Megacam from 2003 until 2009 (Boulade et al., 2003). The CFHTLenS covers 154 square degrees, across four fields: W1 centred at RA=02h18m00s, Dec=-07d00m00s with 72 pointings; W2 centred at RA=08h54m00s, Dec=-04d15m00s with 33 pointings; W3 centred at RA=14h17m54s, Dec=+54d30m31s with 49 pointings and W4 centred at RA=22h13m18s, Dec=+01d19m00s (Erben et al., 2013). The pointings within each field have an overlap of 3′ in right ascension and 6′ in

Filter	exposure time (s)	m_{lim}	seeing ($''$)
$u*$	5×600	25.24 ± 0.17	0.88 ± 0.11
g'	5×500	25.58 ± 0.15	0.82 ± 0.10
r'	4×500	24.88 ± 0.16	0.72 ± 0.09
i'	7×615	24.54 ± 0.19	0.68 ± 0.11
z'	6×600	23.46 ± 0.20	0.70 ± 0.12

TABLE 4.1: Characteristics of the CFHTLenS survey's five colour bands. Table adapted from Erben et al. (2013).

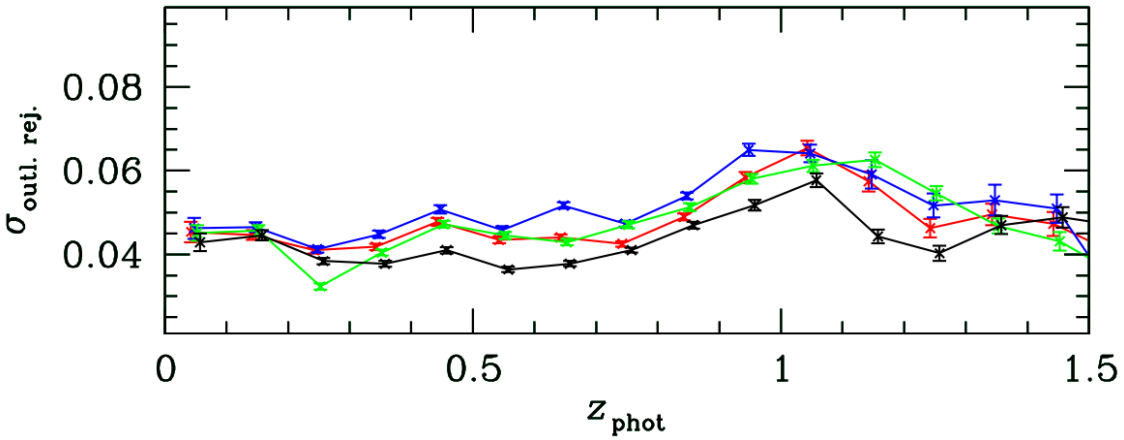

FIGURE 4.2: Photo-z error as a function of redshift for all galaxies in CFHTLenS. The different colours represent different photo-z estimations. Figure from Hildebrandt et al. (2012). This figure shows that the error associated with a given redshift is largely redshift invariant.

declination to ensure full coverage of the survey area. The position of each of these four fields is shown in Figure 4.7 in blue. The 2D density distribution of the W1 field is shown in Figure 2.9, and I reproduce this mass map in Section 4.2.1.

Each field contains a galaxy density of 17 per square arcmin, with high quality shape measurements in four distinct fields. CFHTLenS used five colour bands $u^*g'r'i'z'$ with a limiting magnitude of $g' = 25.6$. Here, the $'$ indicates the filter was designed to match the Sloan Digital Sky Survey (SDSS) $u'g'r'i'z'$ filters as closely as possible (Gunn et al., 1998). The u band, however, differs from SDSS to take advantage of the improved ultraviolet capabilities of Megacam and is named u^* to highlight this difference. Table 4.1 shows the observing time, limiting magnitudes (m_{lim}) and the mean seeing with their associated standard deviations for each of the 5 filters. Here the seeing values are estimated by using the `SExtractor` (Bertin and Arnouts, 2010) parameter FWHM_IMAGE and the limiting magnitude is the 5σ detection limit within a $2''$ aperture (Erben et al., 2013).

The galaxy ellipticities were generated by the CFHTLenS team using the `THELI` (Erben et al., 2013) and `lensfit` (Miller et al., 2013) routines. Photometric redshifts were produced using PSF-matched photometry to an accuracy of $0.04(1+z)$ with a 4% catastrophic outlier rate (Hildebrandt et al., 2012) with a median redshift of 0.75. Figure 4.2 plots the errors on the photo-z estimates against redshift, showing that the accuracy of the estimates.

Generating high quality lensing data is not a trivial task, as shown in Figure 4.1. A galaxy's true shape is firstly sheared via weak lensing, then a point spread function is applied by the telescope during observations. This is then pixelated by the camera's CCDs, which also apply electronic noise.

To achieve accurate galaxy shapes the CFHTLenS team used a likelihood-based method described in Miller et al. (2013), which is briefly reviewed in Section 2.2.4. Errors were measured from the 1D variance of the ellipticity likelihood surface.

Testing the CFHTLenS data

In this section I describe two tests I made to the CFHTLenS data described above to ensure that I was aware of all the conventions associated with the data (such as the signs of the ellipticity) and to get a good understanding of the dataset.

The first test I performed was to use Equation 2.46 to reproduce the work of Covone et al. (2014). I used the shear catalogue from CFHTLenS (described in Section 4.2.1) and an optically selected cluster catalogue from Wen et al. (2012). This catalogue contains 132,684 optically selected galaxy clusters, and found to be 95% complete for clusters with a mass of $M_{200} > 1.0 \times 10^{14} M_{\odot}$ in the redshift range $0.05 \leq z < 0.42$. Selecting those clusters which overlap with the CFHTLenS footprint, a final sample of 1176 clusters was found, which I divided into 6 richness bins.

For each cluster I then determined the shear profile up to a radius of 20Mpc as detailed in Section 4.3.3, using only those CFHTLenS galaxies that have $z_{source} > z_{lens} + 0.2$ to reduce background contamination. These profiles were then stacked within each richness bin to create six stacked cluster profiles.

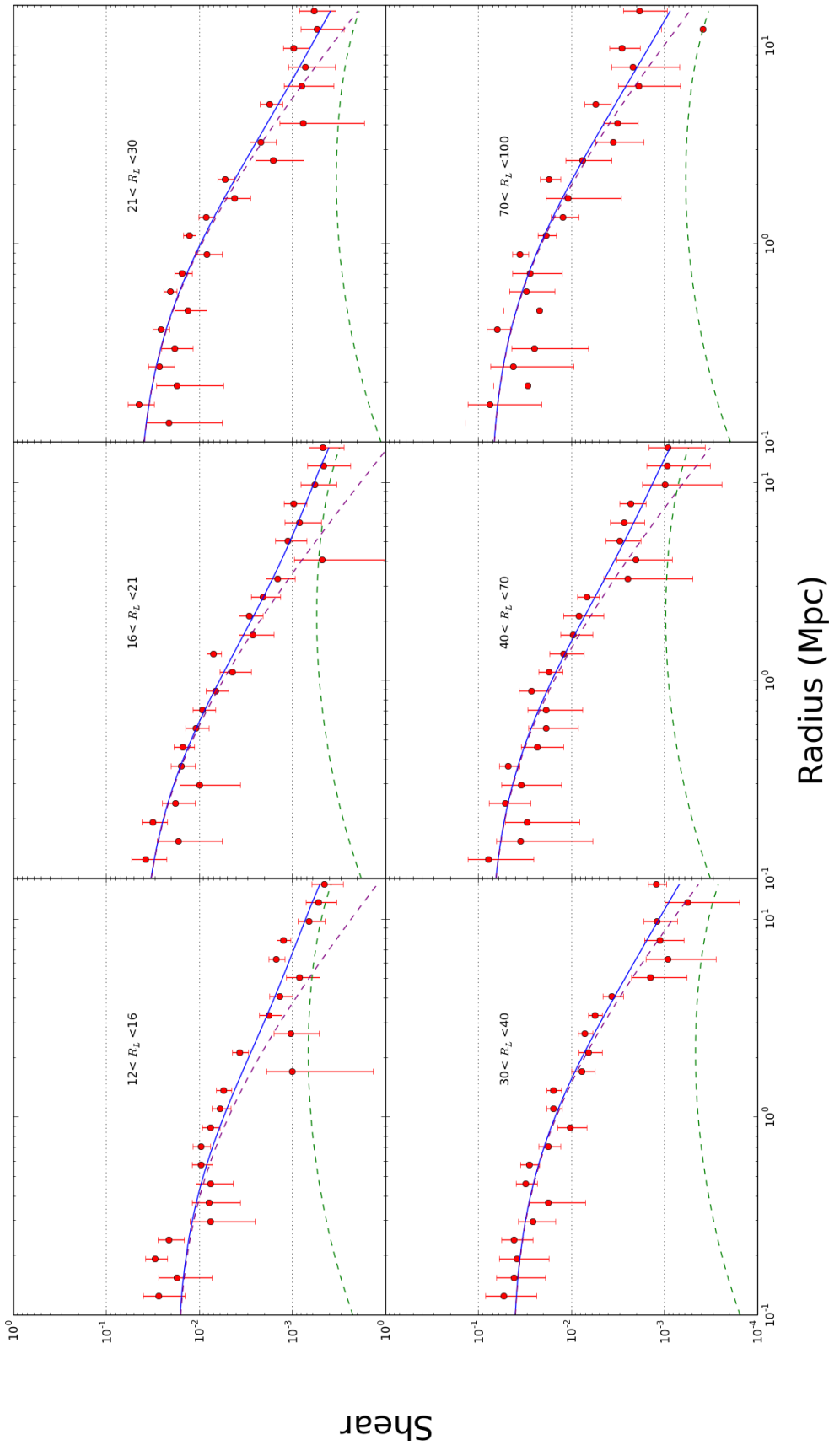

FIGURE 4.3: Radial shear profile around 1176 galaxy clusters binned according to optical richness (R_λ) against radius as red points. In solid blue I show the best fit model to the data. In dashed purple I show the contribution due to the 1-halo term and in dashed green from the 2-halo term.

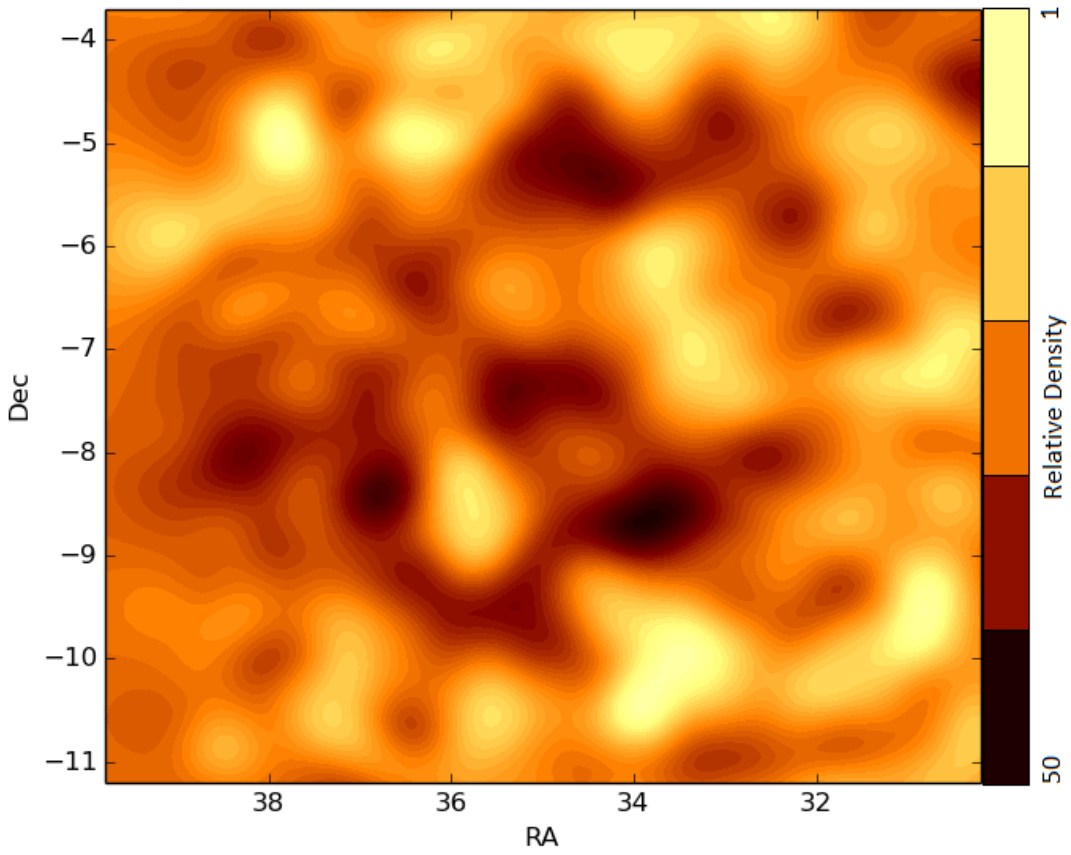

FIGURE 4.4: Projected mass density of 64 square degrees from the CFHTLenS W1 field, lighter areas denote regions of higher density. This figure is a test of the CFHTLenS data made by reproducing the work of Van Waerbeke et al. (2013).

These six binned profiles were then fit using Eqaution 2.45 via an MCMC, minimising a χ^2 parameter. This fit used both the 1 and 2-halo terms, the latter of which employed the prescription for the linear matter power spectrum of Eisenstein and Hu (1999).

In Figure 4.3 I show the best fits for each richness bin (indicated upon each plot) in solid blue, with the 1-halo term in dashed purple and the 2-halo term in dashed green. As can be seen at small radii, the 1-halo term dominates, but as the radius increases the 2-halo term becomes the more significant contribution. This figure visually agrees well with the equivalent figure in Covone et al. (2014), and is confirmation that the shear measurement and fitting procedures, described in detail later, are satisfactory.

The second test I performed was to reproduce the mass map of the W1 field from Van Waerbeke et al. (2013), shown in Figure 2.9. To do this I first obtained the positions, shapes and redshifts of all the galaxies within the W1 field, resulting in the properties

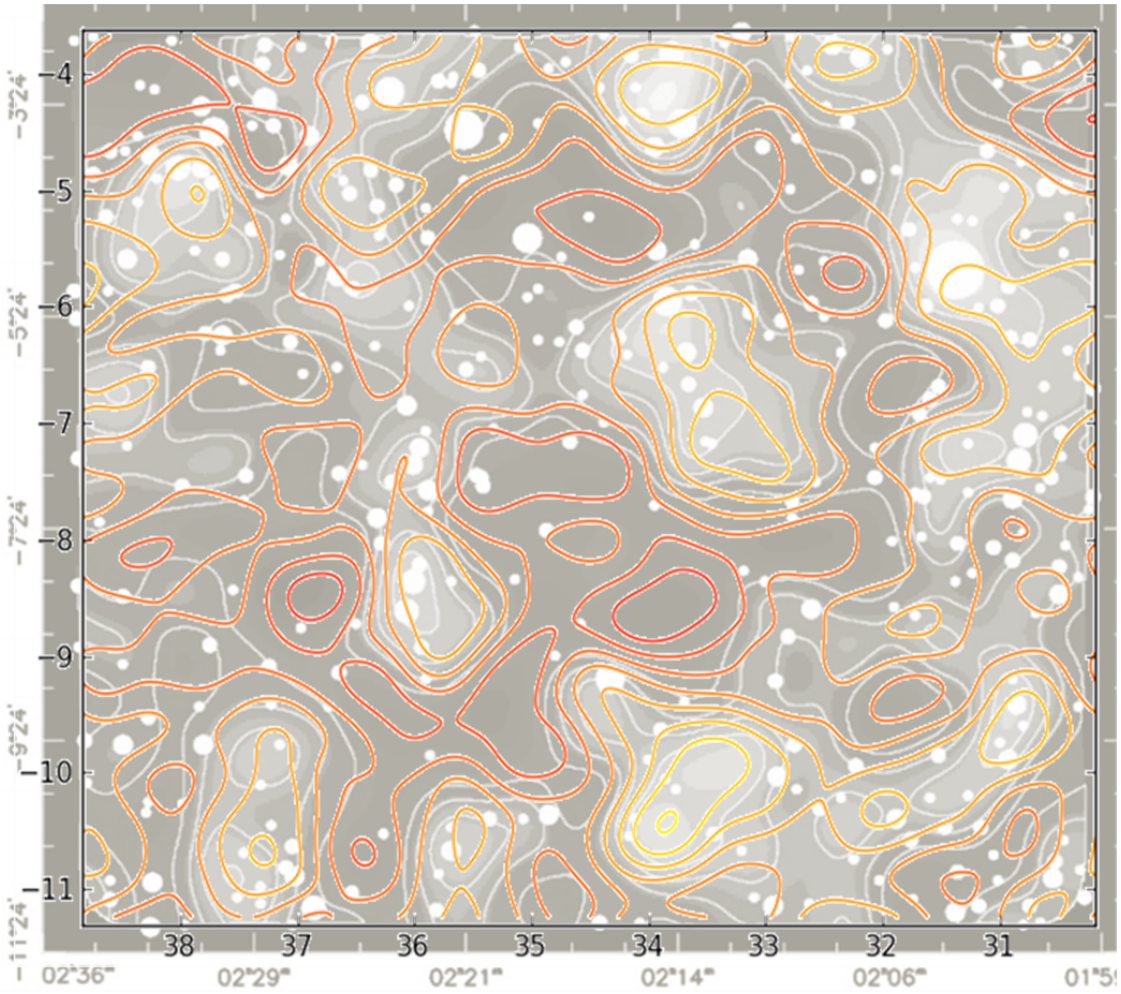

FIGURE 4.5: Projected mass density of 64 square degrees from the CFHTLenS W1 field from Van Waerbeke et al. (2013) where RA is shown along the x-axis and dec along the y-axis. This figure is overlain with my reproduced contours, where orange contours indicate a higher projected density and red a lower projected density.

of $\sim$ 3.5 million galaxies. The shapes of these galaxies were then corrected following the method described in Section 4.3.3 to get an estimate of each galaxy's ellipticity. I then performed a Kaiser-Squires inversion (Kaiser and Squires, 1993) upon the data following the method outlined in Section 2.2.6, using a smoothing scale of 1.8 arcminutes (as described in Equation 2.53) to ensure consistency with Van Waerbeke et al. (2013).

The resultant mass map is shown in Figure 4.4, where lighter areas denote higher densities. It can be seen that this figure is visually consistent with Figure 2.9 through the comparison Figure 4.5, which shows the two plots overlain. Here it is seen that the contours largely agree is further confirmation that my data processing techniques are accurate.

It should be noted that whilst the two sets of contours are broadly similar, there are

definite inconsistencies present. In order to construct Figure 4.4, the Kaiser-Squires inversion requires galaxies had to be binned. This binning will have centred upon different positions, with different bin sizes between the two mass maps, leading to the observed inconsistencies. Further inconsistencies arose from a differing of redshift cuts between the two maps, where Van Waerbeke et al. (2013) has used galaxies with $0.4 < z < 1.1$, while this work has made use of all galaxies $z > 0.4$.

4.2.2 XCS

The XMM (X-ray Multi-Mirror) mission is an ESA satellite designed to observe X-rays in the soft band, from 0.15keV to 15keV (ESA, 2015). After launch, the satellite was renamed XMM-Newton in recognition of the famous UK scientist. Here and throughout I will refer to this satellite as XMM. Launched on December 10th 1999 it sits on a 48 hour highly elliptical orbit with an apogee of $108,900$km and a perigee of $12,200$km.

XMM carries on board three science instruments: the European Photo Imaging Camera (EPIC), used for X-ray imaging, spectroscopy and photometry; a Reflecting Grating Spectrometer (RGS) for high-resolution spectrometry; and an Optical Monitor (OM) for optical and UV imaging.

On-board are three telescopes which focus the X-rays onto the three EPIC cameras. These three cameras are of two different types. Two are Metal Oxide Semi-conductor (MOS) CCDs and the third is a pn CCD array (standing for positive-negative and named for the electrons and holes that form in the silicon of detector when collided with X-ray photons, Strüder et al. 2001). The two MOS cameras have diffracting gratings in their light path, splitting the light beam off to the RGS, while the pn camera has an unobstructed view. Each camera has a field of view of around 30 arcminutes and is optimised for sensitivity over spatial resolution, making it ideal for detecting the diffuse emission of clusters.

Since its launch XMM has been used for many different X-ray surveys such as investigating the X-ray properties of galaxies (Georgakakis et al., 2003), surveying the Small Magellanic Cloud (Haberl et al., 2012) and searching for galaxy clusters (Pacaud et al., 2015). XMM has therefore observed over 1000 square degrees, most of which is publicly available.

The XMM Cluster Survey (XCS, Romer et al. 2001, Lloyd-Davies et al. 2011) is a serendipitous X-ray cluster survey drawn from public archival XMM data. This means that XCS

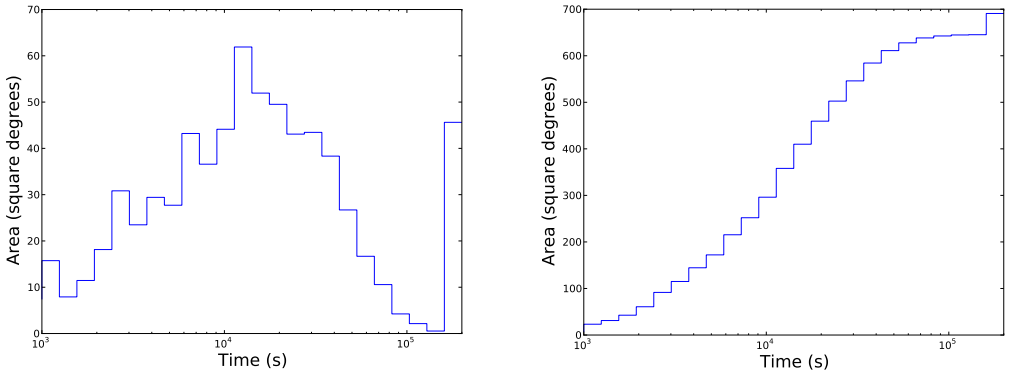

(A) Histogram (B) Cumulative

FIGURE 4.6: Area of XCS as function of exposure time. Figure 4.6a shows this as a histogram and Figure 4.6b as a cumulative histogram. This figure shows that the average exposure time of an XCS exposure is $\approx$ 20ks.

takes all the the publicly available XMM observations and searches them for X-ray clusters (this process is described in Section 4.3.1). Currently these observations cover $\sim$ 1030 square degrees of the sky. However only $\sim$ 690 square degrees of this is useful for cluster searches, the other $\sim$ 340 square degrees lies within 20 degrees of the galactic plane or within 5 (3) degrees of the Large (Small) Magellanic Cloud. Shown in Figure 4.6a is a histogram of the area of sky covered by XCS as a function of exposure time and in Figure 4.6b a cumulative plot of the same data. The final bin in Figure 4.6a is large due to all exposure times $>$ 150ks being placed together. These plots show that over half the total XCS area has been observed for $>$ 10ks.

XCS therefore compares favourably to other X-ray cluster surveys: such as the MAssive Cluster Survey (MACS, Ebeling et al. 2001), which has surveyed an area of $22,735$ square degrees, although it has only done so with a flux limit 2 orders of magnitude less than XCS or XXL.

XXL (Pierre et al., 2015) is the largest targeted XMM survey, covering 50 square degrees and aims to constrain dark energy (as discussed in Section 1.3) through the distribution of clusters. The observations XXL made were split into two 25 square degree fields, with one centred in the CFHTlenS W1 footprint. This site was selected due to the large of amount of complementary data at a range of wavelengths that is available and the (already available), substantial XMM coverage from XMM-LSS (Pierre et al., 2004). XXL recently released a bright cluster sample (flux limited to 3×10^{-14}ergs^{-1}) containing 51 clusters in the W1 field (Pacaud et al., 2015) spanning the redshift range $0.05 < z < 1.05$ (median

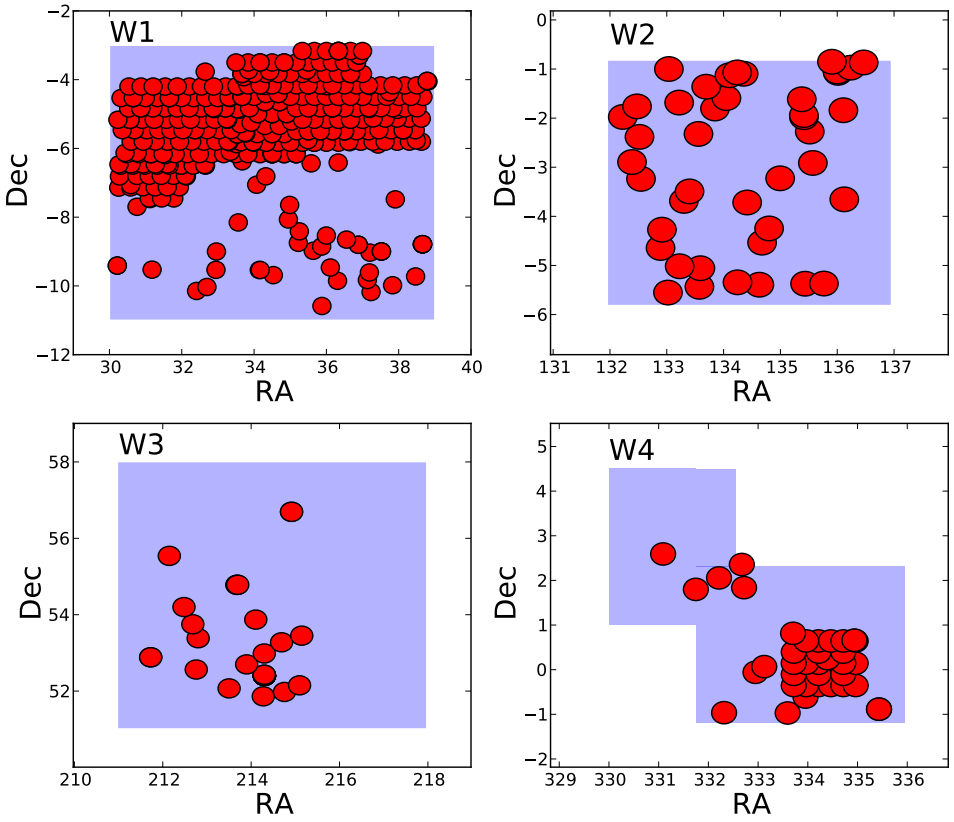

FIGURE 4.7: The four CFHTLenS fields (W1, W2, W3 and W4) in blue and the XMM observations that fall within these fields in red. This figure aims to illustrate that concentration of exposures in the W1 region.

$z = 0.3$) and temperature range $0.6 < T_{\rm x} < 5.5$ keV (median $T_{\rm x} = 3.2$ keV), which is very comparable to the sample discussed below and presented in Table A.1.

XCS is currently the largest X-ray selected cluster catalogue. Its XCS Data Release 1 (XCS-DR1, Mehrtens et al. 2012) contains 503 optically confirmed clusters. Of these 463 have measured redshifts, ranging from $0.06 < z < 1.46$. Of these, 401 have measured X-ray temperatures, ranging from $0.4\text{keV} < T_x < 14.7\text{keV}$ (as discussed in Sections 2.2.2 and 4.3.1).

4.3 Methods

4.3.1 Compiling the X-ray Cluster Sample

I investigated the possibility of constraining gravity models using clusters taken from XCS-DR1. I performed a coordinate search to find all the XCS-DR1 clusters within the CFHTLenS footprint. I found 28 overlapping clusters with suitable data, and concluded that this sample was too small to measure competitive constraints from. It has been three years since the last XCS data release, XCS-DR1. There was therefore a good likelihood that additional observations had been made of the four CFHTLenS fields which had the potential to boost the cluster count. In order to increase the cluster sample, XMM exposures within the CFHTLenS footprint were re-analysed by the XCS team and me. Outlined below are the steps taken to do so.

All public X-ray observations from XMM were first obtained using pipelines developed for XCS. I then determined which of the XMM observations overlapped with the CFHTLenS fields. In Figure 4.7 the four CFHTLenS fields are shown in blue. The XMM exposures which overlap with the CFHTLenS footprint are shown in red. In total 497 overlapping XMM exposures were located, with the majority (380 exposures) of these present in the W1 field. This high density of XMM observations within the W1 field is because this field was specially targeted by as part of XXL.

Once the observations were located, the XCS team used their pipelines to carry out the following tasks in an automated manner (as described in Lloyd-Davies et al. 2011 and briefly reviewed here):

- Cleaning the event lists of background flares. It is well documented that XMM observations can suffer from enhanced backgrounds depending upon the satellite position and solar activity (Lumb et al., 2002). To increase the signal-to-noise, a lightcurve was generated for each observation, which was divided into 50 bins. The mean of the lightcurve was calculated and any bin that deviated by more than 3σ from the mean was removed. This process was then iterated until a stable state was found (or 50 iterations was reached).

- Creating detector and exposure images. Each event list, described above, was then spatially binned to create images in two bands, soft and hard (as described in Section

2.2.1). Exposure maps encoding vignetting, chip gaps and other effects were also generated. As the EPICs (described in Section 4.2.2) do not possess shutters, events received during readout of the observations are recorded. These are removed by subtracting them from the images before the images and exposure maps from each camera are combined into a single observation.

- Producing duplicate free source lists. Sources were found by XCS using the XCS Automated Pipeline Algorithm (`XAPA`). `XAPA` is based upon the source detection package `WavDetect` (Freeman et al., 2002) and works by first convolving images with a Mexican hat (Slezak et al., 1990) and then identifying pixels that are significantly above the background. `XAPA` then groups together collections of significant detections in sources to generate a source list.

- Identifying extended X-ray sources. The sources identified by `XAPA` were then classified as point-like or extended by comparing them with the Point Spread Function (PSF, a description of the camera's response to point sources). This was achieved using a series of Monte Carlo simulations to compare the source with various realisations of the PSF to establish the source's extent.

By carrying out this process a total of 348 extended XMM sources, with more than 100 background subtracted photon counts, were located in the CFHTLenS fields. However 44 of these were within a couple of arcminutes of the edge of the XMM field of view and were not considered further due to off axis effects being more pronounced. A cut-off limit of 100 photons was selected as this is the minimum photon count required to measure an X-ray temperature. Figure 4.8 shows the XCS measured X-ray temperature for four clusters as their number of source counts is reduced down to 100, demonstrating that reliable X-ray temperatures can be derived down to 100 counts (albeit with a greater uncertainty, Lloyd-Davies et al. 2011).

The majority of these extra sources were not included in the XCS first data release (XCS-DR1, Mehrtens et al. 2012). This meant that these new sources had to classified as clusters (as opposed to other X-ray sources such as AGN or galactic sources) before the sources could be used in the study. This process is non trivial: as shown in Mehrtens et al. 2012, a large fraction of XCS extended sources (especially those with fewer than 300 counts) are either hard to confirm as clusters – because the available imaging is not deep enough

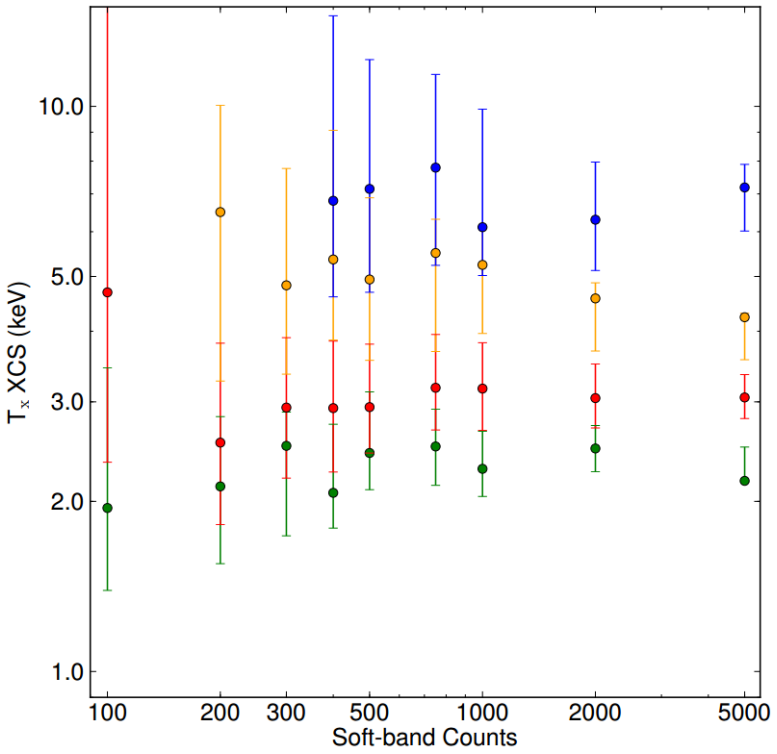

FIGURE 4.8: The XCS measured X-ray temperature against the number of source counts. Each colour represents a different cluster with > 5000 source counts. Figure from Lloyd-Davies et al. (2011). This figure shows that a cluster's measured X-ray temperature is largely invariant of its source count.

– or are associated with other types of X-ray source. Therefore, for this thesis, I have taken a conservative approach and only included XMM extended sources in the study if they correspond to an over density of galaxies in false colour images produced using the CFHTLenS cutout service[1]. This was achieved by combining a script with wget[2] to query CFHTLenS and find and download 3 arcminute by 3 arcminute false colour images centred around each cluster. Each of the 348 images were then loaded onto a web page for optical confirmation by myself and members of XCS. An example of this web page is shown in Figure 4.9, where it is clear to see when a cluster had no lensing data present (such as the two blank images, numbers 0 and 151).

One hundred and eighty six sources were excluded from the study as a result. These were excluded for several different reasons: there was no optical data as the cluster sat in a masked region of the CFHTLenS footprint; there was a bright star or galaxy lying close to the cluster centre that was obscuring it; the image contained poor photometry (usually when the composite image was missing an image in a given band, discolouring the image);

[1] http://www.cadc-ccda.hia-iha.nrc-cnrc.gc.ca/community/CFHTLens/cutout.html
[2] A software package designed to download files over HTTP, https://www.gnu.org/software/wget/.

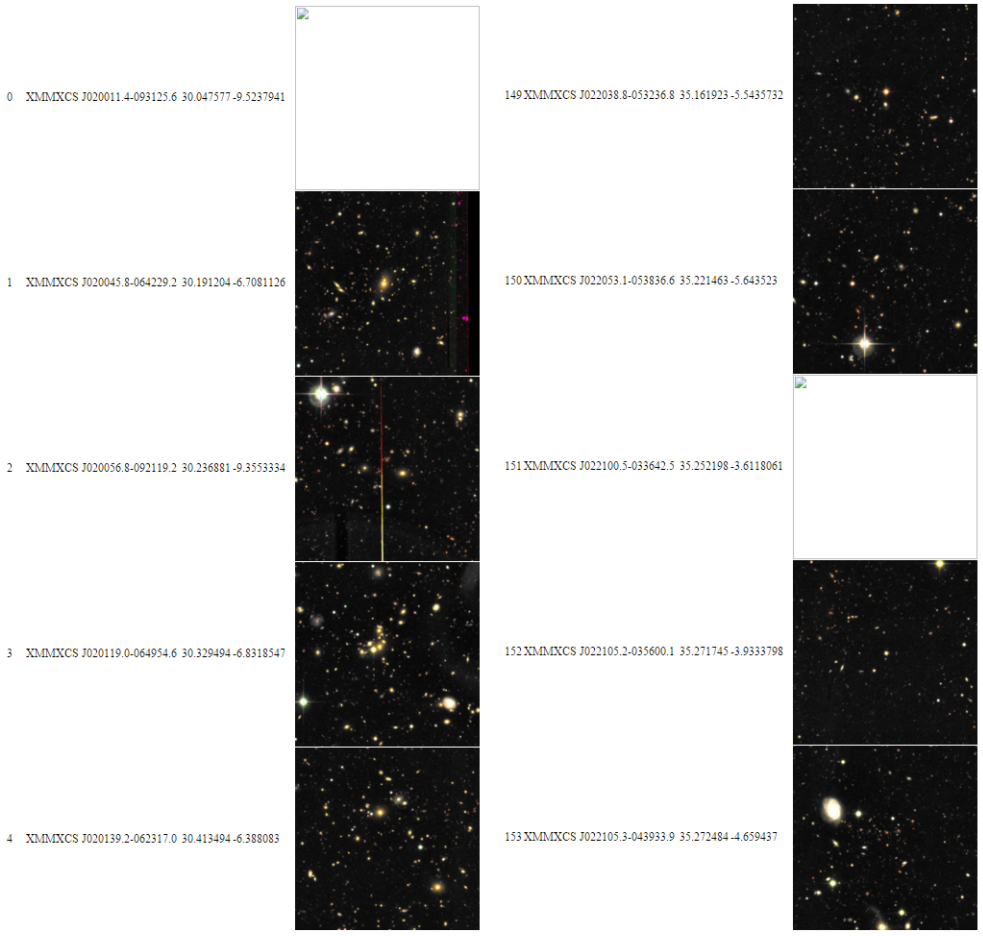

FIGURE 4.9: A screen capture of the web page used when visually identifying clusters for inclusion in the final sample. The two blank images are regions that are not covered by CFHTLenS due to masking. The images shown are $3'' \times 3''$ in area.

or the optical image resembled an AGN rather than a cluster. In the latter case an AGN was classified when, in the images centre, a bright, obvious optical point like source could be seen. Examples of these criteria can be seen in Figure 4.10. The coordinates of the remaining one hundred and nineteen can be found in Table A.1.

As the analysis required information about the distance to the cluster, a further 37 sources were excluded from the study because redshifts were not available at the time of writing. These are flagged with a 2 in Table A.1. The majority (71 of 82) of the redshifts came from the new Gaussian mixture model redshift estimator (GMPhoRCC) described in detail in Hood and Mann (2015). GMPhoRCC works under the assumption that both the redshift and colour distributions of cluster galaxies can be modelled by a mixture of Gaussians (Hao et al., 2010). For each cluster in turn, GMPhoRCC measures the overdensity of galaxies using photometric redshifts, compared to the background density inside conical bins. The bin that maximises the overdensity is then selected as the first guess cluster

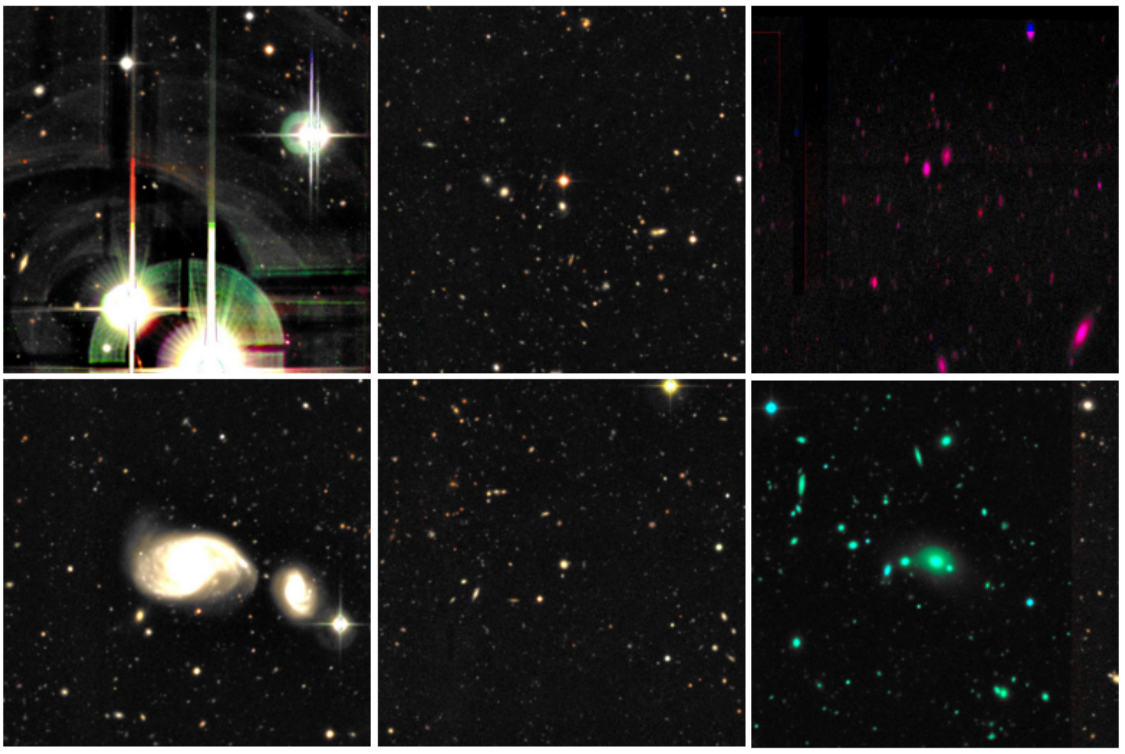

FIGURE 4.10: Examples of optically rejected images from CFHTLenS. The images on the left contain foreground containments, the central images are examples of central bright point source, appearing to be AGN and the rightmost images have bad photometry, in these two cases the images are missing exposures in at least one filter. The images shown here are $3'' \times 3''$ in area.

radius and a photometric redshift is measured. Next, using this redshift estimate, red sequence colour bands are measured, which help set the brightest cluster galaxy, and a new photometric redshift estimate is made from the red sequence.

I also used 8 redshifts taken from NED[3] (Valtchanov et al. 2004, Wen et al. 2010, Durret et al. 2011, Wen and Han 2011, Takey et al. 2013). To locate these redshifts I used the 'near position' search feature to find all extragalactic objects classified as galaxy clusters within $3''$ of the cluster positions.

The final 3 photometric redshifts were obtained from Ford et al. (2014), in which a 3D-Matched-Filter cluster finding algorithm was used (Milkeraitis et al., 2010). This technique involved creating likelihood maps of the CFHTLenS footprint and searching for significant density peaks in the galaxy density.

[3]The NASA/IPAC Extragalactic Database (NED) is operated by the Jet Propulsion Laboratory, California Institute of Technology, under contract with the National Aeronautics and Space Administration.

I judged the remaining 82 XMM extended sources in the CFHTLenS region to be confirmed clusters and the XCS team ran them through the XSPEC based XCS spectral pipeline. X-ray temperatures were determined when the signal to noise was sufficient for a temperature within the sensible parameter range with error bounds that could be fit (as described below). This produced X-ray temperatures of 58 of these clusters which formed my final sample, including 12 clusters new to the literature (I have discussed X-ray spectra in Section 2.2.2). The other 23 clusters were excluded from the analysis due to poor temperature fits and are flagged with a 3 in Table A.1.

The details of this pipeline can be found in Lloyd-Davies et al. 2011 and briefly reviewed below. First, each separate exposure of a candidate was located by matching objects from different observations that lie at the same position, as any candidate was likely to have been observed by each camera (MOS1, MOS2 and pn). Next each exposure is cleaned to remove unwanted X-ray artefacts, such as flares by following the method outlined above. These exposures were then used to generate a spectrum, using photons with energies between 0.3 keV and 7.9 keV. A large annulus was then placed around the cluster to measure the X-ray background for the purpose of background subtraction. In the case of multiple exposures of a candidate, multiple spectra were obtained.

The spectra measured for each cluster were then simultaneously fit by XCS via XSPEC using a maximum likelihood Cash statistic (Cash, 1979). The photons comprising each spectra were then binned, and four different models fit to the data. Each model included a hydrogen absorption component (WABS, Morrison and McCammon 1983) and a hot plasma component (MEKAL, Mewe et al. 1985). Using the best fitting of these models, a temperature and luminosity were measured for each candidate, providing they fall within a sensible parameter range (defined to be $0.3 < T_{\rm x} < 17$ keV). Uncertainty bounds were then found for each fit by moving off the best fit model until the 1σ confidence is reached to give both an upper and lower temperature bound.

The 58 clusters with measured temperatures span the redshift range $0.1 < z < 1.2$ (median $z = 0.33$) and temperature range $0.2 < T_{\rm x} < 8$ keV (median $T_{\rm x} = 2.3$ keV). Figure 4.11 shows the redshift and X-ray temperature range of the 58 clusters in the sample. A selection of optically confirmed clusters that were new to the literature, along with several clusters that were optically confirmed but excluded due to a lack of redshift, are shown in Figure 4.12.

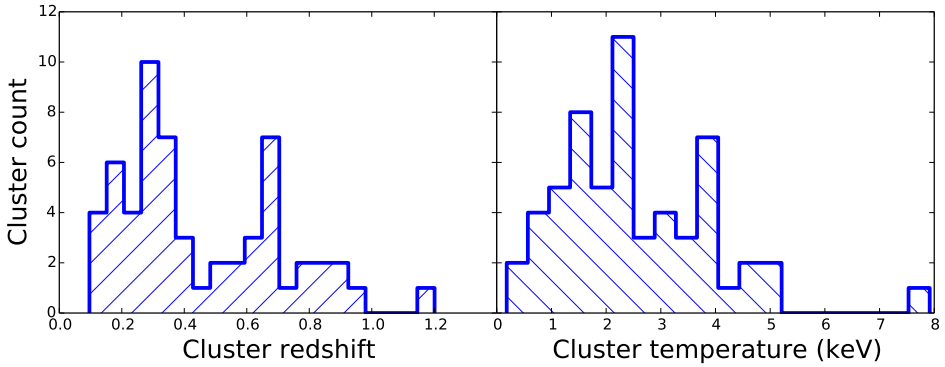

FIGURE 4.11: The redshift and X-ray temperature distributions for the sample of 58 galaxy clusters. This figures show that the sample described here was a large range in both redshift and temperature.

The final sample, as shown in Table A.1, shows a substantial increase in the number of clusters as compared to XCSDR1 (as described in Section 4.2.2) from 28 to 58. This large number of clusters will enable constraints to be put upon $f(R)$ gravity (following the method outlined in Chapter 1 and carried out in Chapter 5) that hopefully overcome the limitations of the measurements performed in Terukina et al. (2014), where just a single cluster was used (such as the limited lensing data available and the non-spherical nature of the Coma cluster, as discussed in Section 1.5.1).

Performing this test with multiple clusters should also allow for greater signal to noise at those radii where the fifth force is theorised to be strongest (i.e. outside the critical radius in the cluster outskirts, as discussed in Section 1.5). The cluster outskirts, however, will contain gas that is less dense than the cluster centres. While this is incredibly useful for probing the fifth force (as the chameleon screening is unsuppressed in low density regions, as discussed in Section 1.4.1) it does mean that the X-ray surface brightness signal is low (as surface brightness is proportional to gas density, as discussed in Section 2.2.2), as is the weak lensing signal (which once again is proportional to the matter density, as discussed in Section 2.2.5). Therefore if I were to measure profiles for individual clusters (as was done using a single cluster in Terukina et al. 2014), I would be limited to investigating a small number of large, very nearby clusters.

To overcome this issue I have stacked the clusters in my sample. By doing so I am be able to drastically improve the signal to noise at all radii of the measured profiles, especially in the cluster outskirts where it will be most beneficial. I describe the methods used to create these stacked profiles in the following sections.

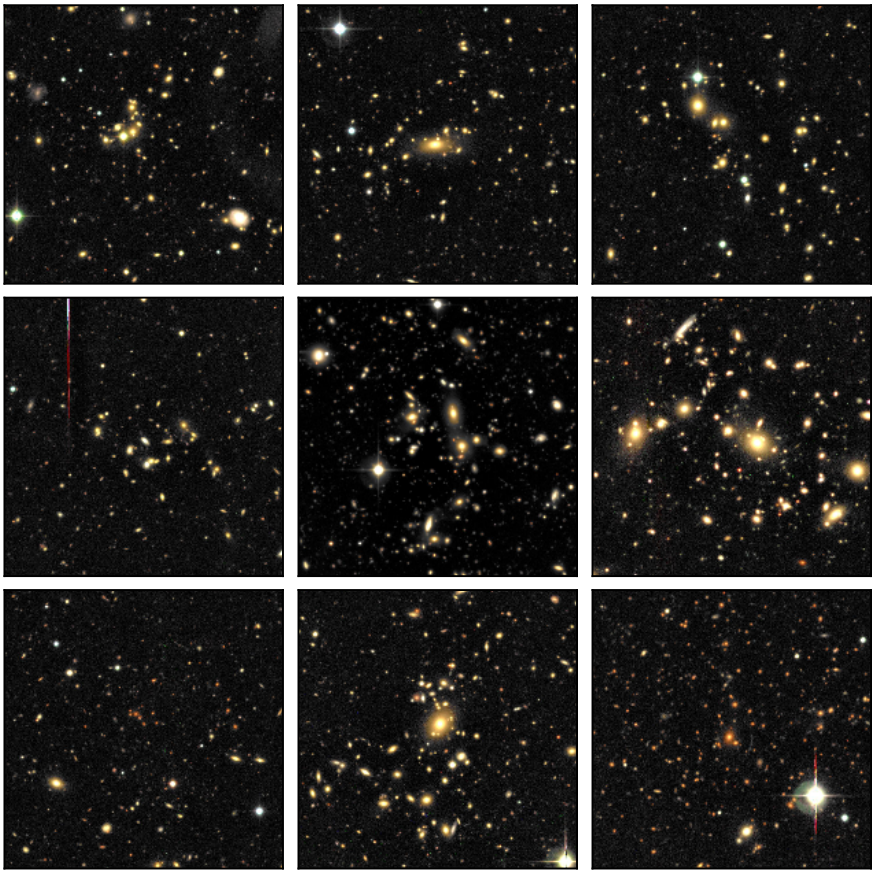

FIGURE 4.12: A selection of optically confirmed clusters as imaged by CFHTLenS. False colour composite images are $3' \times 3'$. From left to right and top to bottom, the compilation shows the clusters: XMMXCS J020119.0-064954.6 at z=0.33; XMMXCS J021226.8-053734.6 at z=0.31; XMMXCS J021527.9-053319.2 at z=0.28 (Wen and Han, 2011); XMMXCS J021843.7-053257.7 at z=0.40; XMMXCS J022433.8-041433.7 at z=0.39; and XMMXCS J023142.2-045253.1 at z=0.21. The redshifts shown here are from Hood and Mann (2015) unless otherwise indicated. These clusters are included in the sample, flagged either with a 0 or 1 in Table A.1. The remaining clusters in the compilation have no measured redshift or temperature and are flagged with a 2 or 3 in Table A.1. Bottom row these clusters are: XMMXCSJ021517.1-0.60432.8; XMMXCSJ022359.2-083543.4; and XMMXCSJ141446.9+544709.1.

4.3.2 Making stacked X-ray Surface Brightness Profiles

The analysis involved stacking multiple XMM observations of the 58 clusters, in order to build up signal-to-noise in the outer parts of the ensemble cluster profile. This process needed to account for the complexities associated with stacking multiple XMM observations of a given cluster: Most of the 58 clusters were covered by more than one XMM observation. Each of these observations had different background properties and flare corrected exposure times. As the X-ray telescope comprises three cameras that operate simultaneously (mos1, mos2, pn, as described in Section 4.2.2), most XMM observations comprise of three separate images with different, energy dependent sensitivities. The clusters all have different energy spectra, because, even if one ignores non-thermal processes, they have different X-ray temperatures, redshifts, and line of sight absorbing column densities. Therefore, for each cluster, I have used XSPEC to calculate camera specific count rate to Luminosity Conversion Factors (LCF) for each XMM observation that it falls in (Lloyd-Davies et al., 2011). I then, for a given cluster, take the photon count images generated by the XCS pipeline, divide these by the respective exposure map, and multiply by the cluster LCF. This allowed me to combine all the images for a cluster in a consistent manner.

To produce a single stack, I first needed to re-scale the 58 combined images of individual clusters to a standard projected size. For this I calulated M_{500}, the mass enclosed within a sphere at which the average density is 500 times the critical density (described by Equation 1.21), using the prescription described in Sahlén et al. (2009). This technique assumes that clusters follow the self-similarity prediction (Kaiser, 1986), with the redshift dependant relationship between X-ray temperature, T, and cluster mass, M_{500},

$$T \propto M_{500}^{2/3}[\Delta_{500}(z)E^2(z)]^{1/3}. \tag{4.1}$$

Here $\Delta_{500}(z)$ is the cluster's mean overdensity within r_{500}, with respect to the critical density. Assuming that the energy density of a flat universe is then dominated by non-relativistic matter and a cosmological constant,

$$E^2(z) = \Omega_m(1+z)^3 + \Omega_k(1+z)^2 + \Omega_\Lambda. \tag{4.2}$$

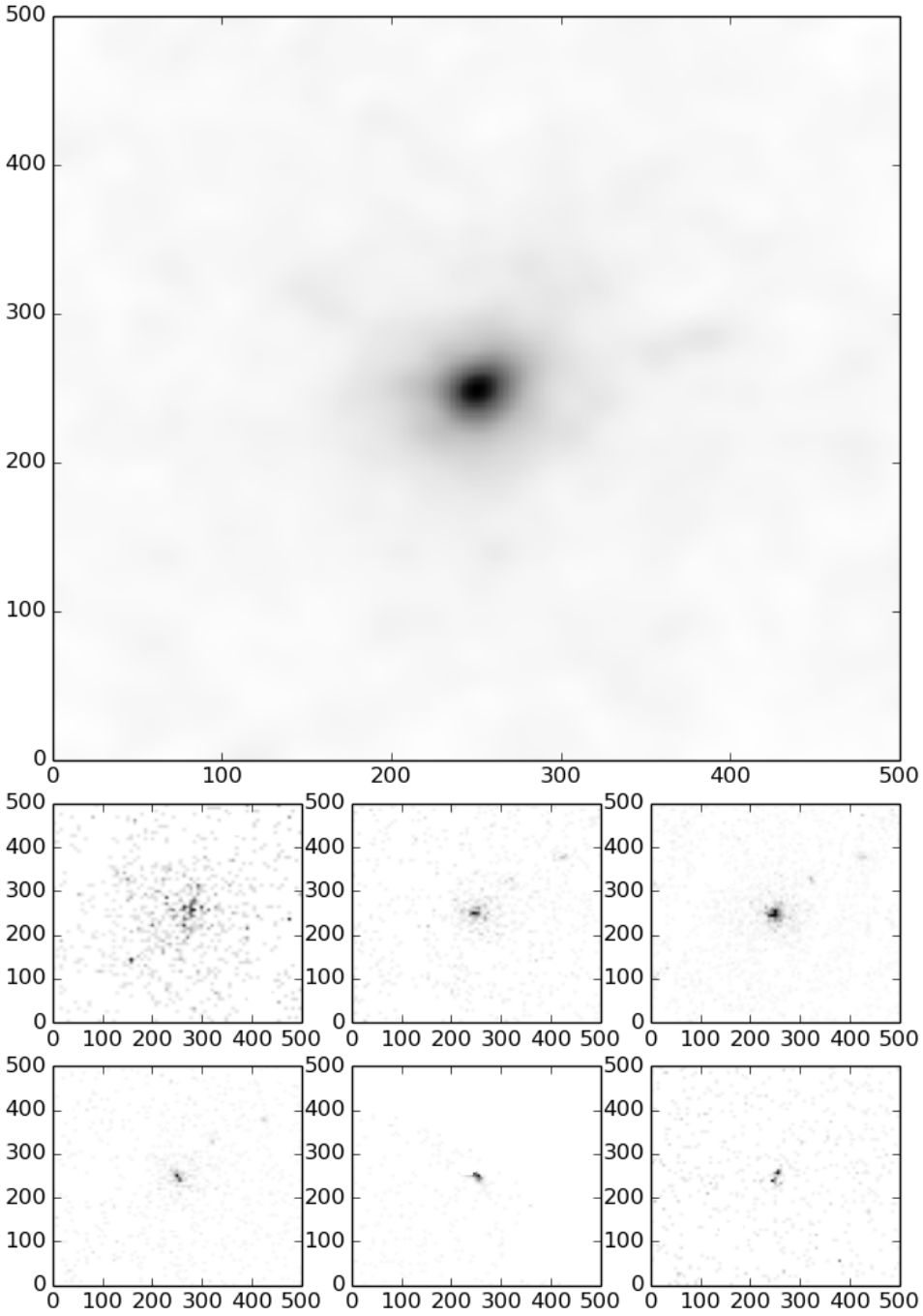

FIGURE 4.13: Stacked 2D surface brightness profile of 58 XCS clusters, made by taking the mean value of each pixel in the individual 2D surface brightnesses in the large top image. The 6 smaller images are a selection of 2D surface brightness profiles from individual clusters. In all these images darker colours indicate higher X-ray photon counts.

I then set the constant of proportionality to be $M_{500} = 3 \times 10^{14} h^{-1} \mathrm{M}_{\odot}$ at $z = 0.05$ for an X-ray temperature of 5 keV. This allows the local abundance of clusters to match that given by the HIFLUGCS catalogue (Reiprich and Böhringer, 2002). This normalisation of the $M - T$ relation also agrees with that derived from X-ray data in Arnaud (2005) and Vikhlinin et al. (2006). Here I have calculated M_{500} as opposed to M_{200} from which the radii are later obtained (below I discuss the conversion between mass estimates) as it is more common in the literature to investigate the mass temperature relation at this radius due to the greater signal to noise ratio, so the M_{500} scaling relation is potentially more robust.

A conversion between M_{500} and M_{200} was made following the formulae derived in Hu and Kravtsov (2003), where I assumed $c = 5$. This mass conversion inverts the NFW profile so that it can relate two different definitions of M_n to better than 1% accuracy at cluster scales. This is an accurate description of the typical density profiles in clusters (Arnaud, 2005). Kettula et al. (2015) measured the lensing signal around 12 X-ray selected galaxy clusters within the CFHTLenS footprint and fit to each profile a best fit NFW. The concentration parameters of each of these clusters were found to lie between 5 and 6, so the assumption made above is consistent with these findings for a similar cluster sample.

Using the M_{200} (Equation 2.4) values, I calculated the radius at which the average density is two hundred times the critical density, r_{200}. The 58 stacked images could then be rescaled using linear interpolation to a common 500 by 500 pixel format, so that they each had an r_{200} radius of 125 pixels. Each of these 500 by 500 images were centred on the source centroid as determined by XCS.

For each individual cluster the surface brightness was binned into 19 equal spaced logarithmic annuli out to a distance of $1.2 \times r_{200}$. The maximum surface brightness was then located for each of these profiles and the mean value of these maximums, $\overline{SB}_{max}$, calculated (it was found that using the median value instead of the mean gave similar results). Then using $\overline{SB}_{max}$ each individual surface brightness profile was rescaled so the original maximum surface brightness became the average maximum, with the data in each other bin scaled accordingly. This was done as adding clusters over a range of different masses and luminosities would result in significant off-diagonal elements in the covariance matrix of the final stacked profile.

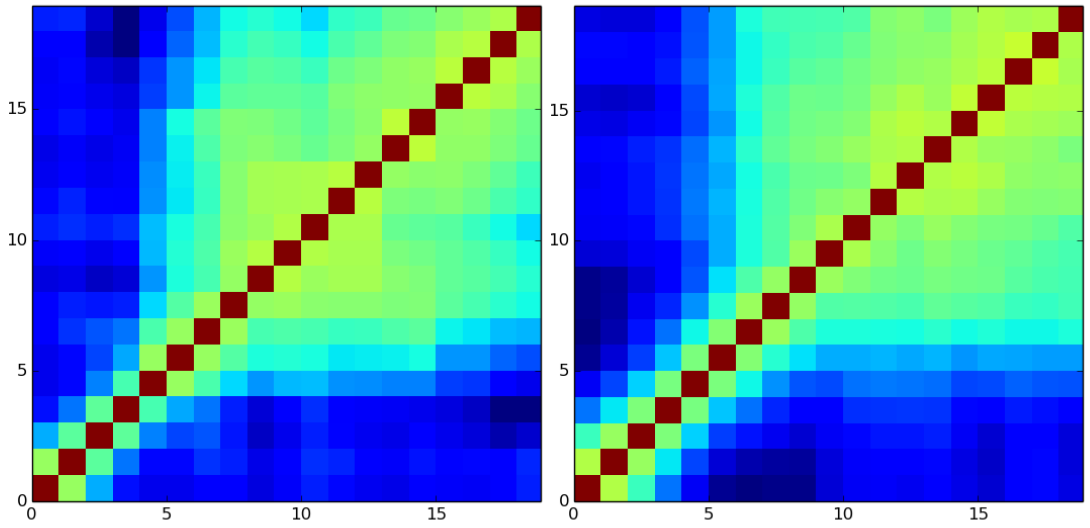

(A) 1a (B) 1b

FIGURE 4.14: Normalised covariance matrix of the X-ray surface brightness profiles from the clusters comprising the stack with $T > 2.5$keV (1a) and $T < 2.5$keV (1b). Along both the x-axis and y-axis is each X-ray bin. This plot therefore shows how correlated the ith and jth X-ray temperature bins are. As each bin is perfectly correlated with itself, the diagonal has a value of 1. The bluer the pixel the less correlated the two bins are.

The covariance here is a measure of how changes in one surface brightness bin affect the values in the other surface brightness bins. The covariance matrix is a visualisation of this and shows how a change in the ith bin affects the jth bin. A red diagonal line was expected, as each bin is perfectly correlated with itself. In an ideal case the rest of the matrix would be blue, indicating that there were no covariances between bins. In reality this is never achieved due to effects such as the telescope point spread function which blurs out the image. The covariance matrix is calculated from

$$C_{i,j} = \frac{1}{n}\sum(x_i - \bar{x})(y_j - \bar{y}), \tag{4.3}$$

where n is the number of bins, x_i and y_j are the surface brightnesses in a given bin for a given profile and $\bar{x}$ and $\bar{y}$ are the average surface brightnesses in those given bins across all profiles.

A final stacked surface brightness map of the 58 individual clusters was then produced by taking the mean value for each pixel across all these maps. The resulting stack can be seen in Figure 4.13.

This re-scaling of the amplitudes is permitted as the constraints on modified gravity parameters focus on the shape of the cluster profiles (as discussed in Section 1.5); I marginalise over the amplitudes of the stacked X-ray surface brightness profiles in Chapter 5. The error covariance matrix of the stacked profile was then measured directly and in Figure 4.14 I show the normalised covariance matrix, where redder areas indicate higher covariance (the reason for the presence of two plots is explained in Section 4.3.4). These two plots also show some off diagonal covariances. Those near the diagonal are likely to be caused by the PSF, while those further from the diagonal may indicate a choice of bins that is too narrow, such that gas in one bin has a strong interaction with that in neighbouring bins. It should be noted however that these aren't overly strong covariances, with a maximum correlation of around 25%.

To generate the final profile, the surface brightness was binned into 19 equal spaced logarithmic annuli out to a distance of $1.2 \times r_{200}$.

4.3.3 Making Stacked Weak Lensing Profiles

I outline here the procedure used to obtain the stacked cluster shear profile, γ_t, using source galaxies from CFHTLenS. The CFHTLenS catalogue provided measurements of both ellipticity components (e_1 and e_2) and photometric redshifts for each source galaxy. Before shears could be derived from these quantities, small multiplicative and additive corrections (m and c_2) were applied. Such corrections are now commonly applied to weak lensing data (Wittman et al. 2006, Massey et al. 2013, Jarvis et al. 2015, Liu et al. 2016). These corrections are required due to biases that arise in the shape measurement pipelines because of inaccurate performance of the measurement methods. The corrections are calibrated empirically from the CFHTLenS data (Miller et al., 2013) by taking the true galaxy shapes from simulations and comparing these to the shapes measured by the pipelines. These two corrections, c_2 and m, could then be calculated for each galaxy as a function of size and signal to noise:

$$c_2 = \max\left(\frac{F log_{10}(\nu_{SN}) - G}{1 + (\frac{r}{r_0})^H}, 0\right), \tag{4.4}$$

$$m = \frac{\beta}{log(\nu_{SN})} e^{-r\alpha\nu_{SN}} \tag{4.5}$$

where ν_{SN} and r are the signal to noise ratio and the size of each galaxy respectively and α, β, F, G, H and r_0 are described in Heymans et al. (2012). Each galaxy was weighted with the CFHTLenS catalogue WEIGHT parameter (described in Equation 4.8) and these corrective values applied to each galaxy by

$$e_{\mathrm{int,i}} = \frac{e_{\mathrm{i}} - c_{2,\mathrm{i}}}{1 + \bar{m}}, \tag{4.6}$$

where c_2 was applied on a galaxy by galaxy basis and $\bar{m}$ is a summation of $1+m$ for each galaxy, applied as an ensemble average to each radial bin (discussed below).

In order to minimise the contamination between the lensed galaxies and the cluster members, only source galaxies with a photometric redshift greater than $z_{\mathrm{cluster}} + 0.2$ were used. The redshift cut was made so that there is negligible contamination between cluster and source galaxies. This approach is consistent with others in the literature, such as Kettula et al. (2015), Applegate et al. (2014) and Battaglia et al. (2015). The photo-z cut did not require a redshift dependence as the photo-z errors of the source galaxies in CFHTLenS were approximately flat close to the redshift of the clusters (Hildebrandt et al., 2012). This can be seen in Figure 4.2, which shows the photo-z error as a function of redshift for all galaxies in CFHTLenS and can be seen to only vary by $\sim 1\%$.

This gave an effective galaxy density, n_{eff}, (Heymans et al., 2012) of 12 galaxies per square arcminute given by

$$n_{\mathrm{eff}} = \frac{1}{\Omega} \frac{(\sum w_i)^2}{\sum w_i^2}, \tag{4.7}$$

where Ω is the total survey area and w_i represents the weights of the galaxies within the survey. The weights used here were provided by CFHTLenS and were defined by (Miller et al., 2013)

$$w = \left(\frac{\sigma_e^2 e_{max}^2}{e_{max}^2 - 2\sigma_e^2} + \sigma_{pop}^2 \right)^{-1}, \tag{4.8}$$

where σ_e is the error of a galaxy's shape, e_{max} is the maximum allowed ellipticity and σ_{pop} is the average error on a galaxy's shape across the whole population.

For each galaxy I calculated the tangential and cross shears (γ_t, γ_x) as a function of their position relative to the cluster position, via the angle ϕ between the cluster's X-ray centroid and galaxy from a baseline of zero declination using

$$\gamma_t = -[\gamma_1 \cos(2\phi) + \gamma_2 \sin(2\phi)], \tag{4.9}$$

$$\gamma_x = -\gamma_1 \sin(2\phi) + \gamma_2 \cos(2\phi). \tag{4.10}$$

The tangential shear is a measure of the orientation of lensed ellipticity of a source galaxy that is exactly tangential to the centre of the lensing mass. The cross shear is similarly defined but at 45° to the tangential shear. The tangential shear is the quantity in which I was interested as it is a measurement of the lensing signal. The cross shear should average out to 0 around a given point, so is a useful measurement to make to test the errors in a lensing measurement.

The tangential shear measured around each XCS determined cluster centroid was binned into 24 equal spaced logarithmic annuli out to a distance of $10 \times r_{200}$ (calculated in Section 4.3.2). The value in each bin was then re-scaled using the same mean used previously to scale the X-ray profiles in Section 4.3.2 to ensure consistency with the X-ray profiles.

Finally, in order to improve the signal to noise of the tangential profiles, the 58 individual cluster profiles were stacked. This was achieved by summing the shear profiles of each cluster and calculating an average shear in each bin across all clusters. Stacking the lensing signal in this way was first used in Sheldon et al. (2001), where 42 clusters were stacked to obtain a higher signal to noise measurement. Since this first instance, stacking clusters to boost the measurable lensing signal has become popular. In McKay et al. (2001) and Sheldon et al. (2009) tens of thousands of objects are stacked to measure a high signal lensing signal. This was achieved by centring on each lens in turn, then summing up the tangential shear (calculated as described above) for each galaxy in radial bins, so a shear measurement is recorded for every galaxy that is a set distance from any lens. The average tangential shear in each bin was then calculated and taken as the average shear value for all the lenses. It is the approach of that Sheldon et al. (2009) that is adopted in this thesis.

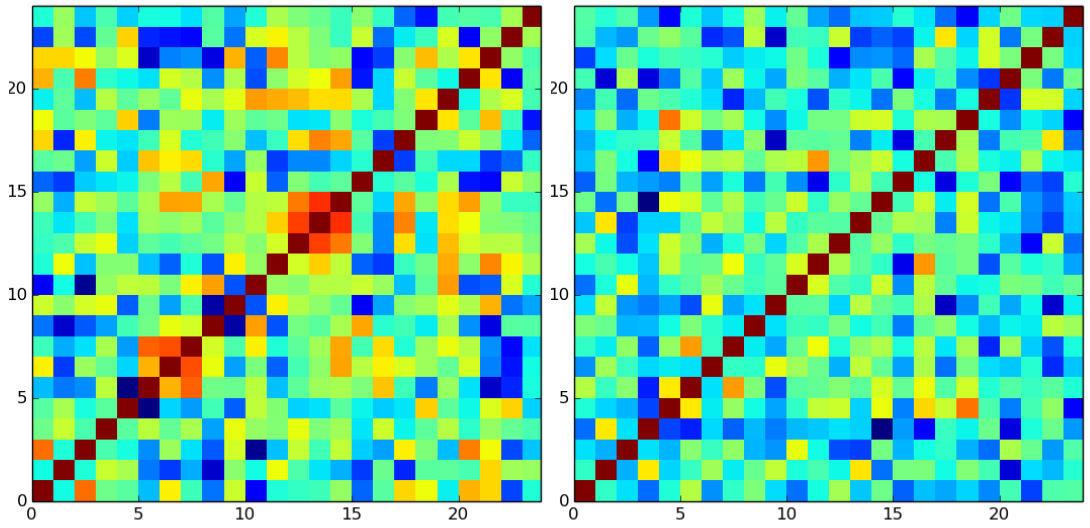

(A) 1a (B) 1b

FIGURE 4.15: Normalised covariance matrix of the weak lensing measurements from the clusters comprising the stack with $T > 2.5$keV (1a) and $T < 2.5$keV (1b). Once again along the x-axis and y-axis is each X-ray bin, showing how correlated the *ith* and *jth* X-ray temperature bins are. As each bin is perfectly correlated with itself, the diagonal has a value of 1. The bluer the pixel the less correlated the two bins are.

The error covariance matrix was then directly measured for the stacked profile (and calculated from Equation 4.3): it is shown in Figure 4.15. Due to the large uncertainty in the central bin, driven by the low number density of galaxies, I exclude the central $0.1 \times r_{200}$.

I performed consistency and null tests on the CFHTLenS shape data to ensure the recovered profiles were unbiased and not artefacts of the data. Figure 4.16a shows the tangential signal (the tangential alignment of sources around the lens is the signal of interest, in solid blue) and the cross shear (the shear signal at 45° to the tangential shear, in dashed red) around the stacked clusters. The tangential shear signal has a detection significance of $> 30\sigma$, while the cross shear signal is consistent with zero at all radii. The tangential shear here is a measurement of the matter within each radial bin. As this profile was centred upon a stack of clusters, known to contain large amounts of matter, a strong tangential shear measurement, such as the one seen, is validation of the shear measurements. Conversely the cross shear is a proxy for any noise or bias in the tangential shear measurement. As it is consistent with zero, I concluded that the shear measurement does not suffer from any significant biases.

Figure 4.16b shows the tangential shear (solid blue) and cross shear (dashed red) around

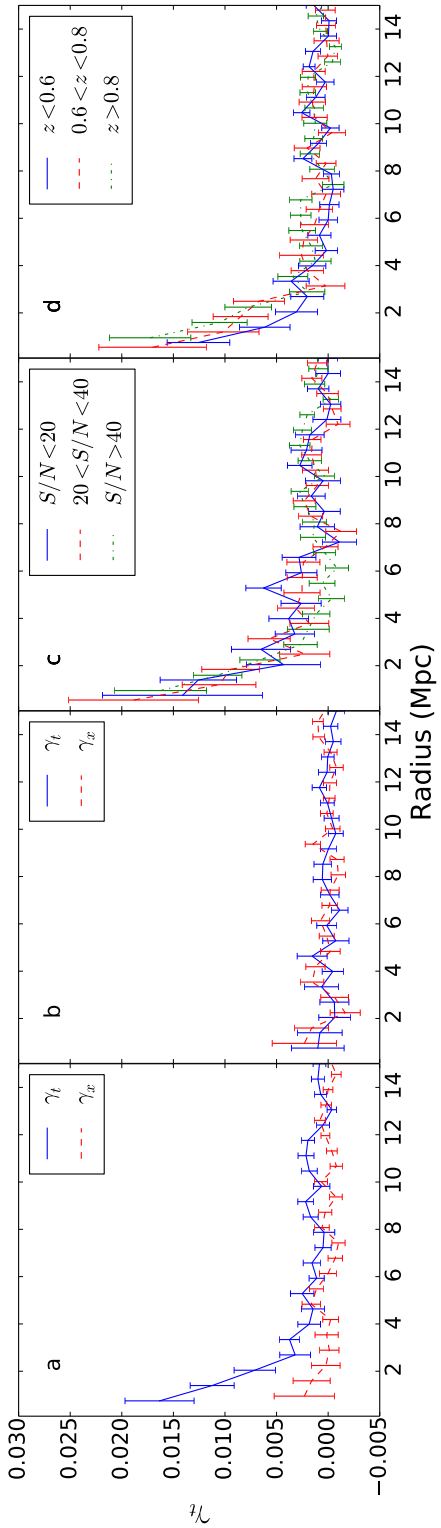

FIGURE 4.16: Tests around the 58 CFHTLenS stacked cluster; details are provided in Section 4.3.3. 1a: Tangential and cross shear. 1b: Tangential and cross shear around 58 stacked random points. 1c: Tangential shear for three different signal to noise bins. 1d: Tangential shear for three different redshift cuts. These tests show that are sample is unbiased.

58 random stacked positions within the overlap of the CFHTLenS region and the XCS footprint. The measurements in both these cases were found to be consistent with zero on all scales. If a random position was selected from among the CFHTLenS data, it was equally likely that the selected position will sit in an underdensity as it was to be located within an overdensity.

As tangential shear probes the projected density, any random selected position is as likely to be in an underdensity (with a negative shear) as it is in an overdensity (with a positive shear). These underdensities should average out any overdensities when enough random positions are stacked, producing no tangential shear signal, as seen in Figure 4.16b. As explained above, the cross shear is a measure of any noise or bias in the tangential shear, so its consistency with zero is further validation of the measurements.

For Figure 4.16c I show the tangential shear around the stacked clusters after I split the source galaxies into three bins based upon their signal-to-noise ratio, $S/N < 20$, $20 < S/N < 40$, and $S/N > 40$, with similar redshift distributions (median redshifts of 0.85, 0.82, 0.79 respectively). The S/N here was taken from CFHTLenS and is a function of the source photon counts over the background photon counts. I found that the three measurements are consistent with each other as predicted by lensing theory (described in Section 2.2.3), as the lensing signal is dependent on the galaxy shape, not on the noise of the signal.

Figure 4.16d shows the tangential shear around the stacked clusters, with the source galaxies cut into three bins based on their photometric redshift, $z < 0.6$, $0.6 < z < 0.8$ and $z > 0.8$. At higher redshifts there is a smaller fraction of cluster galaxies and galaxies in front of the clusters, and the weak lensing signal grows with redshift. I see these effects as the measured signal is strongest in the high redshift bin. I therefore conclude that I am detecting a genuine weak lensing signal.

4.3.4 Binning in X-ray Temperature

One of the largest sources of systematic error within the measurements presented in Chapter 5 came from the mixing of clusters of varying sizes and masses. To try to minimise this effect and generate tighter constraints on the modified gravity parameters the dataset was binned by X-ray temperature. A cluster's X-ray temperature is directly proportional

to its mass (as described by Equation 4.1), so by binning in X-ray temperature the sample was also split by mass. To begin with the sample was cut at an X-ray temperature of $T = 2.5$keV, to give two bins of mass which had profiles with approximately equivalent signal-to-noise ratios. I note that this temperature cut approximately splits the sample into galaxy clusters and galaxy groups (Stott et al., 2012).

Constraints upon the modified gravity parameters were then obtained using the whole sample and again in the two bin case by following the method outline in Chapter 5. It was found that the constraints on the modified gravity were improved by $\sim 25\%$ upon the single bin case by using two temperature bins. The whole cluster sample was then split into three and four temperature bins and the analyses of Chapter 5 repeated. In the three bin case, no improvement upon the modified gravity parameter constraints was found over the two bin case. In the four bin case, the measured constraints were found to have less constraining power on the modified gravity parameters than the two bin case. With each extra binning the signal to noise of the measured profiles dropped, indicating that there is a trade-off to be made between reducing the systematic error caused by mixing clusters and increasing the other noise caused by the low number of clusters present in each bin.

To aid with computation, the analysis presented in Chapter 5 is completed with the simplest two bin case. The low temperature bin ($T < 2.5$keV) then had a median redshift of $z = 0.32$ and is flagged with a 0 in Table A.1, while the other bin (with $T > 2.5$keV) had a median redshift of $z = 0.34$ and a flag of 1.

In Table 4.2 I show the values for the X-ray surface brightness and weak lensing profiles against radius in the two temperature bins that are used to constrain gravity in Chapter 5.

4.4 Summary

In this chapter I have constructed a sample of 58 X-ray selected galaxy clusters. I have done so by re-examining the overlapping exposures between XCS and CFHTLenS. Optical counterparts were then obtained for each cluster and checks made to ensure suitability within the catalogue.

	Radius (Mpc)	T > 2.5keV ($\times 10^{-5}$)	T < 2.5keV ($\times 10^{-5}$)
X-ray Surface Brightness	0.017	6.1 ± 0.4	3.8 ± 0.2
	0.022	5.6 ± 0.38	3.7 ± 0.2
	0.030	5 ± 0.37	3.5 ± 0.19
	0.038	4.1 ± 0.33	3.3 ± 0.19
	0.047	2.9 ± 0.29	3 ± 0.18
	0.063	2.1 ± 0.26	2.6 ± 0.17
	0.080	1.6 ± 0.23	2.3 ± 0.16
	0.111	1.1 ± 0.2	1.9 ± 0.15
	0.135	0.65 ± 0.18	1.4 ± 0.14
	0.186	0.52 ± 0.17	1.2 ± 0.13
	0.231	0.37 ± 0.16	0.9 ± 0.12
	0.294	0.38 ± 0.16	0.69 ± 0.11
	0.391	0.2 ± 0.15	0.43 ± 0.1
	0.532	0.17 ± 0.14	0.28 ± 0.099
	0.689	0.13 ± 0.13	0.23 ± 0.095
	0.919	0.085 ± 0.085	0.2 ± 0.086
	1.163	0.038 ± 0.038	0.026 ± 0.026
	Radius (Mpc)	T > 2.5keV ($\times 10^{-2}$)	T < 2.5keV ($\times 10^{-2}$)
Weak Lensing	0.10	5.7 ± 3.7	7.9 ± 4
	0.12	3.2 ± 3.2	12 ± 5.6
	0.15	6.6 ± 3.4	1.1 ± 1.1
	0.19	2.7 ± 2.5	0.89 ± 0.89
	0.24	1.8 ± 1.8	4.4 ± 2.2
	0.30	3.9 ± 2.8	6.7 ± 1.6
	0.37	2.9 ± 1.8	2.9 ± 1.6
	0.46	2.6 ± 2.4	3.8 ± 1.4
	0.57	3.1 ± 1.7	2.4 ± 0.9
	0.71	1.5 ± 1.2	0.62 ± 0.62
	0.88	1.2 ± 0.83	1.2 ± 0.76
	1.10	1.1 ± 0.57	0.94 ± 0.59
	1.37	1.9 ± 0.41	1.1 ± 0.41
	1.70	1.5 ± 0.39	0.99 ± 0.26
	2.11	1 ± 0.39	1.2 ± 0.39
	2.63	0.038 ± 0.038	0.78 ± 0.27
	3.26	0.47 ± 0.21	0.78 ± 0.22
	4.06	0.46 ± 0.19	0.031 ± 0.031
	5.05	0.033 ± 0.033	0.47 ± 0.15
	6.28	0.36 ± 0.14	0.32 ± 0.11
	7.80	0.18 ± 0.14	0.002 ± 0.002
	9.70	0.08 ± 0.08	0.16 ± 0.093
	12.06	0.021 ± 0.021	0.12 ± 0.087
	15.00	0.044 ± 0.044	0.082 ± 0.077

TABLE 4.2: The values of the X-ray surface brightness and weak lensing against radius in two temperature bins for the profiles generated in Chapter 4 and used in Chapter 5.

A redshift was then measured for each cluster, preferably from a Gaussian mixture technique, but also from secondary sources when this was unavailable. These redshifts were then used to measure X-ray temperatures for each cluster, with the final catalogue shown in Table A.1.

Each temperature was then used to estimate the associated cluster's virial radius so each cluster could be rescaled to a common image size. I continued by stacking the X-ray observations, making sure to correct for the differing backgrounds and observation times. From this image a stacked surface brightness profile was then produced. Errors were then measured for this profile using the error covariance matrix.

Using galaxies from CFHTLenS I then measured the tangential shear around each cluster, ensuring to apply the proper corrections and scalings. Stacking these galaxies I then produced a shear profile and its associated error. Performing several tests on the CFHTLenS data I conclude that the shear profile is the genuine article.

I ended by discussing the benefits of binning the sample by temperature.

Chapter 5

Constraining $f(R)$ using CFHTLenS and XCS

5.1 Overview

This chapter discusses the gravity constraints published in Wilcox et al. (2015).

The technique of using cluster profiles as a test of gravity has been attempted before using a single, nearby cluster (Coma, $z = 0.02$, Terukina et al. 2014 as described in Section 1.5.1) and extensively tested in Chapter 3. Here I apply the technique to the stacked profiles of 58 clusters from Chapter 4, which sit at higher redshifts ($0.1 < z < 1.2$), including that are 12 new to the literature, described in the previous chapter.

In the previous chapter I created a sample of X-ray selected galaxy clusters, and from these, measured stacked X-ray surface brightness and shear profiles in two X-ray temperature bins. In this chapter I have fit modified gravity models to these four profiles, using a multi-parameter MCMC. I achieved this by minimising a χ^2 function and obtaining constraints on the chameleon gravity parameters.

I then considered the implications this result has on $f(R)$ gravity models and calculated the time evolution of this constraint.

I continue by discussing the cluster environment, before moving on to test the assumption of hydrostatic equilibrium. This was done by comparing the mass distribution inferred from the surface brightness with and without additional components.

5.2 MCMC Analysis

The constraining power demonstrated in Terukina et al. (2014) arose from the subtle tension between the lensing and hydrostatic profiles (as discussed in Section 1.5). Using the four stacked cluster profiles (both weak lensing and X-ray surface brightness in the two temperature bins) constructed in the previous chapter (see Sections 4.3.2 and 4.3.3) I used Monte-Carlo Markov-Chains (MCMC, Gilks et al. 1996) to fit modified gravity models by using the *emcee* code (Foreman-Mackey et al., 2013). MCMC codes use a random walk through the parameter space using a step size and direction defined by an algorithim, such as a Metropolis-Hastings algorithm (Metropolis et al. 1953, Hastings 1970), which is used in this work.

The Metropolis-Hastings algorithm works by beginning at an arbitrary position in parameter space, x_t, then selects a trial point, x'. This trial point is selected from a proposed probability distribution function, $q(x'|x_t)$. The probability that the trail point is accepted is then given by

$$\alpha = \frac{p(\theta')}{p(\theta_t)}, \tag{5.1}$$

where θ' is stated at the trial point x', θ_t the state at the iteration t, $p(\theta')$ is the probability at the trial point x' and $p(\theta_t)$ is the probability at the iteration t. If the new position, x', has a higher probability than the initial point, x_t (that is $\alpha > 1$) then the new position is accepted. If however it has a lower probability ($\alpha < 1$), then the new position is accepted with a probability α. This process is repeated until the parameter space has been sufficiently sampled.

When running the MCMC, I allowed all parameters that depended upon the cluster properties to vary for each temperature bin. This led to a total of fourteen free parameters for the four stacked profiles (the measured weak lensing and X-ray profiles in two temperature bins) used to constrain modified gravity. Four of these parameters were used to model the weak lensing mass (defined in Equations 2.1,2.2,2.3, 2.4, describing the NFW profile which models the clusters lensing profile). I introduce the notation I, II to indicate the temperature bins $T < 2.5, T > 2.5$ respectively so c^{I}, c^{II}, M_{200}^{I} and M_{200}^{II} are the concentration and mass parameters for each temperature bin respectively.

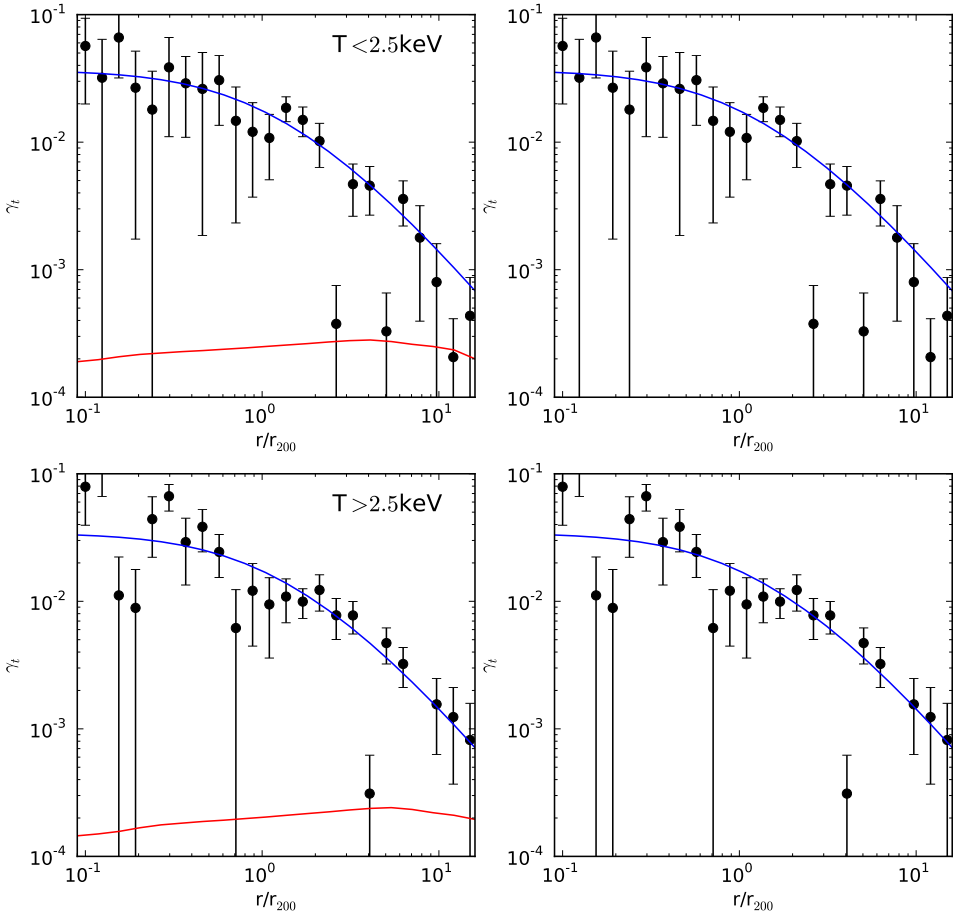

FIGURE 5.1: The best fit model to the shear data with the inclusion of the 2-halo term (left) and with the exclusion of the 2-halo term (right) for the two bins of X-ray temperature: $T < 2.5$keV (top) and $T > 2.5$keV (bottom), against radial distance normalised by r_{200} as black points. Shown in blue is the best fit comprised of both the 1-halo and 2-halo terms and in red the 2-halo component is shown.

To see if the accuracy of the fits to the shear data could be improved, I performed a test fit to the shear data with and without the 2-halo term (discussed in Section 2.2.5). Using both shear profiles independently, I used an MCMC to firstly fit Equation 2.42 (the NFW profile decribing the matter distribution) to the data, using the parameters described in the above paragraph, using a variation of the goodness of fit described in Section 5.2.1. I then repeated the MCMC fitting with the inclusion of the 2-halo term as described in Equation 2.46 (this included the summation of the 1 and 2-halo terms), using the same parameters as before, now with the additional parameter b_h - characterising the 2-halo term. I ran the MCMC with 2000 time steps and removed the first 200 as a 'burn in' phase.

Figure 5.1 shows the results of the four fits, for the two temperature binned profiles, both with and without a 2-halo term. The best fit, shown in blue, is the summation of the 1-halo component and the 2-halo component (It is of note that the best-fit model has an amplitude of the 2-halo term that is consistent with zero, and hence overlaps the 1-halo term). Shown in red is the contribution from the 2-halo term. I found that including the 2-halo term in the fits offered no improvement. Consequently I decided to just use the 1-halo term when fitting for modified gravity to aid computation and reduce the number of free parameters.

I modelled the X-ray surface brightness, using the method described in Section 2.2.2, and specifically Equation 2.20 (the hydrostatic equation in chameleon gravity), by defining, for both temperature bins, the electron number density (itself dependent upon $n_0^{\rm I}$, $n_0^{\rm II}$, $b_1^{\rm I}$, $b_1^{\rm II}$, $r_1^{\rm I}$ and $r_1^{\rm II}$) shown in Equation 2.5, and the normalisation of the gas temperature $T_0^{\rm I}$ and $T_0^{\rm II}$. I reconfigure the chameleon gravity parameters (described in Section 1.4.1) $\beta_2 = \beta/(1+\beta)$ and $\phi_{\infty,2} = 1-\exp(-\phi_\infty/10^{-4}M_{\rm Pl})$ to span the parameter range of β and ϕ_∞ in the interval [0,1].

To obtain the cooling function (a relation of the total amount of energy emitted per volume of the intracluster medium and described in Equation 2.16), I used the XSPEC software (as discussed in Section 4.3.1, Arnaud 1996) and utilised the APEC model (Smith et al., 2001) over a range of 0.5keV to 2keV, i.e. the same energy range as the observations from XMM. This model had as inputs, the gas temperature, the cluster redshift, the cluster metallicity and a normalisation, and provided the X-ray cluster flux. I adopted a metallicity $Z = 0.3Z_\odot$ throughout, found to be the average metallicity of 106 clusters in White (2000) and therefore a suitable average for the sample. Using this model I generated fluxes for a range of temperatures, (from 0.1keV to 20keV) which were interpolated for use in our chameleon gravity model.

The chameleon parameters β_2 and $\phi_{\infty,2}$ (as described in Section 1.4.1) were the same across the two bins, as the modifications to gravity should be independent of the cluster's mass (described in Section 1.4.1).

I performed an MCMC analysis using the *emcee* code. I minimized the goodness of fit using a χ^2 statistic derived from joint fitting of both models (see Section 5.2.1). The MCMC run was a parallelised implementation using 128 walkers with 10000 time steps. I removed the first 2000 iterations as a 'burn in' phase.

5.2.1 Goodness of fit

To characterise the goodness of fit of the profiles I adopted the following χ^2 statistic

$$\chi^2(T_0^{\rm I}, n_0^{\rm I}, b_1^{\rm I}, r_1^{\rm I}, M_{200}^{\rm I}, c^{\rm I}, T_0^{\rm II}, n_0^{\rm II}, b_1^{\rm II}, r_1^{\rm II}, M_{200}^{\rm II}, c^{\rm II}, \beta_2, \phi_{\infty,2}) = {\chi_{\rm WL}^{\rm I}}^2 + {\chi_{\rm WL}^{\rm II}}^2 + {\chi_{\rm SB}^{\rm I}}^2 + {\chi_{\rm SB}^{\rm II}}^2, \tag{5.2}$$

where I adopted the notation I, II to indicate the temperature bins $T < 2.5, T > 2.5$ respectively, and

$${\chi_{\rm WL}^{\rm I}}^2 = \sum_i \frac{(\gamma(r_{\perp,\rm i}^{\rm I}) - \gamma_{\rm i}^{\rm obs,I})^2}{(\sigma\gamma_{\rm i}^{\rm obs,I})^2}, \tag{5.3}$$

$${\chi_{\rm WL}^{\rm II}}^2 = \sum_i \frac{(\gamma(r_{\perp,\rm i}^{\rm II}) - \gamma_{\rm i}^{\rm obs,II})^2}{(\sigma\gamma_{\rm i}^{\rm obs,II})^2}, \tag{5.4}$$

$${\chi_{\rm SB}^{\rm I}}^2 = \sum_{i,j} (S_{\rm B}(r_{\perp,\rm i}^{\rm I}) - S_{\rm B,i}^{\rm obs,I}) C_{i,j}^{-1} (S_{\rm B}(r_{\perp,\rm j}^{\rm I}) - S_{\rm B,j}^{\rm obs,I}), \tag{5.5}$$

$${\chi_{\rm SB}^{\rm II}}^2 = \sum_{i,j} (S_{\rm B}(r_{\perp,\rm i}^{\rm II}) - S_{\rm B,i}^{\rm obs,II}) C_{i,j}^{-1} (S_{\rm B}(r_{\perp,\rm j}^{\rm II}) - S_{\rm B,j}^{\rm obs,II}). \tag{5.6}$$

In the weak lensing case I approximated the covariance matrix as diagonal; I found strong leading diagonals for the measured correlation matrices as seen in Figure 4.15. For the surface brightness fits I minimised over the full covariance matrix due to the covariances that exist between bins; here C is the error covariance matrix (and discussed in Section 4.3.2). Then $\gamma(r_{\perp,\rm i})$ is the value of the lensing model at a distance $r_\perp$ from the cluster's centre; likewise $S_{\rm B}(r_{\perp,\rm i})$ is the value of the surface brightness model at a distance $r_\perp$ from the cluster's centre. $\gamma_{\rm i}^{\rm obs}, S_{\rm B,i}^{\rm obs}$ are the observed shear profile and surface brightness profile respectively, while $\sigma\gamma_{\rm i}^{\rm obs}$ is the observed error on the shear profile.

5.3 Results

Shown in Figure 5.2 is the measured X-ray surface brightness and weak lensing profiles for both X-ray temperature bins. The X-ray surface brightness profiles have been measured out to $1.2 \times r_{200}$ with high signal-to-noise. Likewise for the two weak lensing profiles I have recovered a shear signal out to $10 \times r_{200}$ with high signal to noise. Also shown in Figure 5.2 are the best fit models for the each profile using the parameters outlined in

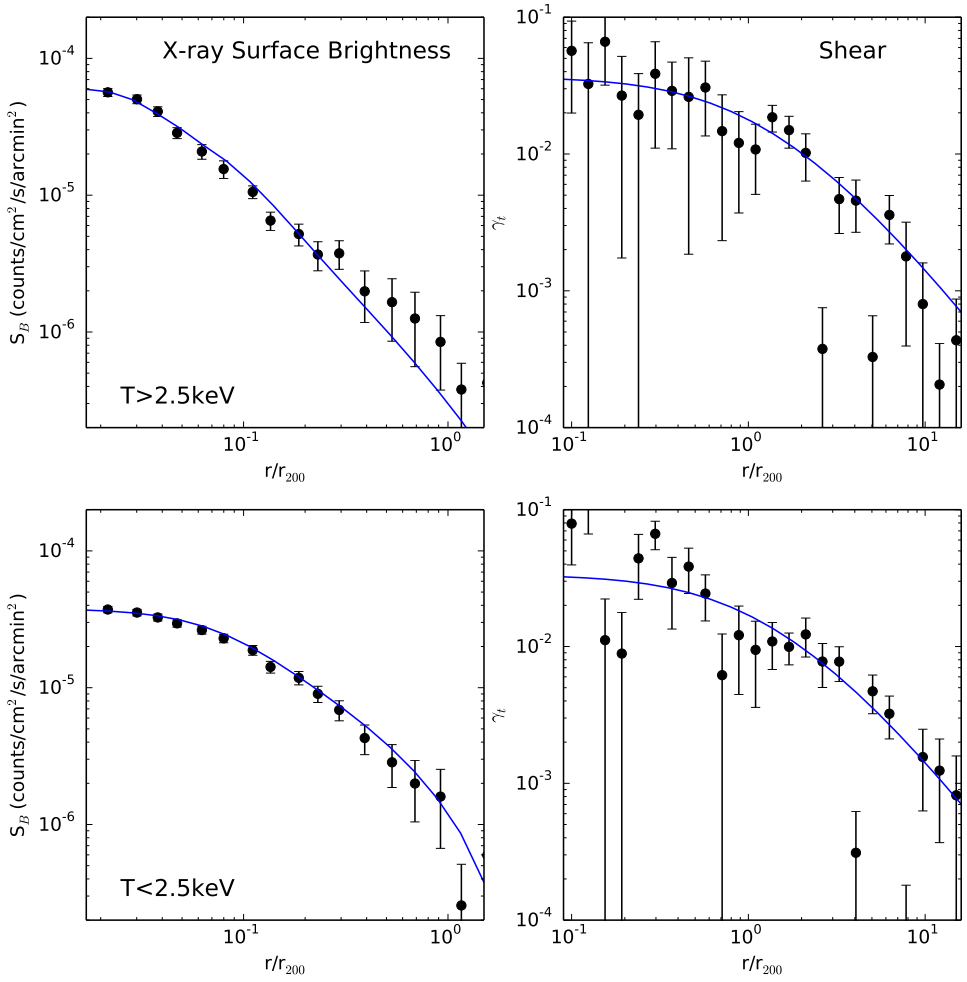

FIGURE 5.2: X-ray surface brightness profiles (left) and weak lensing (right) for the two bins of X-ray temperature: $T < 2.5$keV (top) and $T > 2.5$keV (bottom), against radial distance normalised by r_{200}, the radius at which the density is two hundred times the critical density. I choose to show the modified gravity profiles with the highest likelihood parameters, $T_0^{\rm I} = 12.6$ keV, $n_0^{\rm I} = 2.0 \times 10^{-2}{\rm cm}^{-3}$, $b_1^{\rm I} = -0.42, r_1^{\rm I} = 0.06$ Mpc, $M_{200}^{\rm I} = 12.2 \times 10^{14}{\rm M}_\odot$, $c^{\rm I} = 3.5, T_0^{\rm II} = 7.8$ keV, $n_0^{\rm II} = 4.9 \times 10^{-2}{\rm cm}^{-3}$, $b_1^{\rm II} = -0.89, r_1^{\rm II} = 0.05$ Mpc, $M_{200}^{\rm II} = 13.7 \times 10^{14}{\rm M}_\odot$, $c^{\rm II} = 3.8, \beta = 2, \phi_\infty = 2.1 \times 10^{-4} M_{\rm Pl}$.

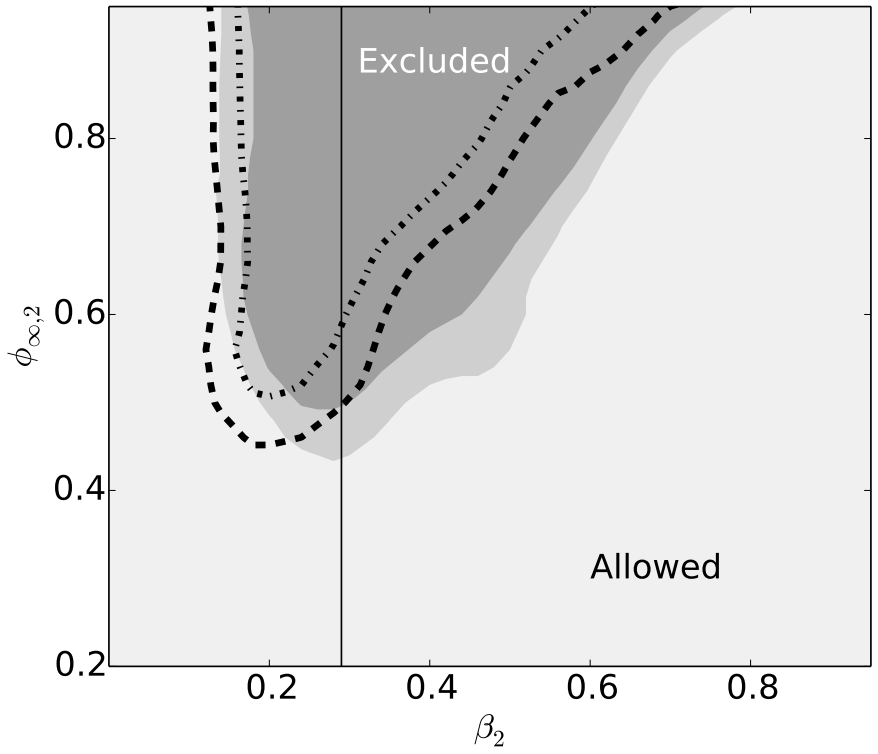

FIGURE 5.3: The 95% (light grey region) and the 99% confidence limit (mid grey region) constraints for the chameleon model parameters renormalised between [0,1], $\beta_2 = \beta/(1+\beta)$ and $\phi_{\infty,2} = 1-\exp(-\phi_\infty/10^{-4}M_{\rm Pl})$ obtained from the MCMC analysis of the combination of weak lensing and X-ray surface brightness for our two cluster stacks. Above the dashed (dash-dot) line is the 95% (99%) confidence limit excluded region from Terukina et al. (2014). The vertical line is at $\beta = \sqrt{1/6}$, showing the constraints for $f(R)$ gravity models.

Section 5.2 and minimising χ^2 as described in Equation 5.2. I show the 2D contours for constraints on all model parameters in Figure 5.4.

Shown in Figure 5.3 is the 2D constraints for β_2 and $\phi_{\infty,2}$. To generate the constraints I have marginalised over the measured likelihoods of the nuisance parameters (those that were not β_2 or $\phi_{\infty,2}$). I was able to do so as the chameleon gravity model outlined in Chapter 1 is insensitive to the overall amplitude of the profiles, only the profile's shape matters for the constraints. In Figure 5.3 I also show the dashed (dash-dot) line which indicated the 95% (99%) confidence limit excluded region from Terukina et al. (2014). The constraints were tighter from this work on larger values of β than in Terukina et al. (2014), whilst the constraints on smaller values of β are looser. As the profiles presented in this work extend further from the cluster's centre than the Coma profile (as shown in

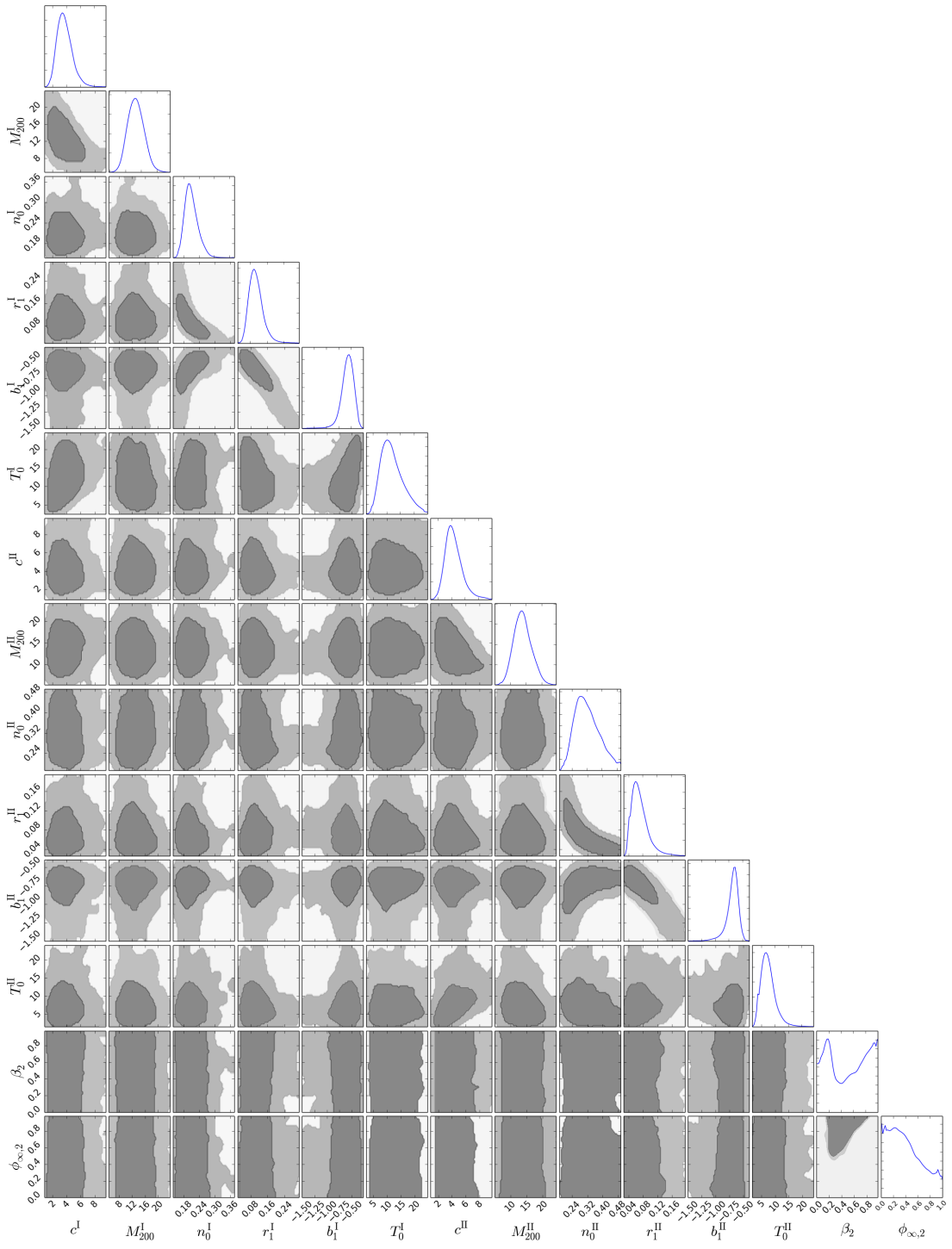

FIGURE 5.4: The 95% (dark grey region) and the 99% CL (mid grey region) 2D marginalised contours for the 14 model parameters $T_0^{\rm I}$ [keV], $n_0^{\rm I}$ [10^{-2}cm^{-3}], $b_1^{\rm I}, r_1^{\rm I}$ [Mpc], $M_{200}^{\rm I}$ [10^{14}M$_\odot$], $c^{\rm I}, T_0^{\rm II}$ [keV], $n_0^{\rm II}$ [10^{-2}cm^{-3}], $b_1^{\rm II}, r_1^{\rm II}$ [Mpc], $M_{200}^{\rm II}$ [10^{14}M$_\odot$], $c^{\rm II}, \beta_2, \phi_{\infty,2}$ used in the MCMC analysis. The rightmost plots show the 1D likelihood distributions.

Figure 5.2), I have probed further outside the critical radius, r_c (the radius at which the fifth force begins to take effect) and was therefore able to better constrain large values of β. However, as the errors on the X-ray profiles (and the lack of available SZ data) used in this work were larger than those measured in Terukina et al. (2014), I was less able to differentiate a chameleon profile from a GR one at lower values of β, leading to less constraining power.

The shape of the contours in Figure 5.3 can be understood by considering the meaning of the parameters used in defining chameleon gravity (as discussed in Section 1.4.1). Recall that β dictates the strength of the fifth force and ϕ_∞ is the effectiveness of the screening mechanism. Therefore at low values of β, the fifth force causes a deviation to the profile which is too small to be distinguished from GR given the observational errors. Likewise as GR gravity is recovered outside the critical radius r_c (as discussed in Section 1.5), this sets an upper limit on β/ϕ_∞. As β increases, a lower value for ϕ_∞ is required to keep r_c within the cluster, giving rise to the triangular shape of the excluded region.

5.3.1 Implications for $f(R)$ Gravity

The constraints presented here have implications for $f(R)$ gravity models (as discussed in detail in Section 1.4.2), which contain a chameleon mechanism for which $\beta = \sqrt{1/6}$ (Starobinsky, 2007) (shown as the vertical line in Figure 5.3).

From Figure 5.3, I estimated an upper bound on $f(R)$ gravity of $\phi_\infty < 5.8 \times 10^{-5} M_{\rm Pl}$ at 95% confidence limit (where the ϕ_∞ value where the $\beta = \sqrt{1/6}$ intersects the light grey region), and therefore using Equation 1.51 (relating $f(R)$ to ϕ_∞), $f_{\rm R}(z = 0.33) < 4.7 \times 10^{-5}$ at 95% confidence limit (where $z = 0.33$ is our cluster samples median redshift). The time-evolution of the background $f_{\rm R}(z)$ for a Hu-Sawicki model follows (Li et al., 2013),

$$f_{\rm R}(z) = |f_{\rm R0}| \frac{1}{n} [(1 + 3\Omega_\Lambda)/(\Omega_{\rm M}(1+z)^3 + 4\Omega_\Lambda)]^{n+1}, \tag{5.7}$$

where n is a free parameter of the model (described in Equation 1.45). At higher redshifts, the background energy density is higher, therefore $f_{\rm R}(z)$ is smaller and the screening is more efficient. So $f_{\rm R}(z)$ decreases by 22% from the median redshift ($z = 0.33$) of the sample to $z = 0$, when $n = 1$, and the constraint at $z = 0$ is $|f_{\rm R0}| < 6 \times 10^{-5}$ at 95% confidence limit. Considering a Hu-Sawicki model with $n = 3$, the constraint becomes

$|f_{R0}| < 2 \times 10^{-4}$ at 95% confidence limit. These results are comparable to the results for the Coma cluster reported in Terukina et al. (2014) of $|f_{R0}| < 6 \times 10^{-5}$, discussed in detail in Section 1.5.1.

To test this first point, the assumption of $c = 5$ I have remade the profiles seen in Figure 5.2 using both the lowest and highest values of the concentration parameter from scatter in the mass-concentration relation of ≈ 30 (Bahé et al., 2012). Using these new profiles I could then repeat the analysis described in Section 5.2 to generate new constraints for the modified gravity parameters.

In order to measure the constraints above I have made three testable assumptions: when converting between M_{500} and M_{200} (see Section 4.3.2) that $c = 5$; that none of the haloes were mis-centered; and that the 2-halo term really is not present in the data.

To test the second of these assumptions, that all the clusters were correctly centred, I have used the halo mis-centering correction described in Johnston et al. (2007). Using this formulation I have then repeated the procedure in the preceding paragraph to measure more constraints on the modified gravity parameters.

For the final test I have applied the 2-halo term described in Section 4.2.1, now forcing it to have the cosmological value found from simulations in Oguri and Hamana (2011). I have then once more remade lensing and X-ray profiles and fit them using the MCMC described above to constraint the modified gravity parameters.

For each of these tests I have placed constraints of $|f_{R0}| < 7 \times 10^{-5}$. This is a small reduction in the constraining power of this technique, as the systematic errors have been more correctly accounted for. Going forward with this technique these three assumptions should be more fully considered, especially the cluster mis-centering, which was found to be the most material.

Looking at figure 3.12 suggests the constraints presented here were under-estimated and a correction to the analytical model could be determined using the simulations described in Chapter 3. Ideally, I would compare the simulations directly to the data, but it remains computationally intensive to produce sufficiently large simulations for the next generation of cluster samples. For now, the analytical model remains appropriate.

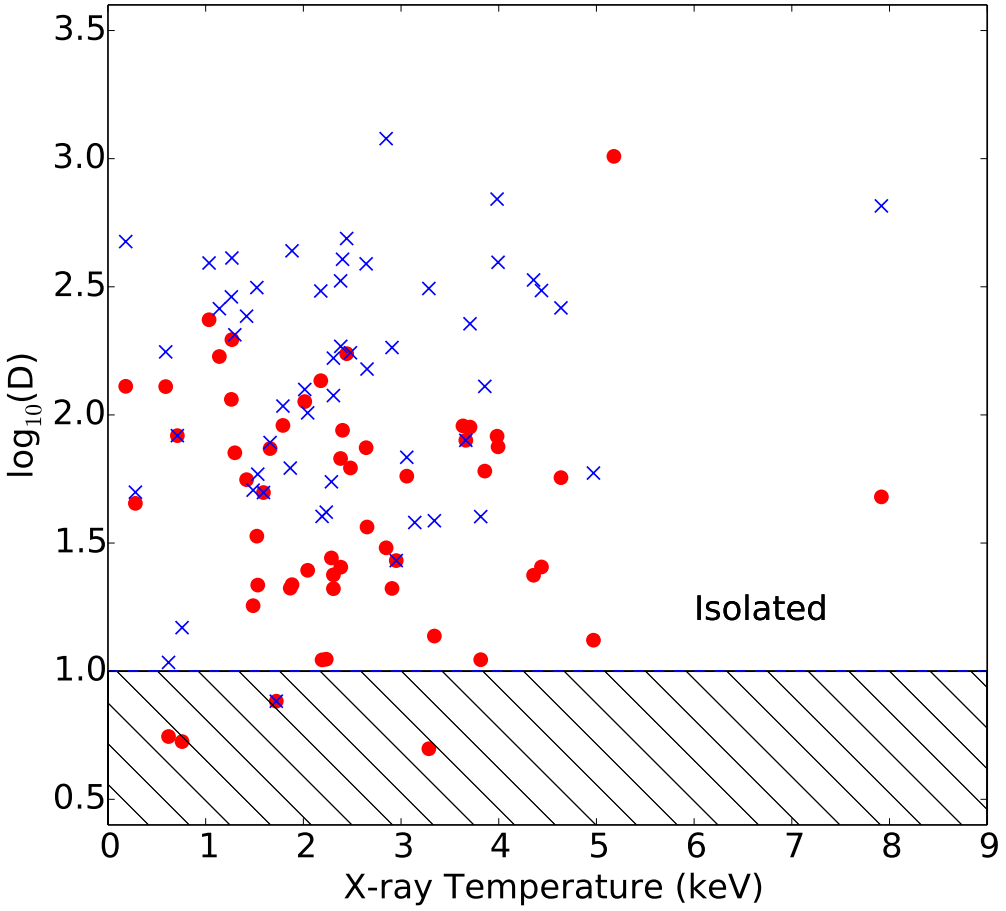

FIGURE 5.5: The minimum D parameter for each cluster against X-ray temperature, where $\log_{10} D$ is a measure of the distance between a cluster and the nearest overdensity in the top 30% (10%) of overdensity values, shown as a red circle (blue cross). The shaded region contains clusters with potential screening from neighbouring overdensities. The majority of the clusters are in an isolated region.

5.4 Influence of Cluster Environment

In addition to self screening, a cluster may be environmentally screened by nearby clusters and therefore still show no evidence of modified gravity, even in its outskirts. To check whether this was expected for any clusters in the sample, I estimated the D parameter for each cluster, detailed in Zhao et al. (2011b). This is a parametrisation of the separation between a given cluster and the nearest larger cluster, scaled by the nearby cluster's r_{200}. This quantity,

$$D = \frac{d_{N,M_{NB}/M_L \geq f}}{r_{200}}, \tag{5.8}$$

is defined for a cluster of mass M_L, as the 3D distance d, to the Nth nearest neighbouring cluster whose mass is at least f times as large as the original cluster, divided by the r_{200} of the neighbouring cluster. In Haas et al. (2012), setting $n = 1$ and $f = 1$ (that is, the rescaled distance to the single nearest cluster that has a mass greater than or equal to the cluster of interest) is found to represent the local density well and is adopted here.

I described clusters with $\log_{10} D > 1$ as 'isolated' and clusters with $\log_{10} D < 1$ as living in dense environments, and therefore environmentally screened. As the X-ray cluster sample used in this thesis is an incomplete set of all clusters in the CFHTLenS footprint, I looked at overdensities in the galaxy density field as a proxy for nearby clusters. I binned the galaxies in the CFHTLenS catalogue into 3-D pixels of volume 1Mpc^2 in area, and 0.01 in redshift.

Figure 5.5 shows X-ray temperature against $\log_{10} D$, where I have calculated $\log_{10} D$ values between each cluster and overdensity and selected the smallest $\log_{10} D$ as a measure of environment. It is seen that only 7% (2%) of the clusters are found to be near ($\log_{10} D < 1$) the most overdense 30% (10%) of the 3-D pixels. I therefore concluded that the sample appeared to be largely environmentally unscreened by nearby clusters, and therefore have applied the analysis to the full cluster sample. I note that it is possible that clusters outside the edge of the CFHTLenS observations could screen at most 6% of the sample, those that lie within $\log_{10} D = 1$ of the edge.

5.5 Assumption of Hydrostatic Equilibrium

Even in the absence of a fifth force, the interpretation of apparent differences in cluster mass profiles derived from X-ray or Sunyaev-Zel'dovich (SZ) observations and lensing measurements is complicated by both astrophysical processes in clusters, such as gas clumping in the cluster outskirts, and systematic errors in the measurements themselves (as discussed in Section 2.1). This has led to uncertainty in mass calibration being the dominant source of error on cosmological constraints derived from SZ cluster catalogues (Hasselfield et al. 2013; Reichardt et al. 2013; Planck Collaboration 2014). The absolute cluster mass scale is affected by uncertainty in the effects of feedback from active galactic nuclei, and non-thermal processes such as bulk motions, on the cluster gas (Nagai et al., 2007). Instrumental calibration uncertainties may also play a role (Schellenberger et al.

2015, Israel et al. 2015). Lensing measurements, which are affected by different systematics, are being used to quantify any bias in the absolute mass scale, but at present, samples are small, and there is some disagreement (von der Linden et al. 2014, Hoekstra et al. 2015).

In this work, I have investigated one of these issues: the impact of non-thermal pressure on the conclusions about chameleon gravity (whilst maintaining the simplifying assumptions of spherical symmetry). I have investigated some of these other issues, using hydrodynamic simulations, in Chapter 3. The thermal mass of a cluster is defined by the gas pressure, density and temperature, which I inferred from the X-ray surface brightness. I followed the parametric fits described in Terukina et al. (2014) to reconstruct the stacked cluster temperature profile and electron number densities from the profile parameters fit for by the MCMC and detailed below. I inferred from X-ray observations,

$$M_{\rm thermal} = \frac{-kT_{\rm gas}r}{\mu m_{\rm p} G}\left(\frac{d\ln n_{\rm e}}{d\ln r} + \frac{d\ln T_{\rm gas}}{d\ln r}\right), \tag{5.9}$$

where k is the Boltzmann constant and $m_{\rm p}$ is the proton mass. According to the hydrodynamical simulations in Shaw et al. (2010), the non-thermal pressure can be modelled as a function of the total pressure, such that $P_{\rm non-thermal}(r) = g(r)P_{\rm total}(r)$, where

$$g(r) = \alpha_{\rm nt}(1+z)^{\beta_{\rm nt}}\left(\frac{\rm r}{r_{500}}\right)^{n_{\rm nt}}\left(\frac{M_{200}}{3\times10^{14}M_{\odot}}\right)^{n_{\rm M}}, \tag{5.10}$$

and $\alpha_{\rm nt}$, $\beta_{\rm nt}$, $n_{\rm nt}$ and $n_{\rm M}$ are constants determined from 16 simulated clusters, with a mass range between $0.35 - 9.02\times10^{14}M_{\odot}$ at $z = 0$ (Lau et al., 2009). I adopted their best fit values of $\beta_{\rm nt}, n_{\rm nt}, n_{\rm M} = 0.5, 0.8, 0.2$ respectively. In order to test the robustness of the assumptions I selected $\alpha = 0.3$, which was the most extreme value found in the 16 clusters in the analysis of Shaw et al. (2010). The extra mass component that would be inferred from X-rays due to such non-thermal pressure would be

$$M_{\rm non-thermal} = \frac{-r^2}{G\rho_{\rm gas}}\frac{d}{dr}\left(\frac{g(r)}{1-g(r)}n_{\rm gas}kT_{\rm gas}\right), \tag{5.11}$$

where r is the radial distance, $g(r)$ is defined in Equation 5.10 and $\rho_{\rm gas}, n_{\rm gas}$ and $T_{\rm gas}$ are the gas density, number density and temperature respectively.

In Figure 5.6 I show the mass profiles for 0.3 Mpc $< r_{\perp} <$ 2 Mpc for the lensing mass and X-ray mass reconstruction, including the effects of non-thermal pressure. The solid

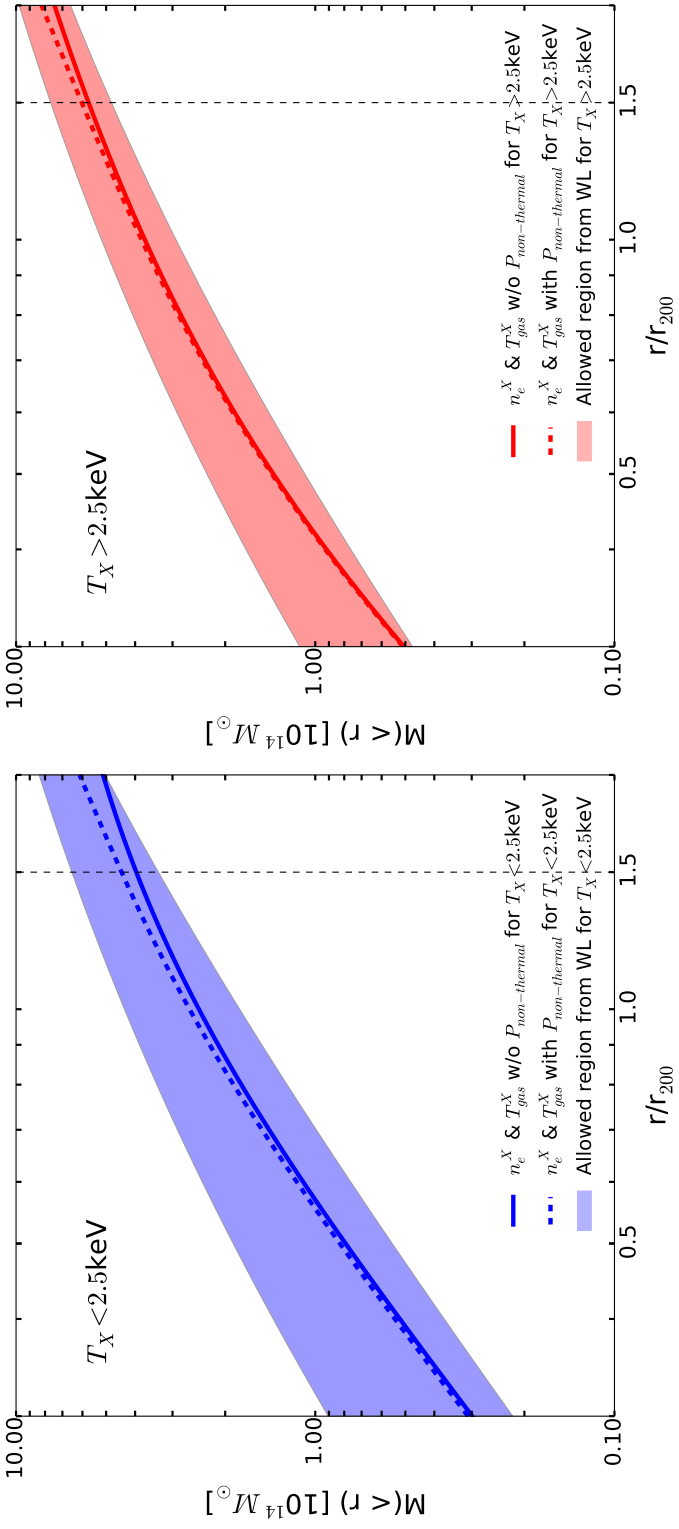

FIGURE 5.6: Mass profile from the $T < 2.5$keV ($T > 2.5$keV) cluster bin in blue (red). The shaded area is the one-sigma allowed region from the weak lensing measurement and the solid line is the thermal mass reconstructed from the X-rays. The dashed line shows the thermal mass with an additional non-thermal component as discussed in the text. The vertical line is the outer extent of our X-ray data; to its right I have extrapolated the X-ray data.

lines are the hydrostatic masses recovered from the X-ray measurements using Equation 5.9, while the dashed lines are the hydrostatic mass plus a non-thermal component from Equation 5.11. The shaded area is the 68% confidence limit allowed region from the weak lensing measurements, fit with an NFW profile. The vertical dotted line is the upper bound of the X-ray data: to the right of this line I have extrapolated to illustrate the possible divergence of the mass estimates with and without significant non-thermal pressure.

At all scales in Figure 5.6 the thermal pressure profile (solid line) is consistent with the shaded region, showing that the mass profiles estimated by the X-rays and lensing mass are consistent. This suggests that hydrostatic equilibrium is an acceptable approximation for our stacked profiles, given the error in the lensing measurements.

I also see in Figure 5.6 that the thermal pressure profile with a non-thermal component (dashed line) enhances the hydrodynamical mass by 20% (10%) in the $T < 2.5$keV ($T > 2.5$keV) cluster bin, but is still seen to be consistent with the lensing measurements. This shows that the non-thermal pressure expected from simulations falls within our present observed errors and that if present, acts in the opposite sense to chameleon gravity, reducing the detectable signal.

With future X-ray measurements I will be able to fit out to a larger distance than in this work, allowing me to better constrain the effect of non-thermal pressure, which would be most prominent at large radii. I also note that our weak lensing profiles have lower signal-to-noise than the X-ray profiles, however with future lensing surveys I will be able to more accurately constrain these profiles, also allowing me to better characterise not only chameleon gravity but non-thermal pressure too.

5.6 Comparison with previous constraints

I find the results are competitive with other cosmological constraints on chameleon models. In particular, the constraints are an order of magnitude stronger than those from the CMB (Raveri et al., 2014). They are comparable to Cataneo et al. (2015), which provides $|f_{\rm R0}| < 2.6 \times 10^{-5}$ for $n = 1$, compared with our measurement of $|f_{\rm R0}| < 6 \times 10^{-5}$, and $|f_{\rm R0}| < 3.1 \times 10^{-4}$ for $n = 3$ compared with our measurement of $|f_{\rm R0}| < 2 \times 10^{-4}$, all at

Scale	Scale	$\log_{10}\lvert f_{R0}\rvert$
Solar System (Hu and Sawicki, 2007)	pc	-6
Dwarf Galaxies (Jain et al., 2013)	kpc	-6.3
Coma cluster (Terukina et al., 2014)	Mpc	-4.2
Cluster abundance (Cataneo et al., 2015)	Mpc	-4.6 $(n=1)$ -3.5 $(n=3)$
Cluster stack (This Work)	Mpc	-4.2 $(n=1)$ -3.7 $(n=3)$
CMB (Raveri et al., 2014)	Gpc	-3.0

TABLE 5.1: Comparison of the constraints on $\log_{10}|f_{R0}|$.

the 95% CL. A comparison of these constraints is shown in Table 5.1. A more thorough discussion of these previous constraints is made in Section 2.3.

5.7 Summary

I have investigated the constraining power of stacked galaxy cluster profiles for testing chameleon gravity. I have examined 58 X-ray selected galaxy clusters, which have both good quality weak lensing data from CFHTLenS and X-ray data from XCS. After binning the clusters by X-ray temperature, I have generated weak lensing profiles and X-ray surface brightness profiles. Chameleon gravity predicts an additional pressure existing within clusters, which causes their gas component to become more compressed than GR gravity predicts. I have therefore investigated this phenomena by comparing the X-ray profile with the weak lensing profile, which is unaffected by the fifth force. Using a multi-parameter MCMC analysis I have obtained constraints on the common chameleon parameters β and ϕ_∞, which in turn lead to constraints for $|f_{R0}|$, a parameter characterising $f(R)$ theories.

I examined the assumption of hydrostatic equilibrium by comparing the masses inferred from the X-ray observations with weak lensing, and found them to be consistent. Deviations from hydrostatic equilibrium would cause a disparity between the weak lensing and X-rays with the opposite sign to that from the chameleon effect. I modelled a non-thermal pressure X-ray component; and given current observational errors found this to have a subdominant effect on the constraints.

As I am interested in the shape of the respective profiles, the absolute mass of the stacked cluster, measured through both weak lensing and X-rays, is a nuisance parameter that I have marginalised over. I therefore am not sensitive to the relative biases between these two techniques, such as reported in von der Linden et al. (2014) and Hoekstra et al. (2015).

Chapter 6

Further work and Conclusions

In this section I will discuss the future potential of the technique presented in this thesis by forecasting constraints for the chameleon parameters for the Dark Energy Survey. I will then present work that has been done to improve the techniques used in Chapters 4 and 5. I will then present the initial investigation into using the methodology outlined in previous chapters to constrain a different popular parametrisation of modified gravity – the Vainshtein mechanism. I finish this chapter by presenting the conclusions to this thesis.

6.1 Improving the weak lensing profiles

The constraints on $|f_{R0}|$ gravity that I have presented in Chapter 5 were limited by the number of clusters, which in turn was limited by the availability of quality weak lensing data. However, with the advent of large scale lensing surveys this issue will soon be mitigated. Here I discuss one of these surveys in particular, the Dark Energy Survey (DES, The Dark Energy Survey Collaboration 2005), and make a forecast on the improvements to the constraints on f_{R0} using Dark Energy Survey (DES) data.

DES is a five year project with the goal of extracting cosmological information about dark energy from four probes: type 1a supernovae (discussed in Section 1.3.1), Baryon Acoustic Oscillations (discussed in Section 1.3.2), cluster abundances and weak lensing (discussed in Section 2.2.3). To achieve this goal DES makes use of the 500 megapixel DECam which has a 2.2 square degree field of view and is mounted upon the 4m Blanco

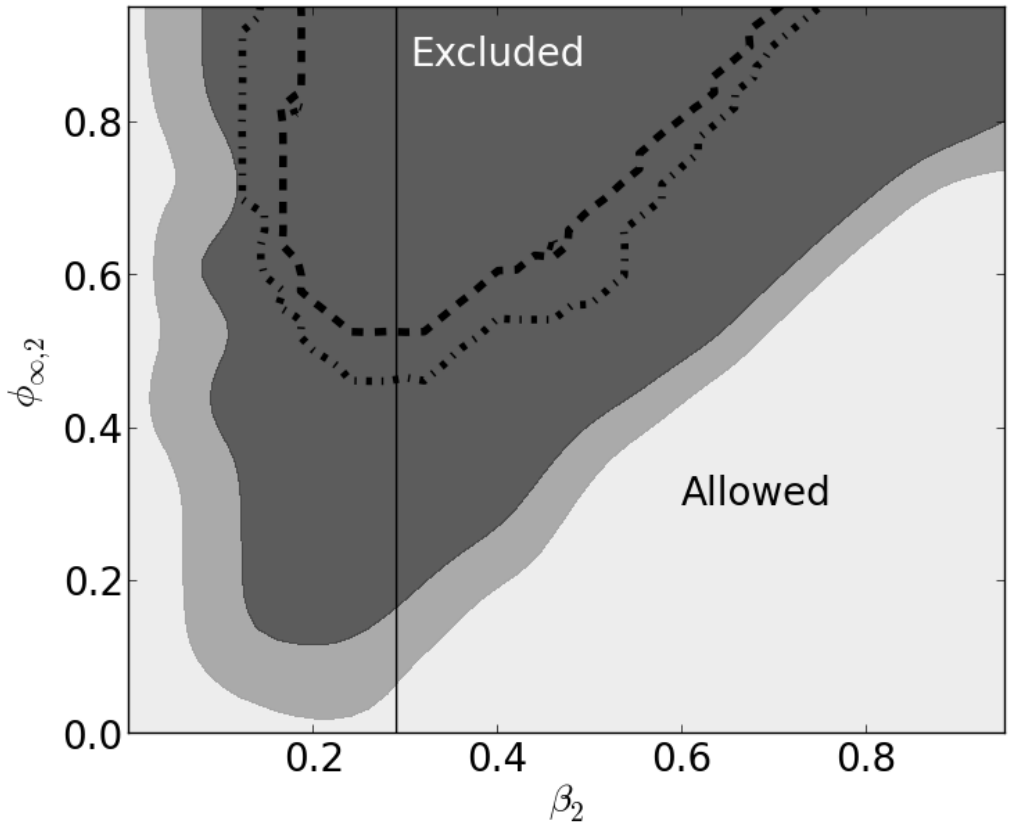

FIGURE 6.1: The 95% (light grey region) and the 99% confidence limit (mid grey region) constraints for the chameleon model parameters renormalised between [0,1], $\beta_2 = \beta/(1+\beta)$ and $\phi_{\infty,2} = 1-\exp(-\phi_\infty/10^{-4}M_{\rm Pl})$ forecasted for the full DES area. Above the dashed (dot-dashed) line is the 95% (99%) confidence limit excluded region from Chapter 5.

telescope at the Cerro Tololo Inter-American Observatory in Chile. Using DECam, DES aims to cover 5000 square degrees in the g,r,i,z,Y wavebands and measure the shapes of ~ 300 million galaxies out to $z = 1.3$.

DES has begun to show promise as the next step in weak lensing surveys. I have have used data from the Science Verification (SV) period to assist in the effort to measure the weak lensing mass of four massive clusters, which were found to be in good agreement with previous works and described in Melchior et al. (2015). I have also assisted in the initial image verification from DES. More recently DES has released full shear catalogues of the 139 square degrees from the SV data, containing ~ 3 million galaxies that pass a variety of null tests (Jarvis et al., 2015).

It is expected that the full 5000 square degree footprint of DES will contain of the order of 1000 X-ray clusters (in XCS), a vast improvement upon the 58 found in Chapter 4. The

number of clusters, however, doesn't scale linearly with area (moving from CFHTLenS to DES is an area increase of $\sim 30\times$, but the cluster count only will increase $\sim 17\times$) due to the observing strategy of XMM. Using this figure I have forecasted the constraining power of the technique when applied to the full DES sample. I have done this by assuming a fiducial model where $|f_{\rm R0}|= 10^{-6}$, chosen as this is the minimum value of $f_{\rm R0}$ constrainable using clusters (Falck et al., 2015). I have then used this model to compute both weak lensing shear and X-ray surface brightness profiles using the analytic model described in Chapter 5. To these profiles I then added noise and the corresponding error bars, based off a reduction of the error bars seen around the profiles generated in Chapter 4 such that they become representative of those expected from DES.

I show the forecasted constraints in Figure 6.1 in grey, contrasted against our results from Chapter 4 in blue. From this, I obtain a $|f_{\rm R0}|< 5 \times 10^{-6}$. This is an improvement of a magnitude upon our previous constraints, and would represent the strongest constraint of $|f_{\rm R0}|$ at these scales. However, this isn't as large an improvement as I would have expected from the increased cluster count itself, suggesting that using ever larger datasets with this technique would give diminishing returns. These constraints were forecast from two cluster temperature bins; moving from one bin to two in Chapter 4 significantly improved the constraints. With $\sim$ 1000 clusters I would be be able to use many more bins, potentially increasing the constraining power significantly.

6.2 Improving the X-ray surface brightness profiles

One improvement to this technique is driven by removing potential sources of contamination from the X-ray images to produce a more accurate representation of the clusters hydrostatic profile. Typically, any XMM observation, such as that shown in Figure 6.2, might contain an obvious extended source – a galaxy cluster in which I am interested, but also many less obvious point-like sources. In the $2-8$keV range, in which XMM observes, essentially all of these point sources are X-ray emitting Active Galactic Nuclei (AGN) (Mushotzky, 2004). As these AGN have an X-ray flux that is significant when compared to the X-ray flux of a cluster, any AGN along the line of sight of a galaxy cluster can artificially boost the flux of a cluster, leading to an overestimated surface brightness and affecting the recovered profiles.

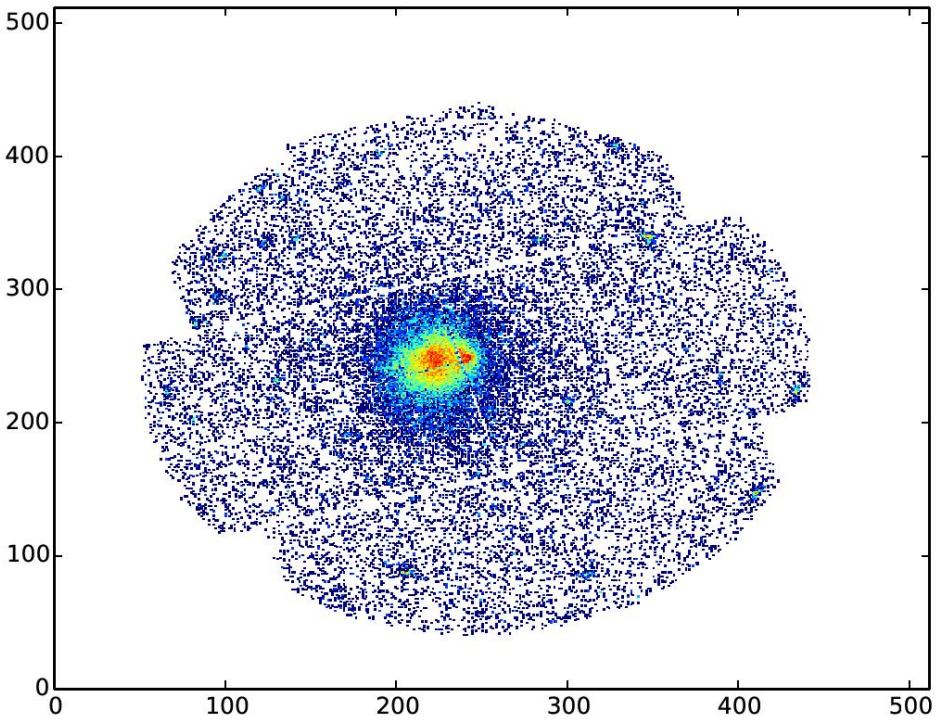

FIGURE 6.2: XMM ObsID 0112980201 taken with the mos2 camera, containing both extended and points sources. The x and y axes here are in pixels and the redder a pixel, the higher the number of counts in that pixel.

To remove these point sources I have used the XCS Automated Pipeline Algorithm (XAPA,) which is used to find both extended and point-like sources in XMM observations. I have then taken each point source identified by XAPA and removed it from the observation before generating X-ray surface brightness profiles as described in Chapter 4, with the technique described below.

6.2.1 XAPA regions

The XAPA region files detailed information about the positions of all the sources detected by XAPA for a corresponding XMM observation (hereafter ObsID). This includes each source's: x and y coordinates; major and minor axis length (which for point sources were equal); angle of orientation; and the source classification between extended or point like. From this information a mask was generated to remove the signal from each point source. A mask was then generated for each ObsID. An example mask can be seen in Figure 6.3.

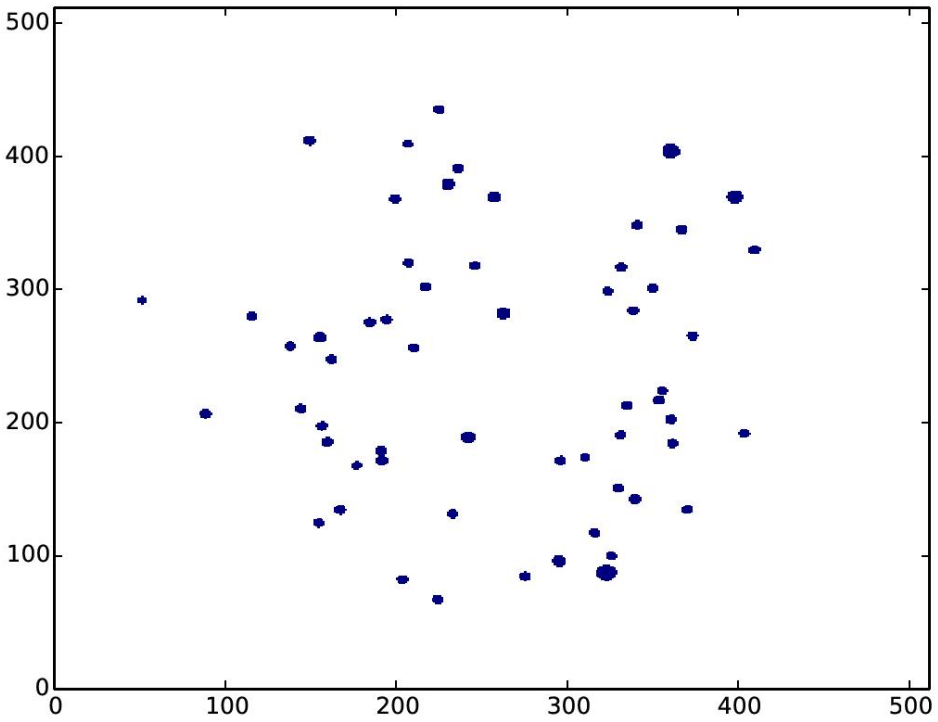

FIGURE 6.3: The mask created to remove point sources identified by XAPA from ObsID 0112980201. This figure shows the number of point sources present in a XMM observation. Once more the x and y axes show the pixel extent.

This mask was then convolved with each observation to remove point sources and leave the extended sources unaltered. An example of a masked image can be seen in Figure 6.4. I show a zoomed in view of the extended source with the removed point sources and point source map in Figure 6.5.

6.2.2 Stacking the images

To stack the X-ray images I followed the procedure outlined in Section 4.3.2, used to previously stack XCS clusters from the CFHTLenS area. These stacks differed in that the masks were included to weight the images. This was done by repeating the cropping and rescaling procedure outlined in Section 6.2.1 for the mask image alongside the exposure. The individual masks were then stacked following the prescription used to stack clusters. This mask stack was then rescaled by the exposure time of each individual exposure, such that any pixel where no masking had occurred was given a value of 1. The value of other pixels depended upon the sum of exposure time of the constituent images. This mask

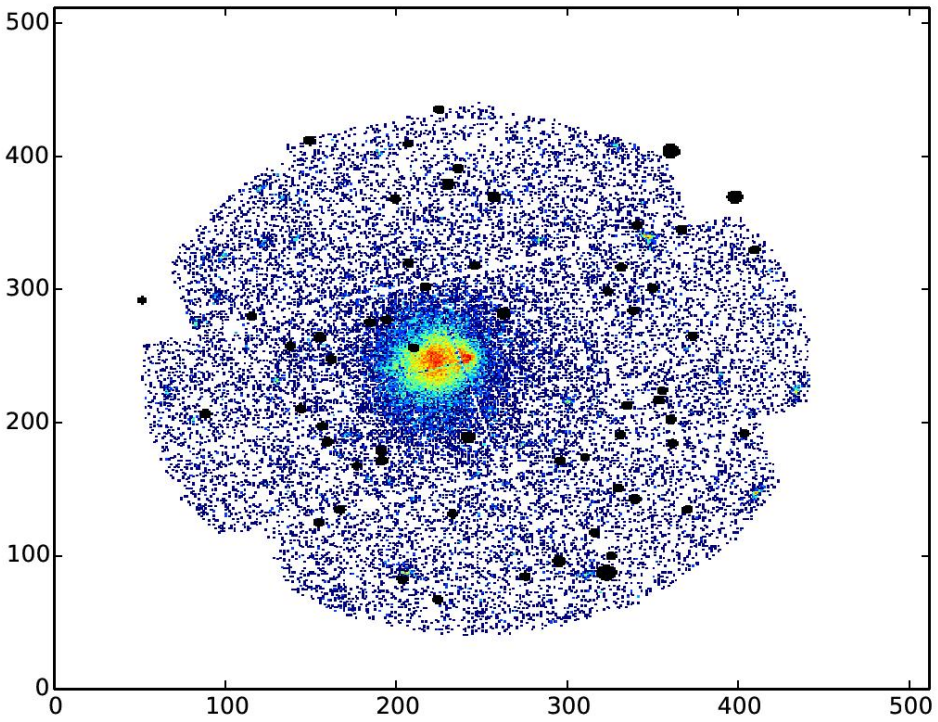

FIGURE 6.4: ObsID 0112980201 convolved with its XAPA mask (shown as black circles) to remove point sources.

stack was then used as a weight map when calculating the final stacked image and shown in Figure 6.6. Doing so ensured that regions that had been masked several times were not biased by having had flux removed.

This mask weighted stacked image was then used to make a X-ray surface brightness profile. I compared this profile to the X-ray surface brightness profile generated without masking and found that the absolute values in each bin were matched to $\sim 1\%$. The implication of this is that contamination within the cluster sample from AGN is small.

An upside of this technique, however, is that I measured a reduction in the standard deviation by $\sim 5\%$. The constraining power upon the chameleon parameters is limited in part by the errors on the profiles. Therefore any reduction of these errors will potentially lead to tighter constraints. Combining this improvement with a larger dataset, such as that described above, suggests that this technique is a suitable one for obtaining further constraints upon $f(R)$ gravity.

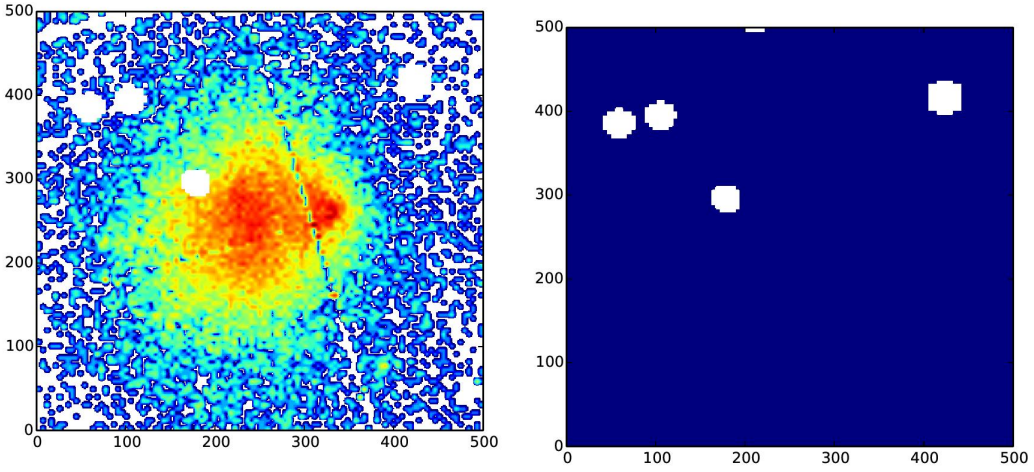

(A) ObsID 0112980201 convolved with its XAPA mask to remove point sources. Once more the x and y axes show the pixel extent.

(B) The mask accompanying ObsID 0112980201.

FIGURE 6.5: Zoom in of Figure 6.4 with its accompanying mask. Once more the x and y axes show the pixel extent.

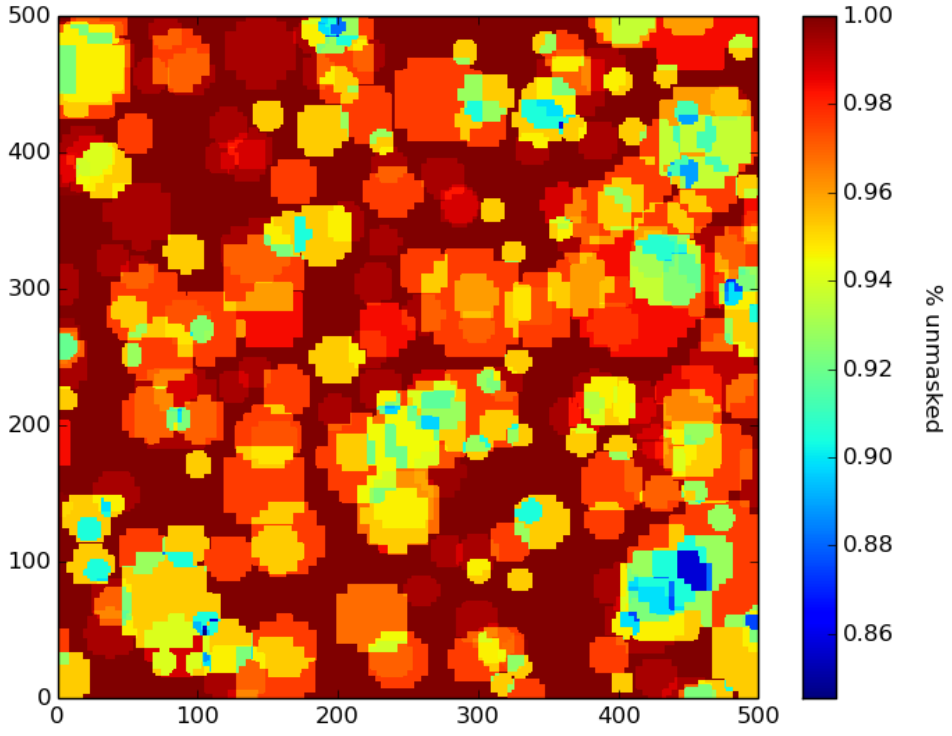

FIGURE 6.6: The whole mask used when calculating the point source removed X-ray surface brightness profile. The redder regions denote areas with few point sources. Once more the x and y axes show the pixel extent. This figure illustrates that a stack of XMM images while include many point sources which require masking.

6.3 Constraining different gravity models

This section discusses the gravity constraints published in Sakstein et al. (2016). In this work Sakstein performed the calculations leading to Equations 6.1 - 6.7. The implementation of these equations to constrain Vainshtein gravity, presented in Section 6.3.1, is my own work.

There are a host of modified gravity theories in addition to $f(R)$ gravity that manifest themselves in a large number of ways (Tsujikawa, 2010). One common feature that the theories which are able to describe accelerated expansion posses is a need to conform to the stringent solar system constraints of GR (discussed in Section 2.3). Aside from the chameleon mechanism, another popular screening method is the Vainshtein mechanism (Vainshtein, 1972), which is invoked in a wide range of modified gravity theories (Babichev et al. 2009, Koyama et al. 2011, Kimura et al. 2012). The Vainshtein mechanism circumvents solar system tests by introducing derivative interactions into the gravitational potential.

A simple case of this is in the cubic galileon model (Nicolis et al., 2009), which predicts that the local field is given by $\nabla^2\phi = 8\pi\beta G\rho$. Introducing Vainshtein screening then alters the potential, which can be seen imposing spherical symmetry

$$\frac{1}{r^2}\frac{\mathrm{d}}{\mathrm{d}r}\left(r^2\frac{\mathrm{d}\phi}{\mathrm{d}r}\right)+\frac{1}{r^2}\frac{\mathrm{d}}{\mathrm{d}r}\left[r\left(\frac{\mathrm{d}\phi}{\mathrm{d}r}\right)^2\right]=8\pi\beta G\rho. \tag{6.1}$$

The first term on the left is $\nabla^2\phi$, while the second is the term arising from the Vainshtein screening. By integrating this, it is possible to calculate the ratio, x, of the fifth force, described in Equation 1.40, to the Newtonian force (Sakstein, 2015)

$$x+\left(\frac{r_V}{r}\right)^3\frac{x}{2\beta^2}=2\beta^2, \tag{6.2}$$

where $r_V^3 \equiv \frac{GM}{\Lambda^2}$ is the Vainshtein Radius and Λ is the theory's mass scale. Far outside this radius $\left(\frac{r_V}{r}\right)^3\frac{x}{2\beta^2} \to 0$, so $x \approx 2\beta^2$ enhances gravity compared to the Newtonian prediction. However, inside this radius $x \approx 2\beta^2\left(\frac{r}{r_V}\right)^{1.5}$, therefore suppressing the fifth force.

Much like chameleon screening in Equation 1.60, the Vainshtein mechanism modifies the hydrostatic equilibrium equation (Koyama and Sakstein, 2015)

$$\frac{1}{\rho_{gas}}\frac{\mathrm{d}P}{\mathrm{d}r} = -\frac{GM}{r^2} - \frac{\Upsilon_1}{4}G\frac{\mathrm{d}^2M}{\mathrm{d}r^2}, \tag{6.3}$$

where $\Upsilon_1 = \frac{4\alpha_H^2}{-1+c_T^2(1+\alpha_B-\alpha_H)}$. Here α_H parametrises the deviation from Horndeski theories, in GR $\alpha_H = 0$ (Gleyzes et al., 2015); α_B is the braiding and contributes to the kinetic energy of the scalar perturbations, in GR $\alpha_B = 0$; and c_T is the tensor speed excess, parametrising the deviation of the speed of gravitational waves from light, in GR $c_T = 1$ (Bellini and Sawicki, 2014).

It is possible to evaluate the modified term in the above equation under the assumption of spherical symmetry as $\frac{\mathrm{d}M}{\mathrm{d}r} = 4\pi r^2\rho(r)$ and that the density follows an NFW (as described in Section 2.1),

$$\frac{\Upsilon_1}{4}G\frac{\mathrm{d}^2M}{\mathrm{d}r^2} = \frac{G\pi(r-r_s)r_s^2\rho_s\Upsilon_1}{(r+r_s)^2}. \tag{6.4}$$

This will cause the hydrostatic profile recovered from a cluster's X-ray profile to deviate from the GR prediction, much like chameleon screening. Vainshtein screening differs, however, because it leads to the lensing profile deviating from the GR prediction, as the lensing potential is modified as well

$$\nabla^2(\Phi+\Psi) = 8\pi G\rho + 8\pi G\rho_{eff}, \tag{6.5}$$

where

$$\rho_{eff} = \frac{1}{8\pi r^2}\frac{\mathrm{d}}{\mathrm{d}r}\left(\frac{\Upsilon_1 r^2}{4}\frac{\mathrm{d}^2M}{\mathrm{d}r^2} - \frac{5\Upsilon_2 r}{4}\frac{\mathrm{d}M}{\mathrm{d}r}\right). \tag{6.6}$$

Here $\Upsilon_2 = \frac{4\alpha_H(-\alpha_B+\alpha_H)}{5(-1+c_T^2(1+\alpha_B-\alpha_H))}$, and and from the definition of $\frac{\mathrm{d}M}{\mathrm{d}r}$,

$$\rho_{eff} = \frac{r_s^4\rho_s(r_s(\Upsilon_1-5\Upsilon_2) - r(2\Upsilon_1+5\Upsilon_2))}{4r(r_s+r)^4}. \tag{6.7}$$

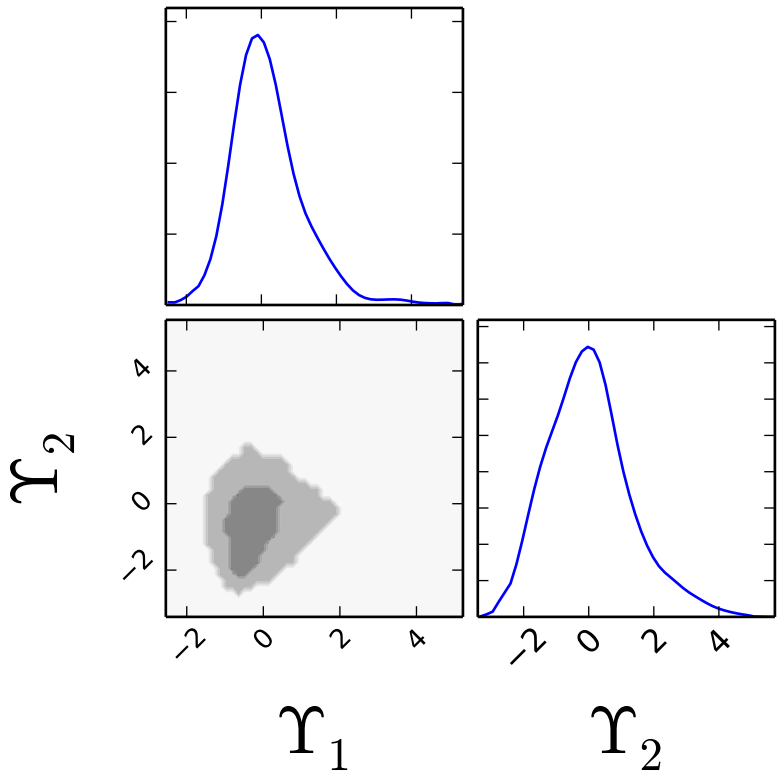

FIGURE 6.7: The 95% (light grey region) and 99% (mid grey region) confidence limit constraints for the Vainshtein model parameters obtained from the MCMC analysis of the combination of weak lensing and X-ray surface brightness profiles for the two cluster stacks.

Finally, from Equation 2.27, the surface density can be written as a function of the GR density plus the modified component, so $\Sigma(r) = \int \rho(r) + \rho_{eff}(r)$. From this it is possible to fit a shear profile.

6.3.1 Constraining Vainshtein

I have adapted the methodology of Chapter 5 to accommodate the modified hydrostatic profile of Equation 6.3 and modified lensing profile of Equation 6.7. Using the X-ray surface brightness and weak lensing profiles of the cluster sample described in Chapter 4, I have run a multi-parameter MCMC, fitting over Υ_1 and Υ_2 as opposed to the chameleon parameters β_2 and $\phi_{\infty,2}$ and the six other parameters describing the clusters (two parameters covering the NFW parameters c and M_{200}, and four covering the cluster properties T_0, n_0, b_1, and r_1). The MCMC run was a parallelised implementation using 128 walkers with 10000 time steps. I removed the 2000 iterations as a 'burn in' phase.

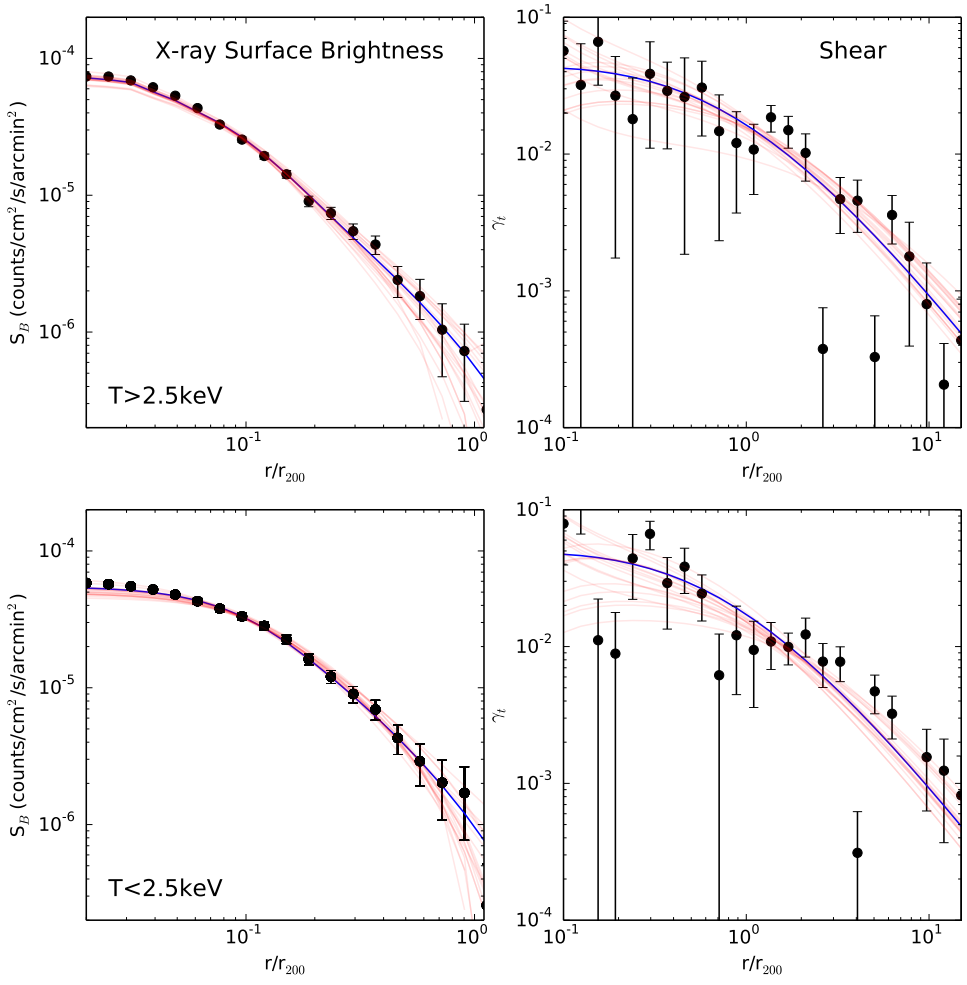

FIGURE 6.8: X-ray surface brightness profiles (left) and weak lensing (right) for the two bins of X-ray temperature: $T < 2.5$keV (top) and $T > 2.5$keV (bottom), against radial distance normalised by r_{200}, the radius at which the density is two hundred times the critical density. In blue the Vainshtein gravity profiles with the highest likelihood parameters are shown, $T_0^{\rm I} = 13.1$ keV, $n_0^{\rm I} = 0.2 \times 10^{-2}{\rm cm}^{-3}$, $b_1^{\rm I} = -0.5, r_1^{\rm I} = 0.07$ Mpc, $M_{200}^{\rm I} = 8.5 \times 10^{14}{\rm M}_\odot$, $c^{\rm I} = 5.2, T_0^{\rm II} = 2.3$ keV, $n_0^{\rm II} = 1.0 \times 10^{-2}{\rm cm}^{-3}$, $b_1^{\rm II} = -0.65, r_1^{\rm II} = 0.05$ Mpc, $M_{200}^{\rm II} = 10.6 \times 10^{14}{\rm M}_\odot$, $c^{\rm II} = 4.2, \Upsilon_1 = -0.06, \Upsilon_2 = -0.11$. In red a selection of models sampled from the Υ_1, Υ_2 1σ plane are shown.

I show the marginalised 2D contraints obtained from the MCMC for Υ_1 and Υ_2 in Figure 6.7. From the fits I was able to obtain bounds on $\Upsilon_1 = -0.11^{+0.93}_{-0.67}$ (95% CL) and $\Upsilon_2 = -0.22^{+1.22}_{-1.19}$ (95% CL). I found that both these results were consistent with GR, in which both parameters are equal to 0. The measurement for Υ_1 is consistent with the literature, with Sakstein (2015) finding $-2/3 < \Upsilon_1 < 0.027$ from measurements of brown and red dwarf stars and Jain et al. (2015) finding $-0.19 < \Upsilon_1 < 0.082$ from measurements of white dwarf stars. The measurement presented here of Υ_2 represents the first constraint upon this parameter.

I also show in Figure 6.8 the best fit Vainshtein gravity model to the four profiles in blue. In red a selection of models sampled from the Υ_1, Υ_2 1σ plane are shown to indicate the range of models allowed within the error bounds of the four profiles.

The constraints presented here for Υ_1 are found to be less stringent than those in the literature, but like the constraints upon the chameleon parameters they are limited by the errors on the profiles. With the advent of future lensing surveys I will be able to reduce these errors to produce more competitive constraints. This technique does, however, have the advantage of being able to constrain Υ_2 simultaneously as, unlike dwarf stars for which only hydrostatic masses are measurable, cluster profiles can be obtained from lensing.

6.4 Conclusions

This thesis has investigated the viability of using the X-ray and weak lensing profiles of stacked galaxy clusters to test modified theories of gravity and tested the models using hydrodynamic simulations.

In Chapter 1 I have presented an overview of the current state of cosmology. I began with a discussion of the linchpin of cosmology – general relativity. During this I discussed how the EFE arise from the combination of the spatial curvature and energy density within the universe. I also show how the hydrostatic equation arises as a consequence of GR. I next move on to discuss how combining the cosmological principle with GR leads to the emergence of the FLRW metric to describe space-time. I continued by discussing some consequences of this metric, starting with the Friedmann equation and the Hubble parameter, then continuing on to discuss redshift and common distance measures used in cosmology.

I then moved on to describe concordance cosmology as well as some its shortfalls, which motivated me to investigate alternate explanations to dark energy for accelerated expansion. As gravity is very well constrained on local scales I began by looking at the chameleon mechanism, which allows gravity to become modified, while still passing Solar system tests. I then looked at a particular set of gravity models, $f(R)$, which exhibit a chameleon but modify gravity on the largest scales. I finished this chapter by describing the effects such a gravity model would present in the universe, showing that a difference would be observed between hydrostatic and lensing measurements.

In Chapter 2 I introduced galaxy clusters as the largest virialised objects that are also thought to have contents representative of the whole universe. I began by discussing the properties of clusters that make them suitable for gravity tests, in particular the adherence of a cluster's density to an NFW profile.

Moving on I then described the mechanisms within clusters that led to the emission of X-rays, and how the surface brightness inferred from these X-rays can be fit in a modified gravity paradigm. Next I looked into how clusters are observed via weak lensing, and how I might fit a profile to the shear, including fitting for shear caused by the large scale structure. I ended this chapter by reviewing other techniques that have been used to constrain these models of gravity by utilising a variety of astronomical and cosmological probes.

In Chapter 3 I presented the analysis of two complementary hydrodynamical simulations, one evolved under ΛCDM+GR and the other under the influence of $f(R)$ gravity. I began by describing the fundamentals of both simulations before focussing on how $f(R)$ gravity is implemented within the simulation. I then described how I found the cluster sample and the rationale for its selection. I then discussed how I have derived usable data products from the simulations, beginning with the techniques used to generate the X-ray images before moving on to the creation of the weak lensing data. I followed the methods used in Chapter 5 to obtain both X-ray surface brightness and weak lensing profiles.

Next I discussed the various tests of the data I have performed. I checked that sphericity was observed when stacking many non-spherical clusters by measuring the ellipticity of the stacks, finding them to have $\epsilon < 0.04$ indicating spherical symmetry. I then tested that the NFW profile is an appropriate model for weak lensing profiles in $f(R)$ gravity and find it to be a suitable representation. I then tested the analytic model used in

Chapter 5 by applying two tests. First I fitted a best fit to the surface brightness profiles and artificially added in a modified gravity component, finding the result agrees with the $f(R)$ measurement. I then repeated the multi-parameter fits from Chapter 5 on the cluster lists from both simulations to constrain gravity. I found in the ΛCDM+GR simulation I was able to make a measurement comparable to that found using the real data with a measurement of $|f_{R0}| < 8.7 \times 10^{-5}$. In the $f(R)$ simulation I found I was able to place much tighter constraints on the model, of $|f_{R0}| < 3.8 \times 10^{-5}$ as there is a real difference in the profiles in this simulation. Finally I repeated the measurements with the inclusion of a systematic error, to model unknown astrophysics within the clusters, and found that this reduced the constraining power by $\sim 30\%$.

In Chapter 4 I described the cluster sample that was later used to test gravity. I began by describing the optical survey and galaxy shape measurements that I used to generate shear profiles. Next I described the X-ray survey that I have used to find the cluster sample before describing the steps taken to produce a usable cluster catalogue from the raw satellite observations.

I then presented the techniques used to stack the individual X-ray observations and produce usable surface brightness profiles from the resulting image. I also discussed how I measured an error on this profile from the covariance matrix. I present the technique to produce stacked shear profiles from individual galaxy shapes and detail tests I have performed to the data to ensure its suitability for gravity tests. I finished the chapter by discussing the optimum binning strategy to maximise the signal.

In Chapter 5 I presented the constraint on $f(R)$ models of gravity. These models posit that under the influence of a chameleon-like fifth force, a cluster's hydrostatic and lensing mass estimates will differ. I investigated this by performing a multi-parameter MCMC fit to the stacked profiles using the modified hydrostatic and shear profile equations. I found a constraint of $|f_{R0}| < 6 \times 10^{-5}$ at 95% confidence limit, which I discussed in the context of previous measurements, finding it to be a competitive constraint at these cosmic scales and redshifts. I have therefore demonstrated that it is possible to constrain chameleon gravity using stacked galaxy clusters. In 6.9 I show an updated version of Figure 2.11 that now includes the results presented in this thesis.

I also investigated the environment in which the cluster sample sits, as this will have some impact upon the strength of the constraints. I found that $> 90\%$ of the clusters are

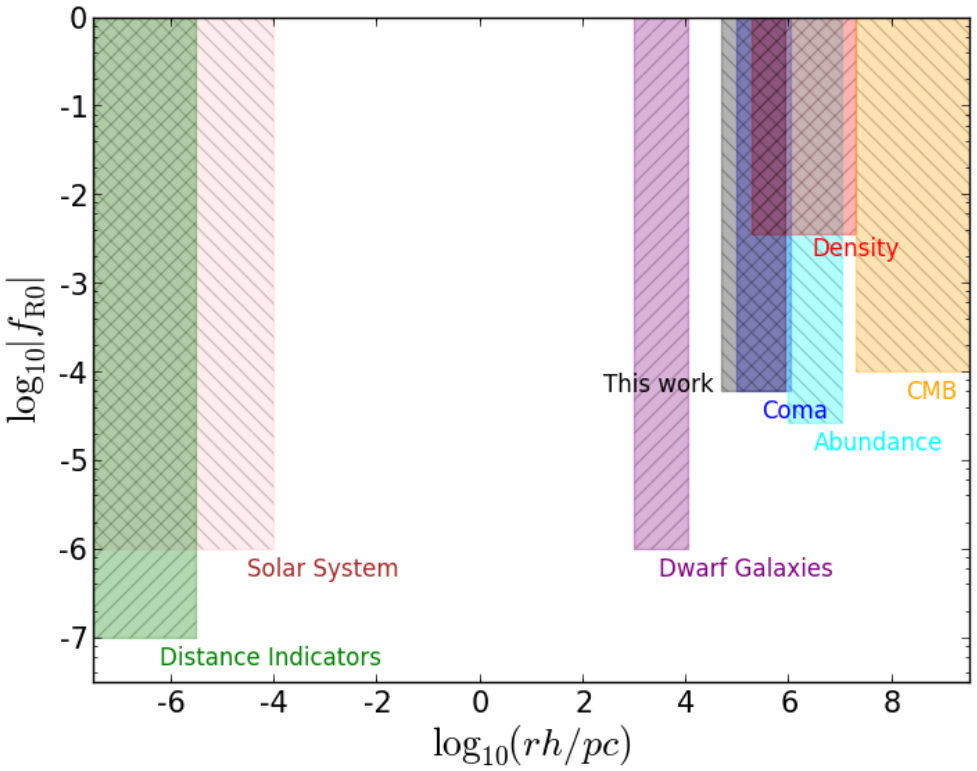

FIGURE 6.9: Comparison of current constraints on $f(R)$ gravity discussed in this Section 2.3 now with the inclusion of the new constraints presented in Chapter 5 against scale. The shaded areas denote regions of parameter space that are ruled out by the associated test. Adapted from Terukina et al. (2014).

isolated, implying the presence of nearby matter is not providing screening and dampening the results. Finally I investigated the assumption of hydrostatic equilibrium within the clusters and concluded that, within the errors of the shear measurements, it is a suitable approximation.

These simulations presented in Chapter 3 prove that the methodology in Chapter 5 is capable of constraining chameleon gravity. I also conclude that I need a larger sample of clusters (with both X-ray and lensing measurements) to create higher signal-to-noise stacked profiles to further test the possibility of a fifth force. Such samples of clusters should be available soon from a number of ongoing, and future, experiments like the Dark Energy Survey (DES, The Dark Energy Survey Collaboration 2005), the KIlo Degree Survey (KIDS, de Jong et al. 2013b), Euclid (Laureijs et al., 2011) and the Large Synoptic Survey Telescope (LSST, LSST Dark Energy Science Collaboration 2012). These surveys should provide thousands of clusters for such tests and push the limits on $|f_{R0}|$ to 10^{-6},

giving more robust constraints, that are complementary to the constraints from dwarf galaxies (Jain et al., 2013).

Finally in Chapter 6 I have forecast the constraints that could be obtained using the techniques outlined throughout this thesis for DES. I found significant improvements to the constraints using this technique, suggesting that this method could be utilised to provide the strongest constraints upon $f(R)$ gravity at cosmological scales. I outlined some refinements to the techniques described in earlier chapters, primarily focussing upon removing potential contamination from the surface brightness profiles. Doing so led to a reduction in the measured errors upon the X-ray surface brightness profiles, potentially leading once more to tighter constraints. I also adapted the methodology to probe the Vainshtein mechanism, another popular screening mechanism. I found the constraints to be consistent with GR and measure $\Upsilon_1 = -0.11^{+0.96}_{-0.69}$ and $\Upsilon_2 = -0.24^{+1.25}_{-1.19}$. Here Υ_1 is found to be competitive with the literature and I present the first measurement of Υ_2. I end with this conclusion.

To summarise, the work done throughout this PhD has investigated the power of combining stacked profiles from galaxy clusters to constrain modified gravity. I have also performed tests of the methodology using high quality hydrodynamical simulations to demonstrate that this is a viable technique which will only improve with the advent of large scale lensing surveys.

Appendix A

XCS clusters in CFHTLenS

Table A.1 lists the cluster sample discussed in detail in Chapter 4. I list the XCS name of the cluster and, where one is measured, its redshift. The redshifts listed here come from GMPhoRCC (Hood and Mann, 2015) unless indicated otherwise by a superscript. I provide several flags to help identify the subset of this list used throughout Chapter 5. A flag of 0 indicates the cluster was included in the analysis and has a measured X-ray temperature of $T < 2.5$keV, while a flag of 1 indicates the cluster was also included but has an X-ray temperature of $T > 2.5$keV. A cluster flagged with a 2 indicates that the cluster has no measured redshift. A flag of 3 is used to indicate the cluster has no measured X-ray temperature. In this case we have chosen to not list its associated redshift.

XCS Name	z	Flag
XMMXCS J020045.8-064229.2	0.36	0
XMMXCS J020119.0-064954.6	0.33	0
XMMXCS J020232.1-073343.8	0.55	1
XMMXCS J020334.3-055049.5		2
XMMXCS J020359.1-055031.6		3
XMMXCS J020405.2-050142.5		2
XMMXCS J020428.5-070221.6		2
XMMXCS J020432.7-064449.4		2
XMMXCS J020514.7-045640.0	0.29	0
XMMXCS J020611.4-061129.2	0.88	1
XMMXCS J020744.0-060956.6	0.35[1]	1
XMMXCS J020846.4-042608.2	0.78	1

Continued on next page

XCS Name	z	Flag
XMMXCS J021027.7-042233.5		2
XMMXCS J021057.8-061156.8		2
XMMXCS J021105.9-034613.9		2
XMMXCS J021114.6-034910.9		2
XMMXCS J021226.8-053734.6	0.31	1
XMMXCS J021228.3-045217.4		2
XMMXCS J021322.8-042134.0		2
XMMXCS J021348.1-050829.9		2
XMMXCS J021415.1-053117.9		3
XMMXCS J021428.3-062722.9	0.3[7]	1
XMMXCS J021444.1-034914.7		2
XMMXCS J021500.9-035429.5	0.2	0
XMMXCS J021511.5-034307.2		2
XMMXCS J021517.1-060432.8		3
XMMXCS J021524.4-034322.1	0.88	1
XMMXCS J021527.9-053319.2	0.28[2]	1
XMMXCS J021531.5-044017.5	0.33[2]	0
XMMXCS J021534.6-050502.7		2
XMMXCS J021538.0-055852.0		2
XMMXCS J021615.0-052150.8		3
XMMXCS J021618.7-050943.1		2
XMMXCS J021619.1-052555.2		2
XMMXCS J021641.0-041842.0		2
XMMXCS J021653.2-041723.7	0.2	0
XMMXCS J021719.1-040333.5	0.67	0
XMMXCS J021722.2-053920.7	0.56	0
XMMXCS J021734.7-051327.6	0.64	0
XMMXCS J021755.3-052707.6	0.67	0
XMMXCS J021808.0-054601.3	0.66	0
XMMXCS J021835.8-053757.4	0.39	0
XMMXCS J021838.9-061323.7		3
XMMXCS J021842.9-050437.7		3

Continued on next page

XCS Name	z	Flag
XMMXCS J021843.7-053257.7	0.4	0
XMMXCS J021911.4-034416.1	0.75	1
XMMXCS J021939.3-040025.5	0.84	0
XMMXCS J021952.0-040919.6		2
XMMXCS J022005.8-042445.4		3
XMMXCS J022037.2-054214.9	0.82	0
XMMXCS J022038.8-053236.8		2
XMMXCS J022053.1-053836.6		2
XMMXCS J022105.5-044101.7	0.23	1
XMMXCS J022129.5-040541.0	0.46	0
XMMXCS J022156.9-034000.4	0.1	0
XMMXCS J022237.0-053356.1		3
XMMXCS J022246.3-035151.2	0.16	0
XMMXCS J022251.6-050712.3		2
XMMXCS J022251.9-053229.5	0.8	0
XMMXCS J022307.4-041307.2		3
XMMXCS J022322.3-041352.2		2
XMMXCS J022327.6-042139.6	0.68	0
XMMXCS J022327.8-040119.1		3
XMMXCS J022352.2-082125.6	0.22[3]	1
XMMXCS J022401.9-050528.4	0.32	0
XMMXCS J022359.2-083543.4		2
XMMXCS J022421.2-040356.3		3
XMMXCS J022427.4-045023.8	0.49[1]	1
XMMXCS J022433.1-040030.5	0.39	1
XMMXCS J022433.8-041433.7	0.28	0
XMMXCS J022456.1-050802.0	0.12	0
XMMXCS J022457.9-034849.4	0.63	1
XMMXCS J022501.7-040752.9	0.64	0
XMMXCS J022505.1-095016.2	0.95	1
XMMXCS J022510.4-041913.1	0.67	0
XMMXCS J022523.4-042640.1		3

Continued on next page

XCS Name	z	Flag
XMMXCS J022524.8-044043.4	0.27	0
XMMXCS J022600.2-044412.6	1.2	1
XMMXCS J022607.8-041842.6	0.39	0
XMMXCS J022610.6-045811.5	0.1[7]	0
XMMXCS J022633.7-042215.9	0.27	1
XMMXCS J022659.6-043521.4	0.11	0
XMMXCS J022723.8-045216.0		3
XMMXCS J022738.4-031756.9	0.84[4]	1
XMMXCS J022740.4-045130.0	0.32	0
XMMXCS J022803.1-045059.9	0.32	1
XMMXCS J022808.5-053542.4	0.22	0
XMMXCS J022812.4-043234.6	0.5	1
XMMXCS J022812.6-100538.6	0.18	0
XMMXCS J022917.7-055345.9	0.31	0
XMMXCS J022933.7-055257.3		2
XMMXCS J023000.4-090033.2		2
XMMXCS J023008.3-043204.1		2
XMMXCS J023014.9-090251.3		2
XMMXCS J023036.7-040937.3		2
XMMXCS J023052.4-045123.5	0.3	0
XMMXCS J023119.9-072112.2		2
XMMXCS J023139.1-051526.0	0.2[7]	1
XMMXCS J023142.2-045253.1	0.21	1
XMMXCS J023143.3-072800.2	0.2[5]	1
XMMXCS J023152.1-072908.2	0.67[6]	0
XMMXCS J023154.0-045106.0		3
XMMXCS J023345.9-054711.1		2
XMMXCS J023351.6-040546.7		2
XMMXCS J140321.3+541946.0		2
XMMXCS J140341.0+541903.5		2
XMMXCS J140355.0+540845.4		2
XMMXCS J140429.1+542353.6		2

Continued on next page

XCS Name	z	Flag
XMMXCS J141446.9+544709.1		3
XMMXCS J141451.5+545557.2		3
XMMXCS J141506.0+545450.6		3
XMMXCS J141544.1+522510.7		3
XMMXCS J141644.0+523008.9		2
XMMXCS J141648.2+521035.1		3
XMMXCS J141651.2+522449.8		3
XMMXCS J141652.4+522053.6		3
XMMXCS J141749.3+522820.2		3
XMMXCS J141823.2+522712.0		3

TABLE A.1: Extended X-ray sources in CFHTLenS footprint. The XCS name and position are listed for all clusters. Redshifts are provided where available. The clusters forming the sample used throughout this work have a flag of 0 in the $T < 2.5$keV bin and a flag of 1 in the $T > 2.5$keV bin. A flag of 2 denotes the source was discounted for having no measured redshift. A flag of 3 denotes the source was discounted for having no measured X-ray temperature. Where the redshift has come from NED, the source is indicated via superscript.

[1]Durret et al. (2011)
[2]Wen and Han (2011)
[3]Wen et al. (2010)
[4]Takey et al. (2013)
[5]Valtchanov et al. (2004)
[6]Wen and Han (2011)
[7]Ford et al. (2014)

Appendix B

Derivation of the Einstein equation

It is possible to derive the EFE by applying the principle of least action to the Einstein-Hilbert action

$$S = \int \left(\frac{c^4}{16\pi G} R + \mathcal{L}_{\mathcal{M}} \right) \sqrt{-g} d^4x, \tag{B.1}$$

Now varying this with respect to the metric tensor $g^{\mu\nu}$

$$\delta S = \int \left(\frac{c^4}{16\pi G} \frac{\delta(\sqrt{-g}R)}{\delta g^{\mu\nu}} + \frac{\delta(\sqrt{-g}\,\mathcal{L}_{\mathcal{M}})}{\delta g^{\mu\nu}} \right) \delta g^{\mu\nu} d^4x. \tag{B.2}$$

This integral can then be broken into three parts by taking out a factor of $\sqrt{-g}$ and apply the product rule

$$\delta S = \int \left(\frac{c^4}{16\pi G} \left(\frac{\delta R}{\delta g^{\mu\nu}} + \frac{R}{\sqrt{-g}} \frac{\delta\sqrt{-g}}{\delta g^{\mu\nu}} \right) + \frac{1}{\sqrt{-g}} \frac{\delta(\sqrt{-g}\,\mathcal{L}_{\mathcal{M}})}{\delta g^{\mu\nu}} \right) \sqrt{-g} \delta g^{\mu\nu} d^4x. \tag{B.3}$$

The action principle says that this variation is equal to 0 so it is possible to equate the terms within the integral

$$\underbrace{\frac{\delta R}{\delta g^{\mu\nu}}}_{①} + \underbrace{\frac{R}{\sqrt{-g}} \frac{\delta\sqrt{-g}}{\delta g^{\mu\nu}}}_{②} = \underbrace{\frac{16\pi G}{c^4} \frac{1}{\sqrt{-g}} \frac{\delta(\sqrt{-g}\,\mathcal{L}_{\mathcal{M}})}{\delta g^{\mu\nu}}}_{③}. \tag{B.4}$$

Parts (1), (2) and (3) form the basis of the Einstein equation and can be further simplified Part (1) of Equation B.4 is the variation of the Ricci scalar. This is calculated by beginning with the Riemann tensor

$$R^{\rho}{}_{\sigma\mu\nu} = \partial_{\mu}\Gamma^{\rho}{}_{\sigma\nu} - \partial_{\nu}\Gamma^{\rho}{}_{\sigma\mu} + \Gamma^{\rho}{}_{\lambda\mu}\Gamma^{\lambda}{}_{\sigma\nu} - \Gamma^{\rho}{}_{\lambda\nu}\Gamma^{\lambda}{}_{\sigma\mu}, \tag{B.5}$$

where Γ are the various Christoffel symbols. Now varying the Riemann tensor

$$\delta R^{\rho}{}_{\sigma\mu\nu} = \partial_{\mu}\delta\Gamma^{\rho}{}_{\sigma\nu} - \partial_{\nu}\delta\Gamma^{\rho}{}_{\sigma\mu} + \delta\Gamma^{\rho}{}_{\lambda\mu}\Gamma^{\lambda}{}_{\sigma\nu} - \delta\Gamma^{\rho}{}_{\lambda\nu}\Gamma^{\lambda}{}_{\sigma\mu} + \Gamma^{\rho}{}_{\lambda\mu}\delta\Gamma^{\lambda}{}_{\sigma\nu} - \Gamma^{\rho}{}_{\lambda\nu}\delta\Gamma^{\lambda}{}_{\sigma\mu}. \tag{B.6}$$

Next it is possible to calculate the two covariant derivatives

$$\nabla_{\mu}(\delta\Gamma^{\rho}{}_{\sigma\nu}) = \partial_{\mu}(\delta\Gamma^{\rho}{}_{\sigma\nu}) + \Gamma^{\rho}{}_{\lambda\mu}\delta\Gamma^{\lambda}{}_{\sigma\nu} - \delta\Gamma^{\rho}{}_{\lambda\sigma}\Gamma^{\lambda}{}_{\mu\nu} - \delta\Gamma^{\rho}{}_{\lambda\nu}\Gamma^{\lambda}{}_{\sigma\mu}, \tag{B.7}$$

$$\nabla_{\nu}(\delta\Gamma^{\rho}{}_{\sigma\mu}) = \partial_{\nu}(\delta\Gamma^{\rho}{}_{\sigma\mu}) + \Gamma^{\rho}{}_{\lambda\nu}\delta\Gamma^{\lambda}{}_{\sigma\mu} - \delta\Gamma^{\rho}{}_{\lambda\sigma}\Gamma^{\lambda}{}_{\mu\nu} - \delta\Gamma^{\rho}{}_{\lambda\mu}\Gamma^{\lambda}{}_{\sigma\nu}. \tag{B.8}$$

It can now be seen that subtracting one of these derivatives from the other leaves identical terms, as seen on the right hand side of Equation B.5, allowing the Riemann tensor to be rewritten as

$$\delta R^{\rho}{}_{\sigma\mu\nu} = \nabla_{\mu}(\delta\Gamma^{\rho}{}_{\sigma\nu}) - \nabla_{\nu}(\delta\Gamma^{\rho}{}_{\sigma\mu}). \tag{B.9}$$

Next, contracting over two of the indices obtains the Ricci tensor

$$\delta R_{\mu\nu} = \delta R^{\rho}{}_{\rho\mu\nu} = \nabla_{\mu}(\delta\Gamma^{\rho}{}_{\rho\nu}) - \nabla_{\nu}(\delta\Gamma^{\rho}{}_{\rho\mu}), \tag{B.10}$$

and contracting this again obtains the Ricci scalar

$$g^{\mu\nu}\delta R_{\mu\nu} = \nabla_{\sigma}(g^{\mu\nu}(\delta\Gamma^{\sigma}{}_{\mu\nu}) - g^{\mu\sigma}(\delta\Gamma^{\rho}{}_{\rho\mu})). \tag{B.11}$$

This is a total derivative, so under Stokes' theorem vanishes at infinity, so does not contribute.

Returning to the part (1) of Equation B.4, using the definition of the Ricci scalar as a contraction of the Ricci tensor, and substituting in Equation B.11

$$\begin{aligned}\frac{\delta R}{\delta g^{\mu\nu}} &= \frac{\delta(g^{\mu\nu}R_{\mu\nu})}{\delta g^{\mu\nu}},\\ &= R_{\mu\nu}\frac{\delta g^{\mu\nu}}{\delta g^{\mu\nu}} + g^{\mu\nu}\frac{\delta R_{\mu\nu}}{\delta g^{\mu\nu}},\\ &= R_{\mu\nu} + \nabla_\sigma(g^{\mu\nu}(\delta\Gamma^\sigma{}_{\mu\nu}) - g^{\mu\sigma}(\delta\Gamma^\rho{}_{\rho\mu})),\\ &= R_{\mu\nu}.\end{aligned} \tag{B.12}$$

Part (1) of Equation B.4 has now been simplified. To find part (2) Jacobi's formula for the derivative of a determinant is considered

$$\delta g = \delta \det(g_{\mu\nu}) = g g^{\mu\nu}\delta g_{\mu\nu}. \tag{B.13}$$

From this

$$\begin{aligned}\delta\sqrt{-g} &= -\frac{1}{2\sqrt{-g}}\delta g\\ &= -\frac{1}{2}\sqrt{-g}(g_{\mu\nu}\delta g^{\mu\nu}).\end{aligned} \tag{B.14}$$

Substituting this into the part (2) of B.4, its simplified form is obtained

$$\frac{R}{\sqrt{-g}}\frac{\delta\sqrt{-g}}{\delta g^{\mu\nu}} = -\frac{1}{2}g_{\mu\nu}R. \tag{B.15}$$

Now the stress energy tensor is defined as the part (3) of Equation B.4

$$\frac{1}{\sqrt{-g}}\frac{\delta(\sqrt{-g}\,\mathcal{L}_\mathcal{M})}{\delta g^{\mu\nu}} = -\frac{1}{2}T_{\mu\nu}. \tag{B.16}$$

Substituting Equations B.12, B.15, B.16 into Equation B.4 we obtain the Einstein equation

$$R_{\mu\nu} - \frac{1}{2}g_{\mu\nu}R = \frac{8\pi G}{c^4}T_{\mu\nu}. \tag{B.17}$$

Bibliography

Abbott, T. et al. (2016). The Dark Energy Survey: more than dark energy - an overview. *ArXiv e-prints*.

Acquaviva, V., Baccigalupi, C., and Perrotta, F. (2004). Weak lensing in generalized gravity theories. *PRD*, 70(2):023515.

Aihara, H., Allende Prieto, C., An, D., Anderson, S. F., Aubourg, É., Balbinot, E., Beers, T. C., Berlind, A. A., Bickerton, S. J., Bizyaev, D., Blanton, M. R., Bochanski, J. J., Bolton, A. S., Bovy, J., Brandt, W. N., Brinkmann, J., Brown, P. J., Brownstein, J. R., Busca, N. G., Campbell, H., Carr, M. A., Chen, Y., Chiappini, C., Comparat, J., Connolly, N., Cortes, M., Croft, R. A. C., Cuesta, A. J., da Costa, L. N., Davenport, J. R. A., Dawson, K., Dhital, S., Ealet, A., Ebelke, G. L., Edmondson, E. M., Eisenstein, D. J., Escoffier, S., Esposito, M., Evans, M. L., Fan, X., Femenía Castellá, B., Font-Ribera, A., Frinchaboy, P. M., Ge, J., Gillespie, B. A., Gilmore, G., González Hernández, J. I., Gott, J. R., Gould, A., Grebel, E. K., Gunn, J. E., Hamilton, J.-C., Harding, P., Harris, D. W., Hawley, S. L., Hearty, F. R., Ho, S., Hogg, D. W., Holtzman, J. A., Honscheid, K., Inada, N., Ivans, I. I., Jiang, L., Johnson, J. A., Jordan, C., Jordan, W. P., Kazin, E. A., Kirkby, D., Klaene, M. A., Knapp, G. R., Kneib, J.-P., Kochanek, C. S., Koesterke, L., Kollmeier, J. A., Kron, R. G., Lampeitl, H., Lang, D., Le Goff, J.-M., Lee, Y. S., Lin, Y.-T., Long, D. C., Loomis, C. P., Lucatello, S., Lundgren, B., Lupton, R. H., Ma, Z., MacDonald, N., Mahadevan, S., Maia, M. A. G., Makler, M., Malanushenko, E., Malanushenko, V., Mandelbaum, R., Maraston, C., Margala, D., Masters, K. L., McBride, C. K., McGehee, P. M., McGreer, I. D., Ménard, B., Miralda-Escudé, J., Morrison, H. L., Mullally, F., Muna, D., Munn, J. A., Murayama, H., Myers, A. D., Naugle, T., Neto, A. F., Nguyen, D. C., Nichol, R. C., O'Connell, R. W., Ogando, R. L. C., Olmstead, M. D., Oravetz, D. J., Padmanabhan, N., Palanque-Delabrouille, N., Pan, K., Pandey, P., Pâris, I., Percival, W. J., Petitjean, P., Pfaffenberger, R., Pforr, J., Phleps, S., Pichon, C., Pieri, M. M., Prada, F., Price-Whelan, A. M., Raddick, M. J., Ramos, B. H. F., Reylé, C., Rich, J., Richards, G. T., Rix, H.-W., Robin, A. C., Rocha-Pinto, H. J., Rockosi, C. M., Roe, N. A., Rollinde, E., Ross, A. J., Ross, N. P., Rossetto, B. M., Sánchez, A. G., Sayres, C., Schlegel, D. J., Schlesinger, K. J., Schmidt, S. J., Schneider, D. P., Sheldon, E., Shu, Y., Simmerer, J., Simmons, A. E., Sivarani, T., Snedden, S. A., Sobeck, J. S., Steinmetz, M., Strauss, M. A., Szalay, A. S., Tanaka, M., Thakar, A. R., Thomas, D., Tinker, J. L., Tofflemire, B. M., Tojeiro, R., Tremonti, C. A., Vandenberg, J., Vargas Magaña, M., Verde, L., Vogt, N. P., Wake, D. A., Wang, J., Weaver, B. A., Weinberg, D. H., White, M., White, S. D. M., Yanny, B., Yasuda, N., Yeche, C., and Zehavi, I.

(2011). The Eighth Data Release of the Sloan Digital Sky Survey: First Data from SDSS-III. *ApJS*, 193:29.

Allen, S. W. (1998). Resolving the discrepancy between X-ray and gravitational lensing mass measurements for clusters of galaxies. *MNRAS*, 296:392–406.

Als-Nielsen, J. and McMorrow, D. (2011). *Elements of Modern X-ray Physics, 2nd Edition*. Wiley.

Amara, A., Lilly, S., Kovač, K., Rhodes, J., Massey, R., Zamorani, G., Carollo, C. M., Contini, T., Kneib, J.-P., Le Fevre, O., Mainieri, V., Renzini, A., Scodeggio, M., Bardelli, S., Bolzonella, M., Bongiorno, A., Caputi, K., Cucciati, O., de la Torre, S., de Ravel, L., Franzetti, P., Garilli, B., Iovino, A., Kampczyk, P., Knobel, C., Lamareille, F., Le Borgne, J.-F., Le Brun, V., Maier, C., Mignoli, M., Pello, R., Peng, Y., Montero, E. P., Presotto, V., Silverman, J., Tanaka, M., Tasca, L., Tresse, L., Vergani, D., Zucca, E., Barnes, L., Bordoloi, R., Cappi, A., Cimatti, A., Coppa, G., Koekoemoer, A., López-Sanjuan, C., McCracken, H. J., Moresco, M., Nair, P., Pozzetti, L., and Welikala, N. (2012). The COSMOS density field: a reconstruction using both weak lensing and galaxy distributions. *MNRAS*, 424:553–563.

Anderson, L., Aubourg, É., Bailey, S., Beutler, F., Bhardwaj, V., Blanton, M., Bolton, A. S., Brinkmann, J., Brownstein, J. R., Burden, A., Chuang, C.-H., Cuesta, A. J., Dawson, K. S., Eisenstein, D. J., Escoffier, S., Gunn, J. E., Guo, H., Ho, S., Honscheid, K., Howlett, C., Kirkby, D., Lupton, R. H., Manera, M., Maraston, C., McBride, C. K., Mena, O., Montesano, F., Nichol, R. C., Nuza, S. E., Olmstead, M. D., Padmanabhan, N., Palanque-Delabrouille, N., Parejko, J., Percival, W. J., Petitjean, P., Prada, F., Price-Whelan, A. M., Reid, B., Roe, N. A., Ross, A. J., Ross, N. P., Sabiu, C. G., Saito, S., Samushia, L., Sánchez, A. G., Schlegel, D. J., Schneider, D. P., Scoccola, C. G., Seo, H.-J., Skibba, R. A., Strauss, M. A., Swanson, M. E. C., Thomas, D., Tinker, J. L., Tojeiro, R., Magaña, M. V., Verde, L., Wake, D. A., Weaver, B. A., Weinberg, D. H., White, M., Xu, X., Yèche, C., Zehavi, I., and Zhao, G.-B. (2014). The clustering of galaxies in the SDSS-III Baryon Oscillation Spectroscopic Survey: baryon acoustic oscillations in the Data Releases 10 and 11 Galaxy samples. *MNRAS*, 441:24–62.

Applegate, D. E., von der Linden, A., Kelly, P. L., Allen, M. T., Allen, S. W., Burchat, P. R., Burke, D. L., Ebeling, H., Mantz, A., and Morris, R. G. (2014). Weighing the Giants - III. Methods and measurements of accurate galaxy cluster weak-lensing masses. *MNRAS*, 439:48–72.

Arnaud, K., Smith, R., and Siemiginowska, A. (2011). *Handbook of X-ray Astronomy*. Cambridge University Press.

Arnaud, K. A. (1996). XSPEC: The First Ten Years. In Jacoby, G. H. and Barnes, J., editors, *Astronomical Data Analysis Software and Systems V*, volume 101 of *Astronomical Society of the Pacific Conference Series*, page 17.

Arnaud, M. (2005). X-ray observations of clusters of galaxies. In Melchiorri, F. and Rephaeli, Y., editors, *Background Microwave Radiation and Intracluster Cosmology*, page 77.

Arnold, C., Puchwein, E., and Springel, V. (2014). Scaling relations and mass bias in hydrodynamical f (R) gravity simulations of galaxy clusters. *MNRAS*, 440:833–842.

Attwood, D T (2000). *Soft x-rays and extreme ultraviolet radiation : principles and applications*. Cambridge University Press.

Babichev, E., Deffayet, C., and Ziour, R. (2009). k-MOUFLAGE Gravity. *Int. J. Mod. Phys. D*, 18:2147–2154.

Bacon, D. J., Massey, R. J., Refregier, A. R., and Ellis, R. S. (2003). Joint cosmic shear measurements with the Keck and William Herschel Telescopes. *MNRAS*, 344:673–685.

Bacon, D. J., Refregier, A. R., and Ellis, R. S. (2000). Detection of weak gravitational lensing by large-scale structure. *MNRAS*, 318:625–640.

Bahé, Y. M., McCarthy, I. G., and King, L. J. (2012). Mock weak lensing analysis of simulated galaxy clusters: bias and scatter in mass and concentration. *MNRAS*, 421:1073–1088.

Bartelmann, M. and Schneider, P. (2001). Weak gravitational lensing. *PhR*, 340:291–472.

Battaglia, N., Leauthaud, A., Miyatake, H., Hasselfield, M., Gralla, M. B., Allison, R., Bond, J. R., Calabrese, E., Crichton, D., Devlin, M. J., Dunkley, J., Dünner, R., Erben, T., Ferrara, S., Halpern, M., Hilton, M., Hill, J. C., Hincks, A. D., Hložek, R., Huffenberger, K. M., Hughes, J. P., Kneib, J. P., Kosowsky, A., Makler, M., Marriage, T. A., Menanteau, F., Miller, L., Moodley, K., Moraes, B., Niemack, M. D., Page, L., Shan, H., Sehgal, N., Sherwin, B. D., Sievers, J. L., Sifón, C., Spergel, D. N., Staggs, S. T., Taylor, J., Thornton, R., van Waerbeke, L., and Wollack, E. J. (2015). Weak-Lensing Mass Calibration of the Atacama Cosmology Telescope Equatorial Sunyaev-Zeldovich Cluster Sample with the Canada-France-Hawaii Telescope Stripe 82 Survey. *ArXiv e-prints*.

Behroozi, P. S., Wechsler, R. H., and Wu, H.-Y. (2013). The ROCKSTAR Phase-space Temporal Halo Finder and the Velocity Offsets of Cluster Cores. *ApJ*, 762:109.

Bellini, E. and Sawicki, I. (2014). Maximal freedom at minimum cost: linear large-scale structure in general modifications of gravity. *JCAP*, 7:050.

Bender, P. L., Currie, D. G., Dicke, R. H., Eckhardt, D. H., Faller, J. E., Kaula, W. M., Mulholland, J. D., Plotkin, H. H., Poultney, S. K., Silverberg, E. C., Wilkinson, D. T., Williams, J. G., and Alley, C. O. (1973). The Lunar Laser Ranging Experiment. *Science*, 182:229–238.

Bennett, C. L., Larson, D., Weiland, J. L., Jarosik, N., Hinshaw, G., Odegard, N., Smith, K. M., Hill, R. S., Gold, B., Halpern, M., Komatsu, E., Nolta, M. R., Page, L., Spergel, D. N., Wollack, E., Dunkley, J., Kogut, A., Limon, M., Meyer, S. S., Tucker, G. S., and Wright, E. L. (2013). Nine-year Wilkinson Microwave Anisotropy Probe (WMAP) Observations: Final Maps and Results. *ApJS*, 208:20.

Bertin, E. and Arnouts, S. (2010). SExtractor: Source Extractor. Astrophysics Source Code Library.

Bertschinger, E. (1998). Simulations of Structure Formation in the Universe. *ARAA*, 36:599–654.

Biffi, V., Dolag, K., Boehringer, H., and Lemson, G. (2011). PHOX: X-ray Photon Simulator. Astrophysics Source Code Library.

Biffi, V., Dolag, K., Böhringer, H., and Lemson, G. (2012). Observing simulated galaxy clusters with PHOX: a novel X-ray photon simulator. *MNRAS*, 420:3545–3556.

Boulade, O., Charlot, X., Abbon, P., Aune, S., Borgeaud, P., Carton, P.-H., Carty, M., Da Costa, J., Deschamps, H., Desforge, D., Eppellé, D., Gallais, P., Gosset, L., Granelli, R., Gros, M., de Kat, J., Loiseau, D., Ritou, J.-., Roussé, J. Y., Starzynski, P., Vignal, N., and Vigroux, L. G. (2003). MegaCam: the new Canada-France-Hawaii Telescope wide-field imaging camera. In Iye, M. and Moorwood, A. F. M., editors, *Instrument Design and Performance for Optical/Infrared Ground-based Telescopes*, volume 4841 of *procspie*, pages 72–81.

Bower, R. G. (1997). The Entropy-Driven X-ray Evolution of Galaxy Clusters. *MNRAS*, 288:355–364.

Brainerd, T. G., Blandford, R. D., and Smail, I. (1996). Weak Gravitational Lensing by Galaxies - Implications for Dark Matter Halos. In *American Astronomical Society Meeting Abstracts #188*, volume 28 of *Bulletin of the American Astronomical Society*, page 843.

Brax, P., van de Bruck, C., Davis, A.-C., and Shaw, D. J. (2008). f(R) gravity and chameleon theories. *PRD*, 78(10):104021.

Bridle, S., Shawe-Taylor, J., Amara, A., Applegate, D., Balan, Berge Joel, S. T., Bernstein, G., Dahle, H., Erben, T., Gill, M., Heavens, A., Heymans, C., High, F. W., Hoekstra, H., Jarvis, M., Kirk, D., Kitching, T., Kneib, J.-P., Kuijken, K., Lagatutta, D., Mandelbaum, R., Massey, R., Mellier, Y., Moghaddam, B., Moudden, Y., Nakajima, R., Paulin-Henriksson, S., Pires, S., Rassat, A., Refregier, A., Rhodes, J., Schrabback, T., Semboloni, E., Shmakova, M., van Waerbeke, L., Witherick, D., Voigt, L., and Wittman, D. (2009). Handbook for the GREAT08 Challenge: An image analysis competition for cosmological lensing. *Annals of Applied Statistics*, 3:6–37.

Briel, U. G., Henry, J. P., and Boehringer, H. (1992). Observation of the Coma cluster of galaxies with ROSAT during the all-sky survey. *AAP*, 259:L31–L34.

Bryan, G. L. and Norman, M. L. (1998). Statistical Properties of X-Ray Clusters: Analytic and Numerical Comparisons. *ApJ*, 495:80–99.

Bryan, G. L., Norman, M. L., O'Shea, B. W., Abel, T., Wise, J. H., Turk, M. J., Reynolds, D. R., Collins, D. C., Wang, P., Skillman, S. W., Smith, B., Harkness, R. P., Bordner, J., Kim, J.-h., Kuhlen, M., Xu, H., Goldbaum, N., Hummels, C., Kritsuk, A. G., Tasker, E., Skory, S., Simpson, C. M., Hahn, O., Oishi, J. S., So, G. C., Zhao, F., Cen, R., Li, Y., and Enzo Collaboration (2014). ENZO: An Adaptive Mesh Refinement Code for Astrophysics. *ApJS*, 211:19.

Buchdahl, H. A. (1970). Non-linear Lagrangians and cosmological theory. *MNRAS*, 150:1.

Burikham, P. and Panpanich, S. (2012). Effects of Chameleon Scalar Field on Rotation Curves of the Galaxies. *Int. J. Mod. Phys.*, D21:1250041.

Burikham, P. and Panpanich, S. (2012). Effects of Chameleon Scalar Field on Rotation Curves of the Galaxies. *Int. J. Mod. Phys. D*, 21:1250041–1–1250041–25.

Calabrese, E., Cooray, A., Martinelli, M., Melchiorri, A., Pagano, L., Slosar, A., and Smoot, G. F. (2009). CMB lensing constraints on dark energy and modified gravity scenarios. *PRD*, 80(10):103516.

Capozziello, S. (2002). Curvature quintessence. *Int.J.Mod.Phys.*, D11:483–492.

Carroll, S. (2002). Dark Energy and the Preposterous Universe. In *KITP: Colloquium Series*.

Carroll, S. M. (1997). Lecture Notes on General Relativity. *ArXiv e-prints*.

Cash, W. (1979). Parameter estimation in astronomy through application of the likelihood ratio. *APJ*, 228:939–947.

Castander, F. J., Nichol, R. C., Merrelli, A., Burles, S., Pope, A., Connolly, A. J., Uomoto, A., Gunn, J. E., Anderson, J. E., Annis, J., Bahcall, N. A., Boroski, W. N., Brinkmann, J., Carey, L., Crocker, J. H., Csabai, I., Doi, M., Frieman, J. A., Fukugita, M., Friedman, S. D., Hilton, E. J., Hindsley, R. B., Ivezić, Ž., Kent, S., Lamb, D. Q., Leger, R. F., Long, D. C., Loveday, J., Lupton, R. H., MacGillivray, H., Meiksin, A., Munn, J. A., Newcomb, M., Okamura, S., Owen, R., Pier, J. R., Rockosi, C. M., Schlegel, D. J., Schneider, D. P., Seigmund, W., Smee, S., Snir, Y., Starkman, L., Stoughton, C., Szokoly, G. P., Stubbs, C., SubbaRao, M., Szalay, A., Thakar, A. R., Tremonti, C., Waddell, P., Yanny, B., and York, D. G. (2001). The First Hour of Extragalactic Data of the Sloan Digital Sky Survey Spectroscopic Commissioning: The Coma Cluster. *AJ*, 121:2331–2357.

Cataneo, M., Rapetti, D., Schmidt, F., Mantz, A. B., Allen, S. W., Applegate, D. E., Kelly, P. L., von der Linden, A., and Morris, R. G. (2015). New constraints on f (R) gravity from clusters of galaxies. *PRD*, 92(4):044009.

Cataneo, M., Rapetti, D., Schmidt, F., Mantz, A. B., Allen, S. W., Applegate, D. E., Kelly, P. L., von der Linden, A., and Morris, R. G. (2015). New constraints on $f(R)$ gravity from clusters of galaxies. *Phys. Rev.*, D92(4):044009.

Cavaliere, A. and Fusco-Femiano, R. (1978). The Distribution of Hot Gas in Clusters of Galaxies. *A&A*, 70:677.

Chang, P. and Hui, L. (2011). Stellar Structure and Tests of Modified Gravity. *APJ*, 732:25.

Chiba, T., Smith, T. L., and Erickcek, A. L. (2007). Solar System constraints to general f(R) gravity. *PRD*, 75(12):124014.

Churazov, E., Vikhlinin, A., Zhuravleva, I., Schekochihin, A., Parrish, I., Sunyaev, R., Forman, W., Böhringer, H., and Randall, S. (2012). X-ray surface brightness and gas density fluctuations in the Coma cluster. *MNRAS*, 421:1123–1135.

Clifton, T., Ferreira, P. G., Padilla, A., and Skordis, C. (2012). Modified gravity and cosmology. *Phys. Rep.*, 513:1–189.

Coe, D., Benítez, N., Broadhurst, T., and Moustakas, L. A. (2010). A High-resolution Mass Map of Galaxy Cluster Substructure: LensPerfect Analysis of A1689. *ApJ*, 723:1678–1702.

Cole, S. and Lacey, C. (1996). The structure of dark matter haloes in hierarchical clustering models. *MNRAS*, 281:716.

Colless, M. and Dunn, A. M. (1996). Structure and Dynamics of the Coma Cluster. *ApJ*, 458:435.

Covone, G., Sereno, M., Kilbinger, M., and Cardone, V. F. (2014). Measurement of the Halo Bias from Stacked Shear Profiles of Galaxy Clusters. *ApJL*, 784:L25.

Daniel, S. F., Linder, E. V., Smith, T. L., Caldwell, R. R., Cooray, A., Leauthaud, A., and Lombriser, L. (2010). Testing general relativity with current cosmological data. *PRD*, 81(12):123508.

Davis, A.-C., Lim, E. A., Sakstein, J., and Shaw, D. J. (2012). Modified gravity makes galaxies brighter. *PRD*, 85(12):123006.

de Jong, J. T. A., Kuijken, K., Applegate, D., Begeman, K., Belikov, A., Blake, C., Bout, J., Boxhoorn, D., Buddelmeijer, H., Buddendiek, A., Cacciato, M., Capaccioli, M., Choi, A., Cordes, O., Covone, G., Dall'Ora, M., Edge, A., Erben, T., Franse, J., Getman, F., Grado, A., Harnois-Deraps, J., Helmich, E., Herbonnet, R., Heymans, C., Hildebrandt, H., Hoekstra, H., Huang, Z., Irisarri, N., Joachimi, B., Köhlinger, F., Kitching, T., La Barbera, F., Lacerda, P., McFarland, J., Miller, L., Nakajima, R., Napolitano, N. R., Paolillo, M., Peacock, J., Pila-Diez, B., Puddu, E., Radovich, M., Rifatto, A., Schneider, P., Schrabback, T., Sifon, C., Sikkema, G., Simon, P., Sutherland, W., Tudorica, A., Valentijn, E., van der Burg, R., van Uitert, E., van Waerbeke, L., Velander, M., Kleijn, G. V., Viola, M., and Vriend, W.-J. (2013a). The Kilo-Degree Survey. *The Messenger*, 154:44–46.

de Jong, J. T. A., Verdoes Kleijn, G. A., Kuijken, K. H., and Valentijn, E. A. (2013b). The Kilo-Degree Survey. *Experimental Astronomy*, 35:25–44.

de Vaucouleurs, G. (1948). Recherches sur les Nebuleuses Extragalactiques. *Annales d'Astrophysique*, 11:247.

Dietrich, J. P. and Hartlap, J. (2010). Cosmology with the shear-peak statistics. *MNRAS*, 402:1049–1058.

Dossett, J., Hu, B., and Parkinson, D. (2014). Constraining models of f(R) gravity with Planck and WiggleZ power spectrum data. *JCAP*, 3:46.

Dubinski, J. and Carlberg, R. G. (1991). The structure of cold dark matter halos. *ApJ*, 378:496–503.

Durret, F., Adami, C., Cappi, A., Maurogordato, S., Márquez, I., Ilbert, O., Coupon, J., Arnouts, S., Benoist, C., Blaizot, J., Edorh, T. M., Garilli, B., Guennou, L., Le Brun, V., Le Fèvre, O., Mazure, A., McCracken, H. J., Mellier, Y., Mezrag, C., Slezak, E.,

Tresse, L., and Ulmer, M. P. (2011). Galaxy cluster searches based on photometric redshifts in the four CFHTLS Wide fields. *AAP*, 535:A65.

Dyson, F. W., Eddington, A. S., and Davidson, C. (1920). A determination of the deflection of light by the sun's gravitational field, from observations made at the total eclipse of may 29, 1919. *Philosophical Transactions of the Royal Society of London A: Mathematical, Physical and Engineering Sciences*, 220(571-581):291–333.

Ebeling, H., Edge, A. C., and Henry, J. P. (2001). MACS: A Quest for the Most Massive Galaxy Clusters in the Universe. *ApJ*, 553:668–676.

Einstein, A. (1916). Die Grundlage der allgemeinen Relativitätstheorie. *Annalen der Physik*, 354:769–822.

Eisenstein, D. J. (2005). Dark energy and cosmic sound [review article]. *NAR*, 49:360–365.

Eisenstein, D. J. and Hu, W. (1999). Power Spectra for Cold Dark Matter and Its Variants. *ApJ*, 511:5–15.

Erben, T., Hildebrandt, H., Miller, L., van Waerbeke, L., Heymans, C., and Hoekstra, H. (2013). CFHTLenS: the Canada-France-Hawaii Telescope Lensing Survey - imaging data and catalogue products. *MNRAS*, 433:2545–2563.

ESA (2015). *XMM-Newton Users Handbook*. ESA.

Ettori, S., Morandi, A., Tozzi, P., Balestra, I., Borgani, S., Rosati, P., Lovisari, L., and Terenziani, F. (2009). The cluster gas mass fraction as a cosmological probe: a revised study. *AAP*, 501:61–73.

Falck, B., Koyama, K., and Zhao, G.-B. (2015). Cosmic web and environmental dependence of screening: Vainshtein vs. chameleon. *JCAP*, 7:049.

Ferrarese, L. et al. (2000). A Database of Cepheid Distance Moduli and Tip of the Red Giant Branch, Globular Cluster Luminosity Function, Planetary Nebula Luminosity Function, and Surface Brightness Fluctuation Data Useful for Distance Determinations. *ApJS*, 128:431–459.

Fitchett, M. and Webster, R. (1987). Substructure in the Coma Cluster. *ApJ*, 317:653–667.

Ford, J., Hildebrandt, H., Van Waerbeke, L., Erben, T., Laigle, C., Milkeraitis, M., and Morrison, C. B. (2014). Cluster magnification and the mass-richness relation in CFHTLenS. *MNRAS*, 439:3755–3764.

Foreman-Mackey, D., Hogg, D. W., Lang, D., and Goodman, J. (2013). emcee: The MCMC Hammer. *PASP*, 125:306–312.

Forman, W., Jones, C., Cominsky, L., Julien, P., Murray, S., Peters, G., Tananbaum, H., and Giacconi, R. (1978). The fourth Uhuru catalog of X-ray sources. *ApJS*, 38:357–412.

Forman, W., Kellogg, E., Gursky, H., Tananbaum, H., and Giacconi, R. (1972). Observations of the Extended X-Ray Sources in the Perseus and Coma Clusters from UHURU. *ApJ*, 178:309–316.

Freedman, W. L. and Madore, B. F. (2010). A Physically Based Method for Scaling Cepheid Light Curves for Future Distance Determinations. *ApJ*, 719:335–340.

Freeman, P. E., Kashyap, V., Rosner, R., and Lamb, D. Q. (2002). A Wavelet-Based Algorithm for the Spatial Analysis of Poisson Data. *ApJS*, 138:185–218.

Friedman, H., Lichtman, S. W., and Byram, E. T. (1951). Photon counter measurements of solar x-rays and extreme ultraviolet light. *Phys. Rev.*, 83:1025–1030.

Friedmann, A. (1922). Über die Krümmung des Raumes. *Zeitschrift fur Physik*, 10:377–386.

Frieman, J. A., Turner, M. S., and Huterer, D. (2008). Dark Energy and the Accelerating Universe. *ARAA*, 46:385–432.

Gaunt, J. A. (1930). Continuous absorption. *Philosophical Transactions of the Royal Society of London A: Mathematical, Physical and Engineering Sciences*, 229(670-680):163–204.

Georgakakis, A., Georgantopoulos, I., Stewart, G. C., Shanks, T., and Boyle, B. J. (2003). The XMM-Newton/2dF survey - I. X-ray properties of normal galaxies. *MNRAS*, 344:161–168.

Giacconi, R. (2003). Nobel Lecture: The dawn of x-ray astronomy. *Reviews of Modern Physics*, 75:995–1010.

Giannantonio, T., Martinelli, M., Silvestri, A., and Melchiorri, A. (2010). New constraints on parametrised modified gravity from correlations of the CMB with large scale structure. *JCAP*, 4:30.

Gilks, W., Richardson, S., and Spiegelhalter, D. (1996). *Markov Chain Monte Carlo in Practice*. Chapman and Hall.

Gleyzes, J., Langlois, D., Piazza, F., and Vernizzi, F. (2015). Exploring gravitational theories beyond Horndeski. *JCAP*, 2:018.

Grego, L., Carlstrom, J. E., Reese, E. D., Holder, G. P., Holzapfel, W. L., Joy, M. K., Mohr, J. J., and Patel, S. (2001). Galaxy cluster gas mass fractions from Sunyaev-Zel'dovich effect measurements: Constraints on Omega(M). *Astrophys. J.*, 552:2.

Gronenschild, E. H. B. M. and Mewe, R. (1978). Calculated X-radiation from optically thin plasmas. III - Abundance effects on continuum emission. *AAPS*, 32:283–305.

Gunn, J. E., Carr, M., Rockosi, C., Sekiguchi, M., Berry, K., Elms, B., de Haas, E., Ivezić, Ž., Knapp, G., Lupton, R., Pauls, G., Simcoe, R., Hirsch, R., Sanford, D., Wang, S., York, D., Harris, F., Annis, J., Bartozek, L., Boroski, W., Bakken, J., Haldeman, M., Kent, S., Holm, S., Holmgren, D., Petravick, D., Prosapio, A., Rechenmacher, R., Doi, M., Fukugita, M., Shimasaku, K., Okada, N., Hull, C., Siegmund, W., Mannery, E., Blouke, M., Heidtman, D., Schneider, D., Lucinio, R., and Brinkman, J. (1998). The Sloan Digital Sky Survey Photometric Camera. *AJ*, 116:3040–3081.

Haas, M. R., Schaye, J., and Jeeson-Daniel, A. (2012). Disentangling galaxy environment and host halo mass. *MNRAS*, 419:2133–2146.

Haberl, F., Sturm, R., Ballet, J., Bomans, D. J., Buckley, D. A. H., Coe, M. J., Corbet, R., Ehle, M., Filipovic, M. D., Gilfanov, M., Hatzidimitriou, D., La Palombara, N., Mereghetti, S., Pietsch, W., Snowden, S., and Tiengo, A. (2012). The XMM-Newton survey of the Small Magellanic Cloud. *AAP*, 545:A128.

Hammami, A., Llinares, C., Mota, D. F., and Winther, H. A. (2015). Hydrodynamic effects in the symmetron and f(R)-gravity models. *MNRAS*, 449:3635–3644.

Hao, J., McKay, T. A., Koester, B. P., Rykoff, E. S., Rozo, E., Annis, J., Wechsler, R. H., Evrard, A., Siegel, S. R., Becker, M., Busha, M., Gerdes, D., Johnston, D. E., and Sheldon, E. (2010). A GMBCG Galaxy Cluster Catalog of 55,424 Rich Clusters from SDSS DR7. *ApJS*, 191:254–274.

Hasselfield, M., Hilton, M., Marriage, T. A., Addison, G. E., Barrientos, L. F., Battaglia, N., Battistelli, E. S., Bond, J. R., Crichton, D., Das, S., Devlin, M. J., Dicker, S. R., Dunkley, J., Dünner, R., Fowler, J. W., Gralla, M. B., Hajian, A., Halpern, M., Hincks, A. D., Hlozek, R., Hughes, J. P., Infante, L., Irwin, K. D., Kosowsky, A., Marsden, D., Menanteau, F., Moodley, K., Niemack, M. D., Nolta, M. R., Page, L. A., Partridge, B., Reese, E. D., Schmitt, B. L., Sehgal, N., Sherwin, B. D., Sievers, J., Sifón, C., Spergel, D. N., Staggs, S. T., Swetz, D. S., Switzer, E. R., Thornton, R., Trac, H., and Wollack, E. J. (2013). The Atacama Cosmology Telescope: Sunyaev-Zel'dovich selected galaxy clusters at 148 GHz from three seasons of data. *JCAP*, 7:008.

Hastings, W. K. (1970). Monte carlo sampling methods using markov chains and their applications. *Biometrika*, 57(1):97–109.

Heisenberg, W. (1927). Über den anschaulichen Inhalt der quantentheoretischen Kinematik und Mechanik. *Zeitschrift fur Physik*, 43:172–198.

Herrnstein, J. R., Moran, J. M., Greenhill, L. J., and Trotter, A. S. (2005). The Geometry of and Mass Accretion Rate through the Maser Accretion Disk in NGC 4258. *ApJ*, 629:719–738.

Heymans, C., Van Waerbeke, L., Miller, L., Erben, T., and Hildebrandt, H. (2012). CFHTLenS: the Canada-France-Hawaii Telescope Lensing Survey. *MNRAS*, 427:146–166.

Hildebrandt, H., Erben, T., Kuijken, K., van Waerbeke, L., Heymans, C., Coupon, J., and Benjamin, J. (2012). CFHTLenS: improving the quality of photometric redshifts with precision photometry. *MNRAS*, 421:2355–2367.

Hinshaw, G., Weiland, J. L., Hill, R. S., Odegard, N., Larson, D., Bennett, C. L., Dunkley, J., Gold, B., Greason, M. R., Jarosik, N., Komatsu, E., Nolta, M. R., Page, L., Spergel, D. N., Wollack, E., Halpern, M., Kogut, A., Limon, M., Meyer, S. S., Tucker, G. S., and Wright, E. L. (2009). Five-Year Wilkinson Microwave Anisotropy Probe Observations: Data Processing, Sky Maps, and Basic Results. *ApJS*, 180:225–245.

Hoekstra, H., Herbonnet, R., Muzzin, A., Babul, A., Mahdavi, A., Viola, M., and Cacciato, M. (2015). The Canadian Cluster Comparison Project: detailed study of systematics and updated weak lensing masses. *ArXiv e-prints*.

Hoekstra, H., Mahdavi, A., Babul, A., and Bildfell, C. (2012). The Canadian Cluster Comparison Project: weak lensing masses and SZ scaling relations. *MNRAS*, 427:1298–1311.

Hood, R. and Mann, R. (2015). Characterising the optical properties of galaxy clusters with GMPhoRCC. *MNRAS submitted*.

Hu, B., Liguori, M., Bartolo, N., and Matarrese, S. (2013). Parametrized modified gravity constraints after Planck. *PRD*, 88(12):123514.

Hu, W. and Kravtsov, A. V. (2003). Sample Variance Considerations for Cluster Surveys. *ApJ*, 584:702–715.

Hu, W. and Sawicki, I. (2007). Models of f(R) Cosmic Acceleration that Evade Solar-System Tests. *PRD*, 76:064004.

Hubble, E. (1929). A Relation between Distance and Radial Velocity among Extra-Galactic Nebulae. *Proceedings of the National Academy of Science*, 15:168–173.

Hui, L., Nicolis, A., and Stubbs, C. W. (2009). Equivalence principle implications of modified gravity models. *PRD*, 80(10):104002.

Israel, H., Schellenberger, G., Nevalainen, J., Massey, R., and Reiprich, T. H. (2015). Reconciling Planck cluster counts and cosmology? Chandra/XMM instrumental calibration and hydrostatic mass bias. *MNRAS*, 448:814–821.

Jain, B. (2011). Designing surveys for tests of gravity. *Philosophical Transactions of the Royal Society of London Series A*, 369:5081–5089.

Jain, B. and Van Waerbeke, L. (2000). Statistics of Dark Matter Halos from Gravitational Lensing. *ApJL*, 530:L1–L4.

Jain, B. and VanderPlas, J. (2011). Tests of modified gravity with dwarf galaxies. *JCAP*, 10:32.

Jain, B., Vikram, V., and Sakstein, J. (2013). Astrophysical Tests of Modified Gravity: Constraints from Distance Indicators in the Nearby Universe. *ApJ*, 779:39.

Jain, R. K., Kouvaris, C., and Grønlund Nielsen, N. (2015). White Dwarf Critical Tests for Modified Gravity. *ArXiv e-prints*.

Jansen, F., Lumb, D., Altieri, B., Clavel, J., Ehle, M., Erd, C., Gabriel, C., Guainazzi, M., Gondoin, P., Much, R., Munoz, R., Santos, M., Schartel, N., Texier, D., and Vacanti, G. (2001). XMM-Newton observatory. I. The spacecraft and operations. *AAP*, 365:L1–L6.

Jarvis, M., Jain, B., Bernstein, G., and Dolney, D. (2006). Dark Energy Constraints from the CTIO Lensing Survey. *ApJ*, 644:71–79.

Jarvis, M., Sheldon, E., Zuntz, J., Kacprzak, T., Bridle, S. L., Amara, A., Armstrong, R., Becker, M. R., Bernstein, G. M., Bonnett, C., Chang, C., Das, R., Dietrich, J. P., Drlica-Wagner, A., Eifler, T. F., Gangkofner, C., Gruen, D., Hirsch, M., Huff, E. M., Jain, B., Kent, S., Kirk, D., MacCrann, N., Melchior, P., Plazas, A. A., Refregier, A., Rowe, B., Rykoff, E. S., Samuroff, S., Sánchez, C., Suchyta, E., Troxel, M. A., Vikram, V., Abbott, T., Abdalla, F. B., Allam, S., Annis, J., Benoit-Lévy, A., Bertin, E.,

Brooks, D., Buckley-Geer, E., Burke, D. L., Capozzi, D., Carnero Rosell, A., Carrasco Kind, M., Carretero, J., Castander, F. J., Crocce, M., Cunha, C. E., D'Andrea, C. B., da Costa, L. N., DePoy, D. L., Desai, S., Diehl, H. T., Doel, P., Fausti Neto, A., Flaugher, B., Fosalba, P., Frieman, J., Gaztanaga, E., Gerdes, D. W., Gruendl, R. A., Gutierrez, G., Honscheid, K., James, D. J., Kuehn, K., Kuropatkin, N., Lahav, O., Li, T. S., Lima, M., March, M., Martini, P., Miquel, R., Mohr, J. J., Neilsen, E., Nord, B., Ogando, R., Reil, K., Romer, A. K., Roodman, A., Sako, M., Sanchez, E., Scarpine, V., Schubnell, M., Sevilla-Noarbe, I., Smith, R. C., Soares-Santos, M., Sobreira, F., Swanson, M. E. C., Tarle, G., Thaler, J., Thomas, D., Walker, A. R., and Wechsler, R. H. (2015). The DES Science Verification Weak Lensing Shear Catalogs. *ArXiv e-prints*.

Jee, M. J., Tyson, J. A., Hilbert, S., Schneider, M. D., Schmidt, S., and Wittman, D. (2015). Cosmic Shear Results from the Deep Lens Survey - II: Full Cosmological Parameter Constraints from Tomography. *ArXiv e-prints*.

Johnston, D. E., Sheldon, E. S., Wechsler, R. H., Rozo, E., Koester, B. P., Frieman, J. A., McKay, T. A., Evrard, A. E., Becker, M. R., and Annis, J. (2007). Cross-correlation Weak Lensing of SDSS galaxy Clusters II: Cluster Density Profiles and the Mass–Richness Relation. *ArXiv e-prints*.

Joyce, A., Jain, B., Khoury, J., and Trodden, M. (2014). Beyond the Cosmological Standard Model. *ArXiv e-prints*.

Jungman, G., Kamionkowski, M., and Griest, K. (1996). Supersymmetric dark matter. *Phys. Rep.*, 267:195–373.

Kaastra, J. S., Paerels, F. B. S., Durret, F., Schindler, S., and Richter, P. (2008). Thermal radiation processes. *Space Sci. Rev.*, 134:155.

Kaiser, N. (1986). Evolution and clustering of rich clusters. *MNRAS*, 222:323–345.

Kaiser, N. (1987). Clustering in real space and in redshift space. *MNRAS*, 227:1–21.

Kaiser, N. and Squires, G. (1993). Mapping the dark matter with weak gravitational lensing. *ApJ*, 404:441–450.

Kaiser, N., Wilson, G., and Luppino, G. A. (2000). Large-Scale Cosmic Shear Measurements. *ArXiv e-prints*.

Kalberla, P. M. W., Burton, W. B., Hartmann, D., Arnal, E. M., Bajaja, E., Morras, R., and Pöppel, W. G. L. (2005). The Leiden/Argentine/Bonn (LAB) Survey of Galactic HI. Final data release of the combined LDS and IAR surveys with improved stray-radiation corrections. *A&A*, 440:775–782.

Kellogg, E., Gursky, H., Leong, C., Schreier, E., Tananbaum, H., and Giacconi, R. (1971). X-Ray Observations of the Virgo Cluster, NGC 5128, and 3c 273 from the UHURU Satellite. *ApJL*, 165:L49.

Kettula, K., Giodini, S., van Uitert, E., Hoekstra, H., Finoguenov, A., Lerchster, M., Erben, T., Heymans, C., Hildebrandt, H., Kitching, T. D., Mahdavi, A., Mellier, Y., Miller, L., Mirkazemi, M., Van Waerbeke, L., Coupon, J., Egami, E., Fu, L., Hudson,

M. J., Kneib, J. P., Kuijken, K., McCracken, H. J., Pereira, M. J., Rowe, B., Schrabback, T., Tanaka, M., and Velander, M. (2015). CFHTLenS: weak lensing calibrated scaling relations for low-mass clusters of galaxies. *MNRAS*, 451:1460–1481.

Khoury, J. and Weltman, A. (2004). Chameleon fields: Awaiting surprises for tests of gravity in space. *PRL*, 93:171104.

Kilbinger, M., Fu, L., Heymans, C., Simpson, F., Benjamin, J., Erben, T., Harnois-Déraps, J., Hoekstra, H., Hildebrandt, H., Kitching, T. D., Mellier, Y., Miller, L., Van Waerbeke, L., Benabed, K., Bonnett, C., Coupon, J., Hudson, M. J., Kuijken, K., Rowe, B., Schrabback, T., Semboloni, E., Vafaei, S., and Velander, M. (2013). CFHTLenS: combined probe cosmological model comparison using 2D weak gravitational lensing. *MNRAS*, 430:2200–2220.

Kimura, R., Kobayashi, T., and Yamamoto, K. (2012). Vainshtein screening in a cosmological background in the most general second-order scalar-tensor theory. *PRD*, 85(2):024023.

Kneib, J.-P. and Natarajan, P. (2011). Cluster lenses. *AApR*, 19:47.

Koyama, K., Niz, G., and Tasinato, G. (2011). Strong interactions and exact solutions in nonlinear massive gravity. *PRD*, 84(6):064033.

Koyama, K. and Sakstein, J. (2015). Astrophysical probes of the Vainshtein mechanism: Stars and galaxies. *PRD*, 91(12):124066.

Lam, T. Y., Nishimichi, T., Schmidt, F., and Takada, M. (2012). Testing Gravity with the Stacked Phase Space around Galaxy Clusters. *PRL*, 109(5):051301.

Larmor, J. (1897). A Dynamical Theory of the Electric and Luminiferous Medium. Part III. Relations with Material Media. *Philosophical Transactions of the Royal Society of London Series A*, 190:205–300.

Lau, E. T., Kravtsov, A. V., and Nagai, D. (2009). Residual Gas Motions in the Intracluster Medium and Bias in Hydrostatic Measurements of Mass Profiles of Clusters. *ApJ*, 705:1129–1138.

Laud, B. B. (2011). *Electromagnetics* . New Age Publishers.

Laureijs, R., Amiaux, J., Arduini, S., Augueres, J. ., Brinchmann, J., Cole, R., Cropper, M., Dabin, C., Duvet, L., Ealet, A., and et al. (2011). Euclid Definition Study Report. *ArXiv e-prints*.

Lea, S. M., Silk, J., Kellogg, E., and Murray, S. (1973). Thermal-Bremsstrahlung Interpretation of Cluster X-Ray Sources. *ApJL*, 184:L105.

Lemaître, G. (1931). Expansion of the universe, A homogeneous universe of constant mass and increasing radius accounting for the radial velocity of extra-galactic nebulae. *MNRAS*, 91:483–490.

Li, B. and Barrow, J. D. (2011a). N-body simulations for coupled scalar-field cosmology. *PRD*, 83(2):024007.

Li, B. and Barrow, J. D. (2011b). On the effects of coupled scalar fields on structure formation. *MNRAS*, 413:262–270.

Li, B., He, J.-h., and Gao, L. (2016). Cluster gas fraction as a test of gravity. *MNRAS*, 456:146–155.

Li, B., Hellwing, W. A., Koyama, K., Zhao, G.-B., Jennings, E., and Baugh, C. M. (2013). The non-linear matter and velocity power spectra in f(R) gravity. *MNRAS*, 428:743–755.

Li, B., Zhao, G.-B., Teyssier, R., and Koyama, K. (2012). ECOSMOG: an Efficient COde for Simulating MOdified Gravity. *JCAP*, 1:51.

Limousin, M., Morandi, A., Sereno, M., Meneghetti, M., Ettori, S., Bartelmann, M., and Verdugo, T. (2013). The Three-Dimensional Shapes of Galaxy Clusters. *SSR*, 177:155–194.

Linder, E. V. and Jenkins, A. (2003). Cosmic structure growth and dark energy. *MNRAS*, 346(2):573–583.

Liu, J., Ortiz-Vazquez, A., and Hill, J. C. (2016). Constraining Multiplicative Bias in CFHTLenS Weak Lensing Shear Data. *ArXiv e-prints*.

Lloyd-Davies, E. J., Romer, A. K., Mehrtens, N., Hosmer, M., Davidson, M., Sabirli, K., Mann, R. G., Hilton, M., Liddle, A. R., Viana, P. T. P., Campbell, H. C., Collins, C. A., Dubois, E. N., Freeman, P., Harrison, C. D., Hoyle, B., Kay, S. T., Kuwertz, E., Miller, C. J., Nichol, R. C., Sahlén, M., Stanford, S. A., and Stott, J. P. (2011). The XMM Cluster Survey: X-ray analysis methodology. *MNRAS*, 418:14–53.

Lombriser, L. (2014). Constraining chameleon models with cosmology. *Annalen der Physik*, 526:259–282.

Lombriser, L., Koyama, K., and Li, B. (2014). Halo modelling in chameleon theories. *JCAP*, 3:21.

Lombriser, L., Koyama, K., Zhao, G.-B., and Li, B. (2012a). Chameleon f(R) gravity in the virialized cluster. *PRD*, 85(12):124054.

Lombriser, L., Schmidt, F., Baldauf, T., Mandelbaum, R., Seljak, U., and Smith, R. E. (2012b). Cluster density profiles as a test of modified gravity. *PRD*, 85(10):102001.

Longair, M. (2011). *High Energy Astrophysics*. Cambridge University Press.

LSST Dark Energy Science Collaboration (2012). Large Synoptic Survey Telescope: Dark Energy Science Collaboration. *ArXiv e-prints*.

Lumb, D. H., Warwick, R. S., Page, M., and De Luca, A. (2002). X-ray background measurements with XMM-Newton EPIC. *AAP*, 389:93–105.

MacKay, D. J. C. (2003). *Information Theory, Inference and Learning Algorithms*. Cambrdige University Press. http://www.inference.phy.cam.ac.uk/mackay/itprnn/book.html.

Makino, N., Sasaki, S., and Suto, Y. (1998). X-Ray Gas Density Profile of Clusters of Galaxies from the Universal Dark Matter Halo. *ApJ*, 497:555–558.

Mantz, A. B., von der Linden, A., Allen, S. W., Applegate, D. E., Kelly, P. L., Morris, R. G., Rapetti, D. A., Schmidt, R. W., Adhikari, S., Allen, M. T., Burchat, P. R., Burke, D. L., Cataneo, M., Donovan, D., Ebeling, H., Shandera, S., and Wright, A. (2015). Weighing the giants - IV. Cosmology and neutrino mass. *MNRAS*, 446:2205–2225.

Maoli, R., Van Waerbeke, L., Mellier, Y., Schneider, P., Jain, B., Bernardeau, F., Erben, T., and Fort, B. (2001). Cosmic shear analysis in 50 uncorrelated vlt fields. implications for omega˙0, sigma˙8. *A&A*, 368:766–775.

Markevitch, M., Gonzalez, A. H., Clowe, D., Vikhlinin, A., Forman, W., Jones, C., Murray, S., and Tucker, W. (2004). Direct Constraints on the Dark Matter Self-Interaction Cross Section from the Merging Galaxy Cluster 1E 0657-56. *ApJ*, 606:819–824.

Martin, J. (2012). Everything you always wanted to know about the cosmological constant problem (but were afraid to ask). *Comptes Rendus Physique*, 13:566–665.

Massey, R., Hoekstra, H., Kitching, T., Rhodes, J., Cropper, M., Amiaux, J., Harvey, D., Mellier, Y., Meneghetti, M., Miller, L., Paulin-Henriksson, S., Pires, S., Scaramella, R., and Schrabback, T. (2013). Origins of weak lensing systematics, and requirements on future instrumentation (or knowledge of instrumentation). *MNRAS*, 429:661–678.

Matsushita, K., Böhringer, H., Takahashi, I., and Ikebe, Y. (2007). The abundance pattern of O, Mg, Si, and Fe in the intracluster medium of the Centaurus cluster observed with XMM-Newton. *AAP*, 462:953–963.

Maughan, B. J., Giles, P. A., Randall, S. W., Jones, C., and Forman, W. R. (2012). Self-similar scaling and evolution in the galaxy cluster X-ray luminosity-temperature relation. *MNRAS*, 421:1583–1602.

Maughan, B. J., Giles, P. A., Rines, K. J., Diaferio, A., Geller, M. J., Van Der Pyl, N., and Bonamente, M. (2015). Hydrostatic and Caustic Mass Profiles of Galaxy Clusters. *ArXiv e-prints*.

Maxwell, J. (1860). On the Dynamical Theory of Gases. *Scientific Letters*, 1:616.

Mazzali, P. A., Röpke, F. K., Benetti, S., and Hillebrandt, W. (2007). A Common Explosion Mechanism for Type Ia Supernovae. *Science*, 315:825.

McKay, T. A., Sheldon, E. S., Racusin, J., Fischer, P., Seljak, U., Stebbins, A., Johnston, D., Frieman, J. A., Bahcall, N., Brinkmann, J., Csabai, I., Fukugita, M., Hennessy, G. S., Ivezic, Z., Lamb, D. Q., Loveday, J., Lupton, R. H., Munn, J. A., Nichol, R. C., Pier, J. R., and York, D. G. (2001). Galaxy Mass and Luminosity Scaling Laws Determined by Weak Gravitational Lensing. *ArXiv e-prints*.

Mehrtens, N., Romer, A. K., Hilton, M., Lloyd-Davies, E. J., Miller, C. J., Stanford, S. A., Hosmer, M., Hoyle, B., Collins, C. A., Liddle, A. R., Viana, P. T. P., Nichol, R. C., Stott, J. P., Dubois, E. N., Kay, S. T., Sahlén, M., Young, O., Short, C. J.,

Christodoulou, L., Watson, W. A., Davidson, M., Harrison, C. D., Baruah, L., Smith, M., Burke, C., Mayers, J. A., Deadman, P.-J., Rooney, P. J., Edmondson, E. M., West, M., Campbell, H. C., Edge, A. C., Mann, R. G., Sabirli, K., Wake, D., Benoist, C., da Costa, L., Maia, M. A. G., and Ogando, R. (2012). The XMM Cluster Survey: optical analysis methodology and the first data release. *MNRAS*, 423:1024–1052.

Melchior, P., Suchyta, E., Huff, E., Hirsch, M., Kacprzak, T., Rykoff, E., Gruen, D., Armstrong, R., Bacon, D., Bechtol, K., Bernstein, G. M., Bridle, S., Clampitt, J., Honscheid, K., Jain, B., Jouvel, S., Krause, E., Lin, H., MacCrann, N., Patton, K., Plazas, A., Rowe, B., Vikram, V., Wilcox, H., Young, J., Zuntz, J., Abbott, T., Abdalla, F. B., Allam, S. S., Banerji, M., Bernstein, J. P., Bernstein, R. A., Bertin, E., Buckley-Geer, E., Burke, D. L., Castander, F. J., da Costa, L. N., Cunha, C. E., Depoy, D. L., Desai, S., Diehl, H. T., Doel, P., Estrada, J., Evrard, A. E., Neto, A. F., Fernandez, E., Finley, D. A., Flaugher, B., Frieman, J. A., Gaztanaga, E., Gerdes, D., Gruendl, R. A., Gutierrez, G. R., Jarvis, M., Karliner, I., Kent, S., Kuehn, K., Kuropatkin, N., Lahav, O., Maia, M. A. G., Makler, M., Marriner, J., Marshall, J. L., Merritt, K. W., Miller, C. J., Miquel, R., Mohr, J., Neilsen, E., Nichol, R. C., Nord, B. D., Reil, K., Roe, N. A., Roodman, A., Sako, M., Sanchez, E., Santiago, B. X., Schindler, R., Schubnell, M., Sevilla-Noarbe, I., Sheldon, E., Smith, C., Soares-Santos, M., Swanson, M. E. C., Sypniewski, A. J., Tarle, G., Thaler, J., Thomas, D., Tucker, D. L., Walker, A., Wechsler, R., Weller, J., and Wester, W. (2015). Mass and galaxy distributions of four massive galaxy clusters from Dark Energy Survey Science Verification data. *MNRAS*, 449:2219–2238.

Metropolis, N., Rosenbluth, A. W., Rosenbluth, M. N., Teller, A. H., and Teller, E. (1953). Equation of state calculations by fast computing machines. *The journal of chemical physics*, 21(6):1087–1092.

Mewe, R., Gronenschild, E. H. B. M., and van den Oord, G. H. J. (1985). Calculated X-radiation from optically thin plasmas. V. *A&AS*, 62:197–254.

Milgrom, M. (1983). A modification of the Newtonian dynamics as a possible alternative to the hidden mass hypothesis. *ApJ*, 270:365–370.

Milkeraitis, M., van Waerbeke, L., Heymans, C., Hildebrandt, H., Dietrich, J. P., and Erben, T. (2010). 3D-Matched-Filter galaxy cluster finder - I. Selection functions and CFHTLS Deep clusters. *MNRAS*, 406:673–688.

Miller, L., Heymans, C., Kitching, T. D., van Waerbeke, L., Erben, T., Hildebrandt, H., and Hoekstra, H. (2013). Bayesian galaxy shape measurement for weak lensing surveys - III. Application to the Canada-France-Hawaii Telescope Lensing Survey. *MNRAS*, 429:2858–2880.

Mitsuda, K., Bautz, M., Inoue, H., Kelley, R. L., Koyama, K., Kunieda, H., Makishima, K., Ogawara, Y., Petre, R., Takahashi, T., Tsunemi, H., White, N. E., Anabuki, N., Angelini, L., Arnaud, K., Awaki, H., Bamba, A., Boyce, K., Brown, G. V., Chan, K.-W., Cottam, J., Dotani, T., Doty, J., Ebisawa, K., Ezoe, Y., Fabian, A. C., Figueroa, E., Fujimoto, R., Fukazawa, Y., Furusho, T., Furuzawa, A., Gendreau, K., Griffiths, R. E., Haba, Y., Hamaguchi, K., Harrus, I., Hasinger, G., Hatsukade, I., Hayashida, K., Henry, P. J., Hiraga, J. S., Holt, S. S., Hornschemeier, A., Hughes, J. P., Hwang, U., Ishida, M., Ishisaki, Y., Isobe, N., Itoh, M., Iyomoto, N., Kahn, S. M., Kamae,

T., Katagiri, H., Kataoka, J., Katayama, H., Kawai, N., Kilbourne, C., Kinugasa, K., Kissel, S., Kitamoto, S., Kohama, M., Kohmura, T., Kokubun, M., Kotani, T., Kotoku, J., Kubota, A., Madejski, G. M., Maeda, Y., Makino, F., Markowitz, A., Matsumoto, C., Matsumoto, H., Matsuoka, M., Matsushita, K., McCammon, D., Mihara, T., Misaki, K., Miyata, E., Mizuno, T., Mori, K., Mori, H., Morii, M., Moseley, H., Mukai, K., Murakami, H., Murakami, T., Mushotzky, R., Nagase, F., Namiki, M., Negoro, H., Nakazawa, K., Nousek, J. A., Okajima, T., Ogasaka, Y., Ohashi, T., Oshima, T., Ota, N., Ozaki, M., Ozawa, H., Parmar, A. N., Pence, W. D., Porter, F. S., Reeves, J. N., Ricker, G. R., Sakurai, I., Sanders, W. T., Senda, A., Serlemitsos, P., Shibata, R., Soong, Y., Smith, R., Suzuki, M., Szymkowiak, A. E., Takahashi, H., Tamagawa, T., Tamura, K., Tamura, T., Tanaka, Y., Tashiro, M., Tawara, Y., Terada, Y., Terashima, Y., Tomida, H., Torii, K., Tsuboi, Y., Tsujimoto, M., Tsuru, T. G., Turner, M. J. L. ., Ueda, Y., Ueno, S., Ueno, M., Uno, S., Urata, Y., Watanabe, S., Yamamoto, N., Yamaoka, K., Yamasaki, N. Y., Yamashita, K., Yamauchi, M., Yamauchi, S., Yaqoob, T., Yonetoku, D., and Yoshida, A. (2007). The X-Ray Observatory Suzaku. *PASJ*, 59:1–7.

Moran, C. C., Teyssier, R., and Li, B. (2015). Chameleon f(r) gravity on the virgo cluster scale. *Monthly Notices of the Royal Astronomical Society*, 448(1):307–327.

Morrison, R. and McCammon, D. (1983). Interstellar photoelectric absorption cross sections, 0.03-10 keV. *ApJ*, 270:119–122.

Mushotzky, R. (2004). How are AGN Found? In Barger, A. J., editor, *Supermassive Black Holes in the Distant Universe*, volume 308 of *Astrophysics and Space Science Library*, page 53.

Nagai, D., Kravtsov, A. V., and Vikhlinin, A. (2007). Effects of Galaxy Formation on Thermodynamics of the Intracluster Medium. *ApJ*, 668:1–14.

Narikawa, T. and Yamamoto, K. (2012). Testing gravity with halo density profiles observed through gravitational lensing. *JCAP*, 5:016.

Navarro, J. F., Frenk, C. S., and White, S. D. M. (1996). The Structure of Cold Dark Matter Halos. *ApJ*, 462:563.

Nelson, K., Lau, E. T., Nagai, D., Rudd, D. H., and Yu, L. (2014). Weighing Galaxy Clusters with Gas. II. On the Origin of Hydrostatic Mass Bias in ΛCDM Galaxy Clusters. *ApJ*, 782:107.

Nelson, K., Rudd, D. H., Shaw, L., and Nagai, D. (2012). Evolution of the Merger-induced Hydrostatic Mass Bias in Galaxy Clusters. *ApJ*, 751:121.

Nicolis, A., Rattazzi, R., and Trincherini, E. (2009). Galileon as a local modification of gravity. *PRD*, 79(6):064036.

Niikura, H., Takada, M., Okabe, N., Martino, R., and Takahashi, R. (2015). Detection of universality of dark matter profile from Subaru weak lensing measurements of 50 massive clusters. *PASJ*.

Nojiri, S. and Odintsov, S. D. (2003). Modified gravity with negative and positive powers of the curvature: Unification of the inflation and of the cosmic acceleration. *Phys.Rev.*, D68:123512.

Noller, J., von Braun-Bates, F., and Ferreira, P. G. (2014). Relativistic scalar fields and the quasistatic approximation in theories of modified gravity. *PRD*, 89(2):023521.

Oguri, M. and Hamana, T. (2011). Detailed cluster lensing profiles at large radii and the impact on cluster weak lensing studies. *MNRAS*, 414:1851–1861.

Oguri, M. and Takada, M. (2011). Combining cluster observables and stacked weak lensing to probe dark energy: Self-calibration of systematic uncertainties. *PRD*, 83(2):023008.

Okabe, N. and Smith, G. P. (2015). LoCuSS: Weak-lensing mass calibration of galaxy clusters. *ArXiv e-prints*.

Okabe, N., Zhang, Y.-Y., Finoguenov, A., Takada, M., Smith, G. P., Umetsu, K., and Futamase, T. (2010). LoCuSS: Calibrating Mass-observable Scaling Relations for Cluster Cosmology with Subaru Weak-lensing Observations. *ApJ*, 721:875–885.

Oppenheimer, J. R. and Volkoff, G. M. (1939). On Massive Neutron Cores. *Phys. Rev.*, 55:374–381.

Osterbrock, D. E. (1974). *Astrophysics of gaseous nebulae*. University Science Books.

Ostriker, J. P. and Vishniac, E. T. (1986). Effect of gravitational lenses on the microwave background, and 1146+111B,C. *Nat*, 322:804.

Ota, N. and Yoshida, H. (2015). Search for gas bulk motions in eight nearby clusters of galaxies with Suzaku. *ArXiv e-prints*.

Ota, N. and Yoshida, H. (2016). Search for gas bulk motions in eight nearby clusters of galaxies with Suzaku. *PASJ*.

Oyaizu, H. (2008a). Nonlinear evolution of f(R) cosmologies. I. Methodology. *PRD*, 78(12):123523.

Oyaizu, H. (2008b). Nonlinear evolution of f(R) cosmologies. I. Methodology. *PRD*, 78(12):123523.

Pacaud, F., Clerc, N., Giles, P. A., Adami, C., Sadibekova, T., Pierre, M., Maughan, B. J., Lieu, M., Le Fèvre, J.-P., Alis, S., Altieri, B., Ardila, F., Baldry, I., Benoist, C., Birkinshaw, M., Chiappetti, L., Démoclès, J., Eckert, D., Evrard, A. E., Faccioli, L., Gastaldello, F., Guennou, L., Horellou, C., Iovino, A., Koulouridis, E., Le Brun, V., Lidman, C., Liske, J., Maurogordato, S., Menanteau, F., Owers, M., Poggianti, B., Pomarède, D., Pompei, E., Ponman, T. J., Rapetti, D., Reiprich, T. H., Smith, G. P., Tuffs, R., Valageas, P., Valtchanov, I., Willis, J. P., and Ziparo, F. (2015). The XXL Survey. II. The bright cluster sample: catalogue and luminosity function. *ArXiv e-prints*.

Percival, W. J. and White, M. (2009). Testing cosmological structure formation using redshift-space distortions. *MNRAS*, 393:297–308.

Perlmutter, S. et al. (1999). Measurements of Ω and Λ from 42 High-Redshift Supernovae. *ApJ*, 517:565–586.

Phillips, M. M. (1993). The absolute magnitudes of Type IA supernovae. *ApJL*, 413:L105–L108.

Pierre, M., Pacaud, F., Adami, C., Alis, S., Altieri, B., Baran, B., Benoist, C., Birkinshaw, M., Bongiorno, A., Bremer, M. N., Brusa, M., Butler, A., Ciliegi, P., Chiappetti, L., Clerc, N., Corasaniti, P. S., Coupon, J., De Breuck, C., Democles, J., Desai, S., Delhaize, J., Devriendt, J., Dubois, Y., Eckert, D., Elyiv, A., Ettori, S., Evrard, A., Faccioli, L., Farahi, A., Ferrari, C., Finet, F., Fotopoulou, S., Fourmanoit, N., Gandhi, P., Gastaldello, F., Gastaud, R., Georgantopoulos, I., Giles, P., Guennou, L., Guglielmo, V., Horellou, C., Husband, K., Huynh, M., Iovino, A., Kilbinger, M., Koulouridis, E., Lavoie, S., Le Brun, A. M. C., Le Fevre, J. P., Lidman, C., Lieu, M., Lin, C. A., Mantz, A., Maughan, B. J., Maurogordato, S., McCarthy, I. G., McGee, S., Melin, J. B., Melnyk, O., Menanteau, F., Novak, M., Paltani, S., Plionis, M., Poggianti, B. M., Pomarede, D., Pompei, E., Ponman, T. J., Ramos-Ceja, M. E., Ranalli, P., Rapetti, D., Raychaudury, S., Reiprich, T. H., Rottgering, H., Rozo, E., Rykoff, E., Sadibekova, T., Santos, J., Sauvageot, J. L., Schimd, C., Sereno, M., Smith, G. P., Smolčić, V., Snowden, S., Spergel, D., Stanford, S., Surdej, J., Valageas, P., Valotti, A., Valtchanov, I., Vignali, C., Willis, J., and Ziparo, F. (2015). The XXL Survey: I. Scientific motivations - XMM-Newton observing plan - Follow-up observations and simulation programme. *ArXiv e-prints*.

Pierre, M., Valtchanov, I., Altieri, B., Andreon, S., Bolzonella, M., Bremer, M., Disseau, L., Dos Santos, S., Gandhi, P., Jean, C., Pacaud, F., Read, A., Refregier, A., Willis, J., Adami, C., Alloin, D., Birkinshaw, M., Chiappetti, L., Cohen, A., Detal, A., Duc, P.-A., Gosset, E., Hjorth, J., Jones, L., Le Fèvre, O., Lonsdale, C., Maccagni, D., Mazure, A., McBreen, B., McCracken, H., Mellier, Y., Ponman, T., Quintana, H., Rottgering, H., Smette, A., Surdej, J., Starck, J.-L., Vigroux, L., and White, S. (2004). The XMM-LSS survey. Survey design and first results. *JCAP*, 9:011.

Pizzella, A., Corsini, E. M., Sarzi, M., Magorrian, J., Méndez-Abreu, J., Coccato, L., Morelli, L., and Bertola, F. (2008). Structure and dynamics of galaxies with a low surface-brightness disc - I. The stellar and ionized-gas kinematics. *MNRAS*, 387:1099–1116.

Planck Collaboration (2013). Planck intermediate results. X. Physics of the hot gas in the Coma cluster. *AAP*, 554:A140.

Planck Collaboration (2014). Planck 2013 results. XX. Cosmology from Sunyaev-Zeldovich cluster counts. *AAP*, 571:A20.

Planck Collaboration (2015a). Planck 2015 results. XI. CMB power spectra, likelihoods, and robustness of parameters. *ArXiv e-prints*.

Planck Collaboration (2015b). Planck 2015 results. XIII. Cosmological parameters. *ArXiv e-prints*.

Pourhasan, R., Afshordi, N., Mann, R. B., and Davis, A. C. (2011). Chameleon gravity, electrostatics, and kinematics in the outer galaxy. *JCAP*, 12:005.

Press, W. H. and Schechter, P. (1974). Formation of Galaxies and Clusters of Galaxies by Self-Similar Gravitational Condensation. *ApJ*, 187:425–438.

Puchwein, E., Baldi, M., and Springel, V. (2013). Modified-Gravity-GADGET: a new code for cosmological hydrodynamical simulations of modified gravity models. *MNRAS*, 436:348–360.

Rasia, E., Tormen, G., and Moscardini, L. (2004). A dynamical model for the distribution of dark matter and gas in galaxy clusters. *MNRAS*, 351:237–252.

Raveri, M., Hu, B., Frusciante, N., and Silvestri, A. (2014). Effective field theory of cosmic acceleration: Constraining dark energy with CMB data. *PRD*, 90(4):043513.

Reichardt, C. L. et al. (2013). Galaxy Clusters Discovered via the Sunyaev-Zel'dovich Effect in the First 720 Square Degrees of the South Pole Telescope Survey. *ApJ*, 763:127.

Reiprich, T. H. and Böhringer, H. (2002). The Mass Function of an X-Ray Flux-limited Sample of Galaxy Clusters. *ApJ*, 567:716–740.

Riess, A. G. et al. (1998). Observational Evidence from Supernovae for an Accelerating Universe and a Cosmological Constant. *AJ*, 116:1009–1038.

Robertson, H. P. (1935). Kinematics and World-Structure. *ApJ*, 82:284.

Romer, A. K., Viana, P. T. P., Liddle, A. R., and Mann, R. G. (2001). A Serendipitous Galaxy Cluster Survey with XMM: Expected Catalog Properties and Scientific Applications. *ApJ*, 547:594–608.

Sachs, R. K. and Wolfe, A. M. (1967). Perturbations of a Cosmological Model and Angular Variations of the Microwave Background. *ApJ*, 147:73.

Sahlén, M., Viana, P. T. P., Liddle, A. R., Romer, A. K., Davidson, M., Hosmer, M., Lloyd-Davies, E., Sabirli, K., Collins, C. A., Freeman, P. E., Hilton, M., Hoyle, B., Kay, S. T., Mann, R. G., Mehrtens, N., Miller, C. J., Nichol, R. C., Stanford, S. A., and West, M. J. (2009). The XMM Cluster Survey: forecasting cosmological and cluster scaling-relation parameter constraints. *MNRAS*, 397:577–607.

Sakstein, J. (2015). Testing gravity using dwarf stars. *PRD*, 92(12):124045.

Sakstein, J., Wilcox, H., Bacon, D., Koyama, K., and Nichol, R. C. (2016). Testing gravity using galaxy clusters: new constraints on beyond Horndeski theories. *JCAP*, 7:019.

Sànchez, N. G. and Parijskij, Y. N. (2012). *The Early Universe and the Cosmic Microwave Background: Theory and Observations*. Springer Science & Business Media.

Sarazin, C. L. (1986). X-ray emission from clusters of galaxies. *Rev. Mod. Phys.*, 58:1–115.

Sarazin, C. L. (1986). X-ray emission from clusters of galaxies. *Rev. Mod. Phys.*, 58:1–115.

Sato, T., Sasaki, T., Matsushita, K., Sakuma, E., Sato, K., Fujita, Y., Okabe, N., Fukazawa, Y., Ichikawa, K., Kawaharada, M., Nakazawa, K., Ohashi, T., Ota, N., Takizawa, M., and Tamura, T. (2012). Suzaku Observations of the Hydra A Cluster out to the Virial Radius. *PASJ*, 64.

Schellenberger, G., Reiprich, T. H., Lovisari, L., Nevalainen, J., and David, L. (2015). XMM-Newton and Chandra cross-calibration using HIFLUGCS galaxy clusters . Systematic temperature differences and cosmological impact. *AAP*, 575:A30.

Schmidt, F. (2009). Cosmological simulations of normal-branch braneworld gravity. *PRD*, 80(12):123003.

Schmidt, F., Lima, M., Oyaizu, H., and Hu, W. (2009). Nonlinear evolution of f(R) cosmologies. III. Halo statistics. *PRD*, 79(8):083518.

Schneider, P., Ehlers, J., and Falco, E. E. (1992). *Gravitational Lenses*. Springer.

Schutz, B. F. (1985). *A First Course in General Relativity*. Cambridge University Press.

Sérsic, J. L. (1963). Influence of the atmospheric and instrumental dispersion on the brightness distribution in a galaxy. *Boletin de la Asociacion Argentina de Astronomia La Plata Argentina*, 6:41.

Shan, H. Y., Kneib, J.-P., Comparat, J., Jullo, E., Charbonnier, A., Erben, T., Makler, M., Moraes, B., Van Waerbeke, L., Courbin, F., Meylan, G., Tao, C., and Taylor, J. E. (2014). Weak lensing mass map and peak statistics in Canada-France-Hawaii Telescope Stripe 82 survey. *MNRAS*, 442:2534–2542.

Shandarin, S., Feldman, H. A., Heitmann, K., and Habib, S. (2006). Shapes and sizes of voids in the Lambda cold dark matter universe: excursion set approach. *MNRAS*, 367:1629–1640.

Shaw, L. D., Nagai, D., Bhattacharya, S., and Lau, E. T. (2010). Impact of Cluster Physics on the Sunyaev-Zel'dovich Power Spectrum. *ApJ*, 725:1452–1465.

Sheldon, E. S., Annis, J., Böhringer, H., Fischer, P., Frieman, J. A., Joffre, M., Johnston, D., McKay, T. A., Miller, C., Nichol, R. C., Stebbins, A., Voges, W., Anderson, S. F., Bahcall, N. A., Brinkmann, J., Brunner, R., Csabai, I., Fukugita, M., Hennessy, G. S., Ivezić, Ž., Lupton, R. H., Munn, J. A., Pier, J. R., and York, D. G. (2001). Weak-Lensing Measurements of 42 SDSS/RASS Galaxy Clusters. *ApJ*, 554:881–887.

Sheldon, E. S., Johnston, D. E., Scranton, R., Koester, B. P., McKay, T. A., Oyaizu, H., Cunha, C., Lima, M., Lin, H., Frieman, J. A., Wechsler, R. H., Annis, J., Mandelbaum, R., Bahcall, N. A., and Fukugita, M. (2009). Cross-correlation Weak Lensing of SDSS Galaxy Clusters. I. Measurements. *ApJ*, 703:2217–2231.

Sheth, R. K. and Tormen, G. (1999). Large-scale bias and the peak background split. *MNRAS*, 308:119–126.

Simionescu, A., Allen, S. W., Mantz, A., Werner, N., Takei, Y., Morris, R. G., Fabian, A. C., Sanders, J. S., Nulsen, P. E. J., George, M. R., and Taylor, G. B. (2011). Baryons at the Edge of the X-ray-Brightest Galaxy Cluster. *Science*, 331:1576–.

Slezak, E., Bijaoui, A., and Mars, G. (1990). Identification of structures from galaxy counts - Use of the wavelet transform. *AAP*, 227:301–316.

Smith, R. K., Brickhouse, N. S., Liedahl, D. A., and Raymond, J. C. (2001). Collisional Plasma Models with APEC/APED: Emission-Line Diagnostics of Hydrogen-like and Helium-like Ions. *ApJL*, 556:L91–L95.

Snowden, S. L., Mushotzky, R. F., Kuntz, K. D., and Davis, D. S. (2008). A catalog of galaxy clusters observed by XMM-Newton. *AAP*, 478:615–658.

Song, Y.-S., Hu, W., and Sawicki, I. (2007). Large scale structure of f(R) gravity. *PRD*, 75(4):044004.

Sotiriou, T. P. and Faraoni, V. (2010). f(R) theories of gravity. *Reviews of Modern Physics*, 82:451–497.

Spiga, D., Cotroneo, V., Basso, S., and Conconi, P. (2009). Analytical computation of the off-axis effective area of grazing incidence X-ray mirrors. *AAP*, 505:373–384.

Spitzer, Jr., L. and Greenstein, J. L. (1951). Continuous Emission from Planetary Nebulae. *ApJ*, 114:407.

Starobinsky, A. A. (2007). Disappearing cosmological constant in f(R) gravity. *Soviet Journal of Experimental and Theoretical Physics Letters*, 86:157–163.

Stott, J. P., Hickox, R. C., Edge, A. C., Collins, C. A., Hilton, M., Harrison, C. D., Romer, A. K., Rooney, P. J., Kay, S. T., Miller, C. J., Sahlén, M., Lloyd-Davies, E. J., Mehrtens, N., Hoyle, B., Liddle, A. R., Viana, P. T. P., McCarthy, I. G., Schaye, J., and Booth, C. M. (2012). The XMM Cluster Survey: the interplay between the brightest cluster galaxy and the intracluster medium via AGN feedback. *MNRAS*, 422:2213–2229.

Strüder, L., Briel, U., Dennerl, K., Hartmann, R., Kendziorra, E., Meidinger, N., Pfeffermann, E., Reppin, C., Aschenbach, B., Bornemann, W., Bräuninger, H., Burkert, W., Elender, M., Freyberg, M., Haberl, F., Hartner, G., Heuschmann, F., Hippmann, H., Kastelic, E., Kemmer, S., Kettenring, G., Kink, W., Krause, N., Müller, S., Oppitz, A., Pietsch, W., Popp, M., Predehl, P., Read, A., Stephan, K. H., Stötter, D., Trümper, J., Holl, P., Kemmer, J., Soltau, H., Stötter, R., Weber, U., Weichert, U., von Zanthier, C., Carathanassis, D., Lutz, G., Richter, R. H., Solc, P., Böttcher, H., Kuster, M., Staubert, R., Abbey, A., Holland, A., Turner, M., Balasini, M., Bignami, G. F., La Palombara, N., Villa, G., Buttler, W., Gianini, F., Lainé, R., Lumb, D., and Dhez, P. (2001). The European Photon Imaging Camera on XMM-Newton: The pn-CCD camera. *AAP*, 365:L18–L26.

Stubbs, C. W., Adelberger, E. G., Raab, F. J., Gundlach, J. H., Heckel, B. R., McMurry, K. D., Swanson, H. E., and Watanabe, R. (1987). Search for an intermediate-range interaction. *PRL*, 58:1070–1073.

Suzuki, N., Rubin, D., Lidman, C., Aldering, G., Amanullah, R., Barbary, K., Barrientos, L. F., Botyanszki, J., Brodwin, M., Connolly, N., Dawson, K. S., Dey, A., Doi, M., Donahue, M., Deustua, S., Eisenhardt, P., Ellingson, E., Faccioli, L., Fadeyev, V., Fakhouri, H. K., Fruchter, A. S., Gilbank, D. G., Gladders, M. D., Goldhaber, G., Gonzalez, A. H., Goobar, A., Gude, A., Hattori, T., Hoekstra, H., Hsiao, E., Huang, X., Ihara, Y., Jee, M. J., Johnston, D., Kashikawa, N., Koester, B., Konishi, K., Kowalski, M., Linder, E. V., Lubin, L., Melbourne, J., Meyers, J., Morokuma, T., Munshi, F., Mullis, C., Oda, T., Panagia, N., Perlmutter, S., Postman, M., Pritchard, T., Rhodes, J., Ripoche, P., Rosati, P., Schlegel, D. J., Spadafora, A., Stanford, S. A., Stanishev, V., Stern, D., Strovink, M., Takanashi, N., Tokita, K., Wagner, M., Wang, L., Yasuda, N., Yee, H. K. C., and Supernova Cosmology Project, T. (2012). The Hubble Space Telescope Cluster Supernova Survey. V. Improving the Dark-energy Constraints above $z > 1$ and Building an Early-type-hosted Supernova Sample. *ApJ*, 746:85.

Takey, A., Schwope, A., and Lamer, G. (2013). The 2XMMi/SDSS Galaxy Cluster Survey. II. The optically confirmed cluster sample and the L_X - T relation. *AAP*, 558:A75.

Terukina, A., Lombriser, L., Yamamoto, K., Bacon, D., Koyama, K., and Nichol, R. C. (2014). Testing chameleon gravity with the Coma cluster. *JCAP*, 4:13.

Terukina, A. and Yamamoto, K. (2012). Gas Density Profile in Dark Matter Halo in Chameleon Cosmology. *PRD*, 86(10):103503.

The Dark Energy Survey Collaboration (2005). The Dark Energy Survey. *ArXiv e-prints*.

Thölken, S., Lovisari, L., Reiprich, T. H., and Hasenbusch, J. (2016). X-ray analysis of the galaxy group UGC03957 beyond R200 with Suzaku. *ArXiv e-prints*.

Thomson, S. J. J. and Thomson, G. P. (1933). Conduction of electricity through gases. *The Journal of Physical Chemistry*, 38(7):987–987.

Tinker, J., Kravtsov, A. V., Klypin, A., Abazajian, K., Warren, M., Yepes, G., Gottlöber, S., and Holz, D. E. (2008). Toward a Halo Mass Function for Precision Cosmology: The Limits of Universality. *ApJ*, 688:709–728.

Tinker, J. L., Sheldon, E. S., Wechsler, R. H., Becker, M. R., Rozo, E., Zu, Y., Weinberg, D. H., Zehavi, I., Blanton, M. R., Busha, M. T., and Koester, B. P. (2012). Cosmological Constraints from Galaxy Clustering and the Mass-to-number Ratio of Galaxy Clusters. *ApJ*, 745:16.

Tissera, P. B. and Dominguez-Tenreiro, R. (1998). Dark matter halo structure in CDM hydrodynamical simulations. *MNRAS*, 297:177–194.

Tojeiro, R. (2006). Understanding the cosmic microwave background temperature power spectrum. *alm*, 2:6.

Tsujikawa, S. (2010). Modified Gravity Models of Dark Energy. In Wolschin, G., editor, *Lecture Notes in Physics, Berlin Springer Verlag*, volume 800 of *Lecture Notes in Physics, Berlin Springer Verlag*, pages 99–145.

Turner, M. S. (1990). Windows on the axion. *Phys. Rep.*, 197:67–97.

Tyson, J. A., Valdes, F., and Wenk, R. A. (1990). Detection of systematic gravitational lens galaxy image alignments - Mapping dark matter in galaxy clusters. *ApJL*, 349:L1–L4.

Udalski, A., Soszynski, I., Szymanski, M., Kubiak, M., Pietrzynski, G., Wozniak, P., and Zebrun, K. (1999). The Optical Gravitational Lensing Experiment. Cepheids in the Magellanic Clouds. IV. Catalog of Cepheids from the Large Magellanic Cloud. *ActAa*, 49:223–317.

Vafaei, S., Lu, T., van Waerbeke, L., Semboloni, E., Heymans, C., and Pen, U.-L. (2010). Breaking the degeneracy: Optimal use of three-point weak lensing statistics. *Astroparticle Physics*, 32:340–351.

Vainshtein, A. I. (1972). To the problem of nonvanishing gravitation mass. *Physics Letters B*, 39:393–394.

Valtchanov, I., Pierre, M., Willis, J., Dos Santos, S., Jones, L., Andreon, S., Adami, C., Altieri, B., Bolzonella, M., Bremer, M., Duc, P.-A., Gosset, E., Jean, C., and Surdej, J. (2004). The XMM-LSS survey. First high redshift galaxy clusters: Relaxed and collapsing systems. *AAp*, 423:75–85.

Van Waerbeke, L., Benjamin, J., Erben, T., Heymans, C., Hildebrandt, H., Hoekstra, H., Kitching, T. D., Mellier, Y., Miller, L., Coupon, J., Harnois-Déraps, J., Fu, L., Hudson, M., Kilbinger, M., Kuijken, K., Rowe, B., Schrabback, T., Semboloni, E., Vafaei, S., van Uitert, E., and Velander, M. (2013). CFHTLenS: mapping the large-scale structure with gravitational lensing. *MNRAS*, 433:3373–3388.

Van Waerbeke, L., Mellier, Y., Radovich, M., Bertin, E., Dantel-Fort, M., McCracken, H. J., Le Fèvre, O., Foucaud, S., Cuillandre, J.-C., Erben, T., Jain, B., Schneider, P., Bernardeau, F., and Fort, B. (2001). Cosmic shear statistics and cosmology. *AAP*, 374:757–769.

Vikhlinin, A., Kravtsov, A., Forman, W., Jones, C., Markevitch, M., Murray, S. S., and Van Speybroeck, L. (2006). Chandra Sample of Nearby Relaxed Galaxy Clusters: Mass, Gas Fraction, and Mass-Temperature Relation. *ApJ*, 640:691–709.

Vikram, V., Cabré, A., Jain, B., and VanderPlas, J. T. (2013). Astrophysical tests of modified gravity: the morphology and kinematics of dwarf galaxies. *JCAP*, 8:20.

Vikram, V., Chang, C., Jain, B., Bacon, D., Amara, A., Becker, M. R., Bernstein, G., Bonnett, C., Bridle, S., Brout, D., Busha, M., Frieman, J., Gaztanaga, E., Hartley, W., Jarvis, M., Kacprzak, T., Kovács, A., Lahav, O., Leistedt, B., Lin, H., Melchior, P., Peiris, H., Rozo, E., Rykoff, E., Sánchez, C., Sheldon, E., Troxel, M. A., Wechsler, R., Zuntz, J., Abbott, T., Abdalla, F. B., Armstrong, R., Banerji, M., Bauer, A. H., Benoit-Lévy, A., Bertin, E., Brooks, D., Buckley-Geer, E., Burke, D. L., Capozzi, D., Carnero Rosell, A., Carrasco Kind, M., Castander, F. J., Crocce, M., Cunha, C. E., D'Andrea, C. B., da Costa, L. N., DePoy, D. L., Desai, S., Diehl, H. T., Dietrich, J. P., Estrada, J., Evrard, A. E., Fausti Neto, A., Fernandez, E., Flaugher, B., Fosalba, P., Gerdes, D., Gruen, D., Gruendl, R. A., Honscheid, K., James, D., Kent, S., Kuehn, K., Kuropatkin, N., Li, T. S., Maia, M. A. G., Makler, M., March, M., Marshall, J., Martini, P., Merritt, K. W., Miller, C. J., Miquel, R., Neilsen, E., Nichol, R. C., Nord, B., Ogando, R., Plazas, A. A., Romer, A. K., Roodman, A., Sanchez, E., Scarpine, V., Sevilla, I., Smith, R. C., Soares-Santos, M., Sobreira, F., Suchyta, E., Swanson, M. E. C., Tarle, G., Thaler, J., Thomas, D., Walker, A. R., and Weller, J. (2015). Wide-field lensing mass maps from Dark Energy Survey science verification data: Methodology and detailed analysis. *PRD*, 92(2):022006.

Vikram, V., Sakstein, J., Davis, C., and Neil, A. (2014). Astrophysical Tests of Modified Gravity: Stellar and Gaseous Rotation Curves in Dwarf Galaxies. *ArXiv e-prints*.

von der Linden, A., Allen, M. T., Applegate, D. E., Kelly, P. L., Allen, S. W., Ebeling, H., Burchat, P. R., Burke, D. L., Donovan, D., Morris, R. G., Blandford, R., Erben, T., and Mantz, A. (2014). Weighing the Giants - I. Weak-lensing masses for 51 massive galaxy clusters: project overview, data analysis methods and cluster images. *MNRAS*, 439:2–27.

von der Linden, A., Allen, M. T., Applegate, D. E., Kelly, P. L., Allen, S. W., Ebeling, H., Burchat, P. R., Burke, D. L., Donovan, D., Morris, R. G., Blandford, R., Erben, T., and Mantz, A. (2014). Weighing the giants i. weak-lensing masses for 51 massive galaxy clusters: project overview, data analysis methods and cluster images. *MNRAS*.

von der Linden, A., Mantz, A., Allen, S. W., Applegate, D. E., Kelly, P. L., Morris, R. G., Wright, A., Allen, M. T., Burchat, P. R., Burke, D. L., Donovan, D., and Ebeling, H. (2014). Robust weak-lensing mass calibration of Planck galaxy clusters. *MNRAS*, 443:1973–1978.

Wagner, T. A., Schlamminger, S., Gundlach, J. H., and Adelberger, E. G. (2012). Torsion-balance tests of the weak equivalence principle. *Classical and Quantum Gravity*, 29(18):184002.

Wagner, T. A., Schlamminger, S., Gundlach, J. H., and Adelberger, E. G. (2012). Torsion-balance tests of the weak equivalence principle. *Class. Quant. Grav.*, 29:184002.

Walker, A. G. (1937). On milne's theory of world-structure. *Proceedings of the London Mathematical Society*, s2-42(1):90–127.

Wambsganss, J. (1998). Gravitational lensing in astronomy. *Living Reviews in Relativity*, 1(12).

Weinberg, S. (1989). The cosmological constant problem. *Reviews of Modern Physics*, 61:1–23.

Weisskopf, M. C., Tananbaum, H. D., Van Speybroeck, L. P., and O'Dell, S. L. (2000). Chandra X-ray Observatory (CXO): overview. In Truemper, J. E. and Aschenbach, B., editors, *X-Ray Optics, Instruments, and Missions III*, volume 4012 of *ProcSPIE*, pages 2–16.

Wen, Z. L. and Han, J. L. (2011). Galaxy Clusters at High Redshift and Evolution of Brightest Cluster Galaxies. *ApJ*, 734:68.

Wen, Z. L., Han, J. L., and Liu, F. S. (2010). Erratum: Galaxy Clusters Identified from the Sloan Digital Sky Survey DR6 and their Properties. *ApJS*, 187:272–273.

Wen, Z. L., Han, J. L., and Liu, F. S. (2012). VizieR Online Data Catalog: Clusters of galaxies in SDSS-III (Wen+, 2012). *VizieR Online Data Catalog*, 219:90034.

Wheeler, J. A. (2010). *Geons, Black Holes, and Quantum Foam: A Life in Physics*. W. W. Norton & Company.

White, D. A. (2000). Deconvolution of ASCA X-ray data - II. Radial temperature and metallicity profiles for 106 galaxy clusters. *MNRAS*, 312:663–688.

Wik, D. R., Sarazin, C. L., Finoguenov, A., Matsushita, K., Nakazawa, K., and Clarke, T. E. (2009). A Suzaku Search for Nonthermal Emission at Hard X-Ray Energies in the Coma Cluster. *ApJ*, 696:1700–1711.

Wilcox, H., Bacon, D., Nichol, R. C., Rooney, P. J., Terukina, A., Romer, A. K., Koyama, K., Zhao, G.-B., Hood, R., Mann, R. G., Hilton, M., Manolopoulou, M., Sahlén, M., Collins, C. A., Liddle, A. R., Mayers, J. A., Mehrtens, N., Miller, C. J., Stott, J. P.,

and Viana, P. T. P. (2015). The XMM Cluster Survey: testing chameleon gravity using the profiles of clusters. *MNRAS*, 452:1171–1183.

Wilcox, H., Nichol, R. C., Zhao, G.-b., Bacon, D., Koyama, K., and Romer, A. K. (2016). Simulation tests of galaxy cluster constraints on chameleon gravity. *ArXiv e-prints*.

Williams, J. G., Turyshev, S. G., and Boggs, D. H. (2012). Lunar laser ranging tests of the equivalence principle. *Classical and Quantum Gravity*, 29(18):184004.

Winther, H. A., Schmidt, F., Barreira, A., Arnold, C., Bose, S., Llinares, C., Baldi, M., Falck, B., Hellwing, W. A., Koyama, K., Li, B., Mota, D. F., Puchwein, E., Smith, R. E., and Zhao, G.-B. (2015). Modified gravity N-body code comparison project. *MNRAS*, 454:4208–4234.

Wittman, D. M., Jain, B., Jarvis, M., Knox, L., Margoniner, V., Takada, M., Tyson, J., Zhan, H., and LSST Weak Lensing Science Collaboration (2006). Weak Lensing with LSST. In *American Astronomical Society Meeting Abstracts*, volume 38 of *Bulletin of the American Astronomical Society*, page 1019.

Wittman, D. M., Tyson, J. A., Kirkman, D., Dell'Antonio, I., and Bernstein, G. (2000). Detection of weak gravitational lensing distortions of distant galaxies by cosmic dark matter at large scales. *Nature*, 405:143–148.

Wright, C. O. and Brainerd, T. G. (2000). Gravitational lensing by nfw halos. *The Astrophysical Journal*, 534(1):34.

Zhao, G.-B., Li, B., and Koyama, K. (2011a). N-body simulations for f(R) gravity using a self-adaptive particle-mesh code. *PRD*, 83(4):044007.

Zhao, G.-B., Li, B., and Koyama, K. (2011b). Testing Gravity Using the Environmental Dependence of Dark Matter Halos. *PRL*, 107(7):071303.

ZuHone, J. A., Biffi, V., Hallman, E. J., Randall, S. W., Foster, A. R., and Schmid, C. (2014). Simulating X-ray Observations with Python. *ArXiv e-prints*.

Zwicky, F. (1933). Die Rotverschiebung von extragalaktischen Nebeln. *Helvetica Physica Acta*, 6:110–127.

Zwicky, F. (1937). On the Masses of Nebulae and of Clusters of Nebulae. *ApJ*, 86:217.